

**COMPRESSIONAL-TO-SHEAR-WAVE VELOCITY RATIO IN ORGANIC SHALES  
AND ACOUSTIC DISPERSION IN LOW PERMEABILITY UNCONVENTIONAL  
RESERVOIR ROCKS**

**By**

**Sheyore John Omovie**

**A Dissertation submitted to the**

**the Department of Earth and Atmospheric Sciences,**

**College of Natural Sciences and Mathematics**

**In Partial Fulfillment of the Requirements for the Degree of**

**Doctor of Philosophy**

**in Geophysics**

**Chair of Committee: John P. Castagna**

**Committee Member: Evgeny Chesnokov**

**Committee Member: Yingcai Zheng**

**Committee Member: Mike Myers**

**University of Houston**

**December 2019**

## **ACKNOWLEDGEMENTS**

I would like to begin this section by saying a big thank you to Dr. John Castagna, my advisor. This research work would not have seen the light of day without his support, guidance and patience with me. Beyond guiding me through the process of rigorously applying the scientific method to any research work; he is also responsible in ensuring significant improvement in my scientific writing abilities and thus by extension that the dissertation you are about to read is well written. For that I would always feel greatly indebted to him.

I would also like to thank Dr. Mike Myers for granting me permission to conduct experiments in his Rock Physics laboratory; but more importantly his guidance while conducting those experiments as well as while writing our acoustic dispersion manuscript. I also appreciate the support of Sabya and Mohab – his graduate students – while conducting experiments in the laboratory. Special thanks also go to Occidental Petroleum Corporation (Oxy) for granting me permission to use their data and rock samples in my research work.

Finally, I would also like to say a big thank you to my loving and supportive wife, Goodness. I learned the hard way that completing a doctoral program is no easy task. On more than one occasion I came very close to quitting the program, but because of her encouragement and emotional support that didn't happen.

## ABSTRACT

*In situ* P-wave and S-wave velocity measurements in a variety of organic-rich shales exhibit compressional-to-shear-wave velocity ratios that are significantly lower than lithologically similar fully brine-saturated shales having low organic content. It has been hypothesized that this drop could be explained by the direct influence of kerogen on the rock frame and/or by the presence of free hydrocarbons in the pore space. Theoretical bounding equations, using pure kerogen as an end-member component without associated gas, indicate that kerogen reduces both the P-wave and S-wave velocities but does not in general reduce their ratio. The theoretical modeling is consistent with ultrasonic measurements on organic-shale core samples that show no dependence of velocity ratios on kerogen volume alone. Sonic-log measurements of compressional and shear-wave velocities in seven organic-rich shale formations deviate significantly from the Greenberg-Castagna empirical brine-saturated shale trend towards lower velocity ratios. In these formations, and on core measurements, Gassmann fluid substitution to 100% brine saturation yields velocity ratios consistent with the Greenberg-Castagna velocity trend for fully brine-saturated shales, despite the high organic content. These measurements, as well as theoretical modeling, all suggest that the velocity-ratio reduction in organic shales is best explained by the presence of free hydrocarbons.

The limitation of the Greenberg-Castagna shear-wave velocity prediction method when applied to organic-rich shales has been resolved, by modifying the original Greenberg-Castagna algorithm. The modified workflow accurately predicts shear-wave velocity for seven organic-shale formations with appreciable solid organic matter to within  $\pm 1\%$  percent mean error.

For a number of low-permeability well-lithified shales, utilizing laboratory measurements on dry and fully brine-saturated samples as well as comparing to log data and theoretical modeling, we find no statistically significant intrinsic dispersion from seismic to sonic and laboratory-measurement frequencies due to fluid effects. At *in situ* stress conditions, the Gassmann zero-frequency P-wave velocity prediction for a Permian-basin sample was within 0.2% to 2.2% of the measured velocity on the brine-saturated sample at ultrasonic frequency. Based on the Biot-Gassmann model, the characteristic frequency occurs at about  $10^{10}$  Hz. Applying a squirt-flow model also predicts a transition to the high-frequency regime occurring at about  $10^9$  Hz.

# TABLE OF CONTENTS

<b>ACKNOWLEDGEMENTS .....</b>	<b>ii</b>
<b>ABSTRACT.....</b>	<b>iii</b>
<b>LIST OF TABLES .....</b>	<b>viii</b>
<b>LIST OF FIGURES.....</b>	<b>xii</b>
<b>Chapter 1.....</b>	<b>1</b>
<b>INTRODUCTION .....</b>	<b>1</b>
1.1    MOTIVATION.....	1
1.2    ROCK COMPOSITION AND FLUID PROPERTIES .....	2
<b>Chapter 2.....</b>	<b>5</b>
<b>COMPRESSIONAL-TO-SHEAR-WAVE VELOCITY RATIO IN ORGANIC SHALES .....</b>	<b>5</b>
2.1    INTRODUCTION .....	5
2.2    CORRELATION OF WATER SATURATION AND KEROGEN VOLUME.....	9
2.3    KEROGEN OR SOLID ORGANIC-MATTER EFFECT .....	12
2.4    FLUID EFFECT .....	26
2.5    FLUID SUBSTITUTION .....	34
2.6    SENSITIVITY ANALYSIS.....	38
2.7    APPLICATION OF FLUID SUBSTITUTION TO SONIC LOG MEASUREMENTS IN ORGANIC SHALES.....	42
2.7.1    WOLFCAMP SHALE .....	42
2.7.2    LOWER SPRABERRY SHALE .....	46
2.7.3    AVALON SHALE.....	48
2.7.4    LOWER CLINE SHALE .....	49
2.7.5    WOODFORD SHALE .....	50
2.7.6    BAKKEN SHALE .....	52
2.7.7    EAGLEFORD SHALE .....	53
2.8    DISCUSSION.....	56
2.9    CONCLUSION.....	62
<b>Chapter 3.....</b>	<b>64</b>
<b>A SIMPLE EMPIRICAL SHEAR-WAVE VELOCITY PREDICTION METHOD FOR SHALES WITH HIGH ORGANIC CONTENT .....</b>	<b>64</b>
3.1    INTRODUCTION:.....	64
3.2    MODIFIED GREENBERG-CASTAGNA SHEAR VELOCITY PREDICTION IN ORGANIC-RICH SHALES .....	66

3.3	DETAILED IMPLEMENTATION PROCEDURE FOR MODIFIED GREENBERG-CASTAGNA SHEAR VELOCITY PREDICTION IN ORGANIC-RICH SHALES .....	75
3.4	RESULTS .....	81
3.4.1	Wolfcamp Shale: .....	83
3.4.2	Avalon Shale:.....	90
3.4.3	Lower Spraberry Shale: .....	97
3.4.4	Eagleford Shale: .....	105
3.4.5	Lower Cline Shale: .....	112
3.4.6	Bakken Shale: .....	118
3.4.7	Woodford Shale: .....	124
3.5	COMBINED RESULTS: .....	129
3.6	DISCUSSION.....	138
3.7	CONCLUSION.....	143
<b>Chapter 4</b>	<b>.....</b>	<b>145</b>
	<b>ACOUSTIC DISPERSION IN LOW PERMEABILITY UNCONVENTIONAL RESERVOIR ROCKS AND SHALES AT <i>IN SITU</i> STRESS CONDITIONS .....</b>	<b>145</b>
4.1	INTRODUCTION .....	145
4.2	THEORY .....	147
4.2.1	Biot-Gassmann model:.....	147
4.2.2	Squirt-flow model: .....	150
4.3	METHOD .....	151
4.3.1	Sample Description: .....	151
4.3.2	Experimental Procedure:.....	153
4.4	RESULTS .....	157
4.4.1	Biot-Gassmann Model Evaluation .....	157
4.4.2	Squirt-flow Model Evaluation.....	160
4.4.3	Cotton Valley Shale example .....	164
4.5	COMPARISON OF SONIC LOG TO ULTRASONIC FREQUENCY MEASUREMENTS .....	167
4.5.1	Bonespring formation example .....	169
4.5.2	Wolfcamp formation – Delaware basin example .....	174
4.5.3	Wolfcamp formation – Midland basin example .....	179
4.5.4	Lower Spraberry Shale example: .....	183
4.5.5	Combined results .....	187

4.6	DISCUSSION.....	194
4.6.1	Fluid Type:.....	198
4.7	CONCLUSION.....	198
	<b>BIBLIOGRAPHY.....</b>	<b>200</b>
	<b>APPENDIX A.....</b>	<b>209</b>
	<b>APPENDIX B.....</b>	<b>212</b>
	<b>APPENDIX C.....</b>	<b>214</b>
	<b>APPENDIX D.....</b>	<b>216</b>

## LIST OF TABLES

<b>Table 2.1:</b> .....	21
<b>Table 2.2:</b> .....	31
<b>Table 2.3:</b> .....	33
<b>Table 2.4:</b> .....	34
<b>Table 2.5:</b> .....	38
<b>Table 2.6a:</b> .....	40
<b>Table 2.6b:</b> .....	40
<b>Table 2.6c:</b> .....	41
<b>Table 2.7:</b> .....	55
<b>Table 2.8:</b> .....	55
<b>Table 3.1:</b> .....	77
<b>Table 3.2:</b> .....	82
<b>Table 3.3:</b> .....	82
<b>Table 3.4:</b> .....	83
<b>Table 3.5a:</b> .....	134
<b>Table 3.5b:</b> .....	134

<b>Table 3.6a:</b> .....	135
<b>Table 3.6b:</b> .....	135
<b>Table 3.7a:</b> .....	136
<b>Table 3.7b:</b> .....	136
<b>Table 3.7c:</b> .....	137
<b>Table 3.7d:</b> .....	137
<b>Table 3.7e:</b> .....	138
<b>Table 3.7f:</b> .....	138
<b>Table 3.8:</b> .....	142
<b>Table 4.1:</b> .....	152
<b>Table 4.2a:</b> .....	159
<b>Table 4.2b:</b> .....	160
<b>Table 4.3a:</b> .....	169
<b>Table 4.3b:</b> .....	169
<b>Table 4.4a:</b> .....	173
<b>Table 4.4b:</b> .....	173
<b>Table 4.4c:</b> .....	174

<b>Table 4.5a:</b> .....	178
<b>Table 4.5b:</b> .....	178
<b>Table 4.5c:</b> .....	179
<b>Table 4.6a:</b> .....	182
<b>Table 4.6b:</b> .....	182
<b>Table 4.6c:</b> .....	183
<b>Table 4.7a:</b> .....	186
<b>Table 4.7b:</b> .....	186
<b>Table 4.7c:</b> .....	187
<b>Table 4.8a:</b> .....	189
<b>Table 4.8b:</b> .....	190
<b>Table 4.8c:</b> .....	190
<b>Table 4.9a:</b> .....	191
<b>Table 4.9b:</b> .....	191
<b>Table 4.9c:</b> .....	192
<b>Table 4.10a:</b> .....	192
<b>Table 4.10b:</b> .....	193

<b>Table 4.10c:</b> .....	193
<b>Table A-1:</b> .....	211
<b>Table B-1:</b> .....	213
<b>Table D-1:</b> .....	216

## LIST OF FIGURES

Figure 1.1: .....	4
Figure 2.1: .....	9
Figure 2.2: .....	10
Figure 2.3a: .....	11
Figure 2.3b: .....	12
Figure 2.4a: .....	17
Figure 2.4b: .....	18
Figure 2.5a: .....	19
Figure 2.5b: .....	20
Figure 2.5c: .....	22
Figure 2.6: .....	23
Figure 2.7: .....	25
Figure 2.8: .....	28
Figure 2.9: .....	29
Figure 2.10: .....	30
Figure 2.11: .....	33

<b>Figure 2.12:</b> .....	37
<b>Figure 2.13:</b> .....	44
<b>Figure 2.14:</b> .....	45
<b>Figure 2.15:</b> .....	46
<b>Figure 2.16:</b> .....	47
<b>Figure 2.17:</b> .....	48
<b>Figure 2.18:</b> .....	50
<b>Figure 2.19:</b> .....	51
<b>Figure 2.20:</b> .....	52
<b>Figure 2.21:</b> .....	54
<b>Figure 2.22:</b> .....	61
<b>Figure 3.1a:</b> .....	68
<b>Figure 3.1b:</b> .....	69
<b>Figure 3.2:</b> .....	71
<b>Figure 3.3:</b> .....	74
<b>Figure 3.4a:</b> .....	85
<b>Figure 3.4b:</b> .....	86

Figure 3.4c: .....	87
Figure 3.4d: .....	88
Figure 3.4e: .....	89
Figure 3.4f: .....	90
Figure 3.5a: .....	92
Figure 3.5b: .....	93
Figure 3.5c: .....	94
Figure 3.5d: .....	95
Figure 3.5e: .....	96
Figure 3.5f: .....	97
Figure 3.6a: .....	99
Figure 3.6b: .....	100
Figure 3.6c: .....	101
Figure 3.6d: .....	102
Figure 3.6e: .....	103
Figure 3.6f: .....	104
Figure 3.7a: .....	106

<b>Figure 3.7b:</b> .....	107
<b>Figure 3.7c:</b> .....	108
<b>Figure 3.7d:</b> .....	109
<b>Figure 3.7e:</b> .....	110
<b>Figure 3.7f:</b> .....	111
<b>Figure 3.8a:</b> .....	113
<b>Figure 3.8b:</b> .....	114
<b>Figure 3.8c:</b> .....	115
<b>Figure 3.8d:</b> .....	116
<b>Figure 3.8e:</b> .....	117
<b>Figure 3.8f:</b> .....	118
<b>Figure 3.9a:</b> .....	120
<b>Figure 3.9b:</b> .....	121
<b>Figure 3.9c:</b> .....	122
<b>Figure 3.9d:</b> .....	123
<b>Figure 3.9e:</b> .....	124
<b>Figure 3.10a:</b> .....	125

<b>Figure 3.10b:</b> .....	126
<b>Figure 3.10c:</b> .....	127
<b>Figure 3.10d:</b> .....	128
<b>Figure 3.10e:</b> .....	129
<b>Figure 3.11:</b> .....	131
<b>Figure 3.12:</b> .....	132
<b>Figure 3.13:</b> .....	133
<b>Figure 3.14:</b> .....	142
<b>Figure 4.1:</b> .....	152
<b>Figure 4.2a:</b> .....	154
<b>Figure 4.2b:</b> .....	154
<b>Figures 4.3a:</b> .....	155
<b>Figures 4.3b:</b> .....	155
<b>Figure 4.4:</b> .....	156
<b>Figure 4.5:</b> .....	159
<b>Figure 4.6:</b> .....	162
<b>Figure 4.7:</b> .....	163

<b>Figure 4.8:</b> .....	165
<b>Figure 4.9:</b> .....	166
<b>Figure 4.10:</b> .....	167
<b>Figure 4.11:</b> .....	171
<b>Figure 4.12:</b> .....	172
<b>Figure 4.13:</b> .....	176
<b>Figure 4.14:</b> .....	177
<b>Figure 4.15:</b> .....	181
<b>Figure 4.16:</b> .....	185
<b>Figure 4.17:</b> .....	195
<b>Figure 4.18:</b> .....	195
<b>Figure A-1:</b> .....	211

# Chapter 1

## INTRODUCTION

### 1.1 MOTIVATION

In the acoustic measurements made in organic-rich shale formations, are fluid effects significant and detectable? What is primarily responsible for the low compressional-to-shear-wave velocity ratio observed in organic-rich shale formations when compared to wet inorganic-shale formations? This research project focuses on answering the above questions using data from several organic-rich shale formations. Currently, the general thinking in the industry and academia is that because of the very low permeability and porosity in these shale formations, fluid effects are insignificant and unlikely to be measurable. To our knowledge, no one has done an extensive study of several organic-rich shale formations to address these questions. On the other hand, several authors have explained that the low compressional-to-shear-wave (P-wave to S-wave) velocity ratio ( $V_p/V_s$ ) observed in organic-rich shale formations are due to the presence of kerogen or organic matter in these shale formations. In this dissertation we attempt to answer the question of whether the low  $V_p/V_s$  observed in organic shales is due primarily to the presence of kerogen or if it is due to hydrocarbon fluids.

In organic-rich shales, the Greenberg-Castagna shear-wave velocity ( $V_s$ ) prediction method overestimates shear-wave velocities if kerogen or solid organic matter is not explicitly taken into account. Using this method, we find for well logs in seven different shale reservoirs with average solid organic matter volume fraction varying from 5% to 26% and with formation

fluid varying from dry gas and brine to oil and brine, percent mean signed error to be 1.57% varying from 0.36% to 17.71% in individual reservoirs, when compared to shear-wave velocity logs; and with percent standard error of 4.2%, ranging from 2.4% to 17.9%. Another goal of my research addresses if we can modify the original Greenberg-Castagna shear-wave velocity prediction method such that it yields accurate shear-wave velocity estimates in organic-rich shale formations.

Finally, we address the question of whether for low-permeability well-lithified shales theoretical models and measurements indicate significant dispersion from seismic to sonic and laboratory-measurement frequencies due to fluid effects, at *in situ* stress conditions.

## **1.2 ROCK COMPOSITION AND FLUID PROPERTIES**

For fluid substitution, shear-wave velocity prediction, and dispersion analyses, determination of the effective solid matrix bulk modulus is required. To accomplish this in mixed-lithology formations, an appropriate mixing model is required to mix the constituent lithologies. All mixing models require accurate determination of rock constituent volume fractions. In this study, we will rely on well-log volumetric analyses. We obtain clay volume through a combination of the neutron-density cross plot and uranium stripping of the spectral gamma-ray log. The clay volume is then calibrated to core XRD (X-ray diffraction) clay volumes (see Figure 1.1) when available. TOC (total organic carbon) is estimated using an average of the Passey, and Schmoker methods (Passey et al., 1990; Schmoker and Hester, 1979); then calibrated to core TOC. Given TOC, kerogen or solid organic matter volume is then determined using:

$$K = \frac{TOC\rho_m}{C_k\rho_k}, \quad (1.1)$$

where  $\rho_m, \rho_k$  are the matrix and kerogen density respectively, and  $C_k$  is the carbon concentration in the solid organic matter.  $K$  is kerogen volume (Alfred and Vernik, 2012) and TOC is weight percent of total organic carbon.

The kerogen volume along with the clay volume and open-hole log data are fed into a petrophysical probabilistic interpretation workflow to determine rock composition and total porosity. For a discussion of probabilistic well-log interpretation, we refer the reader to Quirein et al., (2010) and Vosburgh et al., (2013). We check to make sure lithology volumes obtained from the above matches with core XRD mineralogy data (Figure 1.1). Before comparison with XRD weight-percent mineralogy, the core XRD data is first converted to mineralogy on a bulk-rock basis; this process requires core porosity and grain densities.

We use an Archie total-porosity saturation model to obtain water saturation (cementation and saturation exponents were assumed to be 2; brine resistivity is obtained from water salinity report for each of the formations), which is then calibrated to core Gas Research Institute (GRI) water saturation. The equations of Batzle and Wang (1992) and Batzle and Han (2000) are used to obtain brine, oil and gas properties at *in situ* temperatures and pressures. These are required both for the petrophysical interpretation, fluid substitution and shear-wave velocity prediction.

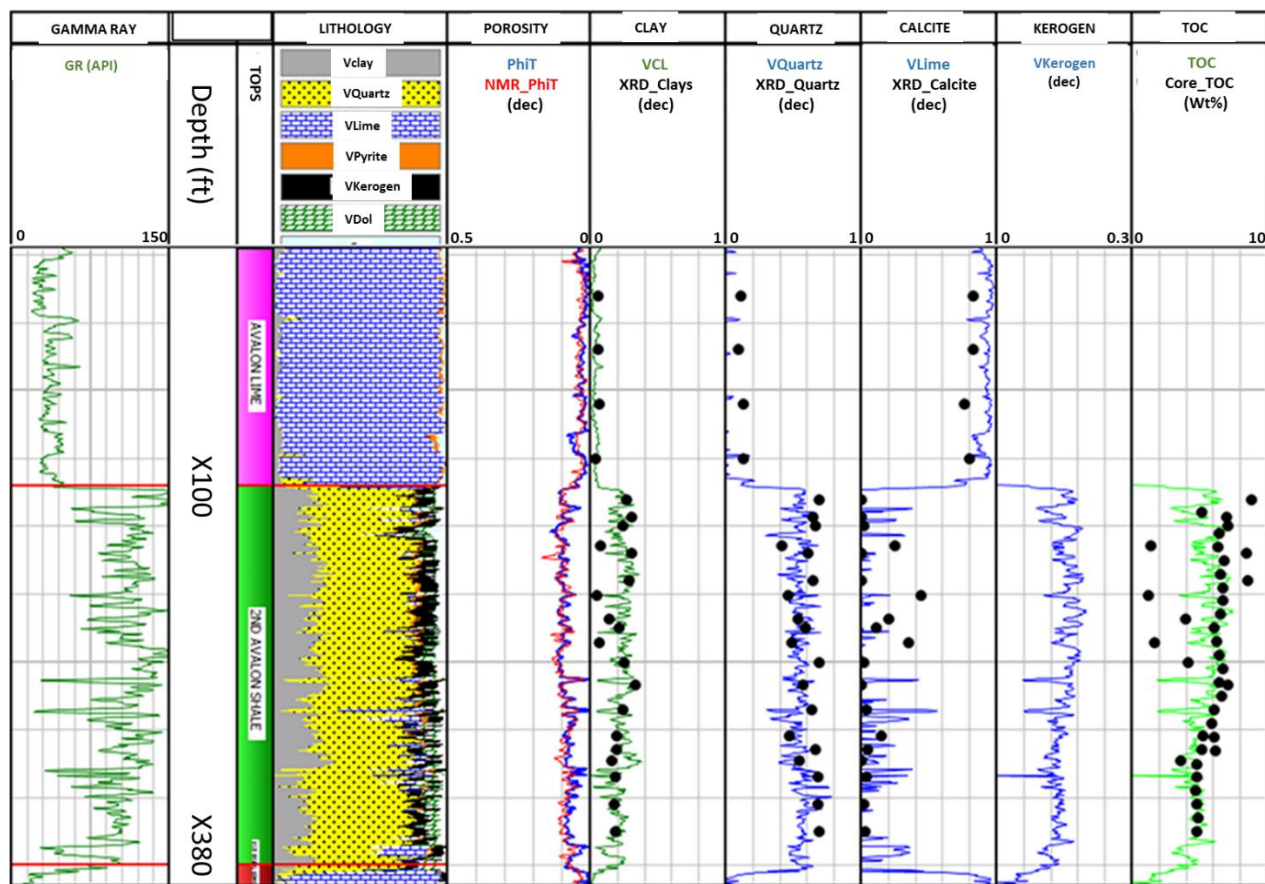


**Figure 1.1:** Volumetric log analysis and TOC prediction in the Avalon Shale. GAMMA RAY Track: Gamma-ray log (solid green curve - GR). TOPS Track: Formation name. LITHOLOGY Track: Formation lithology fractional volumes (decimal units) determined by volumetric log analyses. The volumetric fractions including porosity sum to unity. Clay volume is gray. Quartz volume is yellow. Limestone (calcite) volume is blue. Solid organic volume is black. Pyrite (orange) and dolomite (green) are minor constituents. Pore volume (porosity) is white. POROSITY Track: Total porosity determined from volumetric log analyses (blue curve - PhiT) and porosity from NMR (Nuclear Magnetic Resonance; NMR\_PhiT) log (red curve). CLAY, QUARTZ AND CALCITE Tracks show calculated clay, quartz, and calcite decimal volumes determined from volumetric log analysis respectively (solid curves) and core XRD (X-Ray Diffraction) measurements of these quantities (solid black dots). KEROGEN Track: Estimated kerogen decimal volume from log analysis (VKero). TOC Track: Total organic carbon in weight percent computed from log analysis (solid green curve) and TOC measured on cores (black dots). The agreement between observed and predicted TOC is generally good when repeated core values are similar, suggesting that isolated discrepancies may be due to resolution differences between log and core values. Depths in the depth track are only to indicate depth scale, actual depths are not available for publication.

## Chapter 2

### COMPRESSIONAL-TO-SHEAR-WAVE VELOCITY RATIO IN ORGANIC SHALES

Omovie, S.J. and J.P. Castagna, 2019, P-to-S-wave velocity ratio in Organic shales: GEOPHYSICS  
Vol. 84, No. 6

Omovie, S.J., and J. P. Castagna, 2017, Acoustic response to fluid properties in hydrocarbon rich  
shales, SEG Technical Program Expanded Abstracts

#### 2.1 INTRODUCTION

Compressional-wave to shear-wave velocity ratios ( $V_p/V_s$ ) from acoustic velocity measurements made in organic shales have been observed to be unusually low for some shale formations (e.g., Haynesville shale, Marcellus shale, Bakken shale, Avalon shale, Eagleford shale, Spraberry shale etc.).  $V_p/V_s$  computed from bedding-normal ultrasonic-velocity measurements made by Johnston and Christensen (1995) in an organic-rich New Albany shale core sample have ratios as low as 1.48. Acoustic measurements made by Vernik and Liu (1997) indicate bedding-normal  $V_p/V_s$  as low as 1.48 and 1.59 respectively for organic-rich Monterey and Bakken shale core samples. Synthetic-shale ultrasonic measurements made by Gong et al., (2018) yield bedding-normal  $V_p/V_s$  as low as 1.5. Similar low velocity ratios have been observed on ultrasonic-velocity measurements made in a variety of organic shales (Omovie and Castagna, 2017; Liu et al., 1994). We present below similar observed low velocity ratios from sonic log and ultrasonic-velocity measurements made in the following organic-shale formations: the lower

Spraberry shale, the Wolfcamp shale, the Avalon shale, the lower Cline shale, the Woodford shale, the Bakken shale and the Eagleford shale.

Two possible explanations have been proposed for the low  $V_p/V_s$  observed in organic shales. Vernik et al., (2018), Vernik and Milovac (2011), Tran et al., (2014) and Sayers et al., (2015) indicate that the lower  $V_p/V_s$  observed in organic-rich shales can be explained by the presence of kerogen in these shale formations. Lucier et al., (2011) and Omovie and Castagna (2017) indicate that the low  $V_p/V_s$  ratio could be due to the hydrocarbon-saturation effect in shales, even those with low kerogen content. Omovie and Castagna (2017) also indicated that increasing clay volume lowered both the P-wave and S-wave velocities but not the velocity ratio. Vernik et al., (2018) recognized that the kerogen properties they utilized to make semi-empirical predictions of  $V_p/V_s$  within 3% accuracy could be treated as “effective moduli” as it is possible that both mechanisms are at work and the reduction of  $V_p/V_s$  observed in kerogen-bearing rocks may be related to associated gas within and around the kerogen. The purpose of this paper is to better understand the direct contribution of free fluid hydrocarbons to the observed velocity-ratio reduction in organic-rich shales.

We hypothesize that the abnormally low velocity ratio observed in the laboratory and with sonic logs for dry or partially saturated organic and inorganic shales as compared to fully brine-saturated shales, can be explained by the presence of air, gas or oil in the pore space and associated with the organic material. We also consider an alternative hypothesis; that the effect can be explained by solid organic constituents alone without contribution from associated fluid

hydrocarbons. An objective of this paper is to test these hypotheses using theoretical models and interpretation of measured velocities.

First, we test the hypothesis that solid organic matter alone can cause the observed low velocity ratio. We use Hashin-Shtrikman and Reuss-Voigt bounds, the Backus average and the Hill average to model the impact of gas-free kerogen volume on the elastic moduli of organic shales. Lucier et al., (2011) similarly modeled sonic velocities and found that the kerogen effect was not sufficient to explain the observed velocity-ratio reduction. We also investigate the variation of the velocity ratio with kerogen content under constant saturation conditions. We seek to determine if the measured data supports the hypothesis that solid kerogen volume alone, absent free fluid hydrocarbons, can be responsible for the low velocity ratio observed in organic shales.

Next, we test the hypothesis that the observed abnormally low velocity ratio relative to brine-saturated shales can be explained primarily by the presence of free hydrocarbons in the pore spaces. We begin by presenting laboratory measurements of ultrasonic velocities in dry and partially saturated shales with low organic content and comparing these to the Greenberg and Castagna (1992) (herein after referred to as GC-92) global fully brine-saturated shale P-wave to S-wave velocity ( $V_p$ - $V_s$ ) trend. We then extend the analysis by (1) comparing sonic-log velocities in fully brine-saturated shales to those with reservoir-quality organic volumes (2) comparing dry and fully brine-saturated ultrasonic measurements in organic shales, and (3) performing fluid substitution on ultrasonic and sonic organic-shale measurements to 100% brine saturation and comparing to the GC-92 shale trend.

Given the uncertainty of fluid substitution in low-porosity rocks with uncertain physical properties, in addition to possible dispersion and other types of experimental or theoretical error, we do not take the fluid-substitution predictions as being definitive. Rather, we would like to ascertain if the direction and magnitude of predicted fluid effects can falsify the hypothesis that hydrocarbons are largely responsible for the low velocity ratios. If abnormally low velocity ratios can be explained by fluid substitution, and this is substantiated by measurements, then we will be more confident in accepting the working hypothesis that hydrocarbons are the primary cause of the reduction in the velocity ratio.

While it is well established that in porous and permeable clastic reservoir rock (e.g. Domenico, 1976), the presence of hydrocarbons can often be detected acoustically and seismically and that the equations of Gassmann (1951) are applicable at low frequencies; that is not necessarily the case for low-permeability shale formations. As these equations assume equilibration of pore pressure throughout the pore space, it is not clear that Gassmann's equations are applicable. However, Gor and Gurevich (2018) report that Gassmann's equations apply to synthetic nano-porous media. In addition, Liu et al., (1994) have shown that Biot theory places low permeability rocks in the low-frequency regime at seismic, sonic and ultrasonic frequencies. Lucier et al., (2011) found that sonic velocities in the Haynesville shale were consistent with fluid substitutions between observed velocities in hydrocarbon-saturated intervals and expectations from empirical trends for fully brine-saturated shales. They also alluded to similar effects being seen in a variety of other shale plays. These papers suggest that Gassmann's equations may indeed be applicable, at least to first order, in organic reservoir

shales. In this paper, we present additional velocity measurements and computations relevant to this issue.

## 2.2 CORRELATION OF WATER SATURATION AND KEROGEN VOLUME

A difficulty in separating hydrocarbon from solid organic-carbon effects on *in situ* velocities is the correlation between total solid organic volume and water saturation. As an example, Figure 2.1 shows sonic log  $V_p/V_s$  ratios versus computed kerogen volume and water saturation in the Avalon and Cline Shales. In general, the higher the organic volume, the lower the  $V_p/V_s$  ratio. However, as organic volume increases, the water saturation also decreases. As a consequence of the high correlation between organic volume and water saturation (see Figure 2.2), multiple regression is unable to separate solid organic volume from fluid saturation effects for our data with acceptable statistical significance.

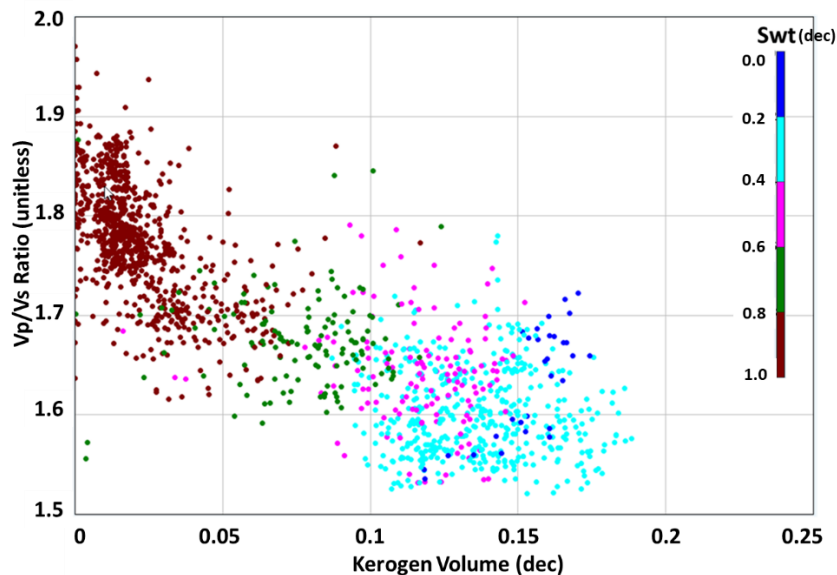


**Figure 2.1:** Sonic log  $V_p/V_s$  ratios (unitless) in the Avalon and Cline shales versus fractional kerogen volume (in decimal units) and colored by water saturation (Swt in decimal units) determined by well-log analysis.

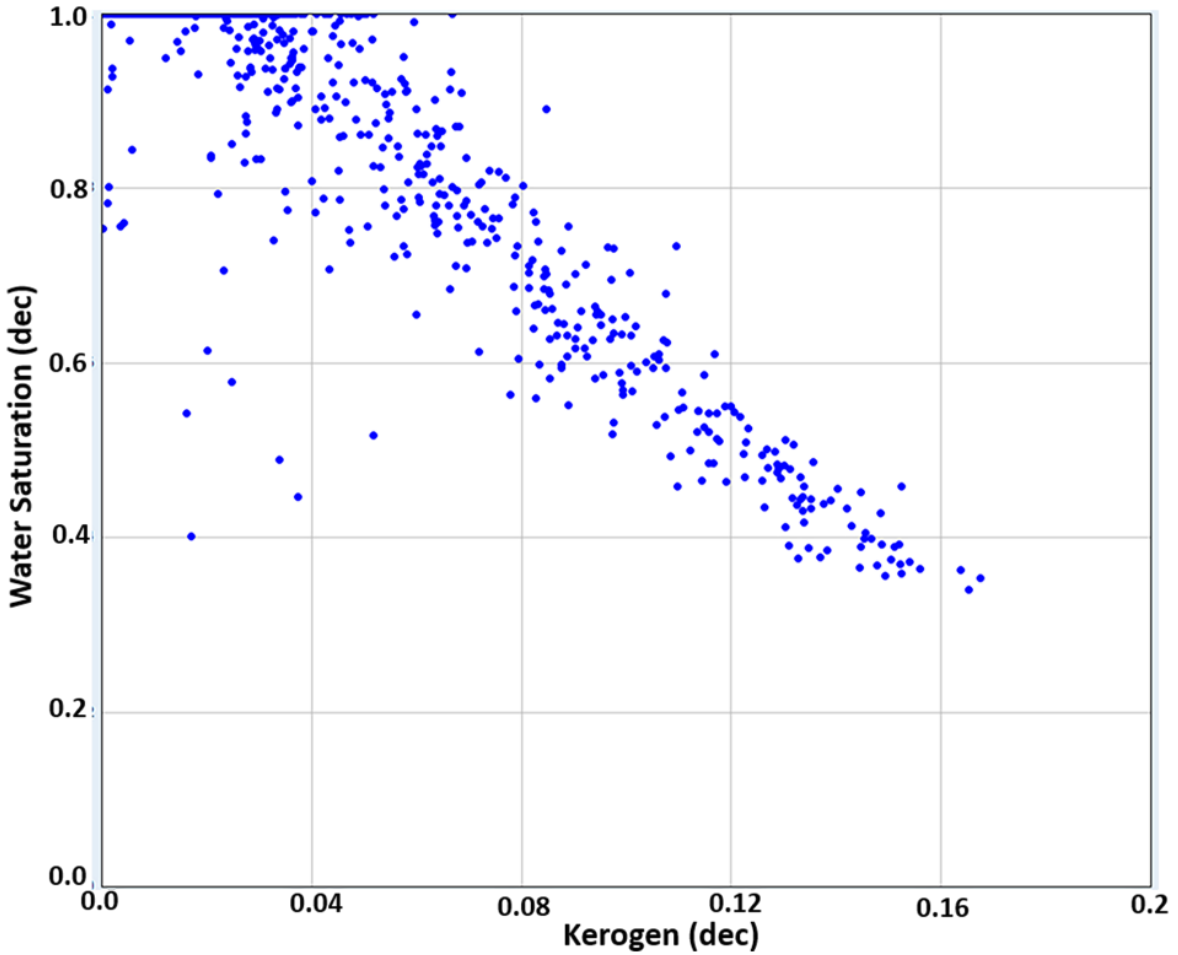


**Figure 2.2:** Decimal water saturation from log analysis versus fractional kerogen volume for the Cline shale.

Figure 2.3a shows that the dynamic bulk modulus derived from velocity and density measurements is strongly affected by water saturation, on the other hand, as shown in Figure 2.3b, the shear modulus is unaffected by water saturation.

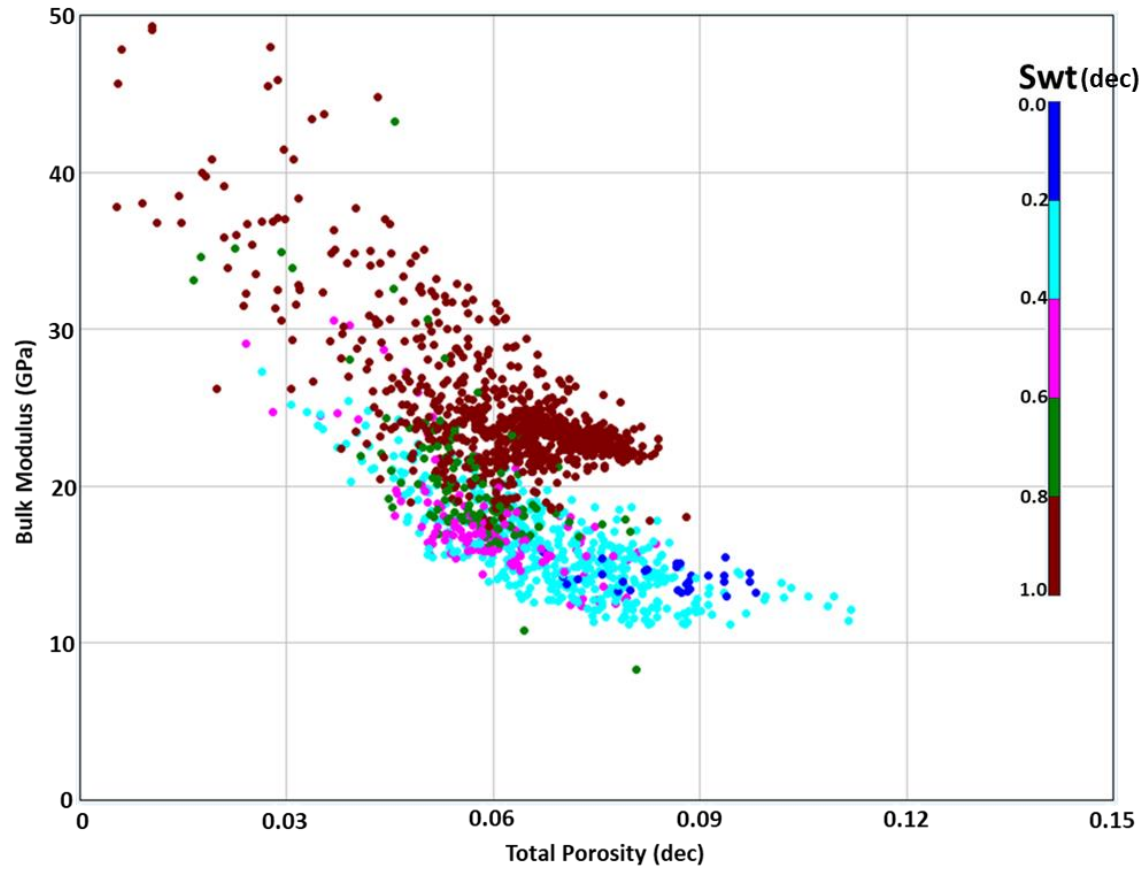


**Figure 2.3a:** (a) Cross plot of dynamic bulk modulus (GPa) versus total porosity (in decimal units) colored by water saturation (Swt in decimal units) for the Avalon and Cline shales.

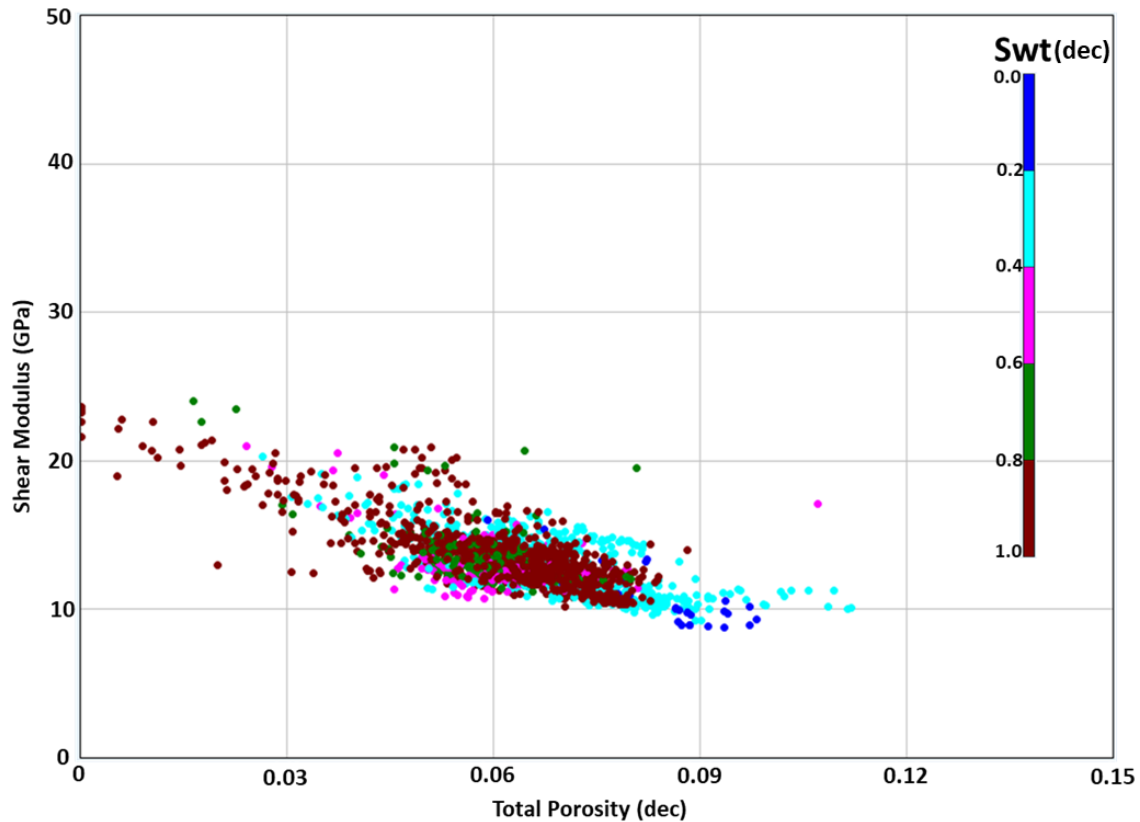


**Figure 2.3b:** Cross plot of dynamic shear modulus (GPa) versus total porosity (decimal) colored by water saturation (decimal) for the Avalon and Cline shales.

### 2.3 KEROGEN OR SOLID ORGANIC-MATTER EFFECT

Hydrocarbon rich shales are often associated with increased organic matter. Some authors have noticed a reduction in  $V_p/V_s$  with increase in kerogen content. Sayers et al., (2015) for example observed that a 5% increase in kerogen volume resulted in  $V_p/V_s$  reducing from an average of 1.8 to 1.7 in the Eagleford Formation, Vernik and Milovac (2011) have observed a similar effect. Our data (see below) also support that conclusion, although, as stated previously, this velocity-ratio reduction could be caused by associated fluid hydrocarbons. It is thus

necessary to address the question: In the absence of associated hydrocarbons, is kerogen or solid organic matter a primary reason why the  $V_p/V_s$  is lower in organic-rich shales?

In this section, we address the hypothesis that the observed low velocity ratio can be explained by solid organic constituents alone. We begin by modeling the impact kerogen inclusions will have on the elastic moduli of a brine-saturated inorganic shale using the Hashin-Shtrikman bounds (Hashin and Shtrikman, 1963), the Backus average (Backus, 1962) and the Voigt-Reuss-Hill average (Hill, 1952). We take the end members of the mixing models to be solid kerogen and brine-saturated inorganic porous shale. We wish to know if mixing fully brine-saturated inorganic shale and kerogen can produce the observed low velocity ratio. For the brine-saturated inorganic-shale end member, we use measured P-wave and S-wave velocities of a Permian basin brine-saturated sample at confining pressure of 20.68 MPa and deviatoric stress (difference between axial and confining stress) of 15.52 MPa; because these values are close to *in situ* stress conditions. The fully brine-saturated inorganic shale is numerically mixed with 0-40% kerogen volume. Dynamic elastic moduli of the brine-saturated inorganic shale are computed from measured velocities and shown in table 2.1 as  $K$  and  $G$ ; we use kerogen elastic moduli from both Vernik and Landis (1996) and Yan and Han (2013). Figure 2.4a shows the observed fluid effect – i.e. the difference between the ultrasonically measured dry and brine-saturated velocity ratio – as compared to the modeled impact of kerogen inclusion on this brine-saturated shale using the Hashin-Shtrikman lower bound (HSLB), the Backus average, and the Voigt-Reuss-Hill (VRH) average with kerogen elastic moduli from Vernik and Landis (1996). For these end members, the Hashin-Shtrikman upper bound yielded

ratios very close to the lower bound and is not plotted here. Note that using the Hashin-Shtrikman lower bound yields the largest change in the velocity ratio, for which 40% kerogen volume resulted in less than 20% of the observed difference between the dry and fully saturated velocity ratios. For most organic-shale reservoirs, kerogen volume is usually less than 20%. On the other hand, as shown in Figure 2.4b, kerogen inclusion using kerogen elastic moduli from Yan and Han (2013) with both the Hill average and Backus average shows a slight increase in the velocity ratio of the mixture with increasing kerogen volume. None of these predictions can be expected to be accurate, yet all of them show a much smaller change in the velocity ratio than the observed difference between the dry and fully saturated velocity ratios. These results corroborate similar calculations made by Lucier et al., (2011).

Bounding equations and related averages are known to yield fairly accurate effective elastic moduli when the bound is narrow or elastic properties of lithological constituents do not differ significantly (Wang et al., 2001; Jaeger et al., 2007). While this may be true for the non-kerogen constituents in the shale formations in this study, it is not clear that this is the case with organic-rich shales. Kerogen elastic moduli are in some cases an order of magnitude lower than the other individual solid components making up the rock composite. We thus also used the Self Consistent Approximation method (Berryman, 1980) to model kerogen inclusion in a non-kerogen matrix. We have used this method because it satisfies the Hashin-Shtrikman bounds while taking into account inclusion shape. A problem we ran into early on is in trying to determine what aspect ratios represent the kerogen or organic inclusions in the rock matrix. Based on observation of scanning electron microscope images, we used aspect ratios that range

from 0.01 to 0.5. While not exhaustive, appropriately apportioning the kerogen volume to these aspect ratios will result in a theoretical model that is representative of the measured rock in this study. At each model step, 40% of the kerogen volume is in aspect ratio of 0.5 while 60% is evenly split between the other 3 aspect ratios. For example, as shown in table 1 at 40% total kerogen volume, 16% is in aspect ratio of 0.5 while aspect ratios 0.1, 0.02 and 0.01 each had 8% kerogen volume. The rock constituent fractional volumes sum to unity at each model step.

For an N-phase composite, the self-consistent approximation is given by the following 2 coupled equations:

$$\sum_{i=1}^N x_i (K_i - K_{SC}^*) P^{*i} = 0, \quad (2.1)$$

$$\sum_{i=1}^N x_i (G_i - G_{SC}^*) Q^{*i} = 0, \quad (2.2)$$

where  $i$  is the  $i$ th constituent,  $x_i$  is its volume fraction,  $K_i$  and  $G_i$  are its elastic moduli, and  $P$  and  $Q$  are geometric factors. For the equations for  $P$  and  $Q$ , we refer the reader to Mavko et al., (1998) or Berryman (1980).  $K_{SC}^*$  and  $G_{SC}^*$  are the self-consistent effective moduli. The equations are solved numerically by iteration.

We model the impact of kerogen inclusion from 0% to 40% on the fully brine-saturated inorganic-shale sample using the self-consistent approximation (SCA). The input parameters to the model are shown in table 2.1, where  $K$  and  $G$  are the bulk and shear modulus respectively computed from the measured velocities and bulk density. The SCA model results (figures 2.4a and 2.4b) again do not show a significant velocity-ratio reduction related to kerogen content.

We also investigated if placing more of the kerogen volume in the thin cracks (aspect ratio of 0.01) would yield different results. While the elastic moduli are lower, there is no significant difference in the velocity ratio.

In addition, the theoretical modeling was also conducted on a zero-porosity solid-aggregate basis; for the solid-aggregate end member we use the Hill average of the inorganic constituents of the Permian shale core sample. As shown in Figures 2.5a and 2.5b, there is an increase in velocity ratio with increasing kerogen volume for all the effective-medium models – Backus, Hashin-Shtrikman lower bound, Hill average and SCA - using both the Yan and Han (2013) and the Vernik and Landis (1996) kerogen elastic moduli.

Based on measured data from Vernik and Liu (1997) on dry organic-shale samples, Sayers (2013) modeled the impact kerogen volume will have on the elastic stiffnesses measured in shales using the Backus average – which for bedding-normal stiffnesses fit the measured data fairly well. The bedding-normal velocity ratio computed from Figures 1 and 2 in Sayers (2013) is shown below in Figure 2.5c. Note that the trend is very similar to Figures 2.5a and 2.5b. Absolute percent difference between the Backus-average velocity ratio in figure 2.5a at 10% kerogen volume and that computed from Sayers (2013) is only 0.3%; and only 0.07% at 40% kerogen volume (This small difference is due to difference in end-member inorganic shale in both models).

These results are consistent with velocity measurements made on 12 synthetic-shale samples by Altowairqi et al., (2015; see Figure 2.6). They observed that given the same inorganic constituents, increase in TOC content resulted in an increase in the velocity ratio of

the synthetic shale. Their inorganic-shale composition includes clay (45%), quartz (40%) and calcite (15%). Xie et al., (2019) similarly observed that increasing kerogen content lowered both the P-wave and S-wave velocity on velocity measurements performed on 10 synthetic shale samples. Of course, synthetic-shale samples are not representative of natural shales with millions of years of geologic history; but the point in including this example is to show the observed trend solid-organic volume has on velocity ratio in shales.

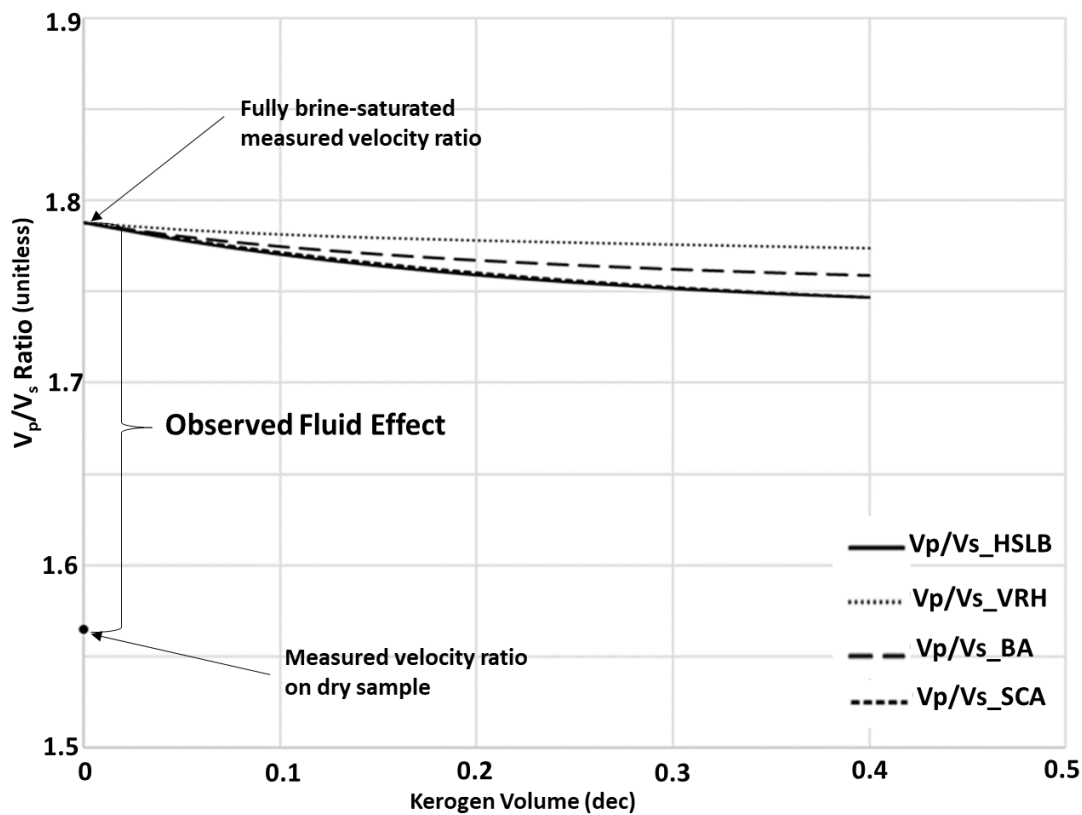


**Figure 2.4a:** Cross plot of  $V_p/V_s$  versus fractional kerogen volume from kerogen inclusion in fully brine-saturated inorganic shale. VRH in the legend stands for Hill average, BA is Backus average, HSLB is Hashin-Shtrikman lower bound, and SCA is self-consistent approximation. For all 4 models, elastic moduli of the brine-saturated inorganic shale end member are obtained from measured bedding-normal velocities at confining pressure of 20.68MPa and deviatoric stress of 15.5 MPa of the sample described in section 4.3. This is shown as  $K$  and  $G$  in table 1. Solid kerogen elastic moduli used are from Vernik and Landis (1996).

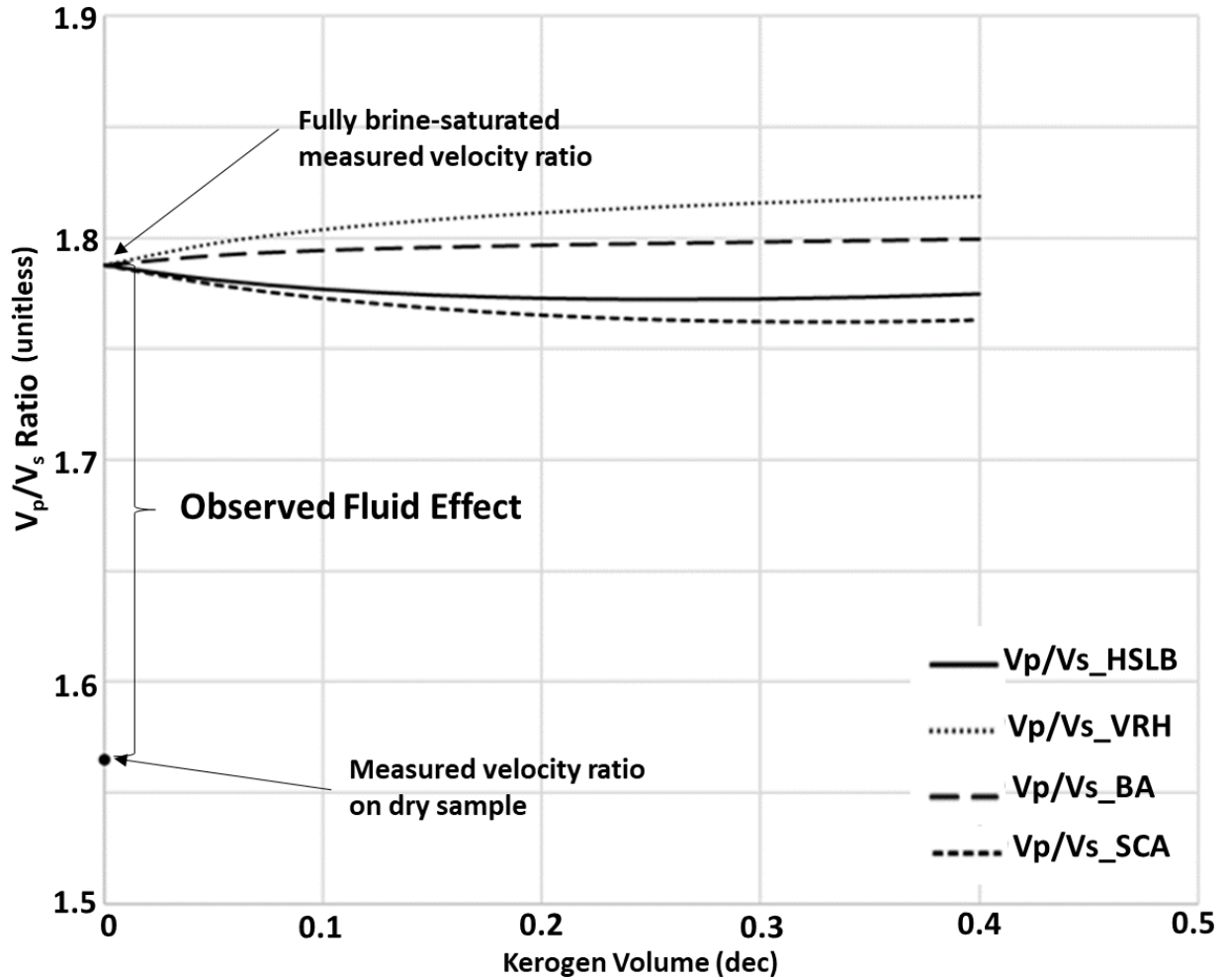


**Figure 2.4b:** Cross plot of  $V_p/V_s$  versus fractional kerogen volume from kerogen inclusion in fully brine-saturated inorganic shale. VRH in the legend stands for Hill average, BA is Backus average, HSLB is Hashin-Shtrikman lower bound, and SCA is self-consistent approximation. For all 4 models, elastic moduli of the brine-saturated inorganic-shale end member are obtained from measured bedding-normal velocities at confining pressure of 20.68 MPa and deviatoric stress of 15.5 MPa of the sample described in section 4.3. This is shown as  $K$  and  $G$  in table 1. Solid kerogen elastic moduli used are from Yan and Han (2013).

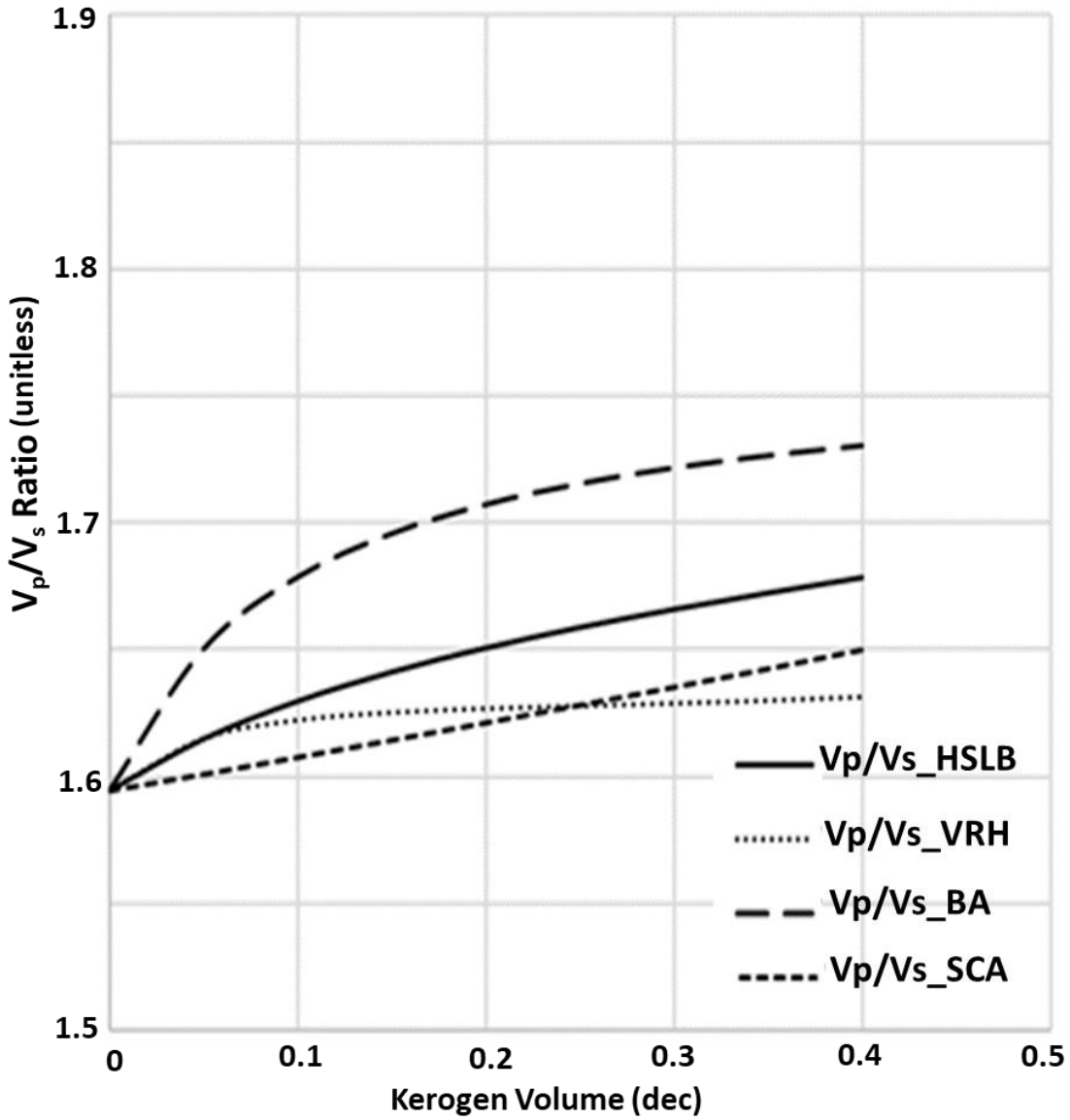


**Figure 2.5a:** Cross plot of  $V_p/V_s$  versus fractional kerogen volume from kerogen inclusion in zero-porosity solid aggregate inorganic shale. VRH in the legend stands for Hill average, BA is Backus average, HSLB is Hashin-Shtrikman lower bound, and SCA is self-consistent approximation. Elastic matrix moduli of inorganic-shale end member are  $K_m$  and  $G_m$  in table 1. Solid kerogen elastic moduli are from Vernik and Landis (1996).

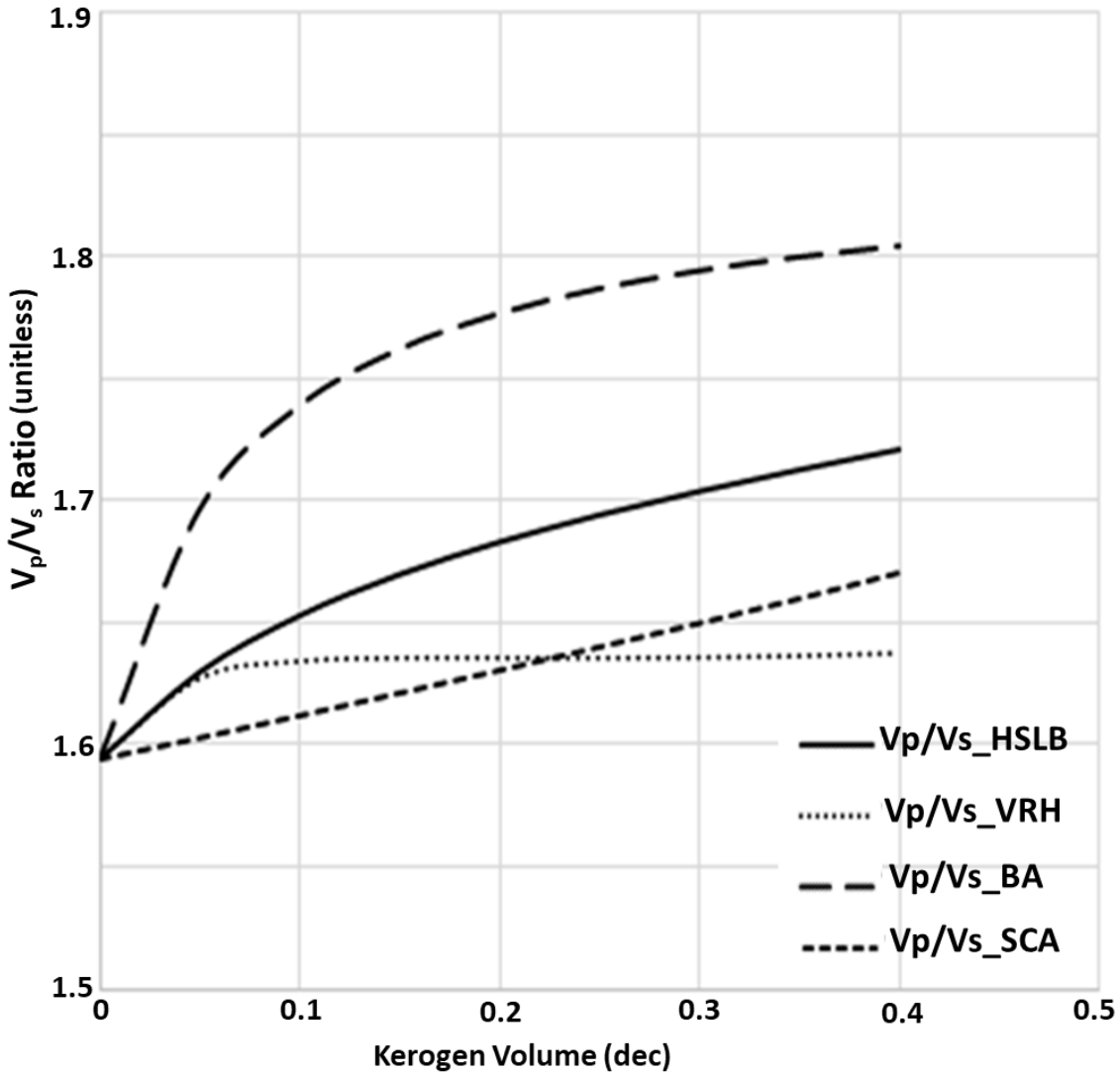


**Figure 2.5b:** Cross plot of  $V_p/V_s$  versus fractional kerogen volume from kerogen inclusion in zero-porosity solid aggregate inorganic shale. VRH in the legend stands for Hill average, BA is Backus average, HSLB is Hashin-Shtrikman lower bound, and SCA is self-consistent approximation. Elastic matrix moduli of inorganic-shale end member are  $K_m$  and  $G_m$  in table 2.1. Solid kerogen elastic moduli are from Yan and Han (2013).

**Table 2.1:** Input parameters for SCA model results shown in figures 2.4 and 2.5.  $K_m$  and  $G_m$  are the zero-porosity solid aggregate inorganic shale-matrix bulk and shear moduli respectively and  $X_m$  is the volume fraction of shale matrix.  $\alpha_{k1}$ -  $\alpha_{k4}$  are the aspect ratios of the kerogen inclusions,  $X_{k1}$  -  $X_{k4}$  are their volume fractions.  $K$  and  $G$  are the bulk and shear moduli of the fully brine-saturated inorganic-shale sample computed from measured velocities.

<b><math>K_m</math></b>	47.5		<b><math>K</math></b>	26.89	
<b><math>G_m</math></b>	39.3		<b><math>G</math></b>	14.44	
	<b><math>\alpha_m</math></b>	<b><math>\alpha_{k1}</math></b>	<b><math>\alpha_{k2}</math></b>	<b><math>\alpha_{k3}</math></b>	<b><math>\alpha_{k4}</math></b>
Aspect ratios	1	0.5	0.1	0.02	0.01
	<b><math>X_m</math></b>	<b><math>X_{k1}</math></b>	<b><math>X_{k2}</math></b>	<b><math>X_{k3}</math></b>	<b><math>X_{k4}</math></b>
	0.95	0.02	0.01	0.01	0.01
	0.9	0.04	0.02	0.02	0.02
	0.85	0.06	0.02	0.02	0.02
	0.8	0.08	0.04	0.04	0.04
	0.75	0.1	0.05	0.05	0.05
	0.7	0.12	0.06	0.06	0.06
	0.65	0.14	0.07	0.07	0.07
	0.6	0.16	0.08	0.08	0.08

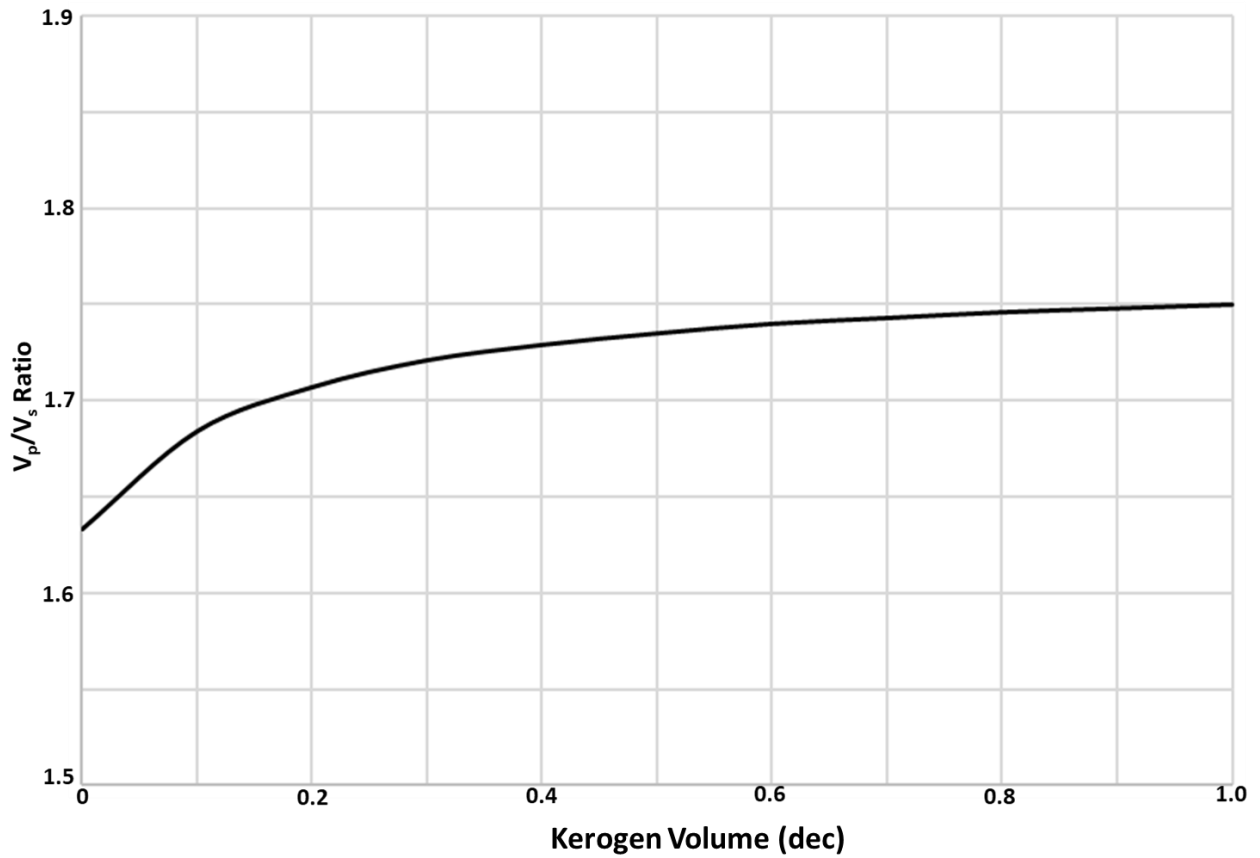


**Figure 2.5c:** Cross plot of  $V_p/V_s$  versus fractional kerogen volume computed from bedding-normal stiffnesses in Figures 1 and 2 of Sayers (2013) in organic-rich shales.

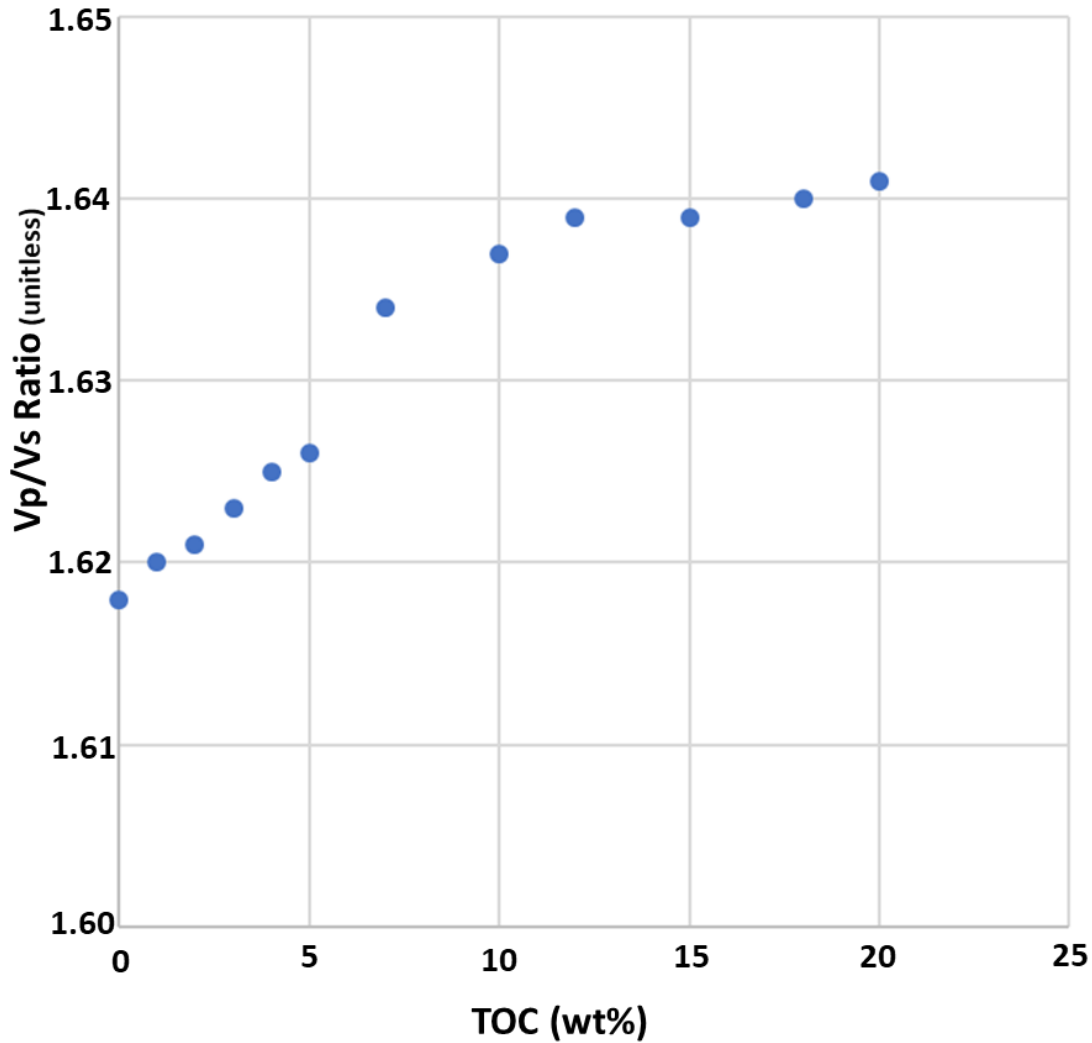


**Figure 2.6:** Cross plot of  $V_p/V_s$  versus TOC from ultrasonic-velocity measurements on synthetic-shale samples by Altowairqi et al., (2015). Data is from table 1 in their paper. While water was used in mixing their synthetic-shale samples, they did not clearly state the saturation state of their samples.

Figure 2.7 shows the bedding-normal ultrasonic  $V_p/V_s$  versus kerogen volume for dry samples from the Bakken, Monterey, Kimmeridge, New Albany, Bazhenov and Chattanooga shales reported by Vernik and Liu (1997) and Johnston and Christensen (1995). For these 6 shale formations combined, there is little discernable dependence of  $V_p/V_s$  of the dry samples on kerogen volume. Individual formations show a tendency for the velocity ratio to increase,

rather than decrease, with increasing kerogen content. Note for example that in the Kimmeridge shale where kerogen volume increases from 5.7% to 20.3%; the corresponding velocity ratio increases from 1.55 to 1.79.

We conclude that neither theoretical calculations, nor laboratory measurements, support the hypothesis that solid kerogen alone will reduce velocity ratios to the extent observed in organic-rich shale reservoirs. An alternative explanation is needed.

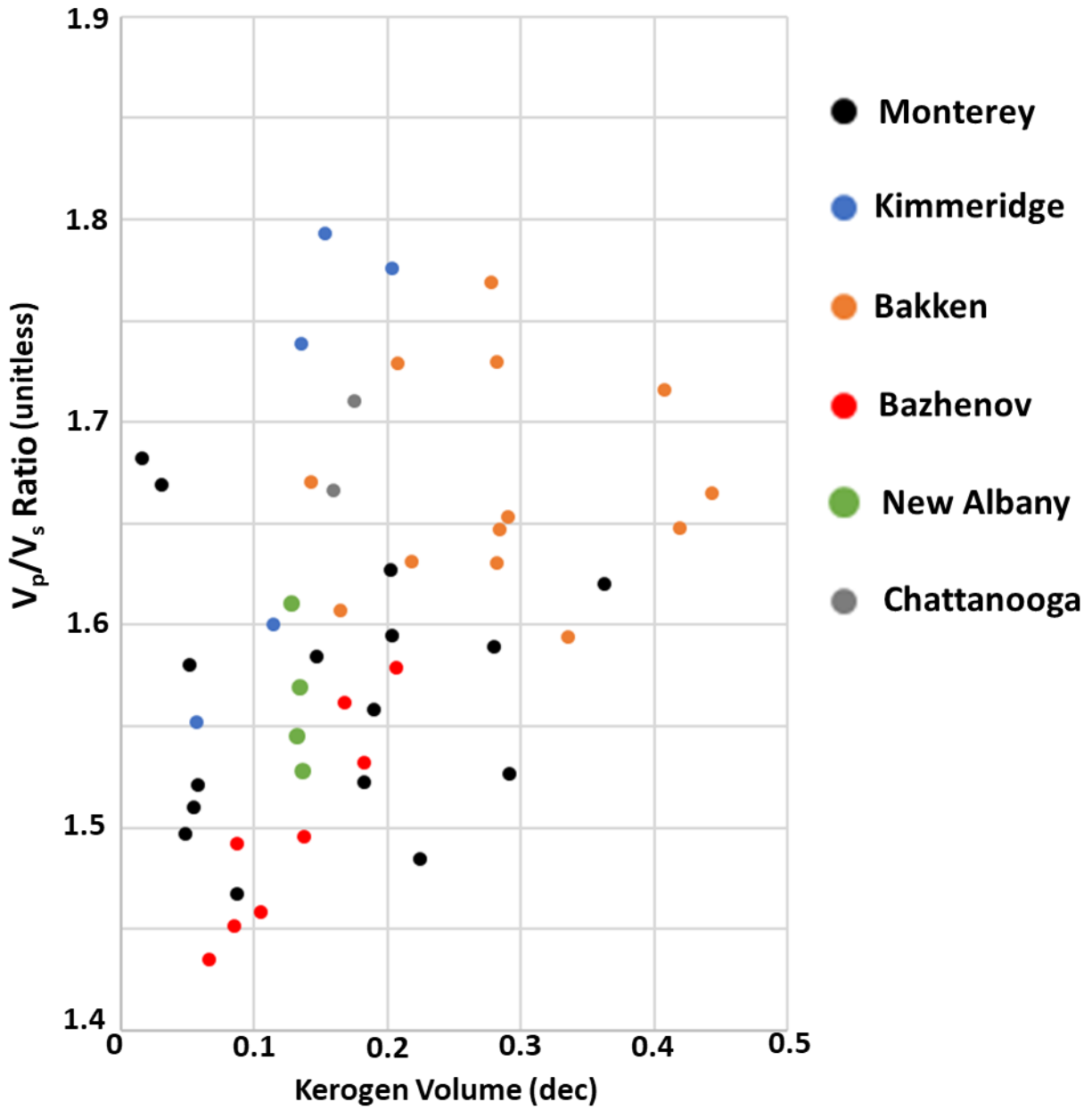


**Figure 2.7:** Cross plot of ultrasonic bedding-normal  $V_p/V_s$  (unitless) versus fractional kerogen volume for dry samples from 6 shale formations. Bakken, Bazhenov, Kimmeridge and Monterey shale datasets are from Vernik and Liu (1997). New Albany and Chattanooga shales are from Johnson and Christensen (1995).

## 2.4 FLUID EFFECT

If kerogen is not responsible for the unusually low  $V_p/V_s$  often observed in organic-shale formations, what is? It is important to note that low  $V_p/V_s$  is not unique to organic-rich shales. We have measured acoustic velocity on an inorganic Permian-basin shale dry core sample with velocity ratio ranging from 1.56 to 1.6 at 20.68MPa confining pressure and deviatoric stress ranging from 15.5MPa to 29.3MPa. (Detailed experimental procedure for these new measurements can be found in section 4.3). On the other hand, ultrasonic-velocity measurements made on the same fully brine-saturated inorganic-shale core sample at the same stresses yield velocity ratios from 1.77 to 1.79. These measurements are shown in Figure 2.8, the fully brine-saturated measurements plot right on or close to the GC-92 brine-saturated shale line, while the dry measurements significantly deviate from this line – indicating a gas-saturation (air) effect or some inexplicable change to the frame due to drying. In Appendix A, we find similar  $V_p-V_s$  trends for dry and partially saturated inorganic shales that deviate from the GC-92 shale trends towards lower velocity ratios. Furthermore, we observed the same gas-saturation effect on measurements made on preserved core samples as shown in Figure 2.9. The velocity ratio for the 5 preserved samples shown in Figure 2.9 range from 1.5 to 1.6. We conclude from these laboratory measurements that both dry and partially saturated samples exhibit anomalously low  $V_p/V_s$  ratios in shales without high organic content.

Acoustic measurements made by Tosaya (1982) also show  $V_p/V_s$  for dry Pierre and Cotton Valley shales - that had no reported organic content - to be as low as 1.45 (see Figure

2.10). The water-saturated velocities plot within 2% of the Greenberg-Castagna fully brine-saturated shale trend, while the dry samples significantly deviate towards lower velocity ratios.

We apply Gassmann fluid substitution to the dry sample acoustic measurements made by us and those made by Tosaya (1982) to see how predictable the water-saturated velocities are given the dry velocities. The Gassmann fluid substitution procedure is described in detail in the next section as well as sensitivity analyses around input parameters for the Permian-basin shale sample. Table 2.2 compares the measured and predicted water-saturated compressional-wave velocities. Note that percent errors in Gassmann fluid substitution prediction for the Permian-basin shale sample, the Pierre shale and Cotton Valley shale are about 1%, 4.6% and 2.5% respectively. As these rocks have vertical transverse isotropic (VTI) symmetry, in appendix B we apply the anisotropic Gassmann fluid substitution equation and compare to the above results.

Liu et al., (1994) observed a similar effect when they measured compressional-wave and shear-wave velocities on Bakken-shale core samples with significant organic content at dry and brine-saturated conditions.  $V_p/V_s$  for their dry organic-rich shale sample ranges from 1.53 to 1.76, with confining pressure ranging from 5 to 70 MPa. On the other hand, when the same organic-rich Bakken-shale samples were brine-saturated and velocities were measured over the same confining pressure range, measured  $V_p/V_s$  was between 1.77 to 1.84. We observe similar increase in velocity ratio when ultrasonic measurements made by Vernik and Liu (1997) on dry organic shales were compared to those made on brine-saturated organic shales from the same formation. In the Bazhenov shale for example, where kerogen content ranges from 10-18%, the

velocity ratios on dry sample measurements range from 1.45 to 1.56. The corresponding brine-saturated measured velocity ratio ranged from 1.69 to 1.76.

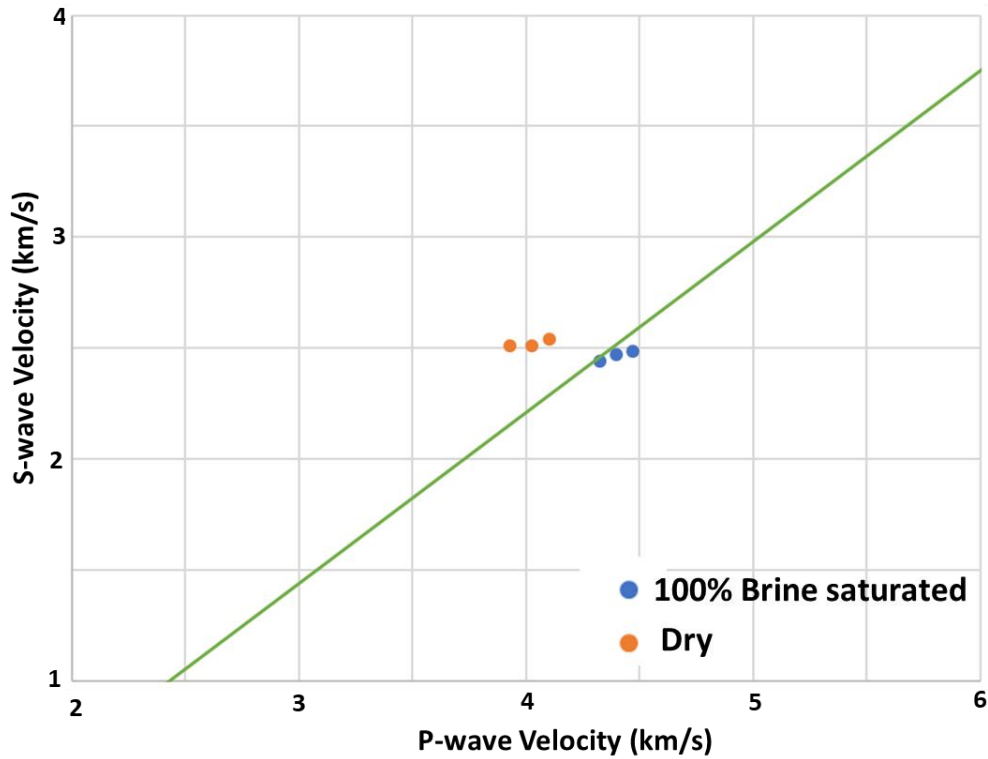


**Figure 2.8:** Cross plot of compressional-wave versus shear-wave velocity measurements on Permian (Delaware Basin) inorganic dry and fully brine-saturated shale sample. The blue discrete datapoints are the fully brine-saturated measurements made at varying deviatoric stresses, the orange datapoints are the dry measurements. The green line is the GC-92 fully brine-saturated shale line.

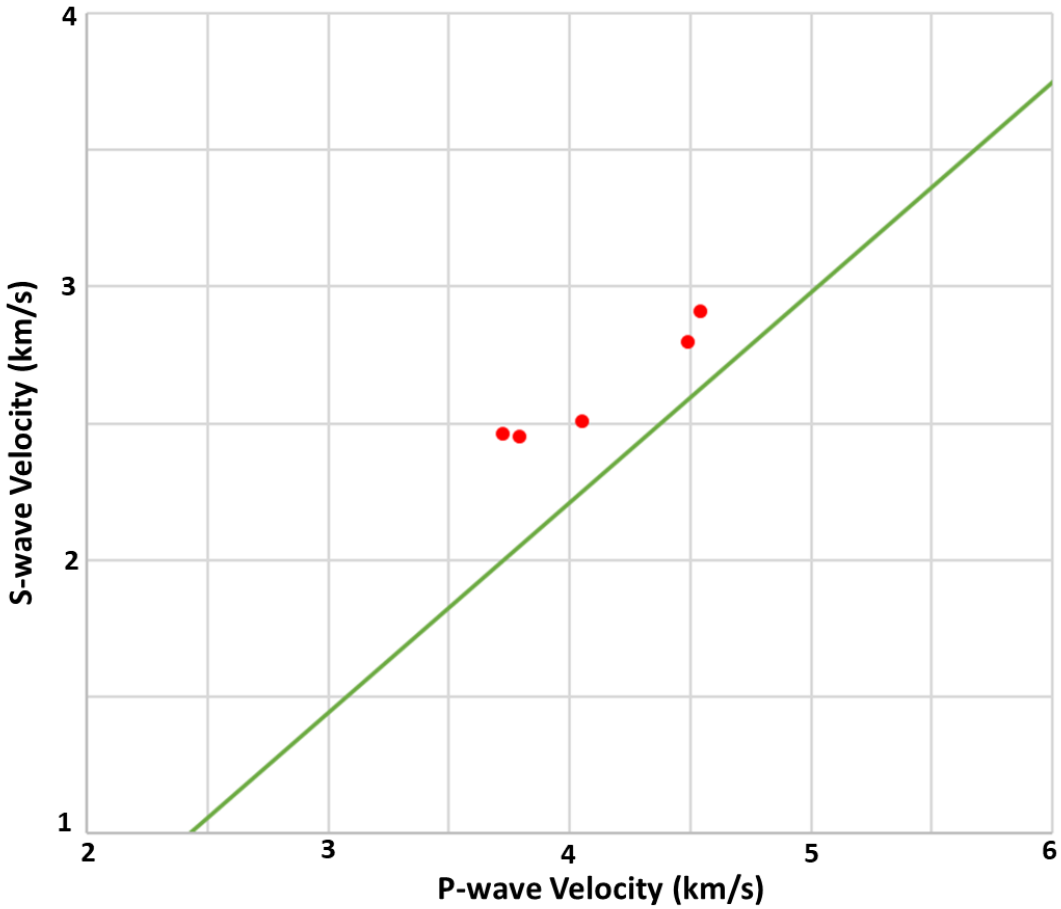


**Figure 2.9:** Cross plot of compressional-wave versus shear-wave velocity measurements on Permian (Delaware basin) inorganic-shale preserved core samples (red points). The green line is the GC-92 fully brine-saturated shale line. Average water saturation for the 5 samples is 45%. These partially saturated shale velocities have distinctly lower  $V_p/V_s$  than would be predicted by the brine-saturated shale trend.

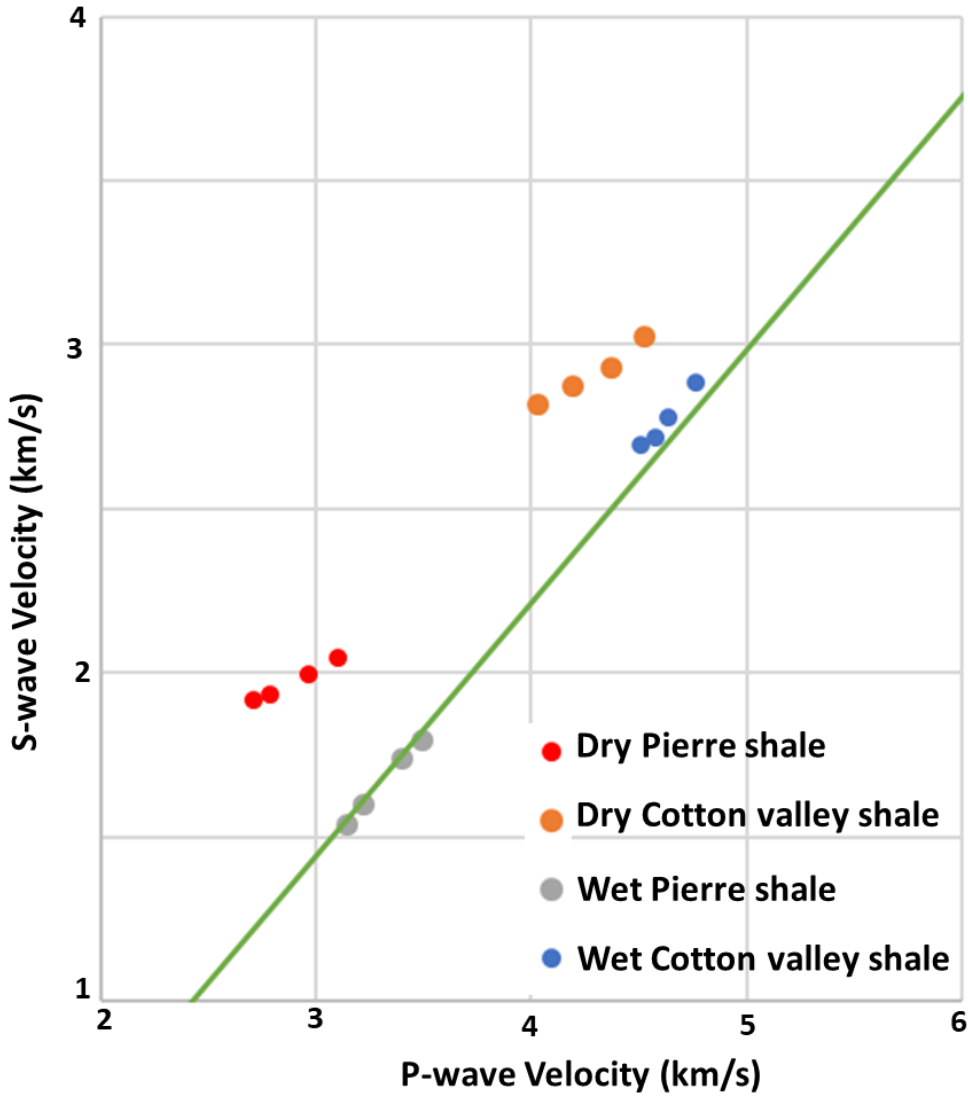


**Figure 2.10:** Cross plot of compressional-wave versus shear-wave velocity measurements made by Tosaya (1982) on Pierre and Cotton Valley dry and water-saturated shale samples. Green line is the GC-92 fully brine-saturated shale line.

**Table 2.2:** Gassmann fluid substitution prediction results compared to measured compressional-wave velocities on water-saturated Permian-basin shale (new data set) and Pierre and Cotton Valley shale samples (both published data set).  $V_p/V_s$  fully brine-saturated is computed from measured P-wave and S-wave velocities on the brine-saturated sample.  $V_p/V_s$  predicted is computed from the Gassmann-predicted brine-saturated P-wave velocity and the dry sample S-wave velocity. Porosity for the Permian-basin shale sample, Cotton Valley shale, Pierre shale are respectively 5.7%, 4.2% and 14.5%.

<b>Permian basin shale</b>			
Vp predicted (km/s)	4.40	4.44	4.48
Vp measured (km/s)	4.32	4.40	4.47
Vp/Vs predicted	1.75	1.76	1.76
Vp/Vs fully brine saturated	1.77	1.78	1.80
Vp/Vs dry	1.57	1.60	1.61
Confining pressure (MPa)	20.68	20.68	20.68
Deviatoric stress (MPa)	15.52	29.34	43.17
Pore pressure (MPa)	0	0	0
% Error in Vp prediction	1.7	0.91	0.18
% Error in Vp/Vs prediction	1.07	0.79	2.00
<b>Cotton valley shale</b>			
Vp predicted (km/s)	4.86	4.77	4.69
Vp measured (km/s)	4.76	4.63	4.57
Vp/Vs predicted	1.61	1.62	1.63
Vp/Vs fully brine saturated	1.65	1.67	1.68
Vp/Vs dry	1.50	1.49	1.46
Confining pressure (MPa)	100	74	49.63
Pore pressure (MPa)	1	1	1
% Error in Vp prediction	2.14	2.85	2.49
% Error in Vp/Vs prediction	2.31	2.66	2.92
<b>Pierre shale</b>			
Vp predicted (km/s)	3.61	3.53	3.43
Vp measured (km/s)	3.49	3.40	3.22
Vp/Vs predicted	1.77	1.77	1.77
Vp/Vs fully brine saturated	1.95	1.96	2.02
Vp/Vs dry	1.52	1.49	1.43
Confining pressure (MPa)	115	95	55
Pore pressure (MPa)	1	1	1
% Error in Vp prediction	3.457	3.928	6.618
% Error in Vp/Vs prediction	9.17	9.40	12.28

Figure 2.11 shows a cross plot of P-wave versus S-wave velocity measurements performed on dry organic-shale samples from 8 different formations, all published data – the Monterey, Kimmeridge, Bakken, New Albany, Chattanooga, Bazhenov, Antrim and Niobrara organic-shale formations. The dashed green line indicates the linear fit to these 8 organic-shale formations.

The regression  $V_p$ - $V_s$  trend (table 2.3) for the dry organic shales is:

$$V_s = .544 V_p + .263 \text{ km/s}, \quad (2.3)$$

The coefficients in equation 2.3 are similar to and within the standard error computed for offshore Gulf of Mexico inorganic dry shales (Appendix A):

$$V_s = .527 V_p + .282 \text{ km/s}, \quad (2.4)$$

which indicates further that dry inorganic shales have velocity-ratio values that are comparable to those of organic shales.

In terms of deviation from the GC-92 fully brine-saturated shale trend, the predicted shear-wave velocity from the dry organic-shale trend is about 60% faster at a P-wave velocity of 2.5 km/s with zero difference at 5 km/s, possibly due to the fact that at high velocities, rock porosity is approaching zero; especially for siliciclastic shales.

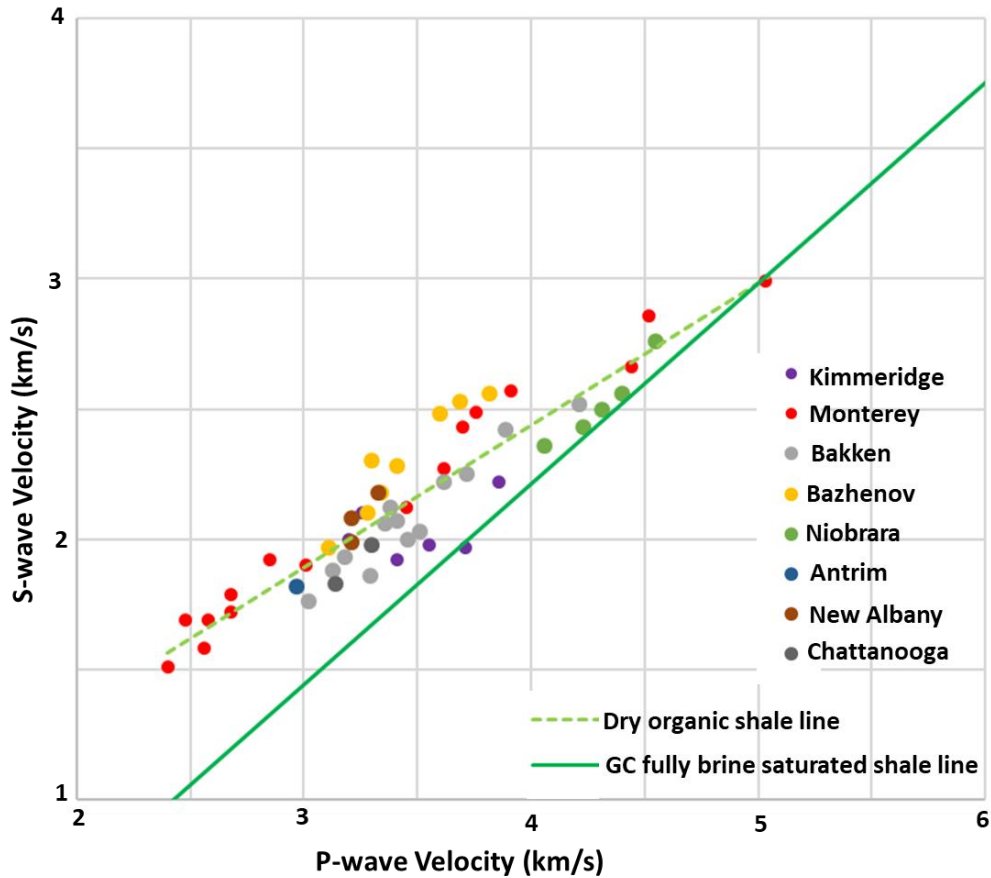


**Figure 2.11:** Cross plot of compressional-wave versus shear-wave velocity measurements on dry organic-shale samples from 8 different formations. The dashed green line is the best fit linear regression to the dry organic-shale dataset.

**Table 2.3:** Linear regression statistics for the dry organic-shale data in Figure 12, where **b** is the intercept and **a** is the slope of the linear equation. Standard error of the regression is 0.13 km/s. Note the high F-statistic and low sig F, indicating that the regression is highly significant. (F is the ratio of explained to unexplained variance. The sig F is the probability that this R-squared could be achieved by uncorrelated random variables, i.e., there is no relationship between the observation and the prediction).

Measurement Type	b	Standard error b	a	Standard error a	R <sup>2</sup>	F	Sig F
Dry organic shale	0.2635	0.1122	0.5433	0.0318	0.8538	291.94	1.62E-22

## 2.5 FLUID SUBSTITUTION

The green data points in Figure 2.12 indicate the P-wave and S-wave velocities measured on three preserved core samples at a confining pressure of 15 MPa and deviatoric stress of 65 MPa. The core samples are from the lower Spraberry shale in the Midland Basin – a sub-basin of the Permian basin. It is noteworthy that these data points plot away from the GC-92 fully brine-saturated shale line. The core composition from x-ray diffraction is shown in table 2.4. The amount of TOC in weight % is from pyrolysis. Water saturation, porosity, bulk density and grain density are from GRI (Gas Research Institute standard; Luffel and Guidry, 1992) measurements on the preserved core samples. Water saturation of the 3 samples shown in Figure 2.12 ranges from 30% to 40%. The question we seek to address in this section is whether the deviation from the GC-92 brine-saturated shale line is possibly due to the presence of hydrocarbons in the core samples.

**Table 2.4:** Composition from XRD and GRI data of the lower Spraberry shale core samples. GD is grain density and Swt is water saturation (new dataset)

Vquartz	Vcalcite	Vclay	Vdolomite	GD	RhoB	Swt	Phit	Vp	Vs	TOC
dec	dec	dec	dec	g/cc	g/cc	%	%	km/s	km/s	wt%
0.63	0.01	0.26	0.02	2.680	2.569	40.55	5.39	4.725	2.898	1.12
0.55	0.00	0.30	0.02	2.640	2.486	32.02	7.37	4.118	2.520	3.69
0.59	0.00	0.30	0.04	2.701	2.546	29.80	7.02	4.417	2.714	1.21

Gassmann's (1951) equation for the bulk modulus of the saturated rock,  $K_c$ , is:

$$K_c = K_d + \frac{\left(1 - \frac{K_d}{K_m}\right)^2}{\Omega - \frac{K_d}{K_m^2}} \quad (2.5)$$

$$\text{where } \Omega = \frac{\phi_t}{K_f} + \frac{(1 - \phi_t)}{K_m}$$

is the reciprocal of the Reuss average of the fluid ( $K_f$ ) and solid matrix bulk modulus (defined below),  $K_d$  is frame bulk modulus, and  $\phi_t$  is total porosity.

For a homogeneous mixture of pore-filling fluid, Wood's equation is commonly used to determine the fluid mixture bulk modulus

$$\frac{1}{K_f} = \frac{S_{wt}}{K_w} + \frac{(1-S_{wt})}{K_{hc}} \quad (2.6)$$

where  $S_{wt}$  is water saturation,  $K_w$  is bulk modulus of brine, and  $K_{hc}$  is bulk modulus of hydrocarbon. We use the Voigt-Reuss-Hill average to estimate the matrix bulk modulus of the non-porous solid material,

$$K_m = 0.5(\{\sum_{i=0}^L X_i K_i\} + \{\sum_{i=0}^L X_i / K_i\}^{-1}) \quad (2.7)$$

where  $K_m$  is the matrix bulk modulus,  $L$  is the number of pure lithology components making up the solid fraction,  $X_i$  is the fraction of solid volume occupied by mineral component  $i$ , and  $K_i$  is the bulk modulus of pure mineral component  $i$ . In the onshore shales in our study, 85-90% of the clay volume is illite, the rest are chlorite and mixed-layer illite/smectite clays. As a first approximation, we have thus used the elastic moduli of illite from Wang et al., (2001) and Katahara (1996). We use the same kerogen elastic moduli used by Sayers (2013) from Vernik and Landis (1996). Table 2.5 shows the end-member elastic moduli used. At kerogen volumes up to 25%, absolute percent difference between Hill average and the SCA model discussed in the kerogen effect sub-section is no more than 5%. We note that average kerogen volume does not exceed 21% for all 7 organic-shale formations in the application to log data section.

From the measured P-wave velocity, S-wave velocity data and bulk density, we determine the bulk modulus of the rock at *in situ* saturation. Once the *in situ* bulk modulus is calculated, it is possible to determine the dry-frame (skeleton) modulus from equation 2.5 above. Note that this gives the frame modulus in the presence of the pore fluids, so effects such as frame softening or hardening are not an issue. If pore pressure is not equilibrated, as would be the case if there is disconnected porosity, this is not the true bulk modulus of the frame, but rather a stiffer modulus. This may cause Gassmann's equations using this dry modulus to misestimate the hydrocarbon effect, but it is instructive to make the calculation and see what Gassmann predicts. We wish to understand how important lack of equilibration may be when applied to predict velocity changes due to hydrocarbons.

Given the frame modulus, the bulk modulus at 100% brine saturation is then given by equation 2.5, bulk density at 100% brine saturation is calculated using the mass-balance equation, and the measured dynamic shear modulus is assumed to be independent of water saturation and is obtained from the measured S-wave velocity and density at the original saturation. The assumption of constant shear-modulus with saturation also requires that equilibration be achieved. These quantities allow calculation of the compressional-wave velocity at 100% brine saturation using Gassmann's equations. After fluid substitution from partial hydrocarbon saturated to fully brine saturated, the velocities now straddle the GC brine-saturated shale line (blue data points in Figure 2.12). The change in  $V_p/V_s$  ratio of measured P- and S-wave velocities on the preserved state samples to calculated fully brine saturated is more than 5%. We are thus able to explain the deviation of the preserved lower Spraberry shale core

samples from the GC-92 fully brine-saturated shale line as being due primarily to the presence of hydrocarbons in the core samples if Gassmann's equations are indeed applicable.

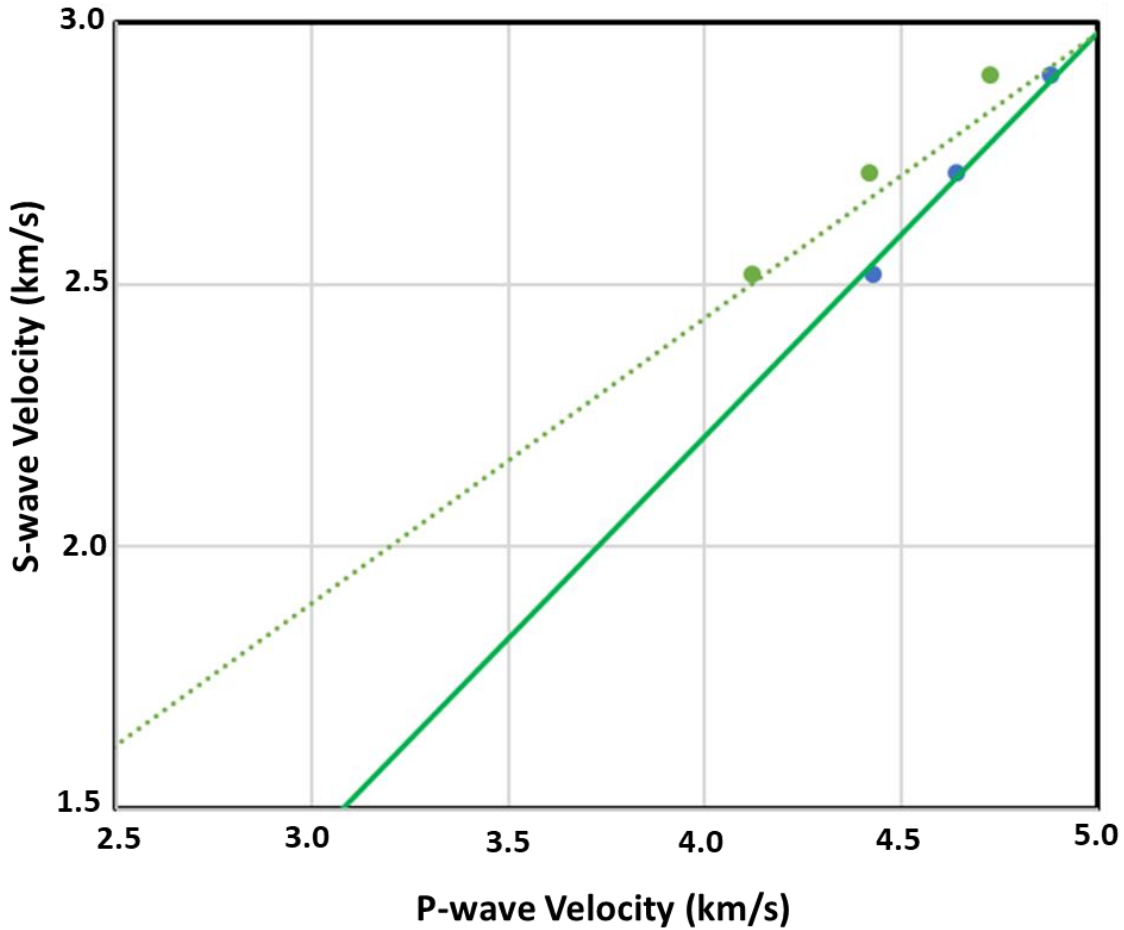


**Figure 2.12:** Cross plot of the measured S-wave versus P-wave velocity for the 3 preserved lower Spraberry shale core sample (green data-points); the blue data-points are after Gassmann fluid substitution. The green solid line in the plot is the Greenberg-Castagna brine-saturated shale line. The dotted green line is the linear fit to dry organic shales.

**Table 2.5:** Mineral end member elastic moduli used for computing matrix bulk and shear moduli for both fluid substitution and effective medium models. Clay elastic moduli are from Katahara (1996); Kerogen\_VnL is from Vernik and Landis (1996), Kerogen\_YnH is from Yan and Han (2013)

<b>Mineral</b>	<b>Bulk Modulus</b>	<b>Shear Modulus</b>
	<b>GPa</b>	<b>GPa</b>
<b>Quartz</b>	<b>38</b>	<b>41.77</b>
<b>Calcite</b>	<b>64.51</b>	<b>27.72</b>
<b>Dolomite</b>	<b>91.76</b>	<b>35.92</b>
<b>Clays (Illite)</b>	<b>52.6</b>	<b>31.5</b>
<b>Pyrite</b>	<b>147.63</b>	<b>129.04</b>
<b>Kerogen_VnL</b>	<b>5.53</b>	<b>3.2</b>
<b>Kerogen_YnH</b>	<b>4.25</b>	<b>2.125</b>

## 2.6 SENSITIVITY ANALYSIS

Showing that Gassmann predictions are consistent with observations is not sufficient to draw conclusions without understanding the errors associated with fluid substitution. There are many possible reasons why Gassmann's equations may not be applicable: dispersion, lack of pore equilibration, non-Biot mechanisms such as squirt flow (Dvorkin et al, 1995), the disparity in solid constituent moduli (e.g., Berryman and Milton; 1991) etc. However, we can ask the question: Assuming Gassmann's equations are entirely applicable, what uncertainty results from errors in the input parameters? As an example, we use the Permian-basin shale core sample to investigate errors in fluid substitution from dry to fully brine saturated because it has dry and brine-saturated measurements. Neglecting experimental error, table 2.6a shows the percent difference in Gassmann P-wave velocity prediction - when compared to measured data - due to uncertainty in each input parameter. Assuming no experimental or theoretical error,

this is the error in the prediction arising entirely from uncertainty in the input parameters.

Input P-wave and S-wave velocities for the sensitivity analyses are in table 2.6b.

A -2 PU (porosity unit) or -35% error in porosity caused a -5.7% error in P-wave velocity prediction at 0.67 MPa deviatoric stress, but the uncertainty in the P-wave velocity prediction drops off to less than 3% at higher deviatoric stresses. The calculated uncertainties seem small. However, they can be of the same order of magnitude as some of our reported changes in velocity ratio. Because error in one or two input parameters is likely to propagate to the other parameters, we have included in the last row the effect of combining all the errors in the parameters; both for the positive and negative deviations. (This, however, is not a true propagation of error; just simply a combination of all the uncertainties. A true -2 PU change in porosity for example, will have an impact on the bulk density, frame modulus, dry P-wave and S-wave velocities. We would have to propagate the -2 PU effect on all input parameters. That is not what we set out to do. Our goal is given a measurement and uncertainty in an input parameter, how well does Gassmann still predict that measurement. This explains why there is no consistent reduction in error with increasing deviatoric stress for uncertainty in some input parameters.) We conclude that Gassmann's equations, even if theoretical assumptions are valid, cannot be used to draw definitive conclusions about the effect of hydrocarbons. However, the fact that velocities consistent with the GC-92 shale trend are obtained by fluid substitution, lends credence to the hypothesis that the low  $V_p/V_s$  ratios in dry organic shales can be explained entirely by fluid compressibility effects.

In addition, in table 2.6c we also include the ratio of the difference between P-wave velocity prediction with uncertainties applied and measured brine-saturated P-wave velocities and the initial change in P-wave velocity prediction without uncertainties using:

$$\Delta V_{pp}(\%) = \frac{V_{pp(input \pm uncertainty)} - V_{p(measured)}}{V_{pp(input)} - V_{p(measured)}} * 100, \quad (2.8)$$

where  $V_{pp(input)}$  is predicted P-wave velocity from fluid substitution and  $V_{pp(input \pm uncertainty)}$  is predicted P-wave velocity with uncertainty applied.

**Table 2.6a:** Sensitivity analysis: Effect of percent error in Gassmann equation input parameters on its P-wave velocity prediction for the Permian basin shale core sample. For the combined row, we have used or combined all the negative uncertainties or all the positive uncertainties from the measured or computed input parameters and propagated those uncertainties through Gassmann’s equations. Dev\_stress is deviatoric stress in MPa. The measured dry and fully brine-saturated bulk densities are 2.533 and 2.59 respectively. Porosity is 5.7%.

Input Parameter changed	Change in Gassmann P-wave Velocity Prediction (%)							
	Dev_stress(MPa) = .67	Dev_Stress = 15.5	Dev_Stress = 29.3	Dev_Stress = 43.2				
Matrix bulk modulus: -10%, +10%	-1.40	1.10	1.34	1.12	2.14	1.17	2.85	1.19
Fluid bulk modulus: -10%, +10%	-2.23	-3.60	0.45	-0.83	1.18	0.02	1.86	0.78
Porosity: -2PU, +2PU	-5.70	-1.03	-2.83	1.58	-1.79	2.18	-0.92	2.78
Dry & Wet RhoB: -10%, +10%	-5.24	-0.97	-2.50	1.74	-1.65	2.47	-0.87	3.13
P-wave velocity_dry: -2%, +2%	-2.40	-3.52	0.38	-0.85	1.24	-0.12	2.00	0.56
S-wave velocity_dry: -2%, +2%	-2.42	-3.48	0.32	-0.76	1.09	0.06	1.80	0.79
<b>Combined: -ve, +ve</b>	<b>-4.77</b>	<b>-2.24</b>	<b>-1.84</b>	<b>0.30</b>	<b>-0.77</b>	<b>0.86</b>	<b>0.13</b>	<b>1.43</b>

**Table 2.6b:** Measured velocity values used for sensitivity analyses.

<b>Dev_Stress (MPa)</b>	<b>0.67</b>	<b>15.52</b>	<b>29.34</b>	<b>43.17</b>
<b>Vp dry (km/s)</b>	<b>3.863</b>	<b>3.968</b>	<b>4.067</b>	<b>4.143</b>
<b>Vs dry (km/s)</b>	<b>2.468</b>	<b>2.51</b>	<b>2.514</b>	<b>2.543</b>
<b>Vp fully brine saturated (km/s)</b>	<b>4.154</b>	<b>4.325</b>	<b>4.395</b>	<b>4.469</b>

**Table 2.6c:** Absolute percent error in P-wave velocity change. I.e., the ratio of the change in P-wave velocity prediction with uncertainty and the initial P-wave velocity prediction without uncertainty; both with respect to the measured brine-saturated P-wave velocity. The fluid substitution uncertainty relative to the change in velocity is enormous.

Input Parameter changed	Absolute Percent Error in Predicted P-wave Velocity change							
	Dev_stress(MPa) = .67	Dev_Stress = 15.5	Dev_Stress = 29.3	Dev_Stress = 43.2				
Matrix bulk modulus: -10%, +10%	46.81	148.17	607.57	742.73	364.34	141.36	215.44	5.81
Fluid bulk modulus: -10%, +10%	75.13	122.99	207.18	384.90	202.83	4.18	142.13	60.63
Porosity: -2PU, +2PU	199.02	34.15	1333.23	711.09	317.84	370.45	72.45	210.56
Dry & Wet RhoB: -10%, +10%	32.13	182.32	781.62	1174.02	418.58	291.00	236.60	68.53

If we accept that Gassmann’s equations will predict the direction of velocity change, if not the accurate magnitude of the change, we can apply fluid substitution to a variety of hydrocarbon-saturated shale reservoirs and determine if fluid substitution produces fully brine-saturated velocities in greater accord with the GC-92 shale trend.

## 2.7 APPLICATION OF FLUID SUBSTITUTION TO SONIC LOG MEASUREMENTS IN ORGANIC SHALES

In this section, we cross plot P-wave and S-wave velocities in organic-rich shale reservoirs and compare to empirical trends and fluid substitution using fluid properties at *in-situ* conditions whose averages are shown in Table 2.7. The fluid substitution follows the procedure described in the fluid substitution section. Average clay volume, water saturation and kerogen volume for each of the formation is shown in table 2.8 below; as well as the average velocity ratios both before and after fluid substitution.

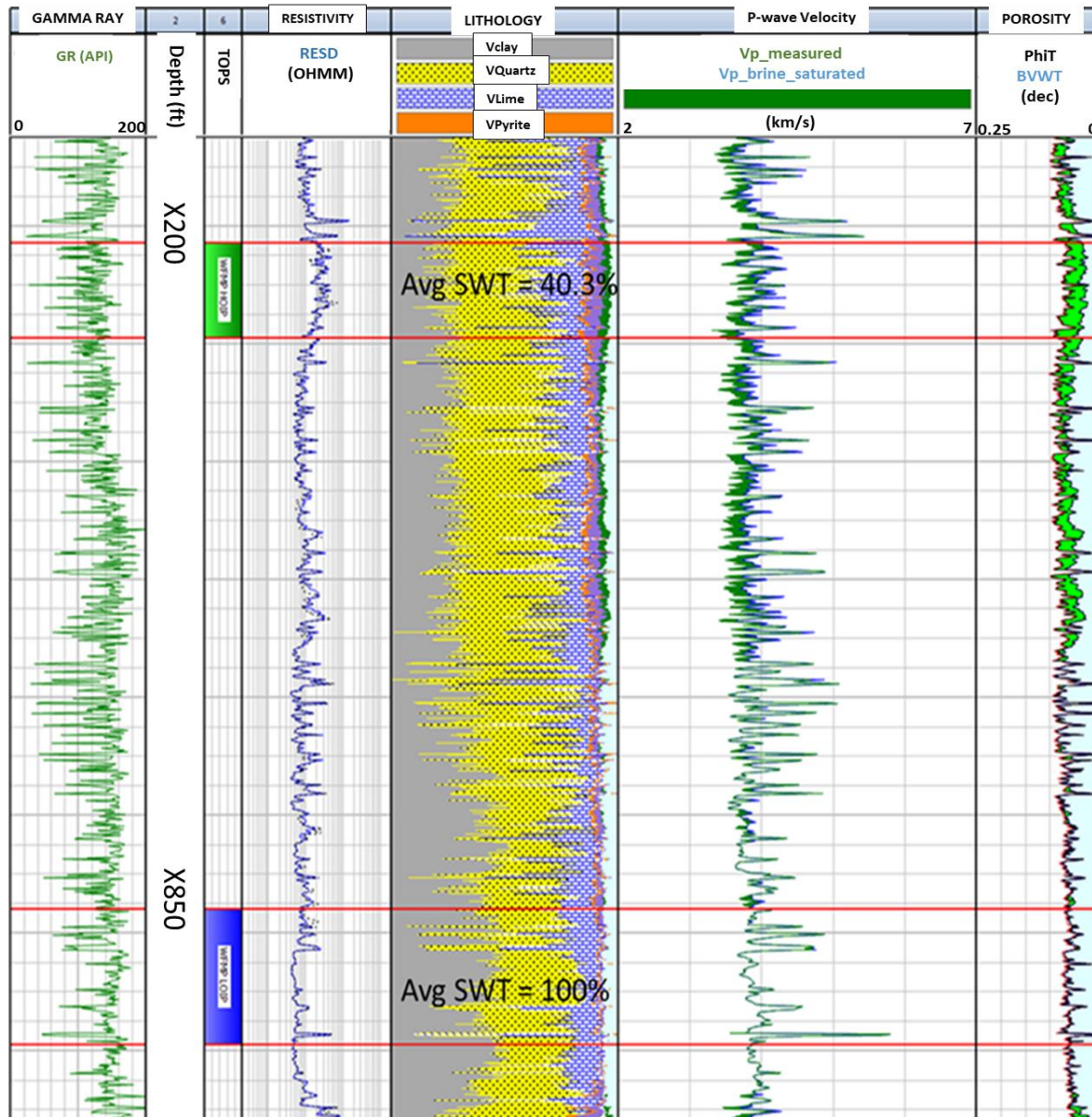
### 2.7.1 WOLFCAMP SHALE

Figure 2.13 below is a log plot from the Wolfcamp Shale in a Permian (Midland) Basin well. The water saturation of two intervals are highlighted; log analysis calculates that one interval has a low average water saturation of 40.3% while the other interval is 100% water saturated.

The Wolfcamp Shale is a Permian-age organic shale in Midland basin – a sub-basin of the Permian basin. In figure 2.14, two intervals are plotted, based on well-log analysis that has been calibrated to core measured data, one interval has a low average water saturation of 40.3% while the other interval is 100% water saturated. The Wolfcamp Shale is a volatile oil shale play. The 100% water-saturated interval velocities straddle the GC-92 fully brine-saturated shale trend. Specifically, the average P-wave and S-wave velocities for this interval plot within 0.9% of the GC-92 shale line. On the other hand, the oil-bearing interval deviates from the 100% brine-saturated line; average P-wave and S-wave velocities for this interval plot 11.2% above the

shale trend. This interval plots below the dry organic-shale line – likely due to hydrocarbon type – as oil is more compressible than brine, but less compressible than air. The interval with an average water saturation of 40.3% has average  $V_p/V_s$  of 1.73, whereas the interval with water saturation of 100% has average  $V_p/V_s$  of 1.83.

Next, we focus on the interval with low water saturation (40.3%). The kerogen volume is in the low to medium range, between 1.5% and 10%, with an average kerogen volume across this interval of 7.4%. We apply Gassmann's equation to numerically fully saturate these intervals with brine. The effect of fluid substitution across this interval is shown in Figure 2.15. The velocities now plot closer to the GC-92 brine-saturated shale line. After fluid substitution, the interval average  $V_p/V_s$  increases from 1.73 to 1.84, slightly more than a 6% change.



**Figure 2.13:** Log plot of the Wolfcamp shale. The GAMMA RAY track contains Gamma-ray (solid green curve). The RESISTIVITY track contains resistivity log (RESD). The LITHOLOGY track contains formation lithology fractional volumes determined by volumetric log analyses. The VP track contains measured P-wave velocity (green curve – Vp\_measured) and P-wave velocity after fluid substitution (blue curve – Vp\_brine\_saturated) to 100% brine-saturation; the difference between both curves is shaded green – an indication of the presence of hydrocarbons. The POROSITY track contains total porosity (PhiT) and bulk volume water (BVWT), the light blue shading in this track is water volume while the green shading is oil volume. Depths in the depth track are only to indicate depth scale, actual depths are not available for publication.

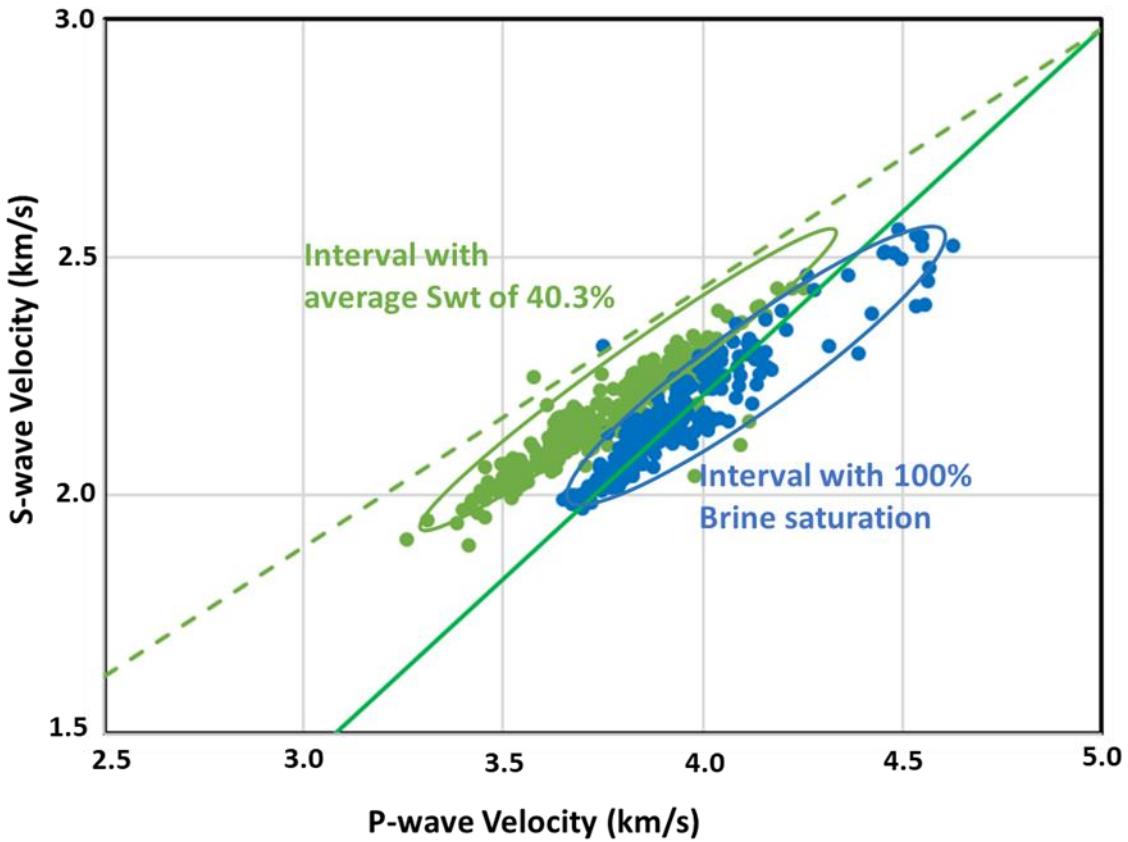


**Figure 2.14:** Cross plot of the measured S-wave and P-wave velocities for the two intervals highlighted in figure 16. The interval with average water saturation of 40.2% are the green data-points; the interval with average water saturation of 100% are the blue data-points. The solid green line in the plot is the Greenberg-Castagna (1992) fully brine-saturated shale trend. The dotted green line is the dry organic-shale line.

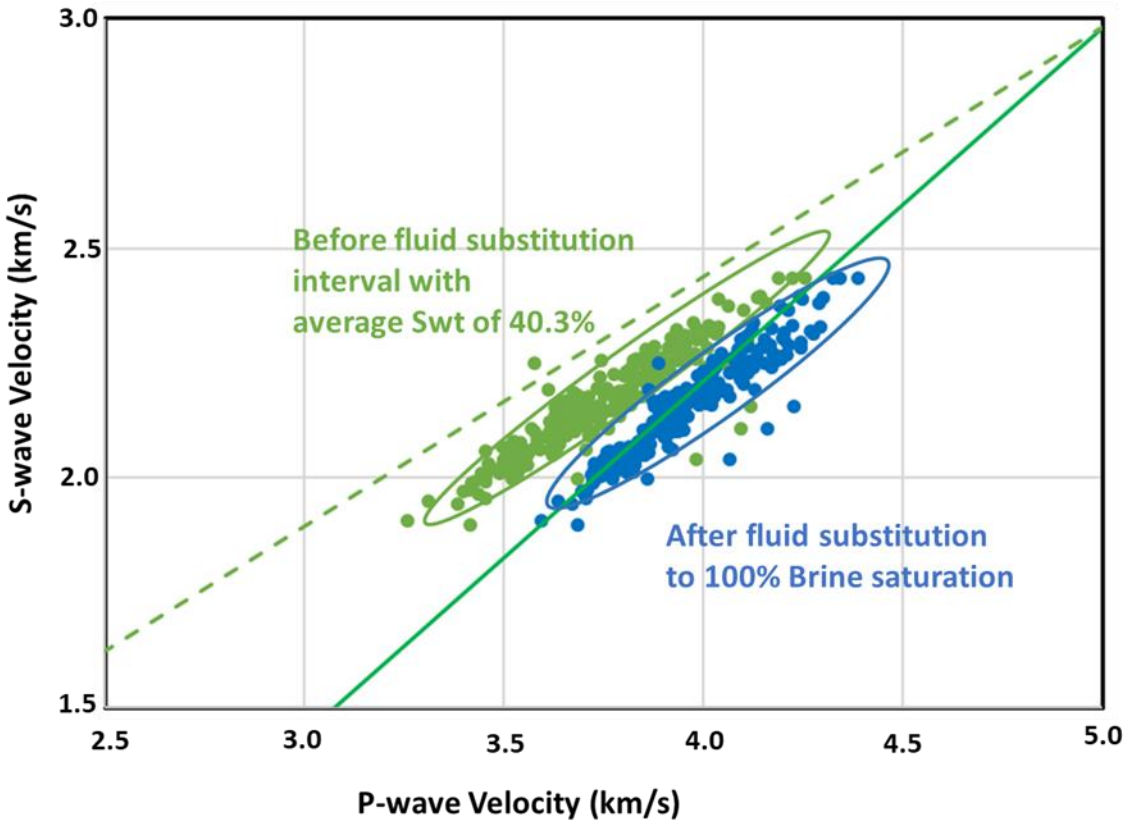


**Figure 2.15:** Cross plot of the S-wave versus P-wave velocity of the Wolfcamp shale interval with average water saturation of 40.3%. The green data points are before fluid substitution; the blue data-points are after fluid substitution. The solid green line in the plot is the GC-92 fully brine-saturated shale line. The dotted green line is the dry organic-shale line.

## 2.7.2 LOWER SPRABERRY SHALE

The lower Spraberry Shale is also a Permian age volatile oil shale play. Kerogen is also in the low to medium range – in our dataset the range is 0.1% to 9%. Average kerogen, water saturation and clay volumes are shown in table 2.8. The fluid-substituted data points plot on the GC-92 shale line (Figure 2.16). After fluid substitution, the percent change in  $V_p/V_s$  ratio is greater than 6%.

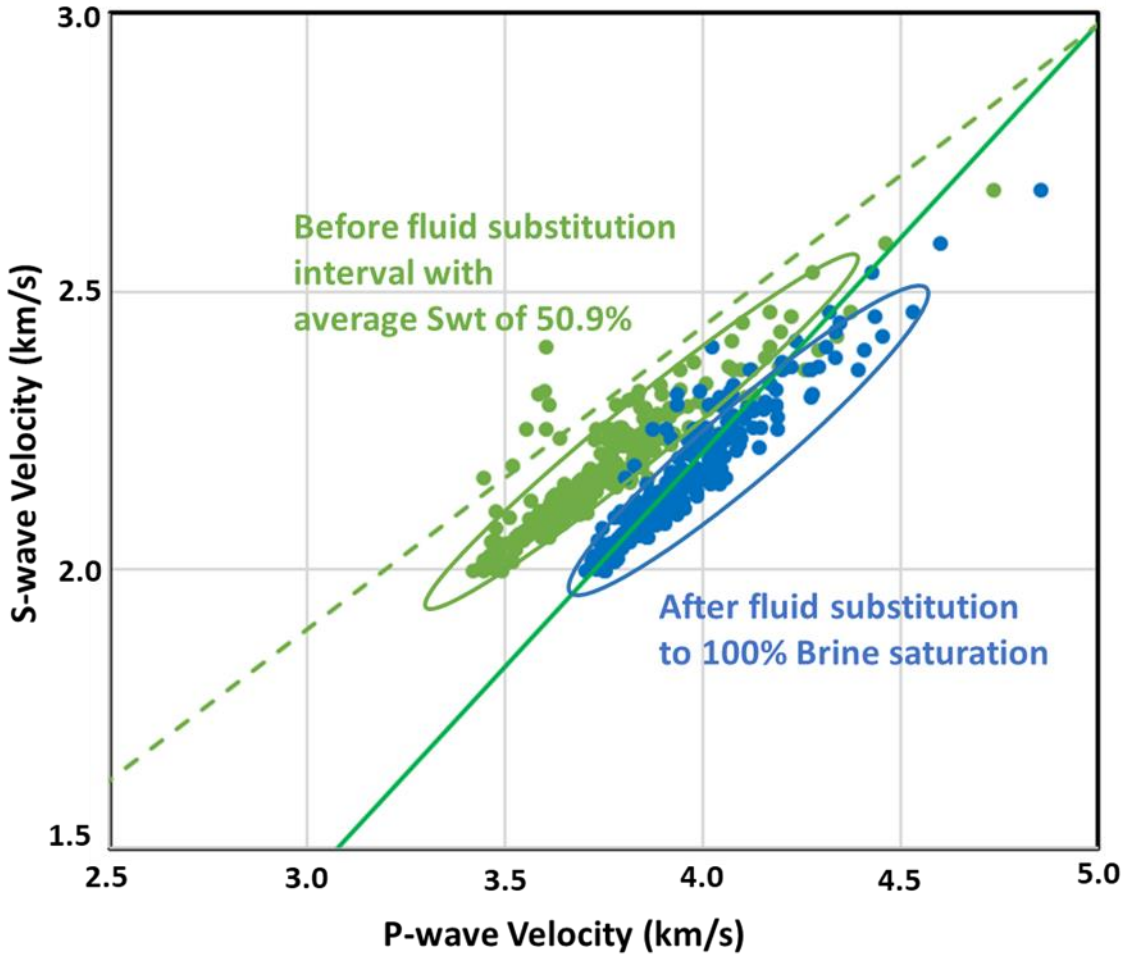


**Figure 2.16:** Cross plot of the S-wave versus P-wave velocity of the Lower Spraberry shale interval with average water saturation of 50.9%. The green data points are before fluid substitution; the blue data points are after fluid substitution. The solid green line in the plot is the Greenberg-Castagna fully brine-saturated shale line. The dotted green line is the dry organic-shale line.

### 2.7.3 AVALON SHALE

The Avalon shale is a Permian-age organic-rich shale in the Delaware basin, a sub-basin of the Permian basin. Kerogen volume is in the medium to fairly high range. For our data, the range is from 7% to 20.4%. Depending on location within the basin, the Avalon shale could be a gas condensate or volatile oil shale play. The average clay volume is 19.6% and there is very little to no carbonate content. Figure 2.17 shows that the *in situ* velocities plot right on the dry organic-shale line. There is over a 7% change in  $V_p/V_s$  ratio after fluid substitution, although it is slightly lower than expected from the GC-92 trend.

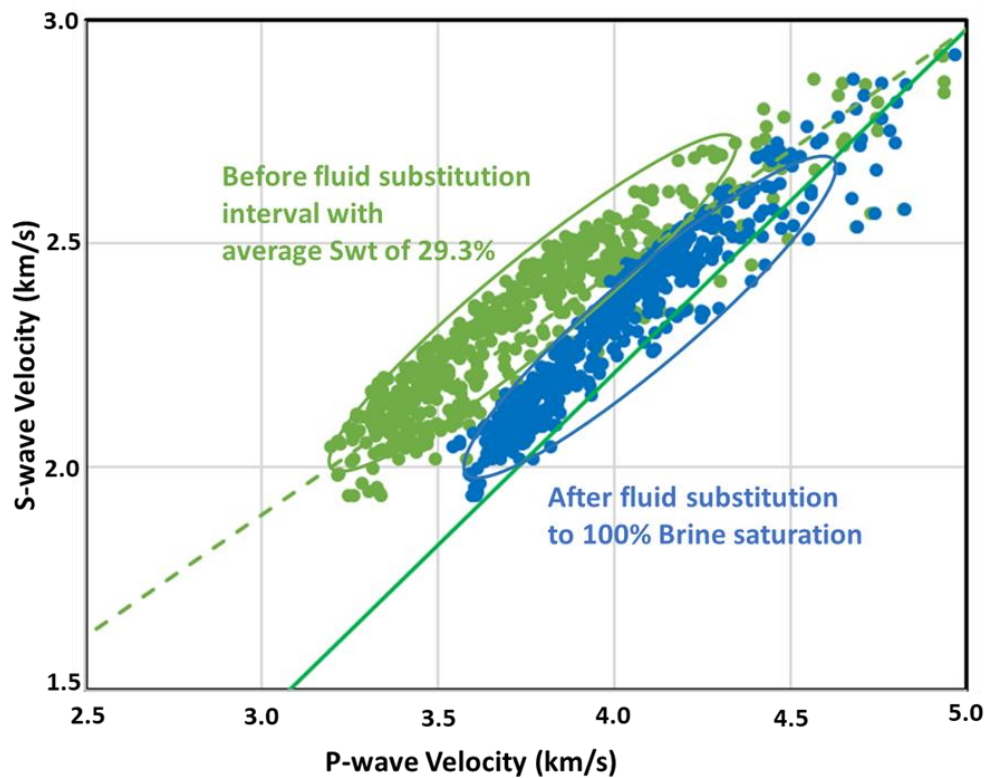


**Figure 2.17:** Cross plot of the shear-wave versus compressional-wave velocity of an Avalon shale interval with average water saturation of 29.3%. The green data points are before fluid substitution; the blue data-points are after fluid substitution. The solid green line in the plot is the Greenberg-Castagna fully brine-saturated shale line. The dotted green line is the dry organic-shale line.

#### 2.7.4 LOWER CLINE SHALE

Within the lower Cline formation, we focus on an interval with average water saturation of 46.6%. The lower Cline is hydrocarbon rich with average clay volume of 30.7%. Average total porosity and kerogen volumes are 5.9% and 13.1% respectively. The kerogen volume is in the low to medium range between 1 and 16.9%. Figure 2.18 shows the S-wave and P-wave velocities of this interval both before and after fluid substitution. Note once again how the blue data points straddle the GC-92 fully brine-saturated shale trend after fluid substitution. The average  $V_p/V_s$  before fluid substitution is 1.63; after Gassmann fluid substitution the  $V_p/V_s$  increases 9% to 1.78.

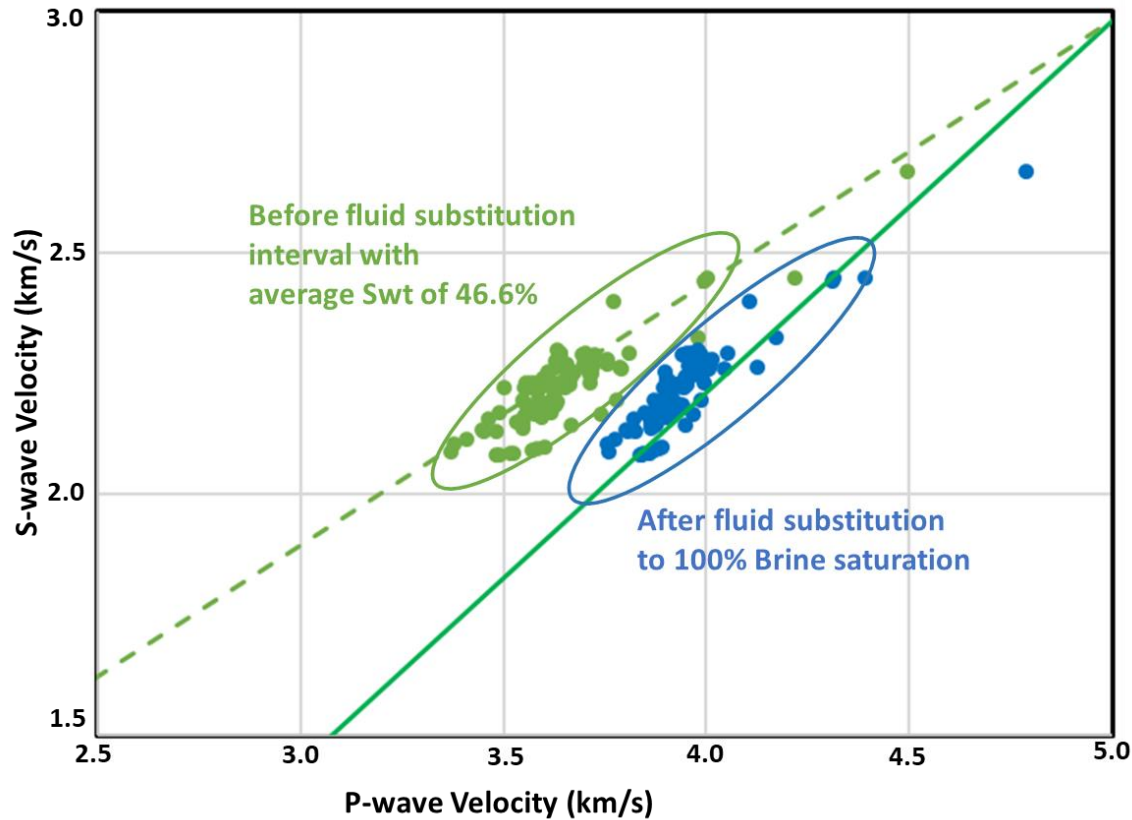


**Figure 2.18:** Cross plot of the shear-wave versus compressional-wave velocity of the Lower Cline shale interval with average water saturation of 46.6%. The green data points are before fluid substitution; the blue data points are after fluid substitution. The solid green line in the plot is the Greenberg-Castagna fully brine-saturated shale line. The dotted green line is the dry organic-shale line.

### 2.7.5 WOODFORD SHALE

The Woodford shale is a late Devonian-age organic-rich shale play in the Midland basin.

The kerogen volume in our dataset is in the medium range, between 8.5 and 14.6%. The

velocities before fluid substitution are near the dry organic-shale line and around the GC-92

fully brine-saturated line after fluid substitution (Figure 2.19). After Gassmann fluid substitution

the average  $V_p/V_s$  increases over 11% to 1.84.

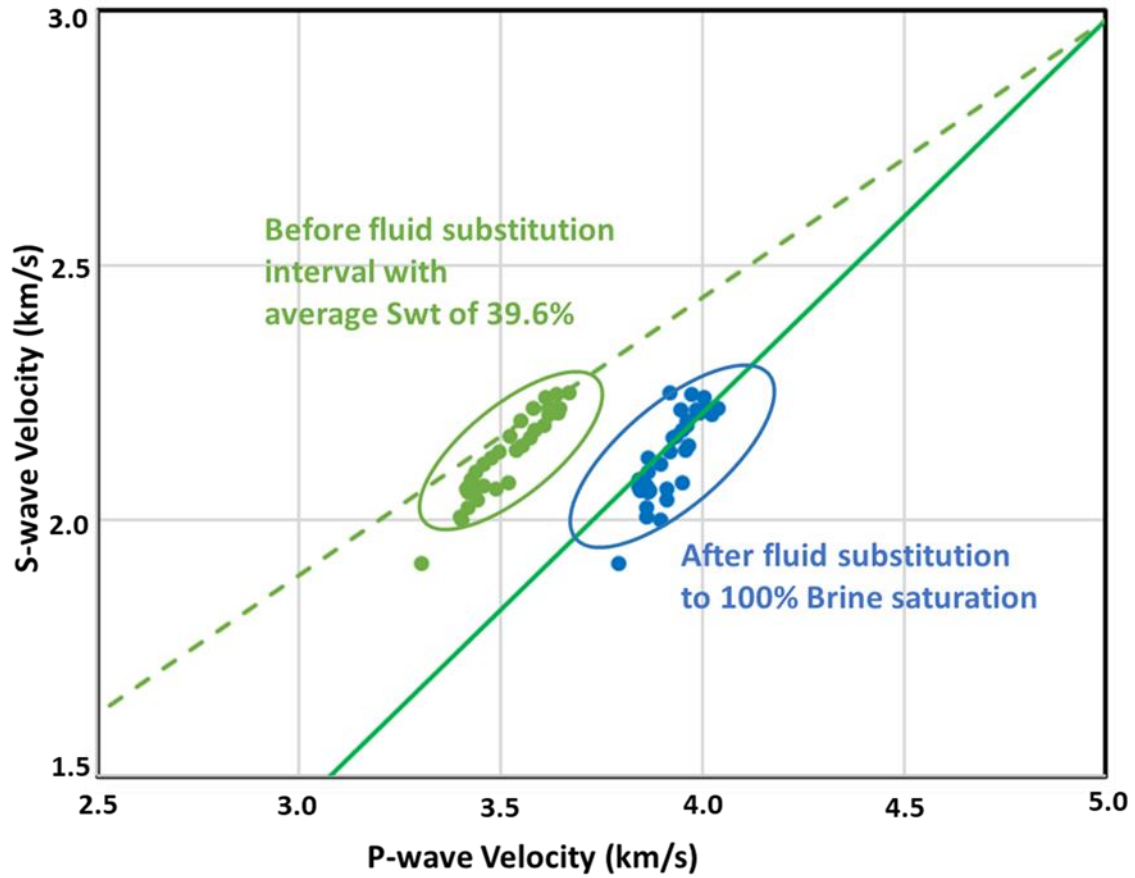


**Figure 2.19:** Cross plot of the shear-wave versus compressional-wave velocity of the Woodford shale interval with average water saturation of 56.6%. The green data points are before fluid substitution; the blue data points are after fluid substitution. The solid green line in the plot is the Greenberg-Castagna fully brine-saturated shale line. The dotted green line is the dry organic-shale line.

### 2.7.6 BAKKEN SHALE

The Bakken is another late Devonian-age organic-rich shale play in the Williston basin. The hydrocarbon type is dead oil which differs from the other datasets in this study. The kerogen volume in our dataset is in the high range: between 9.4 and 32%. The average water saturation is 24%, the lowest encountered in this study. After fluid substitution  $V_p/V_s$  increased by over 12% to 1.9 (see Figure 2.20 and table 2.8).

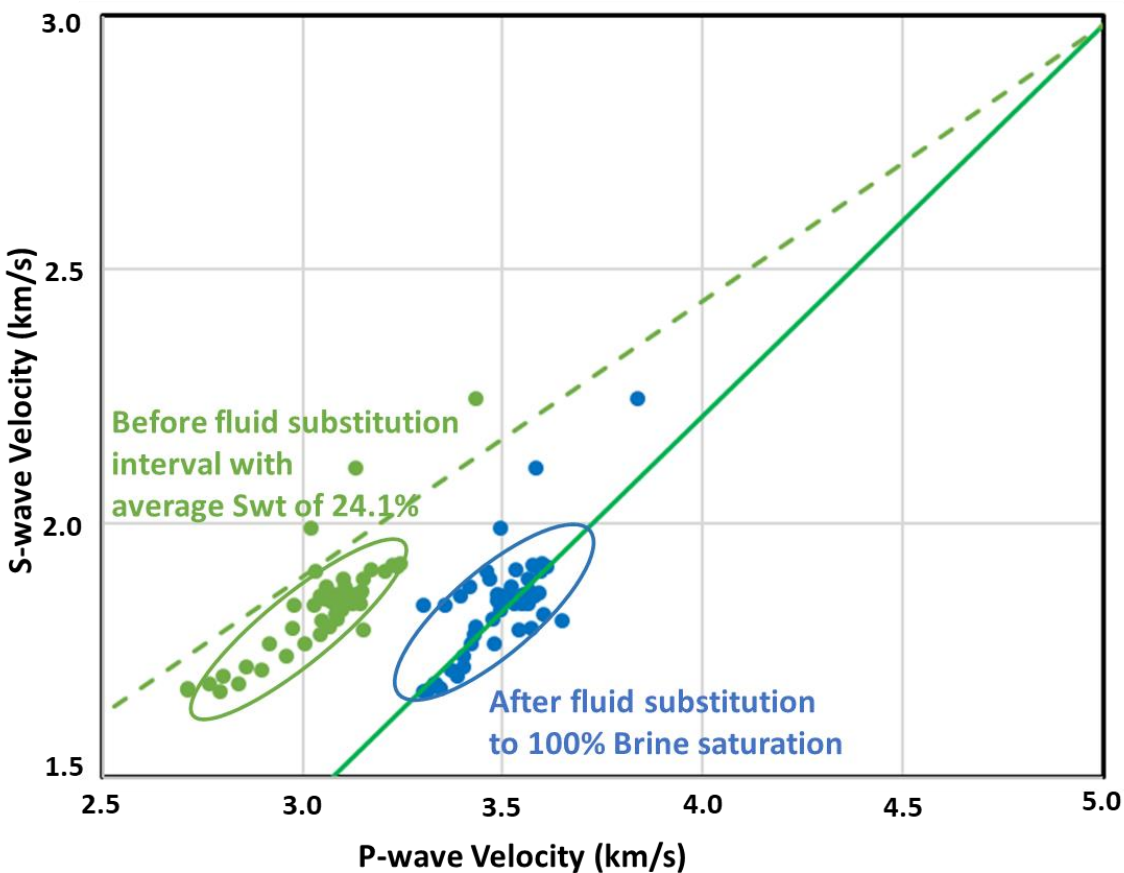


**Figure 2.20:** Cross plot of the S-wave versus P-wave velocity of the Bakken shale formation with the green data points are before fluid substitution; the blue data points are after fluid substitution. The solid green line in the plot is the Greenberg-Castagna fully brine-saturated shale line. The dotted green line is the dry organic-shale line.

### 2.7.7 EAGLEFORD SHALE

The Eagle Ford is a late Cretaceous-age organic shale. The kerogen volume is in the low to medium range – in our dataset, the range is from 1.2% to 9.8%. The hydrocarbon type in this dataset is dry gas. Figure 2.21 shows the cross plot of the S-wave and P-wave velocities both before (green data points) and after fluid substitution (blue data points). Unlike the other formations in which the mineralogy is primarily composed of siliclastics, the Eagleford is a mudrock with significant calcite content. The average calcite volume is 55%. This would likely explain why these gas-saturated velocities (Figure 2.21) plot closer to the GC-92 shale line with higher velocity ratio than the dry organic-shale line, i.e., the true fully brine-saturated shale line for this formation would likely be between the brine-saturated shale line and the GC-92 limestone trend.

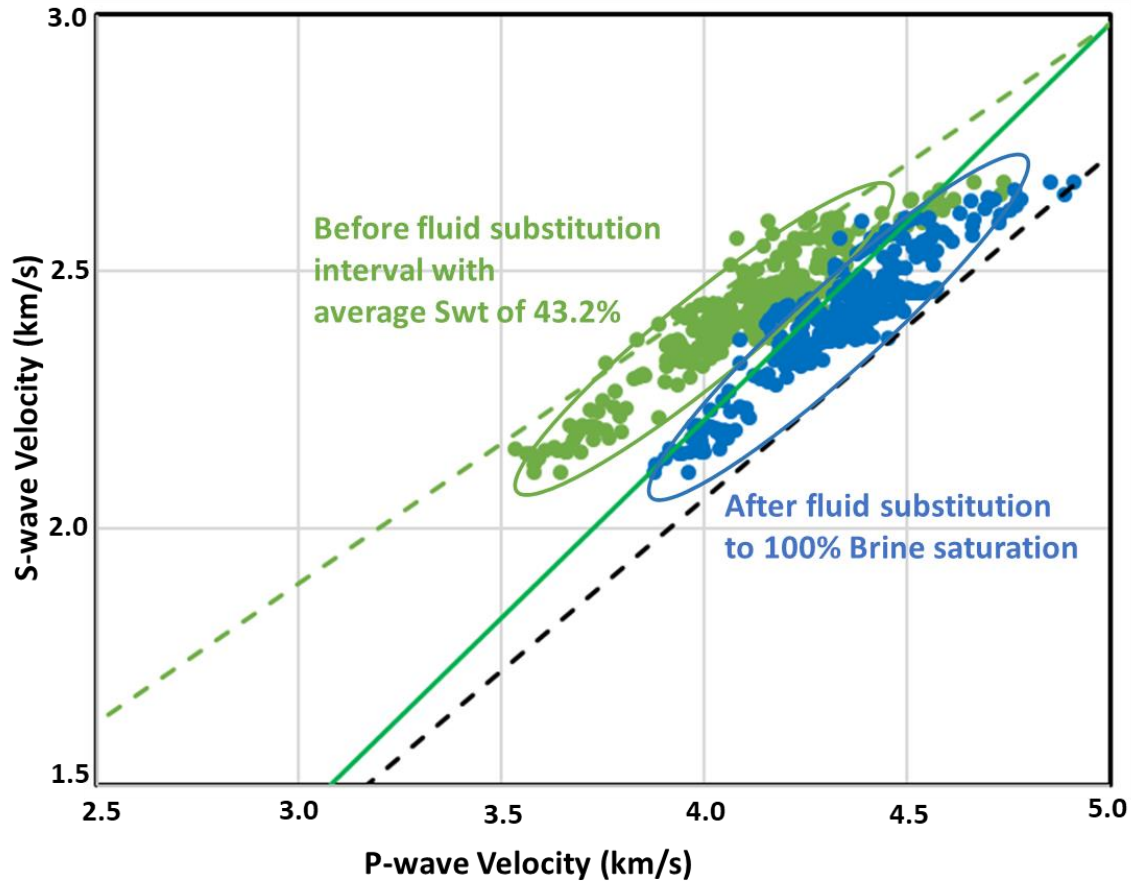


**Figure 2.21:** Eagleford shale. Cross plot of the S-wave versus P-wave velocity of the Bakken shale interval with average water saturation of 43.2%. The green data points are before fluid substitution; the blue data points are after fluid substitution. The solid green line in the plot is the Greenberg-Castagna fully brine-saturated shale line. The dotted green line is the dry organic-shale line.

**Table 2.7:** Average *in situ* reservoir fluid properties used in fluid substitution for each shale formation. *In situ* fluid properties were determined using the equations of Batzle and Wang (1992) and Batzle and Han (2000).

Shale Formation	Hydrocarbon type	Hydrocarbon Bulk Modulus (GPa)	Hydrocarbon density (g/cc)	Brine Bulk Modulus(GPa)	Brine density (g/cc)
Wolfcamp	Volatile oil	0.434	0.677	2.73	1.04
Lower Spraberry	Volatile oil	0.375	0.675	2.75	1.03
2nd Avalon	Volatile oil	0.366	0.67	2.75	1.05
Lower Cline	Volatile oil	0.43	0.675	2.8	1.05
Woodford	Volatile oil	0.43	0.675	2.75	1.05
Bakken	Oil	0.75	0.8	2.75	1.06
Eagleford	Gas	0.13	0.25	2.8	1.06

**Table 2.8:** Average velocity ratio of the 7 organic-shale formations before and after fluid substitution

Organic shale formation	Clay volume (%)	Average Kerogen volume (%)	Average Swt (%)	Vp/Vs before fluid substitution	Vp/Vs after fluid substitution
Wolfcamp	28.1	7.4	40.3	1.73	1.84
Lower Spraberry	32.2	5.7	50.9	1.72	1.83
Avalon	19.6	14.1	29.3	1.61	1.73
Lower Cline	30.7	13.1	46.6	1.63	1.78
Woodford	32.4	11.3	39.6	1.65	1.84
Bakken	20.5	20.5	24.0	1.66	1.90
Eagleford	17.2	5.8	43.1	1.69	1.78

## 2.8 DISCUSSION

In terms of petrophysical and geomechanical properties, the reason that shales are treated differently than other sedimentary rocks is primarily because of the presence of clays resulting in (1) physicochemical interactions with fluids that can change frame moduli, and (2) low permeability (calling into question whether pore equilibration can occur). In granular sandstones under significant effective pressure, it is safer to assume that the rock-fluid interaction is purely mechanical, an effect that can be appropriately modeled by Gassmann fluid substitution assuming pore pressure equilibration. However, that is not necessarily the case with clays. Fluid-clay interactions have been extensively studied in geotechnical engineering. They find that in addition to the mechanical effect that clays have in common with other lithologies found in the subsurface; there is a physicochemical effect (Robinson and Allam, 1998; Cui et al., 2002; Nguyen et al., 2013). The physicochemical effect refers to how ions and water diffuse through the clay-pore water interface. It turns out that not all clays have the same physicochemical properties. Robinson and Allam (1998) for example find that for smectite rich clays the physicochemical effect is dominant at low pressure; in kaolinite and illite, compressibility is controlled primarily by the mechanical effect.

Di Maio et al., (2004) studied 4 clay samples with the mineral composition of the samples ranging from 70-80% rich in smectite to one that is 80% rich in kaolinite. For the sample rich in kaolinite, Di Maio et al., (2004) find that pore fluid salinity had practically no impact on compressibility – the implication is that the mechanical effect will be the primary or dominant effect if not the only effect in kaolinite. Illite behaves in a way similar to kaolinite

(Robinson and Allam, 1998; Di Maio et al., 2004). On the other hand, in the smectite rich sample, the physicochemical effect is the dominant effect controlling compressibility at low stresses. They find that increase in pore fluid salinity resulted in a decrease in compressibility (an increase in bulk modulus). They also observed that the physicochemical effect is suppressed with increasing vertical stress. When a non-polar fluid (cyclohexane) was used to saturate the clay samples, they observed that even for the smectite-rich sample, the physicochemical effect is significantly suppressed; specifically, the compressibility effect on all samples was similar to the 'dry' samples. This is an indication that the presence of non-polar fluid inhibits the physicochemical effect in clays. Drilling engineers know this well, because when they drill through a reactive shale formation with water-based drilling fluid they have wellbore stability issues; on the other hand, drilling through the same formation with oil-based drilling fluid either eliminates or significantly reduces the wellbore stability issue.

The mechanical and physicochemical effect are responsible for the acoustic velocity effect observed by Zhang et al., (2006) when shales with significant smectite content were saturated with brine of increasing salinity with no applied confining stress. Consider for example Zhang et al., (2006) Pierre shale sample: fluid substitution from deionized water to 8 wt% NaCl should result in approximately 1% increase in velocity; however, the observed change in P-wave velocity is close to 4%. This is obviously because of the physicochemical effect, as evidenced by the increase in pore fluid salinity yielding an increase in P-wave velocity more than the salinity effect on bulk modulus would achieve.

On a total clay volume basis, illite makes up about 90% of the clay volume in the shales in this study; other clay constituents are chlorite, kaolinite and smectite making up 10%. On a zero-porosity solid rock basis, smectite content in the shales in this study will be in the 0-3% range. As stated above, illite is not an active clay; as such, the mechanical effect will thus predominate. In addition, at *in situ* stresses the possible physicochemical effect due to the small smectite present in some of our dataset will likely be further suppressed or eliminated. Recall that Di Maio et al., (2004) observe that the physicochemical effect is suppressed with the increase in applied stress. That this would be the case with acoustic velocity measurements is evident from the work of Holt et al., (1996), they find that the increase in P-wave velocity caused by increase in pore fluid salinity was reduced when the measurements were made at an effective confining pressure of 5 MPa versus at atmospheric condition. Consider for example their shale sample exposed to 16% CaCl<sub>2</sub> fluid for 80 hours – at atmospheric conditions, the relative change in velocity was 3%; however, at 5 MPa effective confining pressure and 80 degrees Celsius the relative change in velocity was only 0.6%.

The fluid substitution results for the Pierre and Cotton Valley shales discussed in the “Fluid effect” section are another confirmation that in the absence of smectite and under *in-situ* stress conditions even in the presence of a relatively small percentage of smectite, the fluid effects in clays will be primarily mechanical. The Cotton Valley shale, for example, has no smectite; this would likely explain why the percent error in water-saturated P-wave velocity prediction (2.4-3%) is better than that of the Pierre-shale sample (3.5 -7%) which has a small percentage of smectite. We emphasize that these numbers are fairly accurate for shales

considering that percent error for fluid substitution prediction that we computed from acoustic velocity measurements performed by Tosaya (1982) on Berea sandstone samples that has only 2% clay volume is in the 2-2.6% range. The Pierre shale has 57% clay volume, Cotton Valley shale has 36% clay volume on a solid rock basis.

Theoretical models and experimental data suggest that solid kerogen should not decrease the shale  $V_p/V_s$  ratio as dramatically as the presence of free hydrocarbons; in fact, as the kerogen volume increases, experiments suggest no change to a slight increase in the  $V_p/V_s$ . The velocity ratio of seven different naturally organic-rich shale formations all have a trend that is consistent with the theoretical models as well as with the measured synthetic-shale dataset. We conclude then that both theoretical models and the measured data on organic-rich shale formation do not support the hypothesis that kerogen volume alone is responsible for the abnormally low velocity ratio observed in organic shales when compared to fully brine-saturated shales.

On the other hand, we find that the low velocity ratio in shales is not unique to organic-rich shales. The organic and inorganic dry shales, as well as hydrocarbon-saturated organic and inorganic shales have a low velocity ratio when compared to fully brine-saturated shales – organic and inorganic. In addition, we observe that a significant deviation from the GC-92 shale line for both organic and inorganic shales can be explained by air, gas, or oil saturation. For example, for the Permian basin shale core sample, the velocity ratio ranged from 1.56 to 1.6. However, after full brine saturation, the velocity ratio ranged from 1.77 to 1.79. We observed a similar effect on several other organic and inorganic shale formations – the Wolfcamp shale,

the lower Spraberry shale, the lower Cline shale, the Avalon shale, the Cotton Valley shale, the offshore Gulf of Mexico shales (in Appendix A), the Bakken shale, the Pierre shale and so on.

We find further that using Gassmann fluid substitution, we were able to predict the deviation of dry and hydrocarbon-saturated shales from the GC-92 fully brine-saturated shale trend for both ultrasonic and sonic log measurements and thus explain the unusually low velocity ratio as being due to gas or hydrocarbon saturation. In addition, as shown in table 2.6a, even after incorporating uncertainty in Gassmann input parameters, we observe that the measurements fall within the range of Gassmann predictions. We conclude then that the theoretical model and the measured data support and fail to falsify the hypothesis that the unusually low velocity ratio observed in shales when compared to fully brine-saturated shales is due to hydrocarbon saturation. This has significant implications for the use of acoustic measured data to qualitatively predict the presence of hydrocarbons in both organic and inorganic shales. For example, a significant deviation of a shale formation or interval from the GC-92 fully brine-saturated shale line on a  $V_p$ - $V_s$  cross plot can be used to predict whether or not the formation or interval is hydrocarbon-saturated.

Note, for example, how the difference in bulk modulus before and after fluid substitution for the lower Cline shale log plot shown in Figure 2.22 clearly differentiate the hydrocarbon-saturated and fully brine-saturated intervals. In the absence of enough data to conduct fluid substitution, the velocity ratio – shown in the  $V_p/V_s$  track on the same plot, where the green shading indicate deviation from the GC-92 fully brine-saturated shale trend - could

have been used as a quick look indicator to identify the sweet spot. This also suggests potential for similar pre-drill analysis utilizing pre-stack seismic inversion.

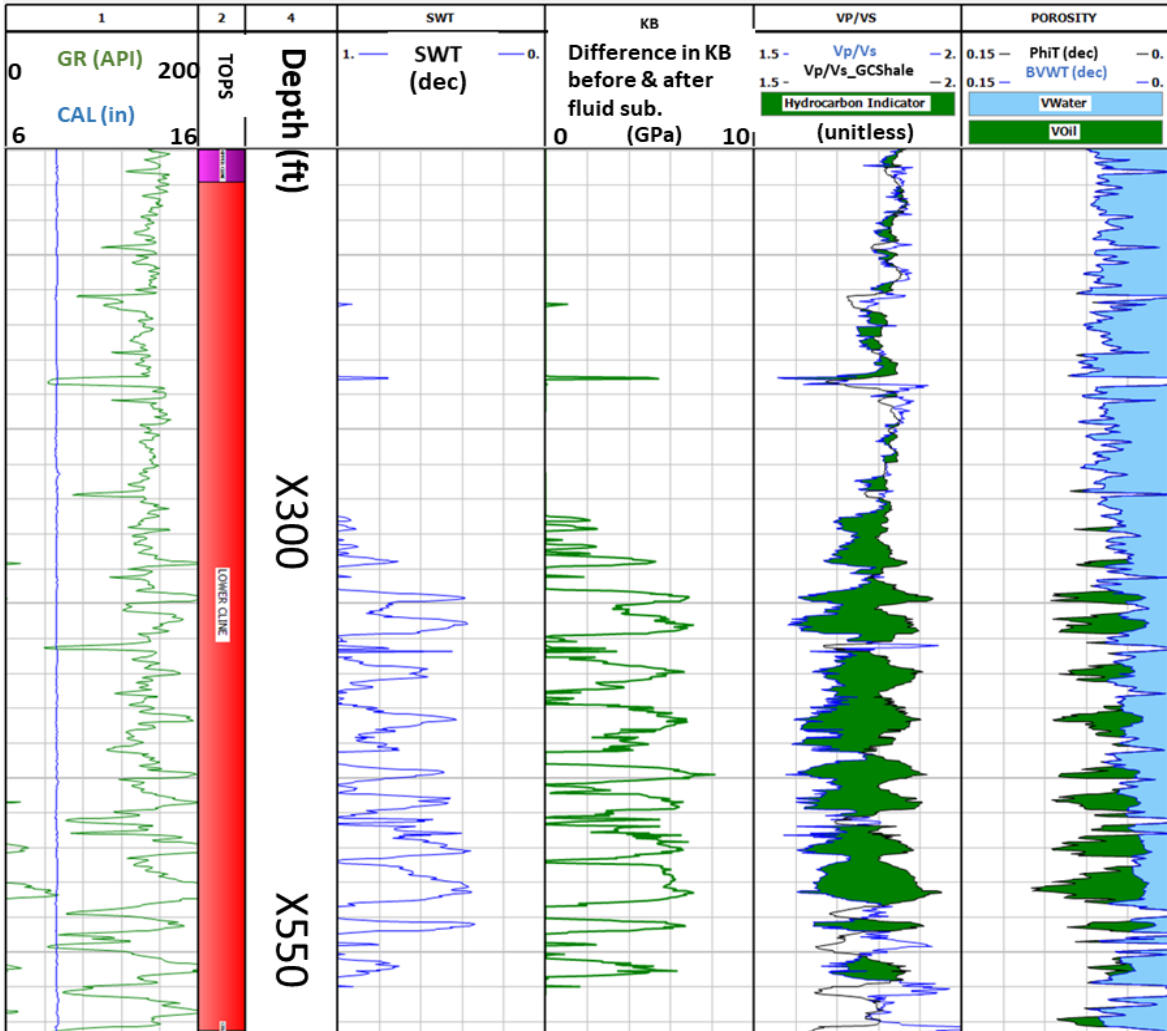


**Figure 2.22:** Log plot of the lower Cline shale. Gamma ray and caliper are plotted in track 1. Blue log in track labeled SWT is water saturation. Difference between bulk modulus after fluid substitution to 100% brine saturation and bulk modulus computed from measured velocities and bulk density is the green log in track labeled **KB**. The measured velocity ratio in track labeled  $V_p/V_s$  is shaded green below the velocity ratio computed from the GC-92 fully brine-saturated shale trend (labeled  $V_p/V_s_{GCShale}$ ). Note how this quick look indicator coincides fairly well with fluid substitution prediction and the bulk volume oil (green shading) in the rightmost track where log total porosity (PhiT) and bulk volume water (BVWT) are also plotted. Depths in the depth track are only to indicate depth scale, actual depths are not available for publication.

## 2.9 CONCLUSION

A wide variety of laboratory and sonic log measurements suggest that organic-rich shale reservoirs have anomalously low  $V_p/V_s$  ratios as compared to fully brine-saturated shales as exemplified by the Greenberg and Castagna fully brine-saturated shale trend. Such anomalously low velocity ratios have been attributed to the presence of kerogen and/or free hydrocarbons, or some combination of the two. Because hydrocarbon saturations and kerogen volumes are highly correlated to each other, it is difficult to separate these effects using *in situ* measurements alone. In this paper, we have used a combination of theoretical modeling, laboratory measurements in various shales under different saturation conditions with kerogen volumes varying from 0% to over 40%, and sonic log analysis in seven shale reservoirs as well as nonreservoir shales to test two hypotheses. The first hypothesis is that the anomalously low velocity ratios can be explained by the presence of solid kerogen. The second hypothesis is that the anomalously low velocity ratios can be explained by the mechanical effect of free hydrocarbon fluids in the pore space.

We find that the lower velocity ratio observed in dry, gas-saturated or oil-saturated shales as compared to fully brine-saturated shales, organic and inorganic, can be explained for the most part by the presence of gas or light oil. We find further that while increased kerogen volume is often associated with hydrocarbon-rich shales, the theoretical models and measured data do not support the hypothesis that solid kerogen alone, without associated hydrocarbons, can be responsible for the lower velocity ratio observed in organic shales.

We also conclude that, despite concerns regarding pore pressure equilibration in low permeability rocks, Gassmann's equations are useful in qualitatively predicting the direction, if not the accurate magnitude, of hydrocarbon effects in shale reservoirs.

## Chapter 3

# A SIMPLE EMPIRICAL SHEAR-WAVE VELOCITY PREDICTION METHOD FOR SHALES WITH HIGH ORGANIC CONTENT

Omovie, S.J., and J. P. Castagna, 2019, A Simple Empirical Shear-Wave Velocity Prediction Method for Shales with High Organic Content: GEOPHYSICS (submitted)

### 3.1 INTRODUCTION:

Given reliable compressional-wave velocities and volumetric rock properties calculations, a number of empirical and semi-empirical methods for shear-wave velocity ( $V_s$ ) prediction given compressional-wave velocity ( $V_p$ ) have been proposed (Greenberg and Castagna, 1992; Xu and White, 1996; Vernik and Kachanov, 2010, Vernik et al., 2018). These methods all employ mixing models in various ways to calculate the effective properties of a rock by treating it as an aggregate mixture of constituents and/or inclusions, without explicitly considering the detailed microstructure of the real rock. If the constituents have similar elastic properties, the prediction error may be tolerable for a given application. However, when the constituent properties are very different (as occurs when fluids are treated explicitly as constituents) the error may be more serious. This is handled by Greenberg and Castagna (1992) by mixing porous components, and by Xu and White (1996) by inclusion modeling utilizing an effective pore aspect ratio. The situation is more complicated when the solid fraction has constituents that vary by an order of magnitude (Berryman and Milton, 1991) as may be the case when there is a significant volume fraction of solid organic matter. These methods thus

have their limitations in organic-shale formations if they do not effectively take solid organic matter into consideration. Following the work of Hu et al., (2015), Yenugu and Vernik (2015) and Vernik (2016) proposed an empirical model for shear-wave velocity prediction that is based on correlations with total organic carbon (TOC) and compressional-wave velocity. Vernik et al., (2018) used both the above empirical model, as well as deterministic considerations resulting in more complicated hybrid approaches based on Vernik and Kachanov (2010) and Greenberg and Castagna (1992) to predict shear-wave velocity in organic-rich shales. Vernik et al., (2018) present two methods. Method 1 does not explicitly utilize fluid properties, but rather incorporates the fluid into the effective properties of the organic matter. Method 2 is more complicated and considers some microstructural details. In this paper, we adopt an alternative and simpler approach, extending the work done by Greenberg and Castagna (1992), without explicitly considering pore or inclusion shape. Our objective is to show that when solid organic matter is explicitly included, the modified Greenberg-Castagna method can predict shear velocities in organic shales within a tolerance that may be acceptable for geophysical, petrophysical, and engineering applications.

All mixing models require accurate determination of rock constituent volume fractions. Greenberg and Castagna (1992; herein referred to as GC-92), for example, noticed significant discrepancy between measured and estimated shear-wave velocity in clastic rocks when clay content was inaccurately estimated. In this study, we rely on well-log volumetric analyses. For a discussion of how rock composition is determined from well-log volumetric analyses - as well as how *in situ* fluid properties are determined – we refer the reader to Omovie and Castagna

(2019) for description and verification of the methods used as inputs for shear-wave velocity prediction in organic-shale reservoirs.

### 3.2 MODIFIED GREENBERG-CASTAGNA SHEAR VELOCITY PREDICTION IN ORGANIC-RICH SHALES

Greenberg and Castagna (1992) present a shear-wave velocity prediction method given well-log volumetric analyses and compressional-wave velocity. They dealt with the primary mineralogies often encountered in hydrocarbon-bearing reservoir rocks – quartz, clay, calcite, and dolomite. However, organic shales, in addition, can contain significant amounts of kerogen and other highly compressible organic matter and thus deviate from the implicit GC-92 mixing model assumption of mineral constituents with similar elastic moduli. In this paper, as we generally do not have available a detailed breakdown of the compositional makeup of the solid organic matter, we will sometimes loosely refer to the total organic content as kerogen while using effective kerogen properties as a first approximation.

In mineralogically complex lithologies, GC-92, utilizes the following empirical mixing model of porous lithological end members at 100% brine saturation:

$$G_c = 0.25\rho_{c1} \left( \left\{ \sum_{i=0}^L X_i \sum_{j=0}^{N_i} a_{ij} V_{pc1}^j \right\} + \left\{ \sum_{i=0}^L X_i \left[ \sum_{j=0}^{N_i} a_{ij} V_{pc1}^j \right]^{-1} \right\}^{-1} \right)^2, \quad (3.1)$$

where  $L$  is the number of pure porous lithologic components making up the rock composite;  $X_i$  is the volume fraction of porous lithology  $i$ ;  $a_{ij}$  are the Greenberg and Castagna (1992)  $V_s$ - $V_p$  trend regression coefficients (see table 1);  $N_i$  are the number of polynomial terms for the  $V_s$ - $V_p$

trend of lithologic component  $i$ ;  $V_{pc}$  is the measured compressional-wave velocity;  $\rho_c$  is rock bulk density and  $G_c$  is rock shear modulus. The subscript 1 indicates 100% brine saturation.

While equation 3.1 does not preclude the inclusion of solid organic matter as a constituent, we encountered difficulty in selecting a physically meaningful and somewhat universal  $V_p$ - $V_s$  relationship for organic solids without explicit consideration of hydrocarbon saturation. Greenberg and Castagna (1992) incorporate Gassmann's equation into a shear-wave velocity prediction workflow that explicitly considers fluid properties. See Omovie and Castagna (2019) for a discussion of the significant fluid saturation effects on velocity in organic-rich shale reservoirs.

Locally, it may be possible to achieve acceptable shear-wave velocity prediction in organic shales using equation 3.1 and a locally calibrated  $V_p$ - $V_s$  trend for solid organic matter. For example, a  $V_p$ - $V_s$  relation for solid organic matter that implies a  $V_p/V_s$  of 0.976 (a nonphysical ratio) that appears to work for a Wolfcamp shale interval with 7.2% average solid organic matter volume, yields a 1.06% mean signed error and percent standard error of 3.59% in  $V_s$  prediction using equation 3.1 (figure 3.1a). However, when using the same  $V_p$ - $V_s$  trend for the Bakken shale with much higher average solid organic matter volume of 26.4%, the  $V_s$  prediction mean signed error was 4.3%, with percent standard error of 5.5% (figure 3.1b).

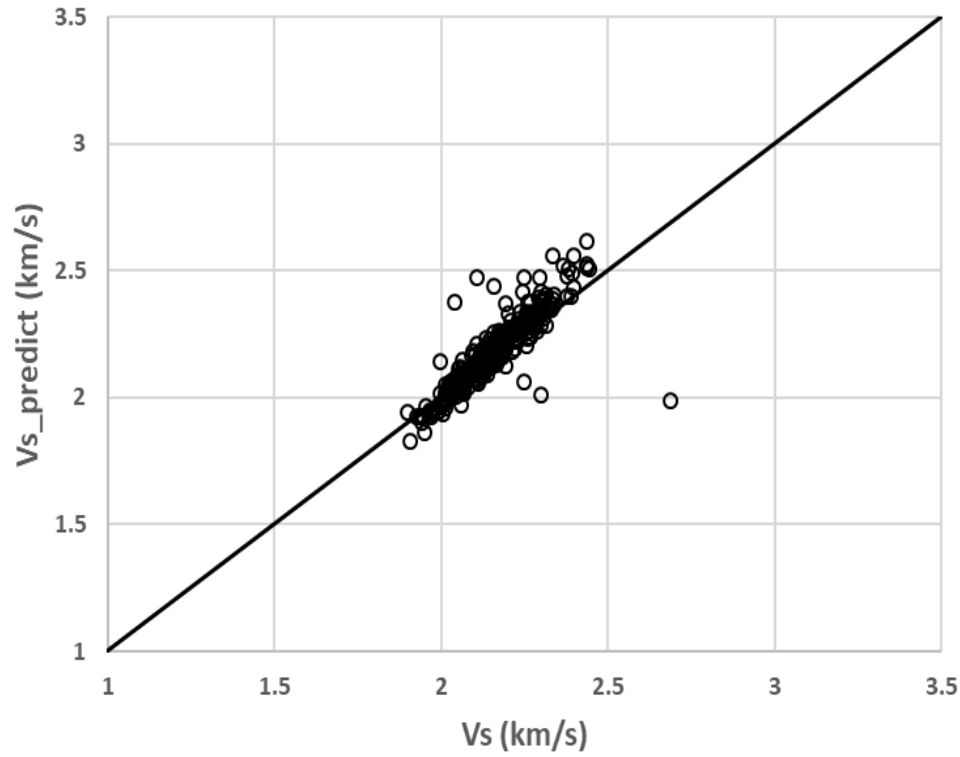


**Figure 3.1a:** Wolfcamp shale.  $V_s$  prediction based on GC-92 equation 1 only using a  $V_p/V_s$  of 0.976 (a nonphysical ratio) for the solid organic matter trend. Percent mean signed error in  $V_s$  prediction is 1.06%, with percent standard error of 3.59%.

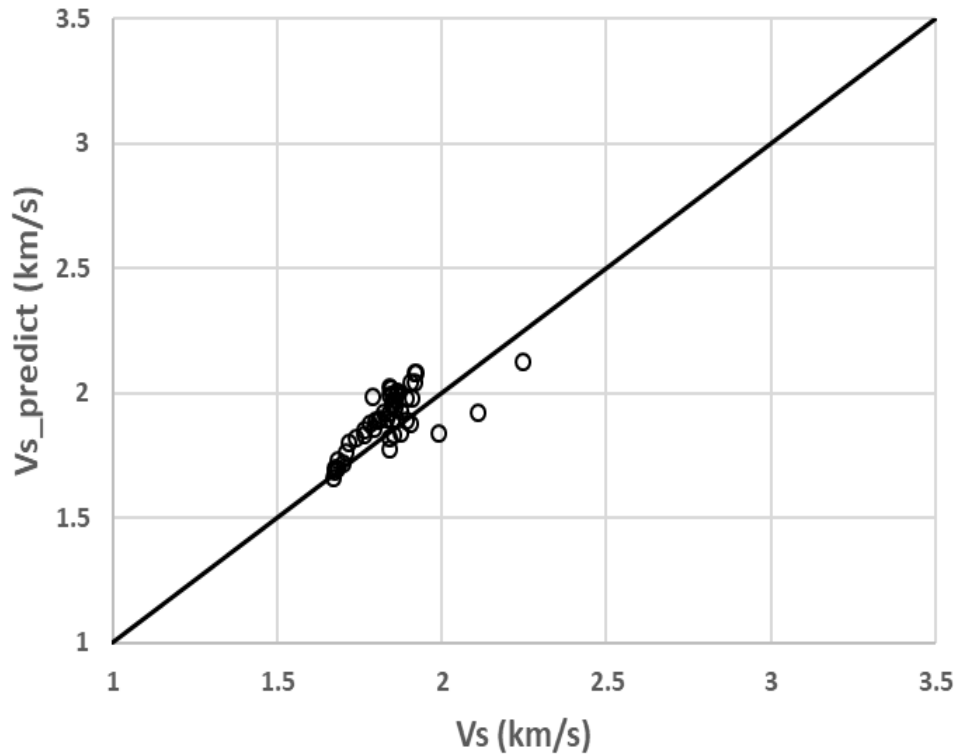


**Figure 3.1b:** Bakken shale.  $V_s$  prediction based on GC-92 equation 1 only using a  $V_p/V_s$  of 0.976 (a nonphysical ratio) for the solid organic matter trend. Percent mean signed error in  $V_s$  prediction is 4.3%, with a percent standard error of 5.5%.

Extrapolation of a velocity relationship calibrated at relatively low organic content to 100% solid organic matter is subject to large error if the variation with organic content is non-linear. This could cause increased prediction error outside the range of organic volumes used for calibration, thus yielding non-physical relationships far from the calibration points. In such a situation, incorporating physical equations into the prediction method that account for the non-linearity could result in more universal relationships.

Using equation 3.1 directly to predict shear-wave velocity implicitly assumes there are no fluid effects (i.e. that hydrocarbons have no explicit impact on the velocity ratio). Vernik at

al., (2018) achieve prediction error generally below 3% without explicitly considering fluid effects by implicitly incorporating hydrocarbons into the solid organic properties. This in effect presumes the hydrocarbons are entirely associated with the organic matter moduli and that free hydrocarbons in the inorganic pore space do not require explicit treatment. One can see how this may work well when calibrated in a specific formation, but extrapolation to other formations or localities with different fluid and/or solid organic matter properties may be more difficult. Our objective is to achieve percent mean signed prediction errors that are within  $\pm 1\%$  (or percent mean absolute error less than 3%, for comparison to Vernik et al., (2018)) for each of the individual organic-shale formations while explicitly considering fluid properties and thereby honoring the physics of fluid substitution in a poroelastic medium, without the requirement of a pore shape factor. The resulting prediction method may be more universal and, thus, less dependent on local calibration due to variations in fluid modulus and pore/inclusion shape.

Finding a relationship that works in many different shale formations of different ages, depths, and mineralogies with different fluid types would not only allow use in a variety of reservoirs, but would increase our overall confidence that we have adequately captured the essential physics of the problem in our formulation.

Inverting the full GC-92 method with explicit consideration of solid organic matter and fluid substitution effects, the compressional-to-shear-wave velocity relationship can be optimized to best predict shear-wave velocity. Since coal is compositionally similar to solid organic matter in organic shales, we started with the coal regression trend from Marcote et al.,

(2010) and perturbed it to minimize shear-wave velocity prediction error for our collection of well-logs in organic-rich shales (see below). The resulting  $V_p$ - $V_s$  trend for solid organic matter obtained in this way is:  $V_s$  (km/s) =  $0.57V_p + 0.00382$ . Solid organic matter elastic moduli from Sayers (2013) (originally from Vernik and Landis, 1996) give  $V_s = 0.571 V_p$  which coincides with our optimized trend and is parallel to the Marcote et al., (2010) trend (figure 3.2). Agreement of these disparate trends suggests a forward model that has at least captured the form of the non-linear velocity variation. Optimizing the modified GC-92  $V_s$  prediction method described below gave the same trend.

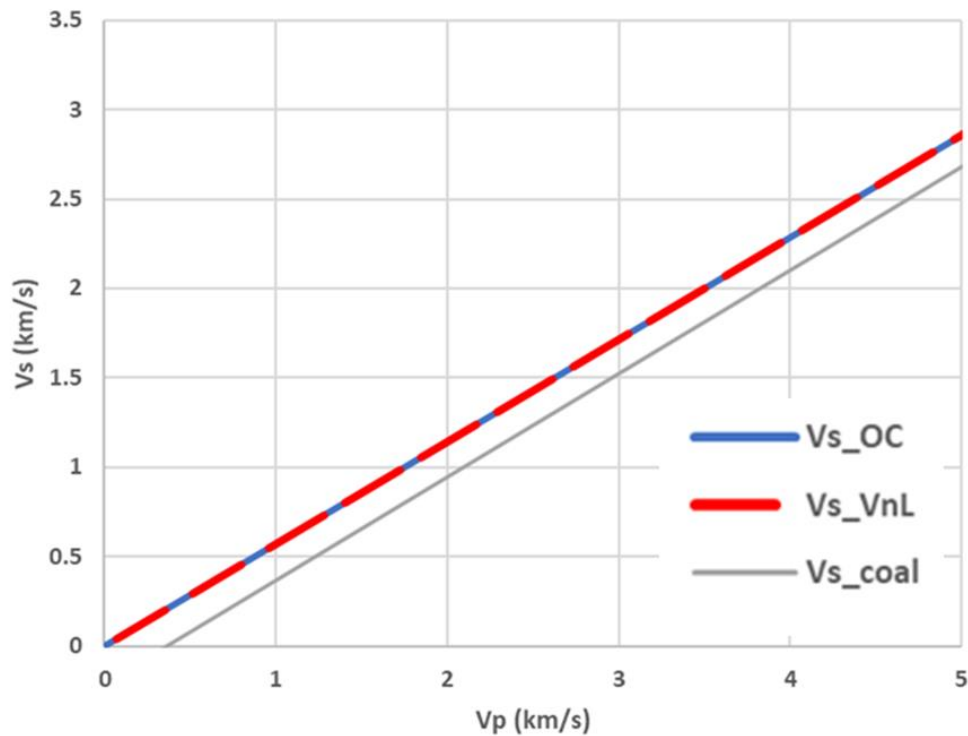


**Figure 3.2:** Solid organic matter  $V_p$ - $V_s$  trend determined by inverting GC-92 (blue line,  $V_s$ \_OC); solid organic matter  $V_p$ - $V_s$  trend from Vernik and Landis (1996) (red dashed line,  $V_s$ \_VnL); and coal  $V_p$ - $V_s$  trend from Marcote et al., (2010) (gray line,  $V_s$ \_coal). Note that our result is almost identical to Vernik and Landis (1996) and the trends overlay.

Incorporating the optimized solid organic matter trend in the full GC-92 workflow including fluid substitution effects yields  $V_s$  predictions that are significantly better than when the same workflow is implemented without the solid organic matter trend. For example, for the Bakken shale with average solid organic matter volume of 26.4%, including the optimized solid organic matter trend resulted in a  $V_s$  prediction mean signed error of 0.14% and percent standard error of 3.05%, compared to 17.71% mean signed error (and percent standard error of 17.86%) when the same workflow is implemented ignoring the solid organic matter fraction. In addition, we present below a modification to the GC-92 workflow, that for the seven organic-shale reservoirs investigated in this study yielded  $V_s$  prediction percent mean signed errors that are below  $\pm 1\%$  for each of the individual organic-shale formations. The modified GC-92 method works to this extent in all organic-shale formations investigated here regardless of solid organic content volume and fluid properties and yields  $V_s$  predictions that are more accurate than those obtained from the original GC-92 workflow using the solid organic matter trend and fluid substitution. For the above Bakken shale example, the  $V_s$  prediction percent mean signed error using the modified GC workflow is 0.17%, with a percent standard error of 1.84% (see below).

Here we briefly describe the changes we have made to GC-92 for application to organic-rich rocks. In the next section, we provide detailed implementation steps. The first modification involves including a  $V_p$ - $V_s$  trend for solid organic matter in equation 1 of GC-92. This is the  $V_p$ - $V_s$  trend determined above for solid organic matter and shown in figure 3.2. Secondly, we compute compressional-wave velocity of a hypothetical rock of the same porosity and inorganic mineral content, but absent any solid organic matter ( $V_{pmk}$ ) by inverting a weighted average of

Voigt and Reuss bounds of solid organic matter with porous inorganic matrix and extrapolating to 0% solid organic matter. In this study, we have used the Hill average (Hill, 1952) as a first approximation.

Our application of Voigt-Reuss bounds is somewhat out of the ordinary and requires some explanation. Usually, each constituent (minerals, organics, fluids) is incorporated into the Voigt and Reuss bounding equations, which are usually so wide as to limit their applicability to porous media. First, we narrow these bounds by incorporating the porosity into porous lithologic components as in the Greenberg and Castagna (1992) formulation. Second, we ask the question, for a given organic shale with measured TOC and compressional-wave velocity, what do the bounds tell us about velocity variation at solid organic volume fractions away from the measured velocity? We can hypothetically predict, if the measured velocity happened to be on either bound, what the implied plane-wave modulus at zero kerogen volume fraction would be, thereby giving a range for likely moduli between those pseudo-bounds (see figure 3.3). This yields a smaller range of realizations than true Voigt and Reuss bounds including fluids as constituents. We then presume that the zero-kerogen volume fraction modulus is somewhere between these pseudo-bounds and take a weighted average between them to estimate a hypothetical zero TOC modulus; the weighting factor being an empirical parameter to be varied with degree of lithification of the rock if necessary.

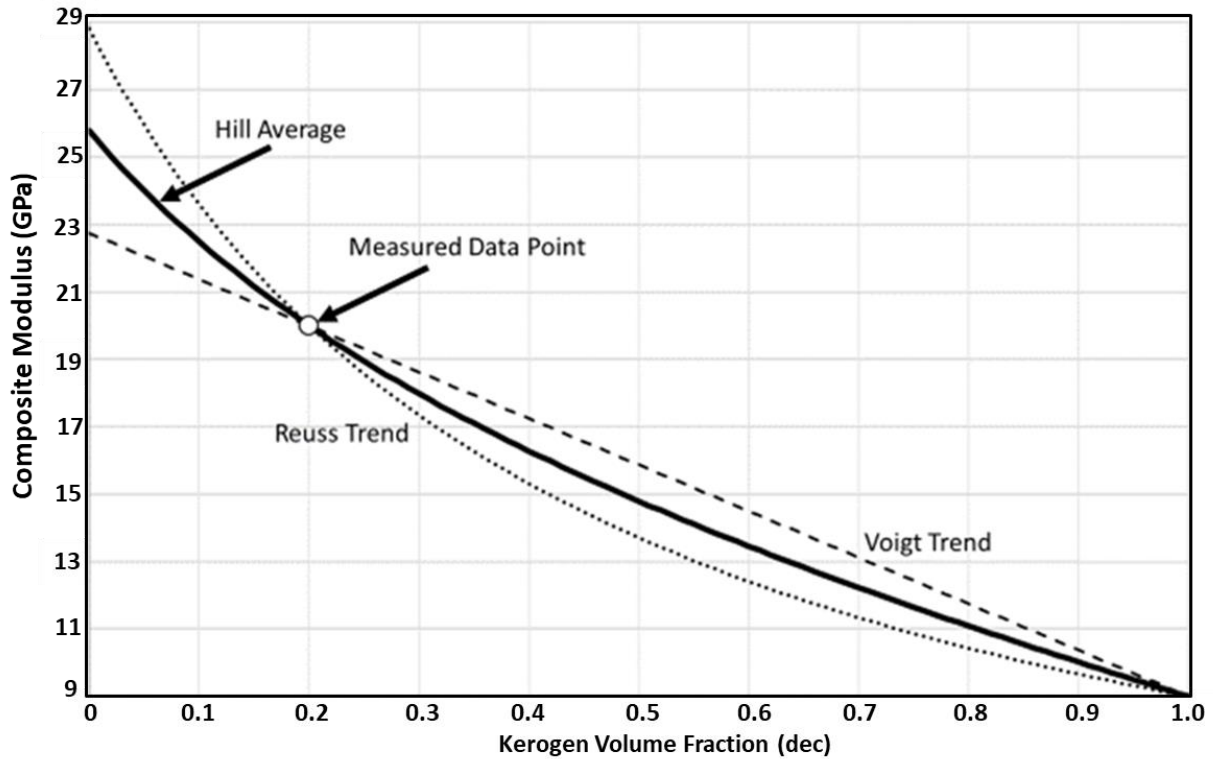


**Figure 3.3:** Plane-wave modulus trends for hypothetical composite porous organic shales of the same porosity and inorganic mineralogy versus volume fraction of kerogen constrained by a single measurement. For this illustrative example, all the solid organic matter is assumed to be kerogen with a plane-wave modulus of 9 GPa. The open circle is the measurement on a single sample. The Reuss (dotted line) and Voigt (dashed line) bounds and Hill average (solid line) are for hypothetical mixtures of kerogen with the porous rock containing no kerogen that coincide for the measurement. These are not true bounds; but establish the likely range of moduli at other kerogen volume fractions that would occur if the measurement at a given kerogen volume fraction coincided with either bound.

### 3.3 DETAILED IMPLEMENTATION PROCEDURE FOR MODIFIED GREENBERG-CASTAGNA SHEAR VELOCITY PREDICTION IN ORGANIC-RICH SHALES

Kerogen is usually the dominant component of the volume of solid organic matter. However, other solid organic constituents, such as bitumen and graphene, may be present in variable quantities. In the rest of this paper, when we refer to “kerogen” properties, we really mean the effective properties of the mixture of all solid organic material. These presumably vary with the organic composition and the pressure/temperature conditions. Lacking additional information, we here loosely use the term “kerogen” to apply to the effective elastic properties and fractional volumes of the total solid organic content.

The modified Greenberg-Castagna prediction methodology steps are:

1. Compute mineral constituent volumes on a zero-porosity solid rock basis (Sum = 1)

$$\sum_{i=0}^L X_i = 1 \quad , \quad (3.2)$$

where  $X_i$  is the volume fraction of mineral constituent  $i$  including all solid organic matter as a single mineral constituent we refer to as kerogen.

2. We use the Voigt-Reuss-Hill average to determine zero-porosity matrix bulk modulus of the composite rock

$$K_m = \frac{\left(\sum_{i=0}^L X_i K_i + \left[\sum_{i=0}^L X_i K_i\right]^{-1}\right)}{2} \quad , \quad (3.3)$$

where  $K_m$  is the matrix bulk modulus, and  $K_i$  is the bulk modulus of pure mineral component  $i$ . The Hill average is known to yield accurate effective elastic moduli when the bounds are narrow or constituent elastic properties do not differ significantly (Wang

et al., 2001; Jaeger et al., 2007) and is exact when the shear moduli of the constituents are equal. There is concern that the Hill average will not be a good approximation when one of the constituents such as organic matter is abnormally soft relative to the inorganic minerals. However, using the self-consistent approximation (Berryman, 1980) to mix inorganic shale with kerogen, Omovie and Castagna (2019) find that, at kerogen volumes up to 25%, absolute percent difference between Hill average and self-consistent approximation matrix bulk modulus may be no more than 5%.

3. Iterate through assumed P-wave velocity at 100% brine saturation ( $V_{pc1}$ ) given measured P-wave velocity (from Greenberg and Castagna; 1992)

$$V_{pc1} = (1 + \delta)V_{pc} \quad , \quad (3.4)$$

where  $V_{pc}$  is the measured compressional velocity at *in situ* brine saturation,  $S_w$ .

$\delta$  is a slack variable. The slack variable is used to correct the measured

compressional-wave velocity at *in situ* water saturation to full water saturation

and is incremented during the iteration described below until a solution is found.

4. Estimate associated shear-wave modulus at 100% brine saturation using assumed  $V_{pc1}$  and equation 3.1 with the  $V_s$ - $V_p$  trend coefficients given in table 3.1 for each of the lithology constituents. The trend included in table 1 for kerogen (solid organic content) is the one we determined in the previous section by optimization. We assume the frame shear modulus is the same as the saturated-rock shear modulus (see for example Omovie and Castagna (2019) for validation of this in organic-shale reservoirs).

**Table 3.1:** Coefficients for shear-wave velocities ( $V_s$  (km/s)) versus compressional velocities ( $V_p$  (km/s)) in pure porous lithologies. Coefficients are from Greenberg and Castagna (1992) with the exception of solid organic matter which was determined here and shown in figure 2. Coefficients are for equations of the form  $V_s = a_{i2}V_p^2 + a_{i1}V_p + a_{i0}$ .

<b>Lithology</b>	<b><math>a_{i2}</math></b>	<b><math>a_{i1}</math></b>	<b><math>a_{i0}</math></b>
<b>Sandstone</b>	<b>0</b>	<b>0.80416</b>	<b>-0.85588</b>
<b>Limestone</b>	<b>-0.05508</b>	<b>1.01677</b>	<b>-1.03049</b>
<b>Dolomite</b>	<b>0</b>	<b>0.58321</b>	<b>-0.07775</b>
<b>Clay</b>	<b>0</b>	<b>0.76969</b>	<b>-0.86735</b>
<b>Solid organic matter</b>	<b>0</b>	<b>0.571</b>	<b>0</b>

5. Compute bulk density at 100% brine saturation ( $\rho_{c1}$ ). Formation bulk density is given by the mass-balance equation:

$$\rho_c = \phi_t(S_w\rho_w + (1 - S_w)\rho_{nw}) + (1 - \phi_t)\sum_{i=0}^L X_i \rho_i \quad , \quad (3.5)$$

where  $\phi_t$  is rock total porosity,  $\rho_w$  is formation water density,  $\rho_{nw}$  is hydrocarbon density,  $\rho_i$  is grain density of lithology constituent  $i$ ,  $L$  is the number of mineral components, and  $S_w$  is water saturation. The mass balance equation is accurate only if the densities and volume fractions of the constituent minerals are known with a measure of certainty; but that is not always the case. For example, illite (which is the primary clay encountered in the formations we have studied) has density reported in the literature varying from 2.52 g/cm<sup>3</sup> to 2.79 g/cm<sup>3</sup>. So rather than compute density, we have instead used the measured bulk density when it is judged to be accurate. When the bulk density at 100% water saturation or the bulk density with no kerogen present is

desired, we have adjusted or corrected the measured bulk density using the mass balance equation. Given formation bulk density  $\rho_c$  at  $S_w$ , the bulk density at 100% water saturation,  $\rho_{c1}$ , will be given by

$$\rho_{c1} = \rho_c + \phi_t(1 - S_w)\rho_w - \phi_t(1 - S_w)\rho_{nw} \quad , \quad (3.6)$$

6. Compute bulk modulus at *in situ* water saturation  $S_w$ , using  $G_c$  from equation 3.1 above and

$$K_c = \rho_c V_{pc}^2 - \left(\frac{4}{3}\right) G_c \quad , \quad (3.7)$$

Note that kerogen volume fraction should be included in equation 3.1 when computing  $G_c$ .

7. Compute fluid mixture bulk modulus using Wood's equation (Wood, 1957) below:

$$\frac{1}{K_f} = \frac{S_w}{K_w} + \frac{(1-S_w)}{K_{nw}} \quad , \quad (3.8)$$

where  $K_f$  is the fluid bulk modulus,  $K_w$  is brine bulk modulus, and  $K_{nw}$  is hydrocarbon bulk modulus.

8. Estimate frame bulk modulus by inverting from Gassmann's equation:

$$K_d = \frac{(K_c \Omega - 1)}{\left(\frac{K_c}{K_m^2} + \Omega - \frac{2}{K_m}\right)} \quad , \quad (3.9)$$

where,  $\Omega = \frac{\phi_t}{K_f} + \frac{(1-\phi_t)}{K_m}$ ,  $K_d$  is frame bulk modulus in the presence of pore fluids,  $\phi_t$  is total porosity, and  $K_f$  is fluid bulk modulus.

9. Estimate bulk modulus at 100% brine saturation using Gassmann equation:

$$K_{c1} = K_d + \frac{\left(1 - \frac{K_d}{K_m}\right)^2}{\frac{\phi_t}{K_w} + \frac{(1-\phi_t)K_d}{K_m} - \frac{K_d}{K_m^2}}, \quad (3.10)$$

10. Compute estimated compressional-wave velocity at 100% brine saturation ( $V'_{pc1}$ ) at the actual kerogen volume fraction using

$$V'_{pc1} = \sqrt{\frac{(K_{c1} + \frac{4}{3}G_c)}{\rho_{c1}}}, \quad (3.11)$$

11. Determine the error in predicting the 100% saturated compressional-wave velocity ( $V'_{pc1} - V_{pc1}$ ) and % error  $(V'_{pc1} - V_{pc1}) * 100 / V'_{pc1}$  and averages over the interval of interest.
12. Iterate through steps 3, 4, 6, 8, 9, 10 and 11 by incrementing the slack variable,  $\delta$ , until the error approaches the observed change in P-wave velocity due to kerogen content, ( $V_{pnk} - V_{pc}$ ), that is computed below. For formations without kerogen content, the iteration stops when the error ( $V'_{pc1} - V_{pc1}$ ) approaches zero and the following steps will not apply.
13. Estimate shear-wave velocity at *in situ* saturation,  $V_{sc}$ , using

$$V_{sc} = 0.5 \left( \left\{ \sum_{i=0}^L X_i \sum_{j=0}^{N_i} a_{ij} (V'_{pc1} / (1 + \delta))^j \right\} + \left\{ \sum_{i=0}^L X_i \left[ \sum_{j=0}^{N_i} a_{ij} (V'_{pc1} / (1 + \delta))^j \right]^{-1} \right\}^{-1} \right), \quad (3.12)$$

Note that unlike the original GC-92 implementation, where shear-wave velocity prediction is determined from shear modulus computed at the final iteration step; here we predict shear-wave velocity directly using equation 3.12 above.

The following steps describe how the non-kerogen P-wave velocity ( $V_{pnk}$ ) is estimated

- Compute bulk density for the hypothetical rock with kerogen removed

$$\rho_{bnk} = \frac{(\rho_b - \rho_k X_k)}{(1 - X_k)} , \quad (3.13)$$

where  $\rho_{bnk}$  is the non-kerogen density and  $X_k$  is kerogen volume fraction.

- Compute the weighted Voigt-Reuss average to estimate the plane wave modulus of the hypothetical rock without kerogen from

$$M = \beta((1 - X_k)M_{nk} + X_k M_k) + (1 - \beta) \left( \frac{1 - X_k}{M_{nk}} + \frac{X_k}{M_k} \right)^{-1} , \quad (3.14)$$

where  $M$  is the plane-wave modulus,  $M_{nk}$  is the hypothetical plane-wave modulus of the porous rock with no kerogen,  $M_k$  is the kerogen plane-wave modulus,  $X_k$  is the kerogen fractional volume, and  $\beta$  is a weighting parameter. Presumably, the weighting factor should vary with degree of lithification. As a first order approximation, we used a weighting parameter of 0.5, which is the Hill average. For the data used in this study, we found no compelling need to be more precise than that. Solving the above equation in terms of the non-kerogen plane-wave modulus of the porous rock,  $M_{nk}$ , will result in a quadratic equation in  $M_{nk}$ :

$$(\beta X_k (1 - X_k)) M_{nk}^2 + (\beta (1 - X_k)^2 M_k + \beta X_k^2 M_k + (1 - \beta) M_k - X_k M) M_{nk} + (\beta X_k (1 - X_k) M_k^2 - (1 - X_k) M_k M) = 0 , \quad (3.15)$$

We use the physical solution which is the positive root of the above equation.

- With the previously determined  $\rho_{bnk}$  compute compressional-wave velocity for the hypothetical rock with zero kerogen,  $V_{pnk}$ , given by:

$$V_{pnk} = \sqrt{\frac{M_{nk}}{\rho_{bnk}}} \quad , \quad (3.16)$$

Compute the difference between the non-kerogen compressional-wave velocity and the measured compressional-wave velocity ( $V_{pnk}-V_{pc}$ ), as well as the percentage change, to determine if the iteration is complete in Step 12 above.

### 3.4 RESULTS

We apply the modified Greenberg-Castagna method described in the previous section to well logs from a variety of shale reservoirs. Each example shown uses well-log data from a single well. Fluid properties used are given in table 3.2 and mineral properties are provided in table 3.3. In addition to the modified GC predictions, we also present the prediction result for 4 additional variations of the GC-92  $V_s$  prediction method listed in table 3.4. While the cross plots in this section correspond to the log plots (where available for publication), only datapoints with water saturation less than 80% are included in the cross plots. Unless otherwise stated, all reported percent errors for individual organic-shale formations in this section are percent mean signed errors. In addition, in the next section, we also present mean absolute error and standard error for the individual organic-shale formation as well as the combined mean signed error, mean absolute error and standard error for all seven organic shales.

**Table 3.2:** Reservoir fluid properties used for each formation.

Shale Formation	Hydrocarbon type	Hydrocarbon Bulk Modulus (GPa)	Hydrocarbon density (g/cc)	Brine Bulk Modulus(GPa)	Brine density (g/cc)
Wolfcamp	Volatile oil	0.434	0.677	2.73	1.05
Lower Spraberry	Volatile oil	0.375	0.675	2.75	1.05
2nd Avalon	Volatile oil	0.366	0.67	2.75	1.05
Lower Cline	Volatile oil	0.43	0.675	2.8	1.05
Woodford	Volatile oil	0.43	0.675	2.75	1.05
Bakken	Oil	0.75	0.8	2.75	1.05
Eagleford	Gas	0.13	0.25	2.8	1.05

**Table 3.3:** Mineral end member elastic moduli used for computing matrix bulk modulus for fluid substitution. Kerogen is from Vernik and Landis (1996) and used to represent all solid organic matter as a first approximation.

Mineral	Bulk Modulus
	GPa
Quartz	38
Calcite	64.51
Dolomite	91.76
Clays (Illite)	52.6
Kerogen	5.53

**Table 3.4:**  $V_s$  prediction methods.

Method Description	Remarks
Modified GC	Includes fluid and solid organic matter effects
Full GC workflow without solid organic matter trend	Includes fluid effects
Full GC workflow with solid organic matter trend	Includes fluid and solid organic matter effects
GC-92 equation 1 only, without solid organic matter trend	Does not include fluid and solid organic matter effects
GC-92 equation 1 only, with solid organic matter trend	Does not include fluid effects

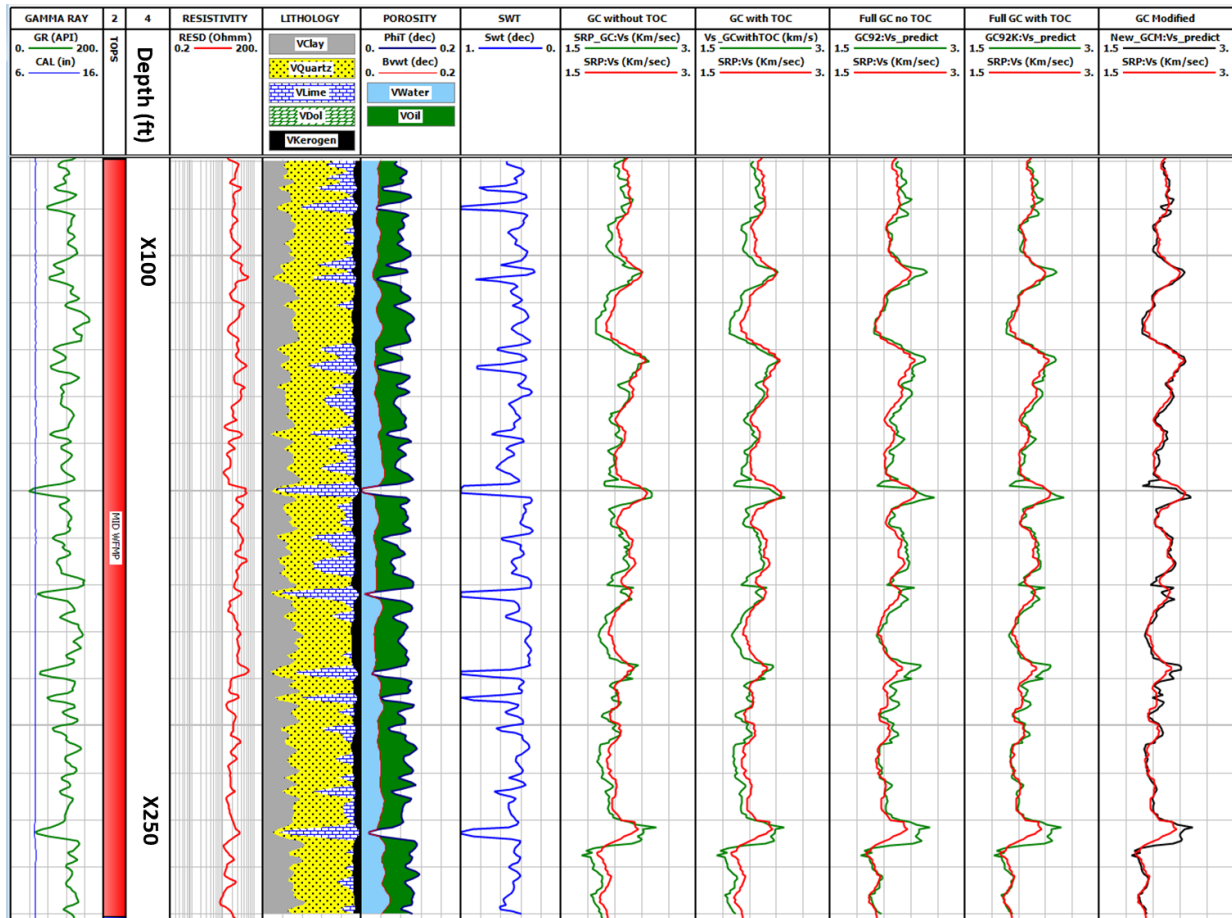
### 3.4.1 WOLFCAMP SHALE:

We begin by applying the modified workflow to a shale formation with low to medium solid organic content. The Wolfcamp shale is a Permian-age volatile oil shale play in the Midland basin – a sub-basin of the Permian basin. Kerogen volume ranges from about 2% to 12% depending on well location within the basin. For our data, kerogen volume ranges from 4.6% to 9.63%, with an average of 7.1%. Average water saturation is 42.9%.

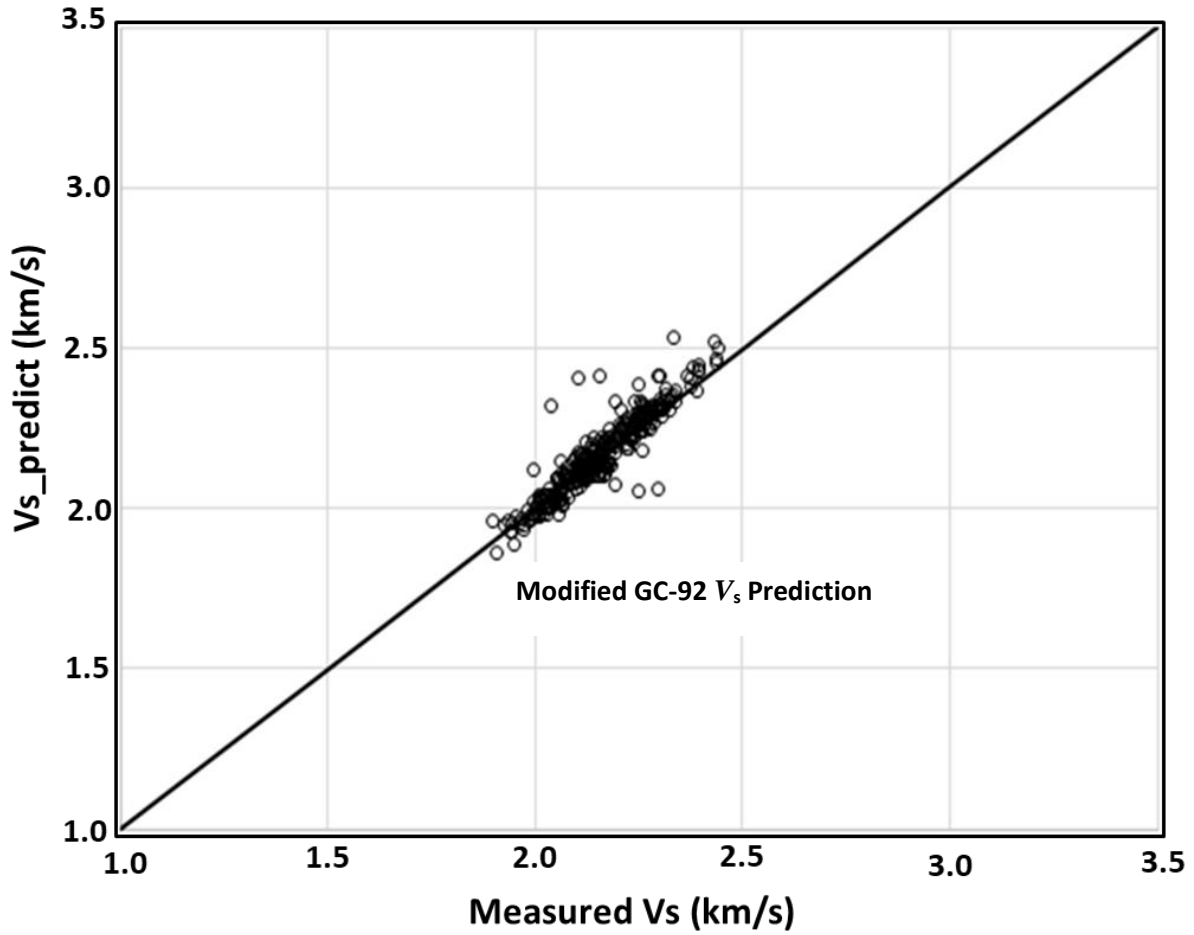
Figure 3.4a compares the Wolfcamp shale  $V_s$  predictions. Figure 3.4b is a cross plot of the  $V_s$  prediction based on the modified workflow and measured  $V_s$ . The percent mean signed error is 0.58%, compared to a percent mean signed error of 2.53% when the original GC-92 workflow with fluid substitution but assuming zero TOC is applied to the dataset or a percent mean signed error of 3.53% for the full GC-92 workflow with fluid substitution that includes the optimized  $V_s$ - $V_p$  trend for solid organic content. These alternative methods exhibit significant bias in the prediction. The percent standard error for the modified workflow is 2.4%

Figure 3.4c shows the result when GC-92 equation 1 is applied directly ignoring solid organic content and fluid effects. Note the bias at lower shear-wave velocities; percent mean

signed error using this approach is -3.5%, with a percent standard error of 4.8%. On the other hand, Figure 3.4d is a cross plot of the  $V_s$  prediction using GC-92 equation 1 only (without fluid substitution) but with the optimized trend for solid organic content included; percent mean signed error with this implementation is -3.33%, with a percent standard error of 4.63%. This is a slight improvement over ignoring TOC; but not as good as implementing the full modified workflow. In Figure 3.4e, the GC-92 workflow including fluid substitution but without solid organic matter is displayed; percent mean signed error in the  $V_s$  prediction is 2.53% with a percent standard error of 3.92%. Figure 3.4f shows the result of the original full GC-92 workflow with fluid substitution and solid organic content included; percent mean signed error in  $V_s$  prediction using this approach is 3.53% with a percent standard error of 3.04%. In the Wolfcamp, those methods that include the effects of both solid organic matter and fluid substitution result in the most accurate and precise shear-wave velocity predictions, with the modified Greenberg-Castagna exhibiting the smallest error of both kinds.



**Figure 3.4a:** Log plot of the Wolfcamp shale. GAMMA RAY Track: Gamma-ray log (solid green curve - GR). Tops Track: Formation name. LITHOLOGY Track: Formation lithology fractional volumes (decimal units) determined by volumetric log analyses. POROSITY Track: Total porosity determined from volumetric log analyses (blue curve - PhiT), BVWT is bulk volume of water, green shading in this track is hydrocarbon pore volume. SWT Track: Total water saturation – blue curve. GC without TOC Track: Green curve is  $V_s$  prediction using GC-92 equation 1; red curve is the measured  $V_s$ . GC with TOC Track: Green curve is the  $V_s$  prediction using GC-92 equation 1 but including a regression trend for kerogen; red curve is the measured  $V_s$ . Full GC no TOC Track: Green curve is the  $V_s$  prediction from implementing the full GC-92 workflow without solid organic matter; red curve is the measured  $V_s$ . Full GC with TOC Track: Green curve is the  $V_s$  prediction from implementing the full GC-92 workflow with solid organic matter regression trend included; red curve is the measured  $V_s$ . GC Modified Track: Black curve is the  $V_s$  prediction from the modified workflow; Red curve is the measured  $V_s$ . Depths in the depth track are only to indicate depth scale, actual depths are not available for publication.



**Figure 3.4b:** Cross plot of measured shear-wave velocity (x axis) and the modified GC shear-wave velocity prediction (y axis) for the Wolfcamp shale. The black line is a 1-to-1 line. Percent mean signed error in  $V_s$  prediction is 0.58%, with percent standard error of 2.4%.

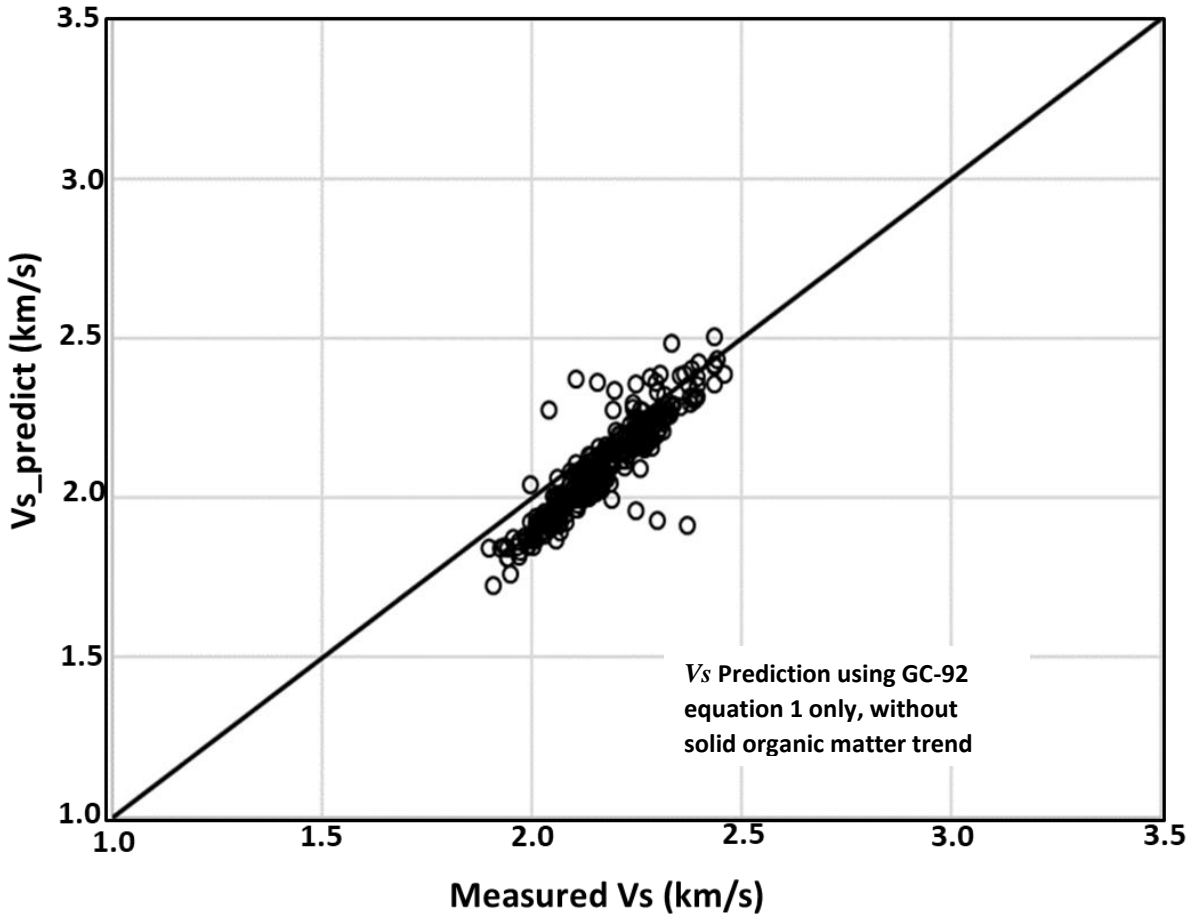


**Figure 3.4c:** Wolfcamp shale. Cross plot of measured shear-wave velocity (x axis) and the shear-wave velocity prediction (y axis) obtained by simply implementing equation 1 of GC-92, i.e. ignoring solid organic matter and fluid effects. The black line is a 1-to-1 line. Percent mean signed error in  $V_s$  prediction is -3.5%, with percent standard error of 4.8%.

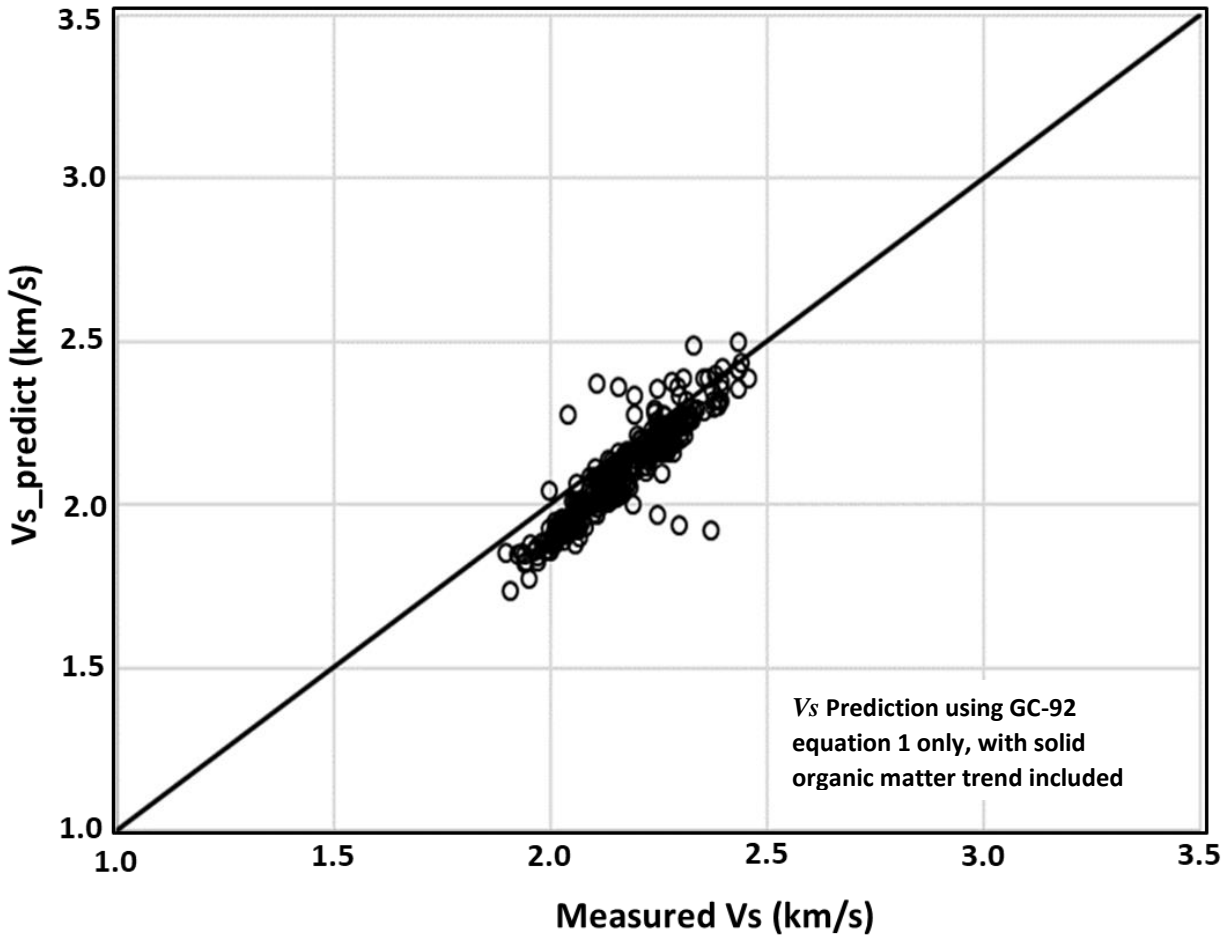


**Figure 3.4d:** Wolfcamp shale. Cross plot of measured shear-wave velocity (x axis) and the shear-wave velocity prediction (y axis) obtained by implementing equation 1 of GC-92, including a trend for solid organic content but ignoring fluid effects. The black line is a 1-to-1 line. Percent mean signed error in  $V_s$  prediction is -3.33%, with percent standard error of 4.63%.

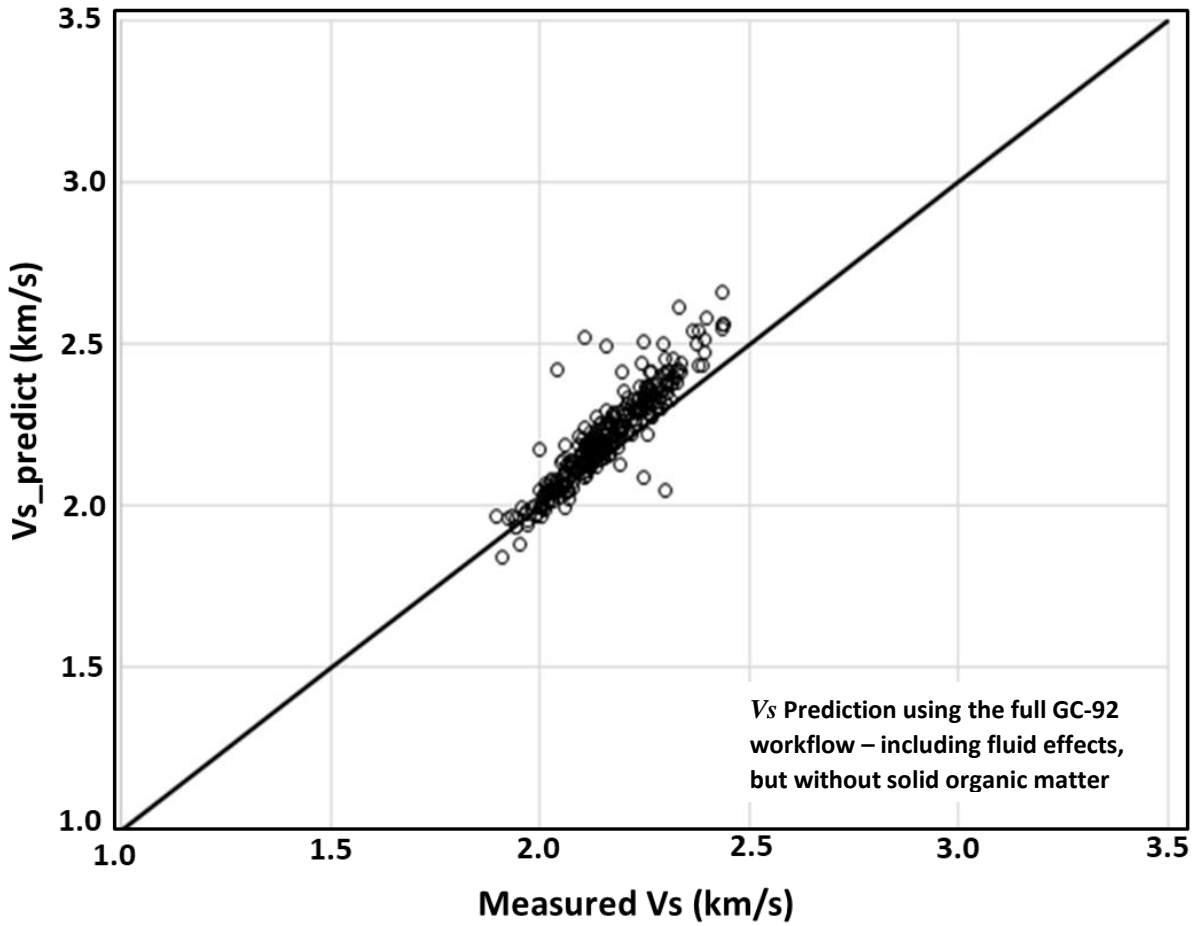


**Figure 3.4e:** Wolfcamp shale. Cross plot of measured shear-wave velocity (x axis) and the shear-wave velocity prediction (y axis) obtained by implementing the full GC-92 workflow without solid organic matter. The black line is a 1-to-1 line. Percent mean signed error in  $V_s$  prediction is 2.53%, with percent standard error of 3.92%.

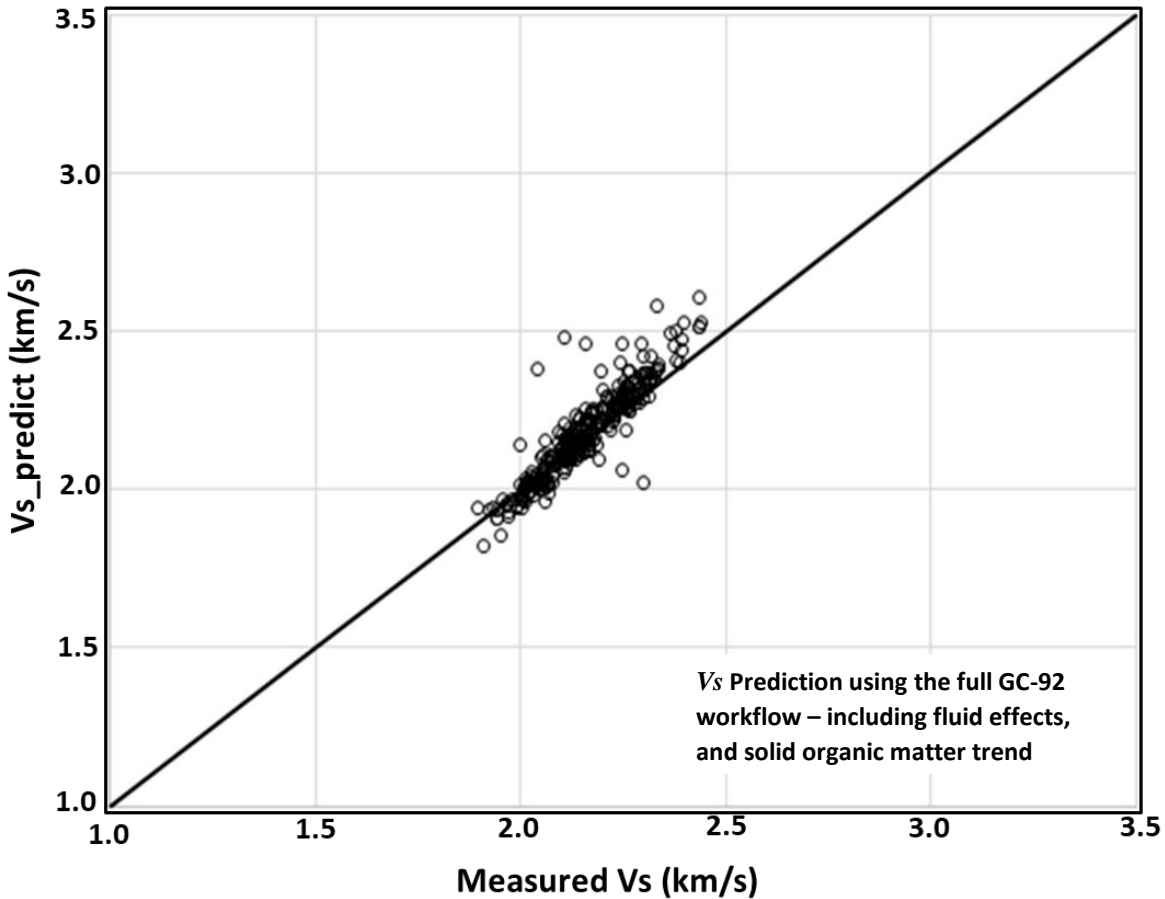


**Figure 3.4f:** Wolfcamp shale. Cross plot of measured shear-wave velocity (x axis) and the shear-wave velocity prediction (y axis) obtained by implementing the full GC-92 workflow including the trend for solid organic content. The black line is a 1-to-1 line. Percent mean signed error in  $V_s$  prediction is 3.53%, with percent standard error of 3.04%.

### 3.4.2 AVALON SHALE:

The Avalon shale is a Permian-age organic shale in the Delaware basin – a sub-basin of the Permian basin. Kerogen volume is usually greater than 10 percent. Depending on location within the basin, the Avalon shale could be a condensate wet gas or volatile oil shale play. In this study we focus on an interval referred to as the 2<sup>nd</sup> Avalon Shale in a location where the

hydrocarbon is volatile oil. Kerogen volume ranges from 11.4% to 20.4% in the interval plotted in figure 3.5a, with an average of 14.9%. The average water saturation is 29%. The modified GC-92 workflow has a percent mean signed error of -0.24% and percent standard error of 3.48% with predicted  $V_s$  now closely straddling the perfect prediction line without bias (figure 3.5b).

Percent mean signed error is -9.4% when both kerogen and fluid effects are ignored and -9.2% when the fluid effect is ignored but the kerogen trend is included in GC-92 equation 1. Both are shown in figures 3.5c and 3.5d respectively (percent standard error is greater than 10% in both cases). Simply applying the original GC-92 workflow including fluid effects but ignoring solid organic matter the percent mean signed error is 2.41% and percent standard error is 5.13% (figure 3.5e). When the solid organic matter trend is included in the original GC-92 workflow, including fluid effects, the percent mean signed error in  $V_s$  prediction is reduced to -1.94% and percent standard error is 4.21% (figure 3.5f). In the Avalon shale, fluid substitution is more important in shear-wave velocity prediction than accounting for solid organic matter. Again, the smallest mean and standard error is achieved using the modified GC-92 method.

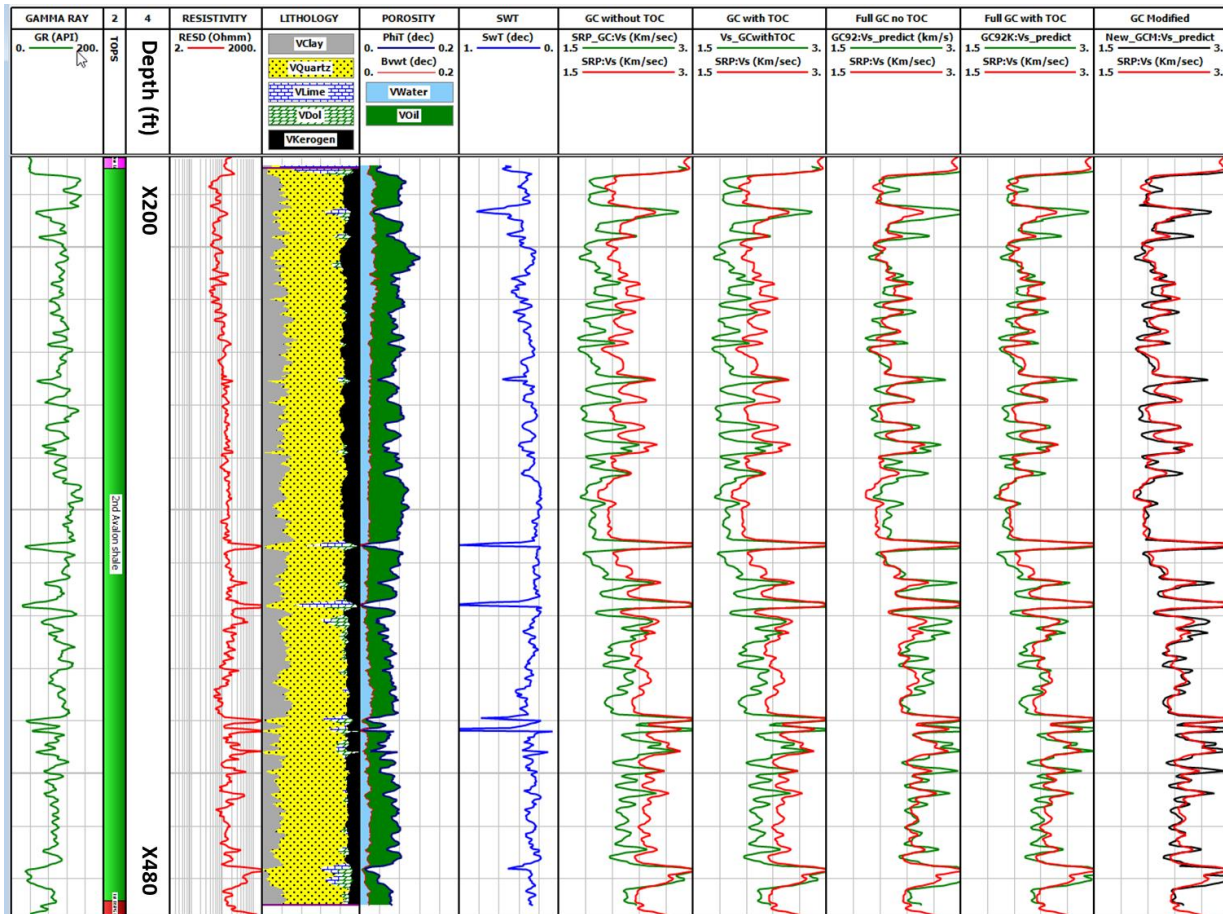


**Figure 3.5a:** Log plot of the Avalon shale. GAMMA RAY Track: Gamma-ray log (solid green curve - GR). Tops Track: Formation name. LITHOLOGY Track: Formation lithology fractional volumes (decimal units) determined by volumetric log analyses. POROSITY Track: Total porosity determined from volumetric log analyses (blue curve - PhiT), BVWT is bulk volume of water, green shading in this track is hydrocarbon pore volume. SWT Track: Total water saturation – blue curve. GC without TOC Track: Green curve is  $V_s$  prediction using GC-92 equation 1; red curve is the measured  $V_s$ . GC with TOC Track: Green curve is the  $V_s$  prediction using GC-92 equation 1 but including a regression trend for kerogen; red curve is the measured  $V_s$ . Full GC no TOC Track: Green curve is the  $V_s$  prediction from implementing the full GC-92 workflow without solid organic matter; red curve is the measured  $V_s$ . GC Modified Track: Black curve is the  $V_s$  prediction from the modified workflow; Red curve is the measured  $V_s$ . Depths in the depth track are only to indicate depth scale, actual depths are not available for publication.

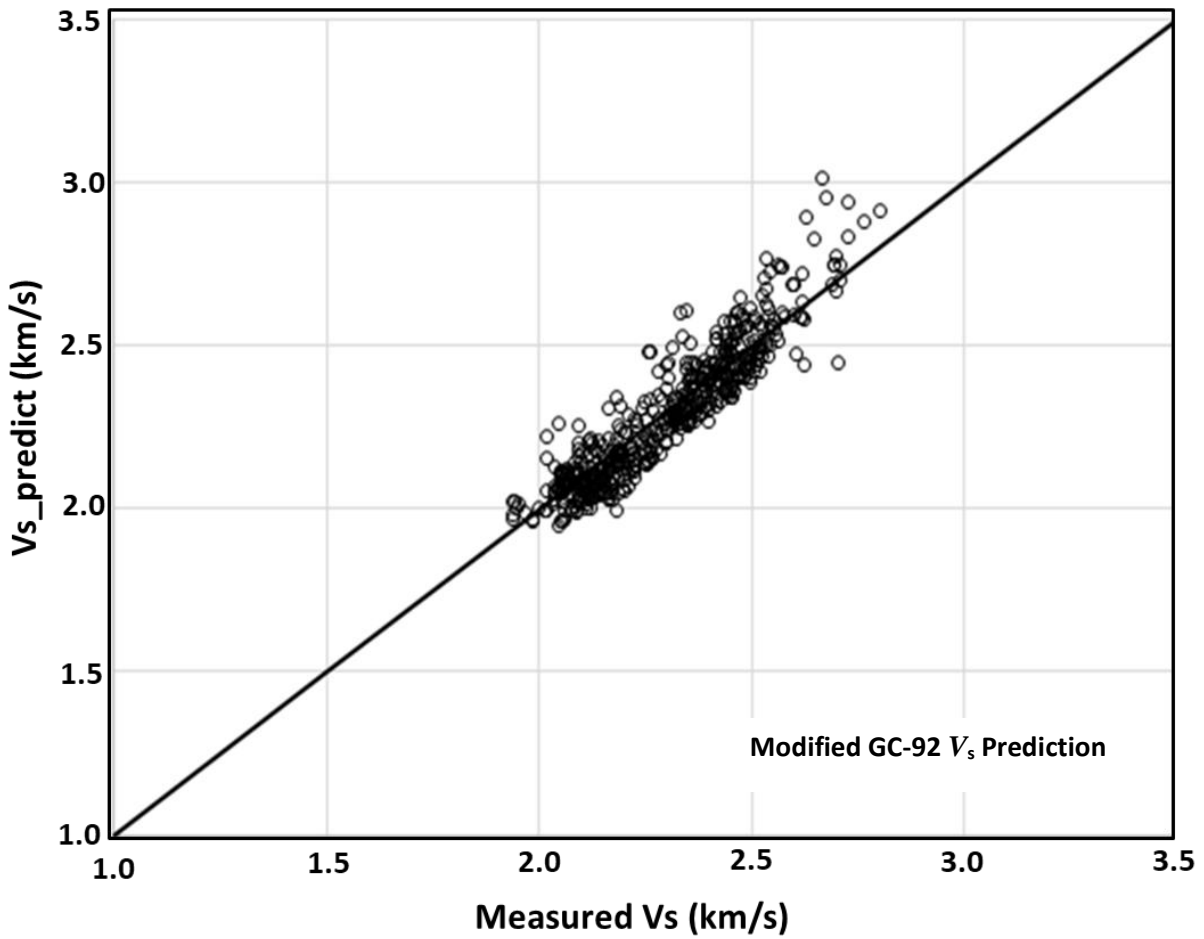


**Figure 3.5b:** Cross plot of measured shear-wave velocity (x axis) and the modified GC shear-wave velocity prediction (y axis) for the Avalon shale. The black line is a 1-to-1 line. Percent mean signed error in  $V_s$  prediction is -0.24%, with percent standard error of 3.49%.

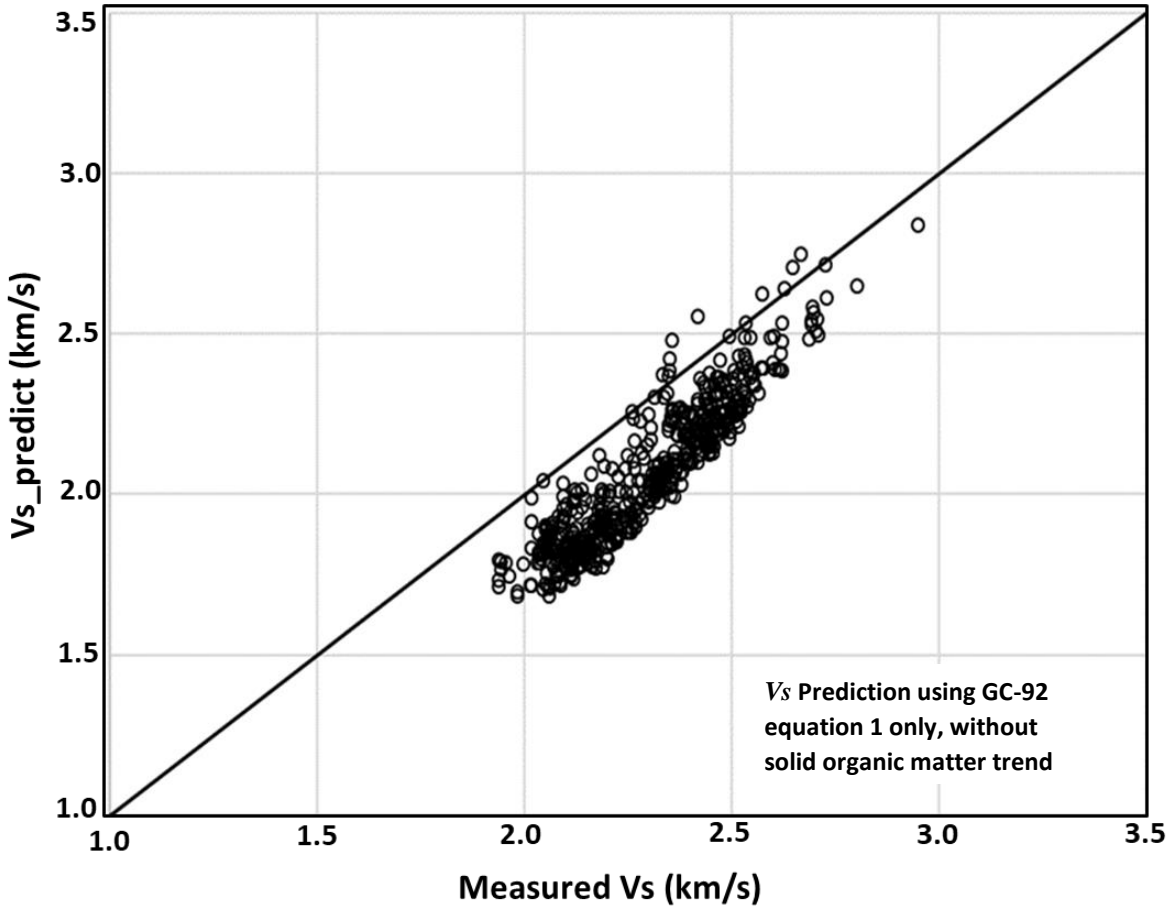


**Figure 3.5c:** Avalon shale. Cross plot of measured shear-wave velocity (x axis) and the shear-wave velocity prediction (y axis) obtained by simply implementing equation 1 of GC-92, i.e. ignoring solid organic matter and fluid effects. The black line is a 1-to-1 line. Percent mean signed error in  $V_s$  prediction is -9.4%, with percent standard error of 10.5%.

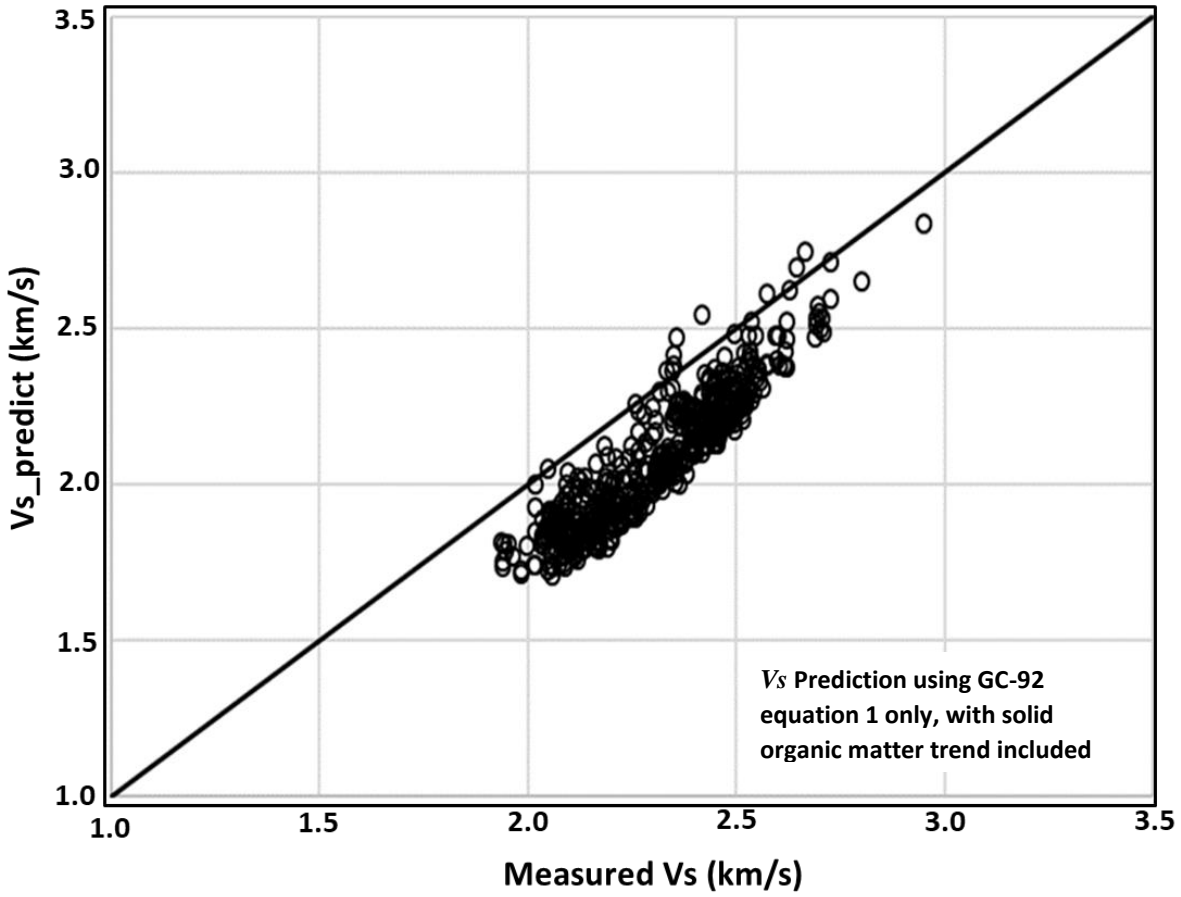


**Figure 3.5d:** Avalon shale. Cross plot of measured shear-wave velocity (x axis) and the shear-wave velocity prediction (y axis) obtained by implementing equation 1 of GC-92, including a trend for solid organic content but ignoring fluid effects. The black line is a 1-to-1 line. Percent mean signed error in  $V_s$  prediction is -9.18%, with percent standard error of 10.18%.

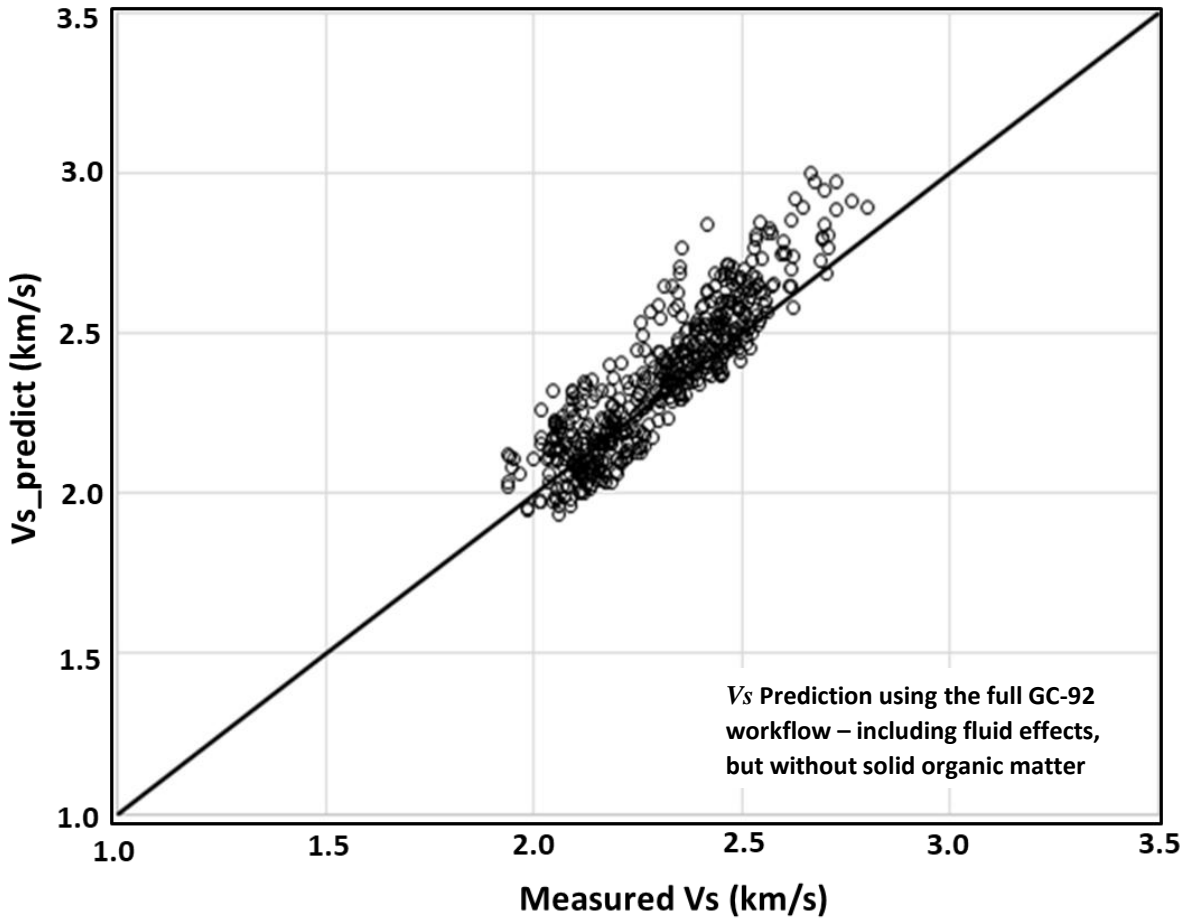


**Figure 3.5e:** Avalon shale. Cross plot of measured shear-wave velocity (x axis) and the shear-wave velocity prediction (y axis) obtained by implementing the full GC-92 workflow without solid organic matter. The black line is a 1-to-1 line. Percent mean signed error in  $V_s$  prediction is 2.41%, with percent standard error of 5.13%.

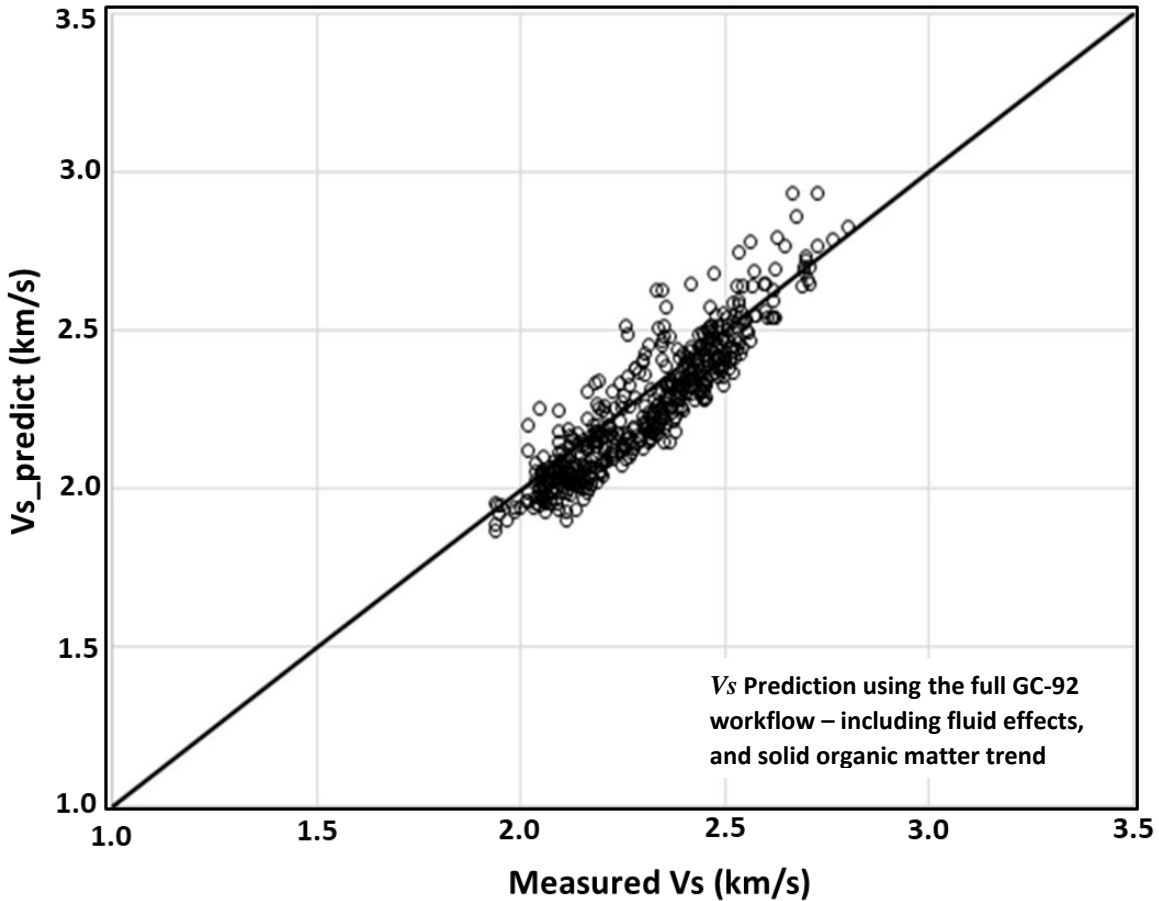


**Figure 3.5f:** Avalon shale. Cross plot of measured shear-wave velocity (x axis) and the shear-wave velocity prediction (y axis) obtained by implementing the full GC-92 workflow including the regression trend for solid organic matter. The black line is a 1-to-1 line. Percent mean signed error in  $V_s$  prediction is -1.94%, with percent standard error of 4.2%.

### 3.4.3 LOWER SPRABERRY SHALE:

The lower Spraberry shale is another Permian-age volatile oil shale play in the Midland basin – a sub-basin of the Permian basin. In our dataset, kerogen volume ranges from 1.6% to 9.1%, with an average of 4.83%. Average water saturation is 55.1%.

After the application of the modified Greenberg-Castagna workflow, percent mean signed error in  $V_s$  prediction was only -0.41% with a percent standard error of 2.26%, (black

curve in the last track in Figure 3.6a and also shown in the cross plot in figure 3.6b) compared to a percent mean signed error of 1.41% and a percent standard error of 3.08% when the full GC-92 workflow ignoring kerogen is applied to the dataset (see figure 3.6e), or percent mean signed error of 0.015% and percent standard error of 2.66% in  $V_s$  prediction when the full GC-92 workflow with fluid substitution is implemented with the solid organic matter trend included (see figure 3.6f). The  $V_s$  prediction results obtained by simply implementing GC-92 equation 1 without solid organic content included is shown in Figures 3.6c; percent mean signed error in  $V_s$  prediction is -4.41%. Figure 3.6d shows the result when GC-92 equation 1 is applied directly ignoring fluid effects but including the trend for solid organic content. As in the Wolfcamp shale example, there is deviation from the 1-to-1 line at lower shear-wave velocities; percent mean signed error using this approach is -4.1% and a percent standard error of 5.1%.

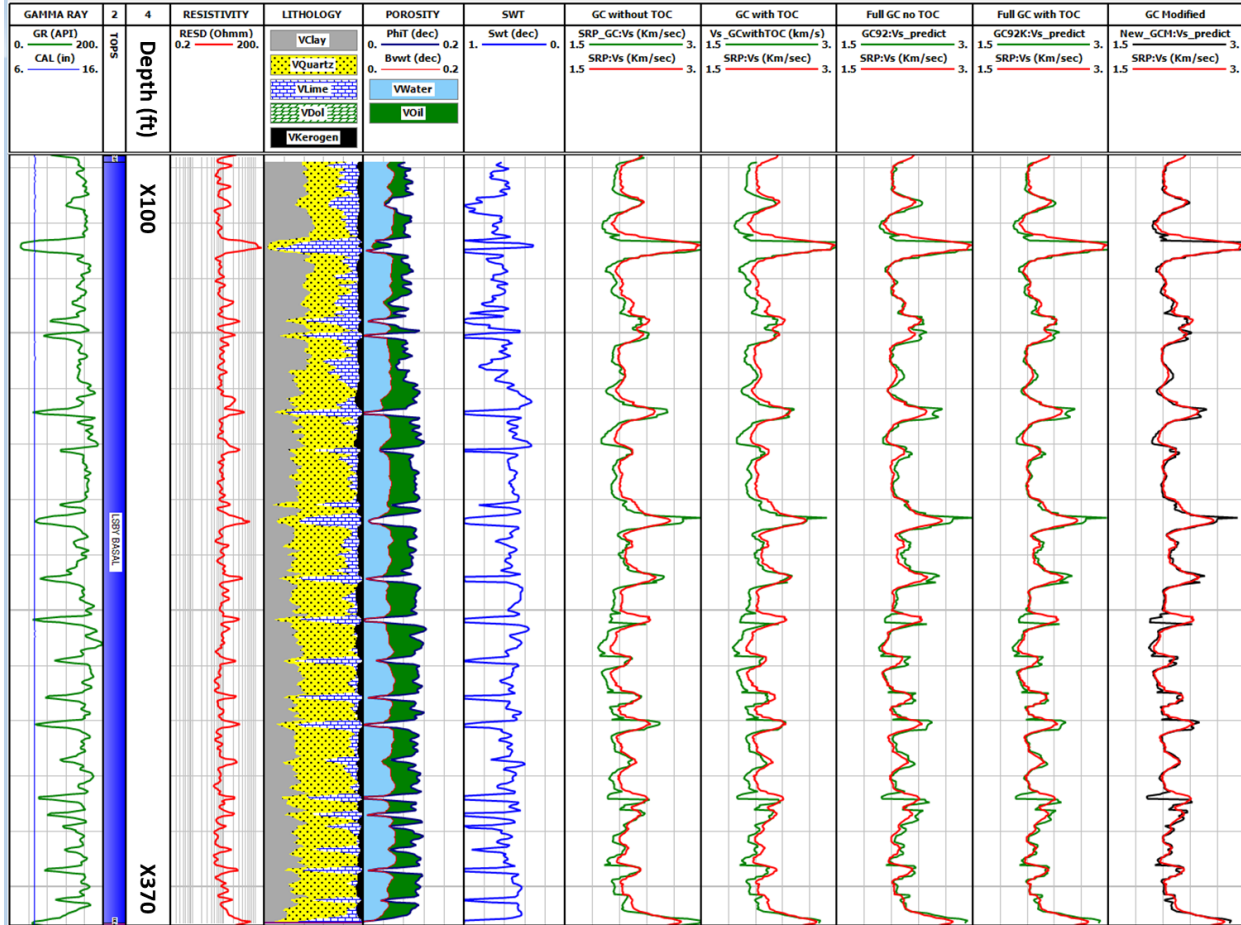


**Figure 3.6a:** Log plot of the Lower Spraberry shale. GAMMA RAY Track: Gamma-ray log (solid green curve - GR). Tops Track: Formation name. LITHOLOGY Track: Formation lithology fractional volumes (decimal units) determined by volumetric log analyses. POROSITY Track: Total porosity determined from volumetric log analyses (blue curve - PhiT), BWWT is bulk volume of water, green shading in this track is hydrocarbon pore volume. SWT Track: Total water saturation – blue curve. GC without TOC Track: Green curve is  $V_s$  prediction using GC-92 equation 1; red curve is the measured  $V_s$ . GC with TOC Track: Green curve is the  $V_s$  prediction using GC-92 equation 1 but including a regression trend for kerogen; red curve is the measured  $V_s$ . Full GC no TOC Track: Green curve is the  $V_s$  prediction from implementing the full GC-92 workflow without solid organic matter; red curve is the measured  $V_s$ . GC Modified Track: Black curve is the  $V_s$  prediction from the modified workflow; Red curve is the measured  $V_s$ . Depths in the depth track are only to indicate depth scale, actual depths are not available for publication.

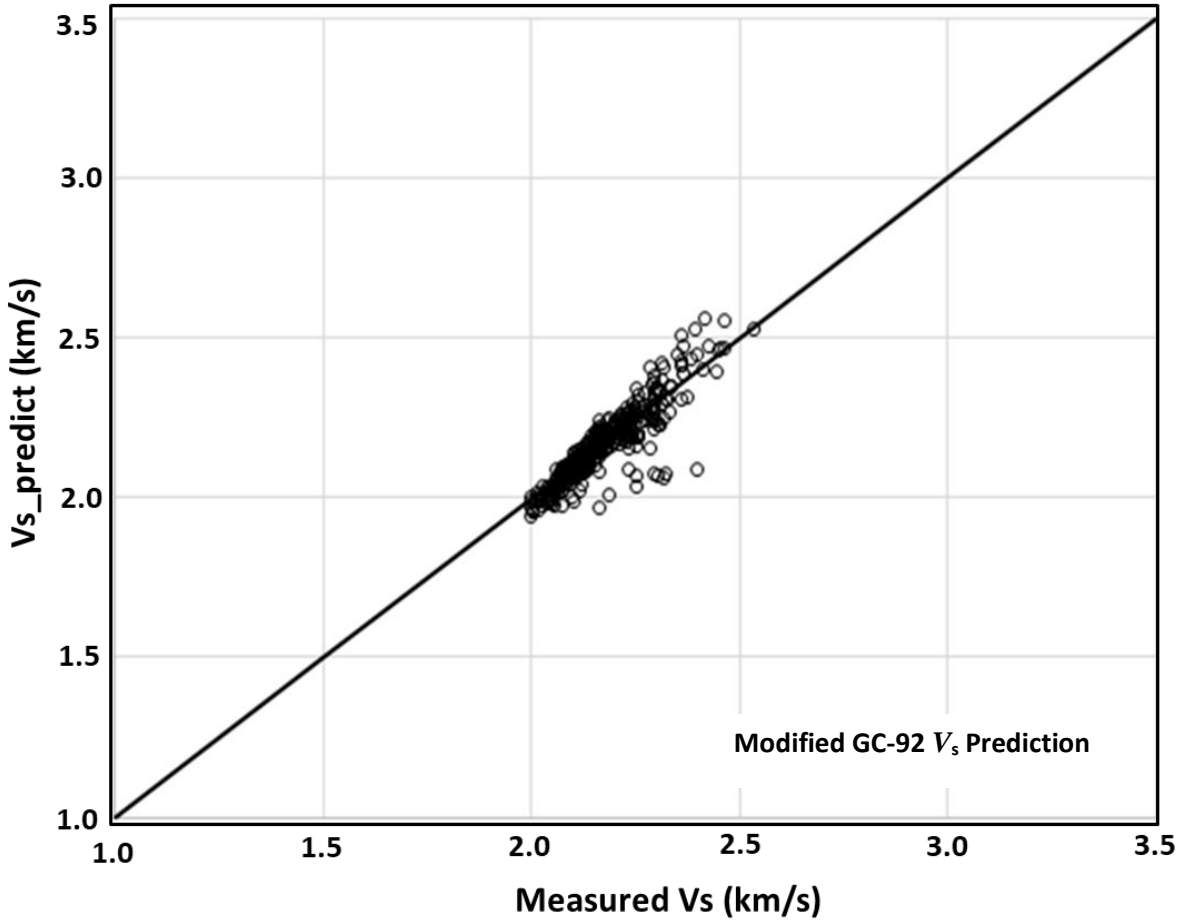


**Figure 3.6b:** Cross plot of measured shear-wave velocity (x axis) and the modified GC shear-wave velocity prediction (y axis) for the lower Spraberry shale. The black line is a 1-to-1 line. Percent mean signed error in  $V_s$  prediction is -0.41%, with percent standard error of 2.26%.

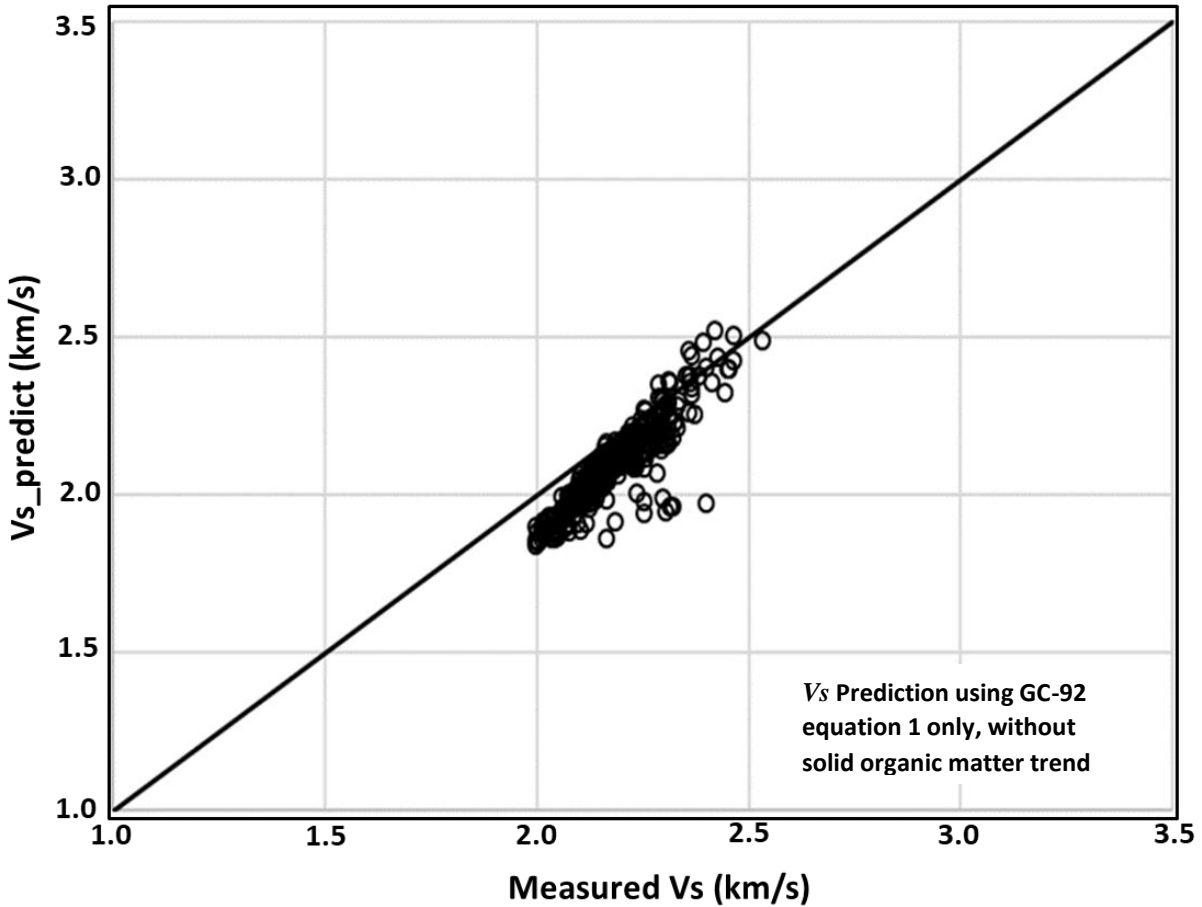


**Figure 3.6c:** Lower Spraberry shale shale. Cross plot of measured shear-wave velocity (x axis) and the shear-wave velocity prediction (y axis) obtained by simply implementing equation 1 of GC-92, i.e. ignoring solid organic matter and fluid effects. The black line is a 1-to-1 line. Percent mean signed error in  $V_s$  prediction is -4.4%, with percent standard error of 4.99%.

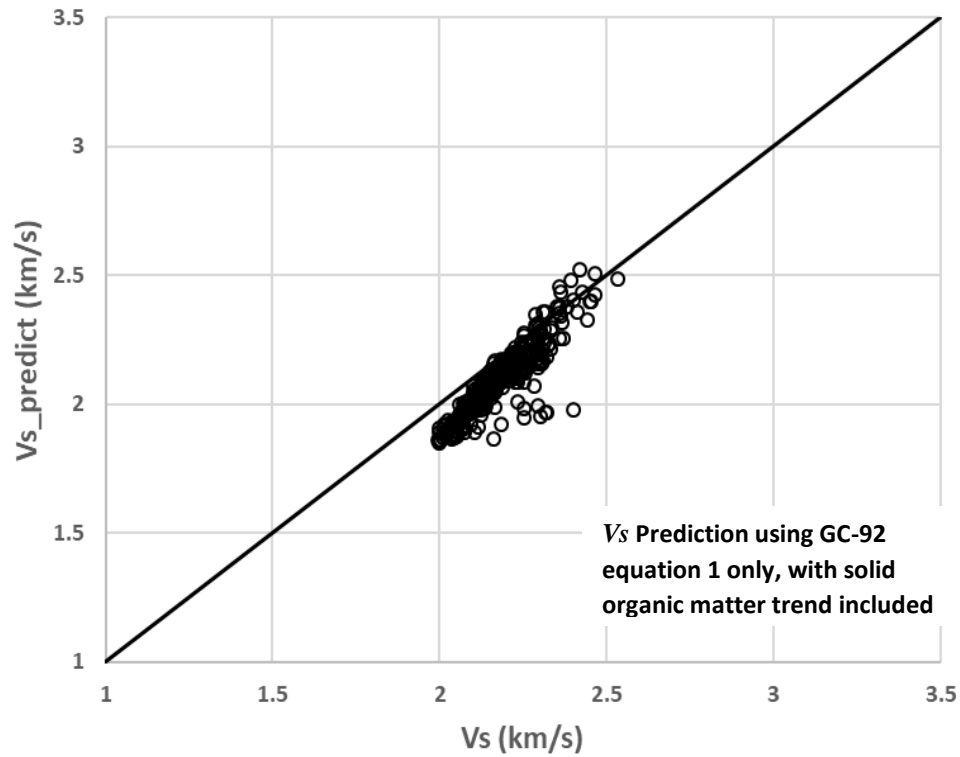


**Figure 3.6d:** Lower Spraberry shale. Cross plot of measured shear-wave velocity (x axis) and the shear-wave velocity prediction (y axis) obtained by implementing equation 1 of GC-92, including a regression trend for solid organic content. The black line is a 1-to-1 line. Percent mean signed error in  $V_s$  prediction is -4.1%, with percent standard error of 5.08%.

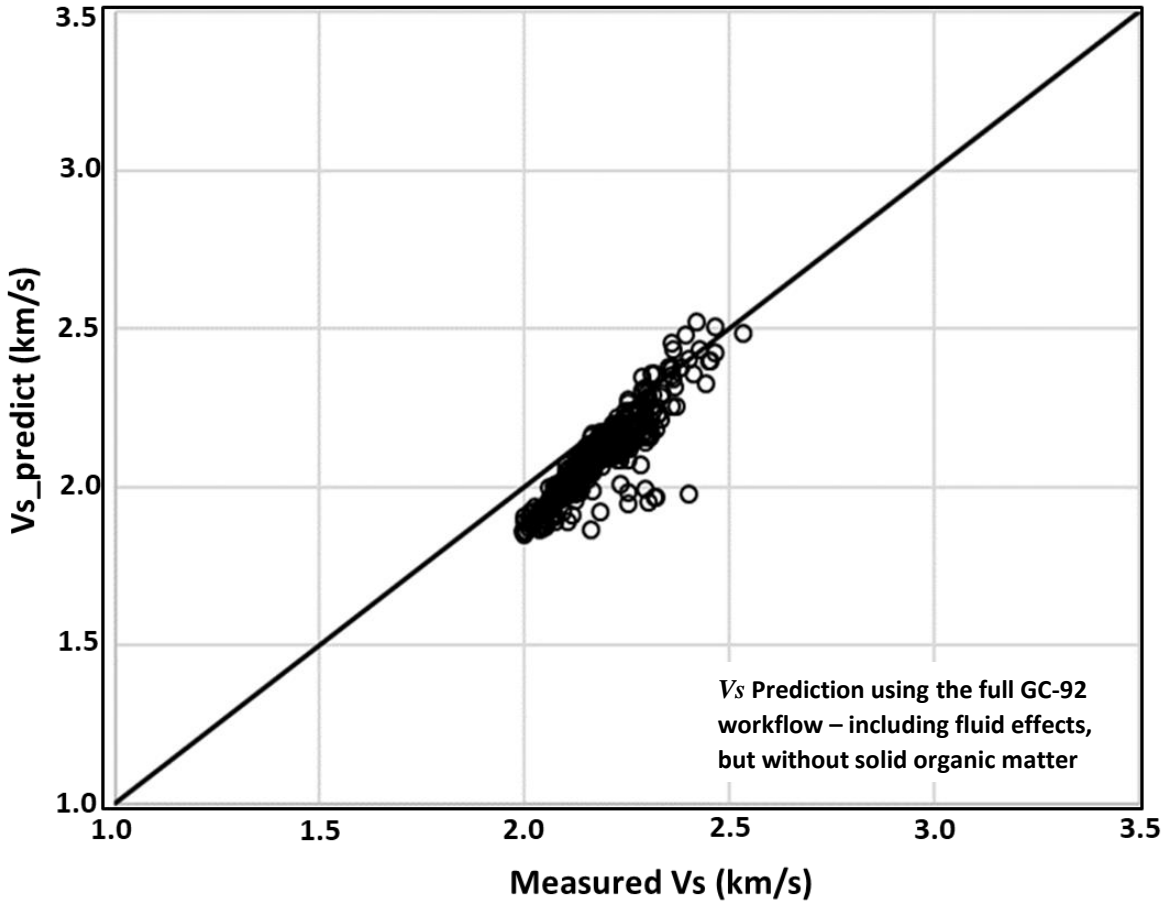


**Figure 3.6e:** Lower Spraberry shale. Cross plot of measured shear-wave velocity (x axis) and the shear-wave velocity prediction (y axis) obtained by implementing the full GC-92 workflow without solid organic matter. The black line is a 1-to-1 line. Percent mean signed error in  $V_s$  prediction is 1.4%, with percent standard error of 3.08%.

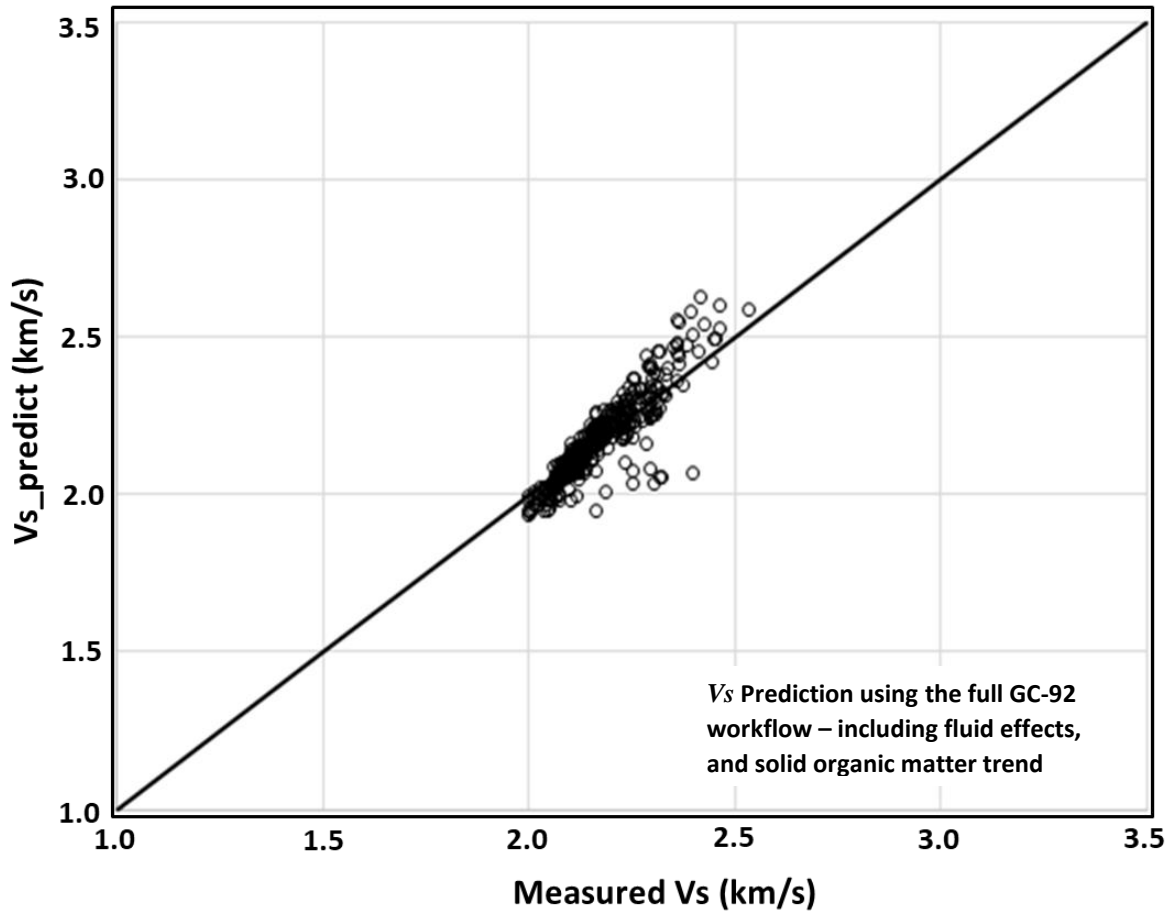
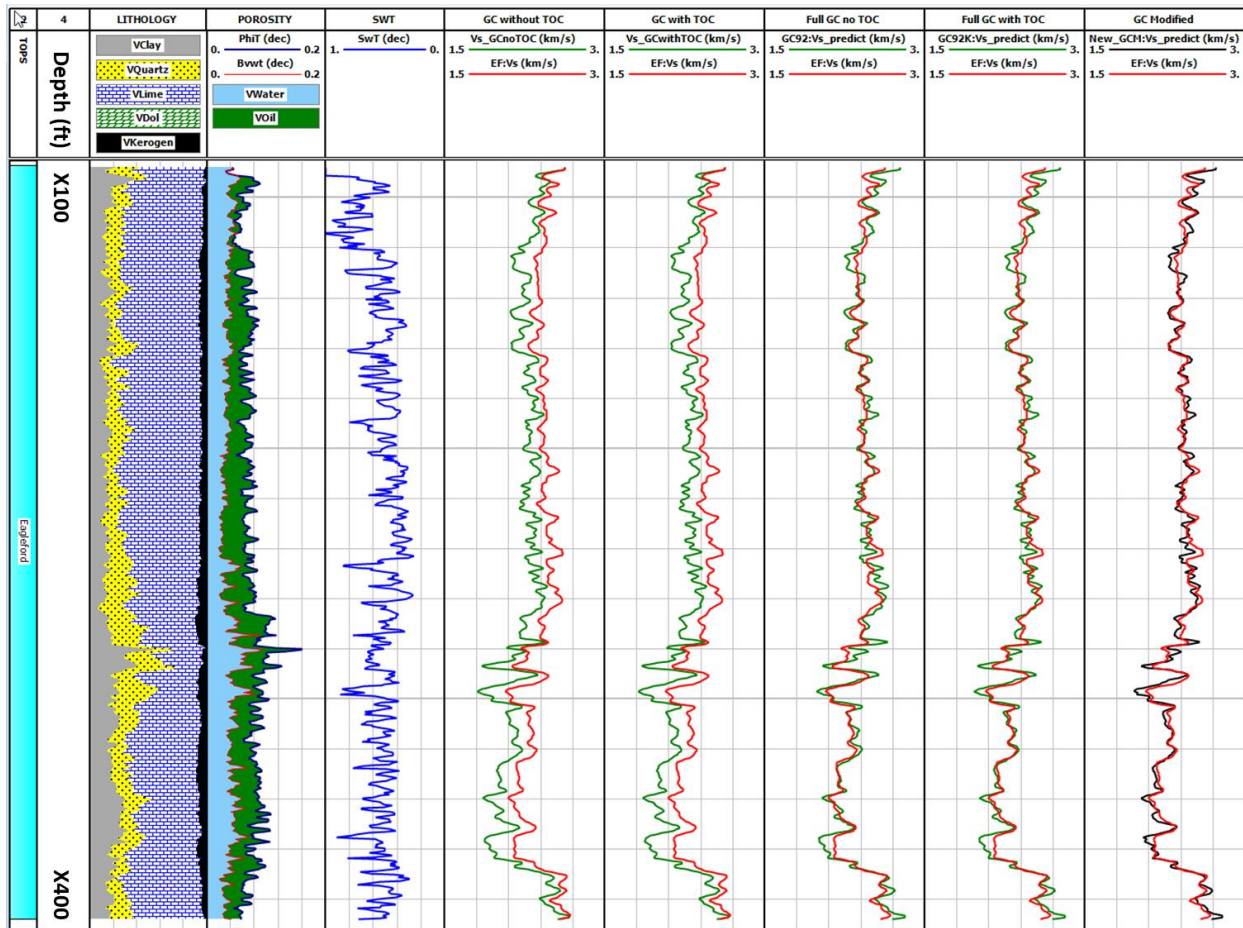


**Figure 3.6f:** Lower Spraberry shale. Cross plot of measured shear-wave velocity (x axis) and the shear-wave velocity prediction (y axis) obtained by implementing the full GC-92 workflow including the regression trend for solid organic matter. Percent mean signed error in  $V_s$  prediction is 0.015%, with percent standard error of 2.66%.

#### 3.4.4 EAGLEFORD SHALE:

The Eagle Ford is a late Cretaceous-age organic shale; depending on location it could be a dry gas, wet gas condensate or volatile oil organic-shale play, our dataset is from the dry gas window. Kerogen volume is relatively low – between 2% and 9%; average kerogen volume is 5.2% and average water saturation is 50.9%. In contrast to the other shales in this study, calcite is the dominant inorganic mineralogical component. The  $V_s$  prediction results for the Eagleford shale are shown in the log plot in figure 3.7a. The  $V_s$  prediction percent mean signed error using the modified GC workflow is -0.31%, with a percent standard error of 2%. Figure 3.7b is the cross plot of the measured shear-wave velocity and modified GC-92 shear-wave velocity prediction. Note how the data straddle the 1-to-1 line. On the other hand, applying the GC-92 equation 1 ignoring fluid effects yields percent mean signed error of -6.48% if solid organic content is ignored and -6.28% if it is included (figures 3.7c and 3.7d). The full GC-92 workflow including fluid effects but ignoring the effect of organic matter yields percent mean signed error of 0.36% with a percent standard error of 2.41% (figure 3.6e). When kerogen is included in the full GC-92 workflow along with fluid substitution, the  $V_s$  prediction percent mean signed error is -0.19% and a percent standard error of 2.23% (figure 3.6f). We conclude that the fluid substitution effect is more important than organic content in this formation, and that the modified GC-92 method has the smallest mean and standard errors.



**3.7a:** Log plot of the Eagleford shale. GAMMA RAY Track: Gamma-ray log (solid green curve - GR). Tops Track: Formation name. LITHOLOGY Track: Formation lithology fractional volumes (decimal units) determined by volumetric log analyses. POROSITY Track: Total porosity determined from volumetric log analyses (blue curve - PhiT), BVWT is bulk volume of water, green shading in this track is hydrocarbon pore volume. SWT Track: Total water saturation – blue curve. GC without TOC Track: Green curve is  $V_s$  prediction using GC-92 equation 1; red curve is the measured  $V_s$ . GC with TOC Track: Green curve is the  $V_s$  prediction using GC-92 equation 1 but including a regression trend for kerogen; red curve is the measured  $V_s$ . Full GC no TOC Track: Green curve is the  $V_s$  prediction from implementing the full GC-92 workflow without solid organic matter; red curve is the measured  $V_s$ . GC Modified Track: Black curve is the  $V_s$  prediction from the modified workflow; Red curve is the measured  $V_s$ . Depths in the depth track are only to indicate depth scale, actual depths are not available for publication.

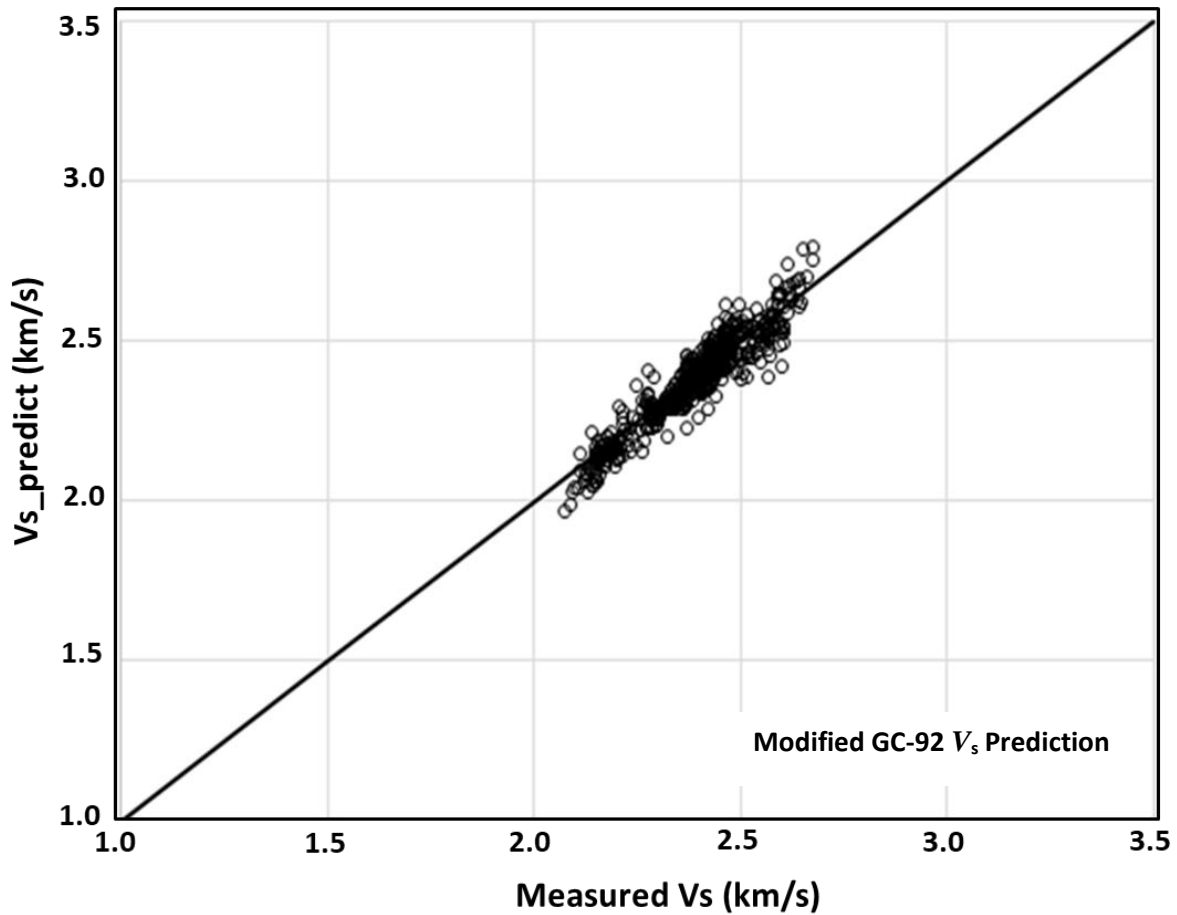


**Figure 3.7b:** Cross plot of measured shear-wave velocity (x axis) and the modified GC shear-wave velocity prediction (y axis) for the Eagleford shale. The black line is a 1-to-1 line. Percent mean signed error in  $V_s$  prediction is -0.31%, with percent standard error of 2%.

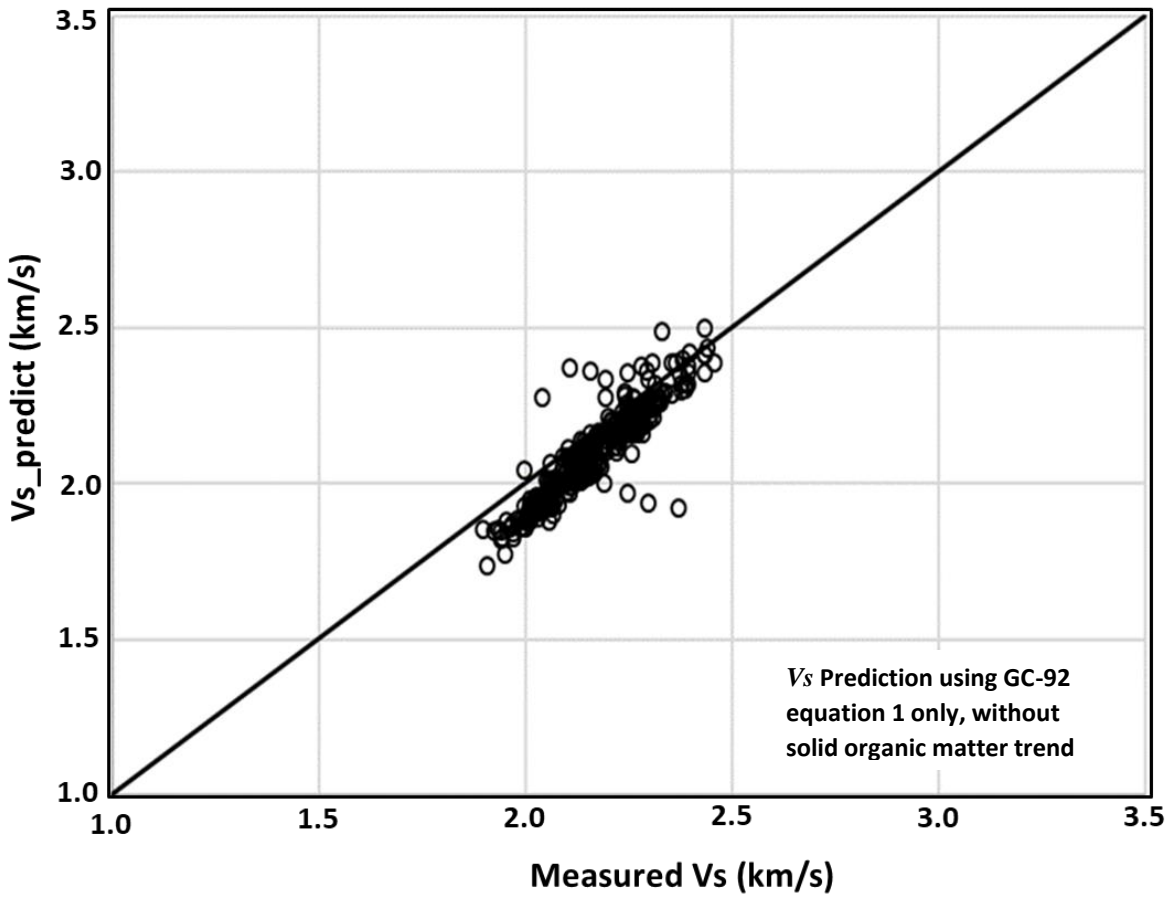


**Figure 3.7c:** Eagleford shale. Cross plot of measured shear-wave velocity (x axis) and the shear-wave velocity prediction (y axis) obtained by simply implementing equation 1 of GC-92, i.e. ignoring solid organic matter and fluid effects. The black line is a 1-to-1 line. Percent mean signed error in  $V_s$  prediction is -6.48%, with percent standard error of 6.87%.

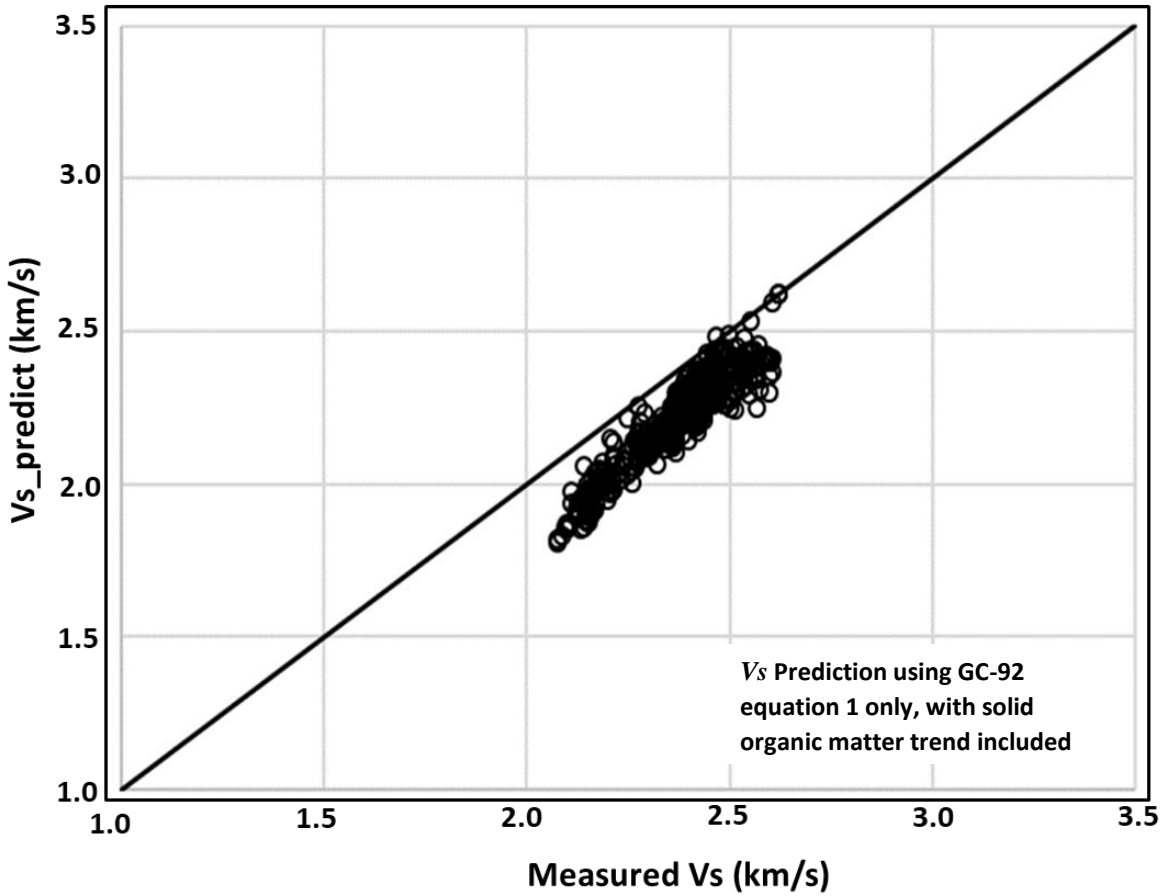


**Figure 3.7d:** Eagleford shale. Cross plot of measured shear-wave velocity (x axis) and the shear-wave velocity prediction (y axis) obtained by implementing equation 1 of GC-92, using coal regression trend for solid organic content. The black line is a 1-to-1 line. Percent mean signed error in  $V_s$  prediction is -6.28%, with percent standard error of 6.67%.

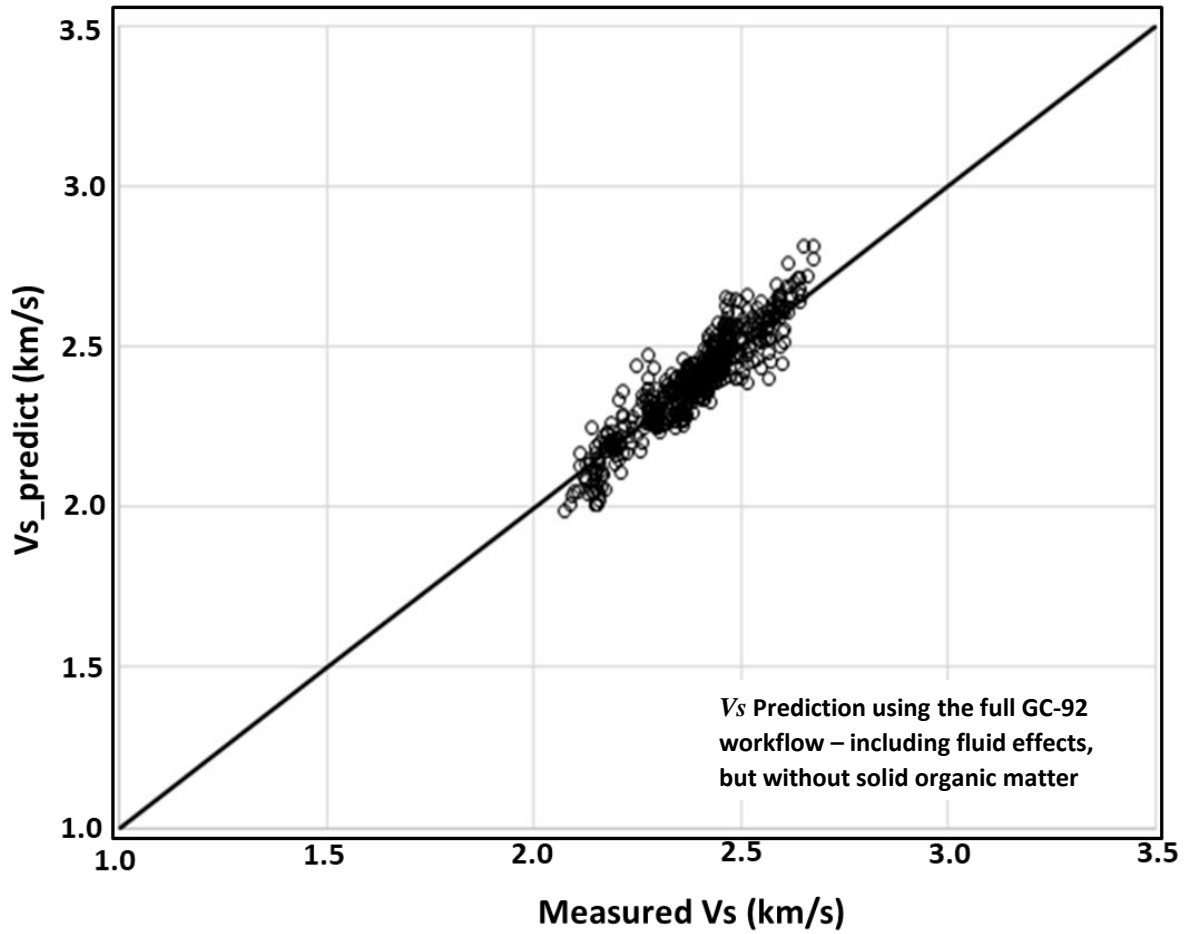


**Figure 3.7e:** Eagleford shale. Cross plot of measured shear-wave velocity (x axis) and the shear-wave velocity prediction (y axis) obtained by implementing the full GC-92 workflow without solid organic matter. The black line is a 1-to-1 line. Percent mean signed error in  $V_s$  prediction is 0.36%, with percent standard error of 2.4%.

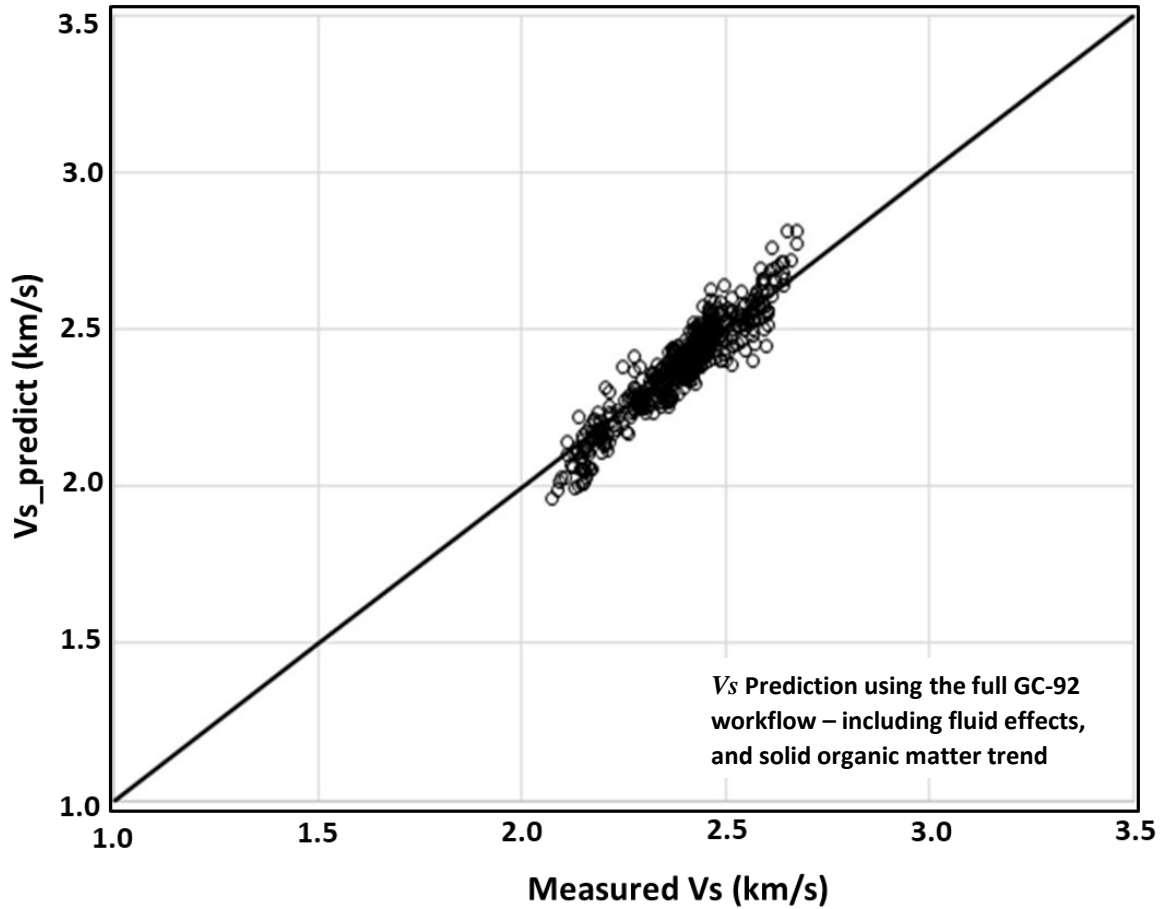


**Figure 3.7f:** Eagleford shale. Cross plot of measured shear-wave velocity (x axis) and the shear-wave velocity prediction (y axis) obtained by implementing the full GC-92 workflow including the regression trend for solid organic matter. The black line is a 1-to-1 line. Percent mean signed error in  $V_s$  prediction is -0.19%, with percent standard error of 2.23%.

### 3.4.5 LOWER CLINE SHALE:

The Lower Cline shale is a Pennsylvanian-age volatile oil shale play in the Midland basin. Kerogen volume is in the low to medium range, for our dataset the range is 3% to 17.6%, with an average of 8%; average water saturation is 59.3%. The result after the modified workflow is applied is shown in Figures 3.8a and 3.8b. Percent mean signed error is -0.49% and percent standard error is 3.48%. Simply applying GC-92 equation 1 with and without the organic trend are shown in Figures 3.8c and 3.8d respectively, percent mean signed errors are respectively -7.46% and -7.2%. On the other hand, when the full GC workflow is implemented and kerogen content is ignored, the  $V_s$  prediction percent mean signed error is 0.44% and percent standard error is 5.32% (figure 3.8e). When the solid organic content trend is included in the full GC-92 workflow with fluid substitution;  $V_s$  prediction percent mean signed error is -2.59% with a 4.3% standard error and this is shown in figure 3.7f. Once again, accounting for fluid effects in shear-wave velocity prediction is more important than accounting for solid organic content, and the modified GC-92 method has the smallest mean error and standard error.

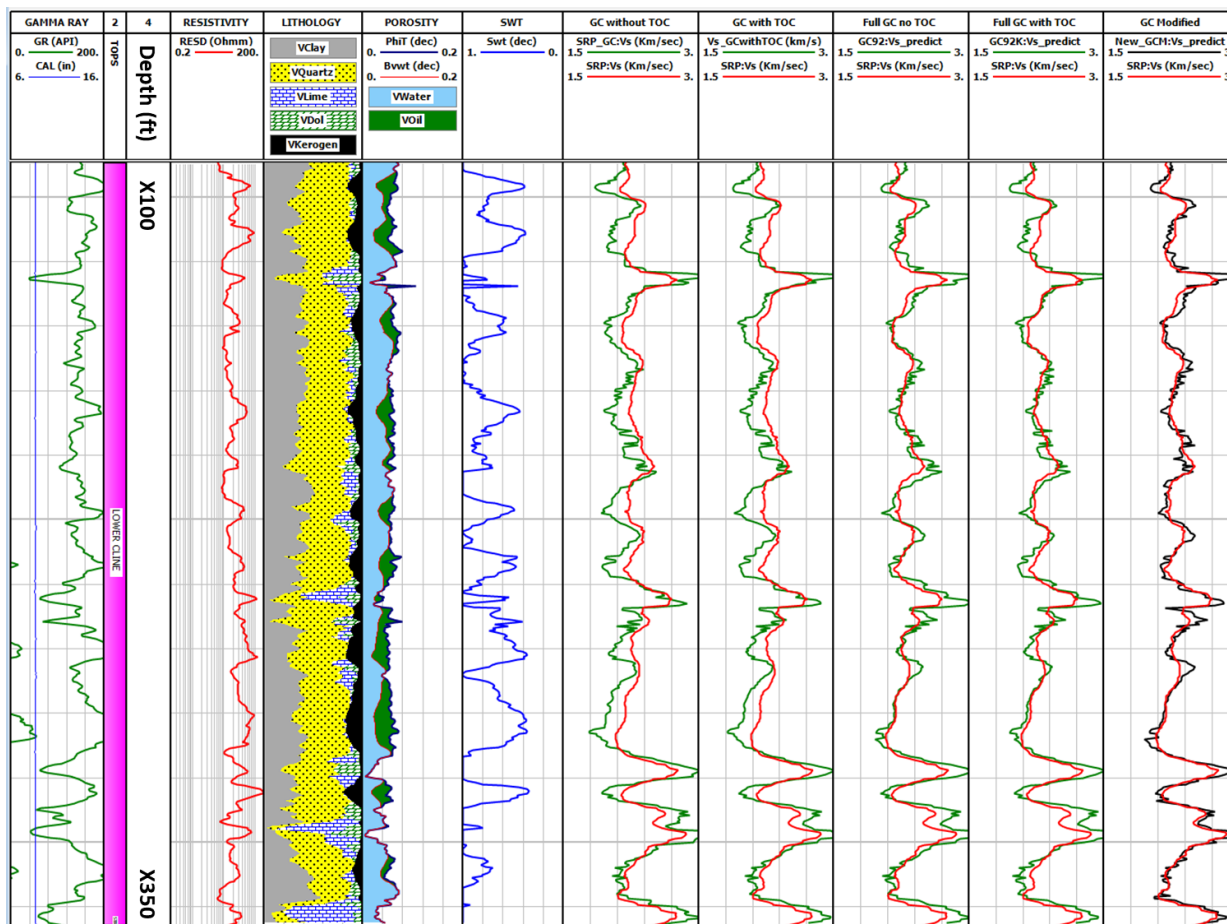


**Figure 3.8a:** Log plot of the Lower Cline shale. GAMMA RAY Track: Gamma-ray log (solid green curve - GR). Tops Track: Formation name. LITHOLOGY Track: Formation lithology fractional volumes (decimal units) determined by volumetric log analyses. POROSITY Track: Total porosity determined from volumetric log analyses (blue curve - PhiT), BVWT is bulk volume of water, green shading in this track is hydrocarbon pore volume. SWT Track: Total water saturation – blue curve. GC without TOC Track: Green curve is  $V_s$  prediction using GC-92 equation 1; red curve is the measured  $V_s$ . GC with TOC Track: Green curve is the  $V_s$  prediction using GC-92 equation 1 but including a regression trend for kerogen; red curve is the measured  $V_s$ . Full GC no TOC Track: Green curve is the  $V_s$  prediction from implementing the full GC-92 workflow without solid organic matter; red curve is the measured  $V_s$ . GC Modified Track: Black curve is the  $V_s$  prediction from the modified workflow; Red curve is the measured  $V_s$ . Depths in the depth track are only to indicate depth scale, actual depths are not available for publication.

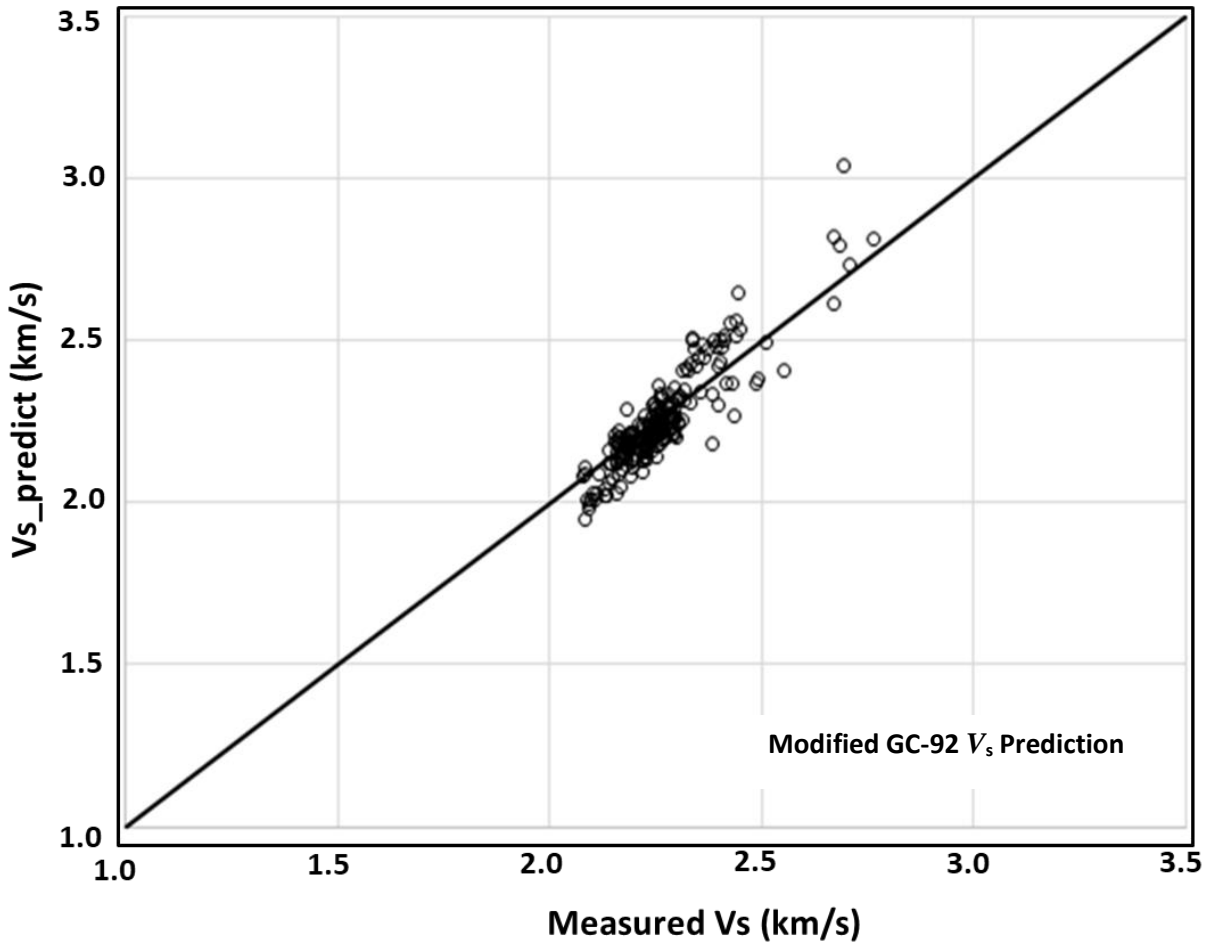


**Figure 3.8b:** Cross plot of measured shear-wave velocity (x axis) and the modified GC shear-wave velocity prediction (y axis) for the lower Cline shale. The black line is a 1-to-1 line. Percent mean signed error in  $V_s$  prediction is -0.49%, with percent standard error of 3.08%.

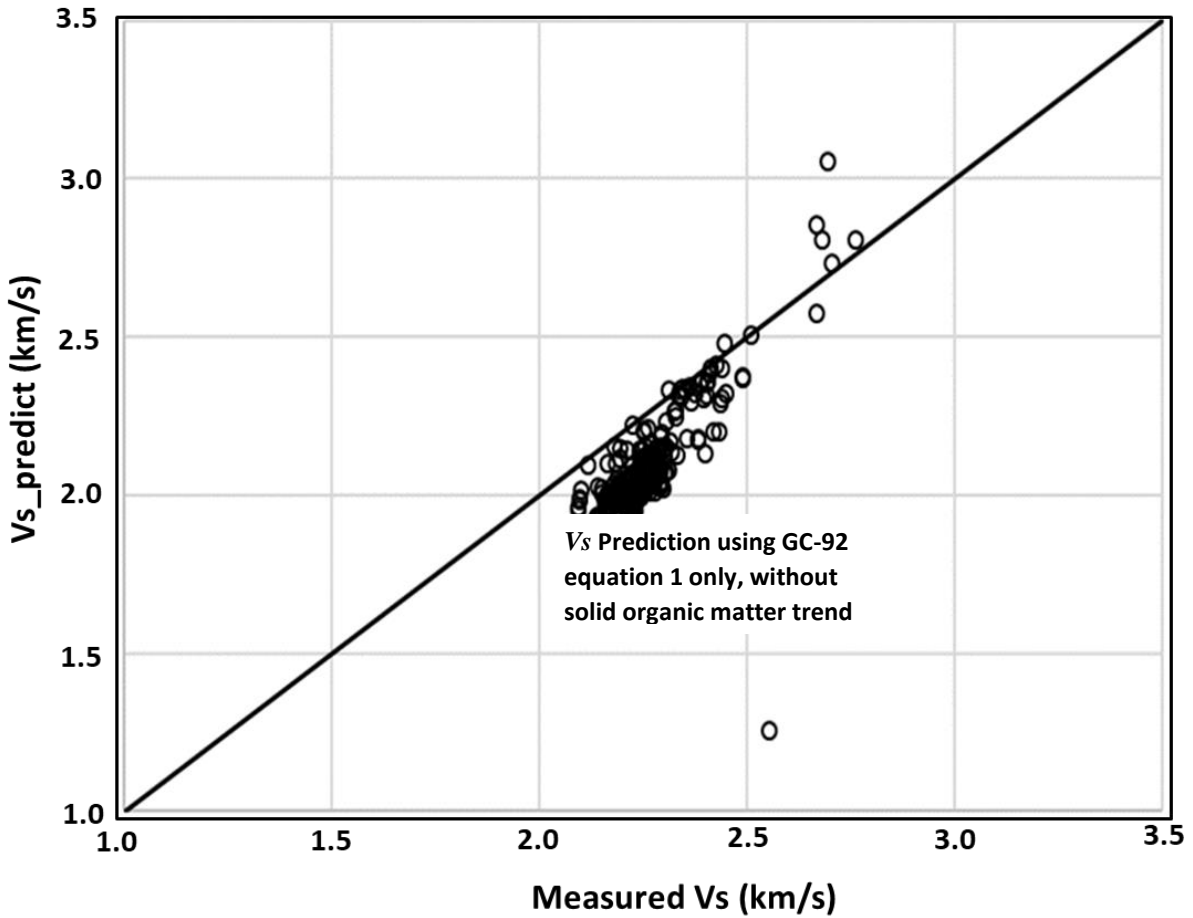


**Figure 3.8c:** Lower Cline shale. Cross plot of measured shear-wave velocity (x axis) and the shear-wave velocity prediction (y axis) obtained by simply implementing equation 1 of GC-92, i.e. ignoring solid organic matter and fluid effects. The black line is a 1-to-1 line. Percent mean signed error in  $V_s$  prediction is -7.46%, with percent standard error of 9.01%.

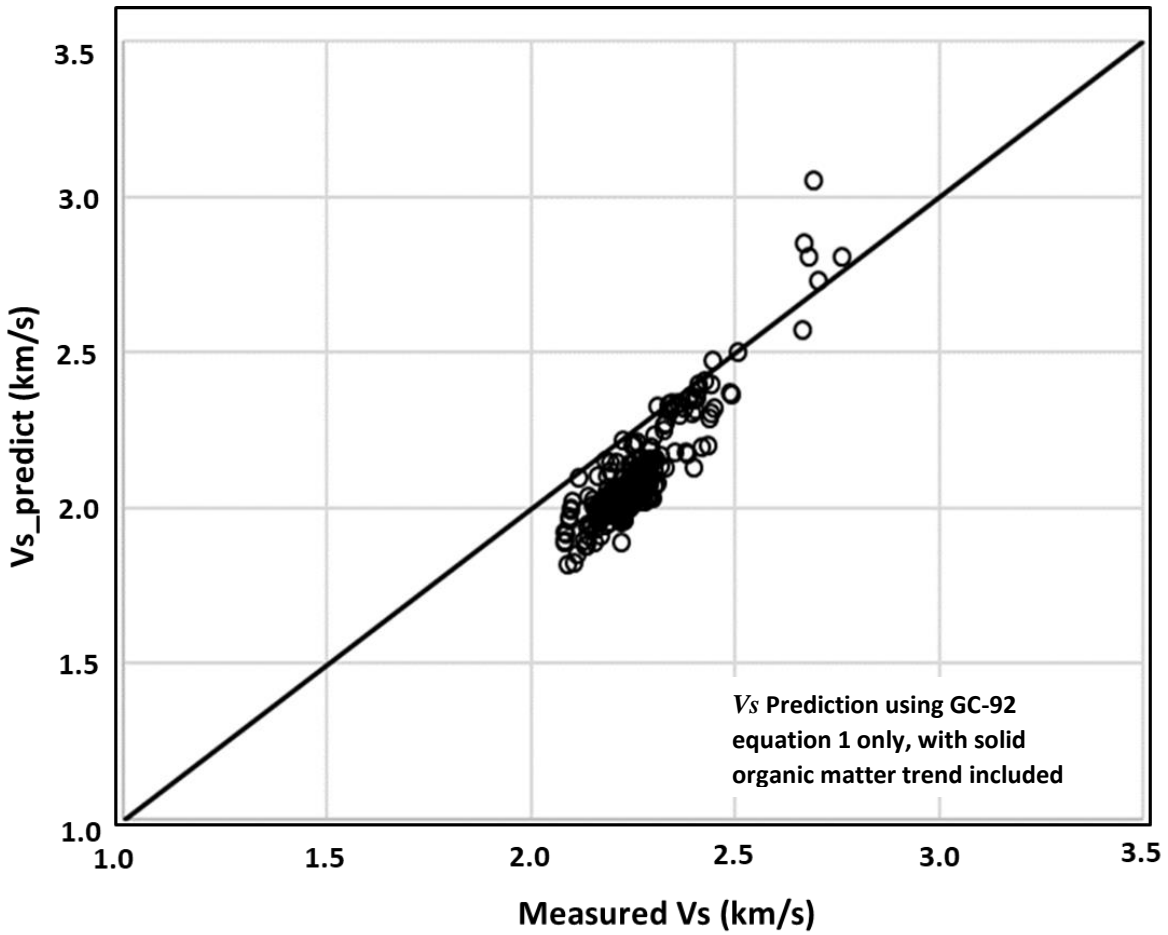


**Figure 3.8d:** Lower Cline shale. Cross plot of measured shear-wave velocity (x axis) and the shear-wave velocity prediction (y axis) obtained by implementing equation 1 of GC-92, including a trend for solid organic content. The black line is a 1-to-1 line. Percent mean signed error in  $V_s$  prediction is -7.2%, with percent standard error of 8.73%.

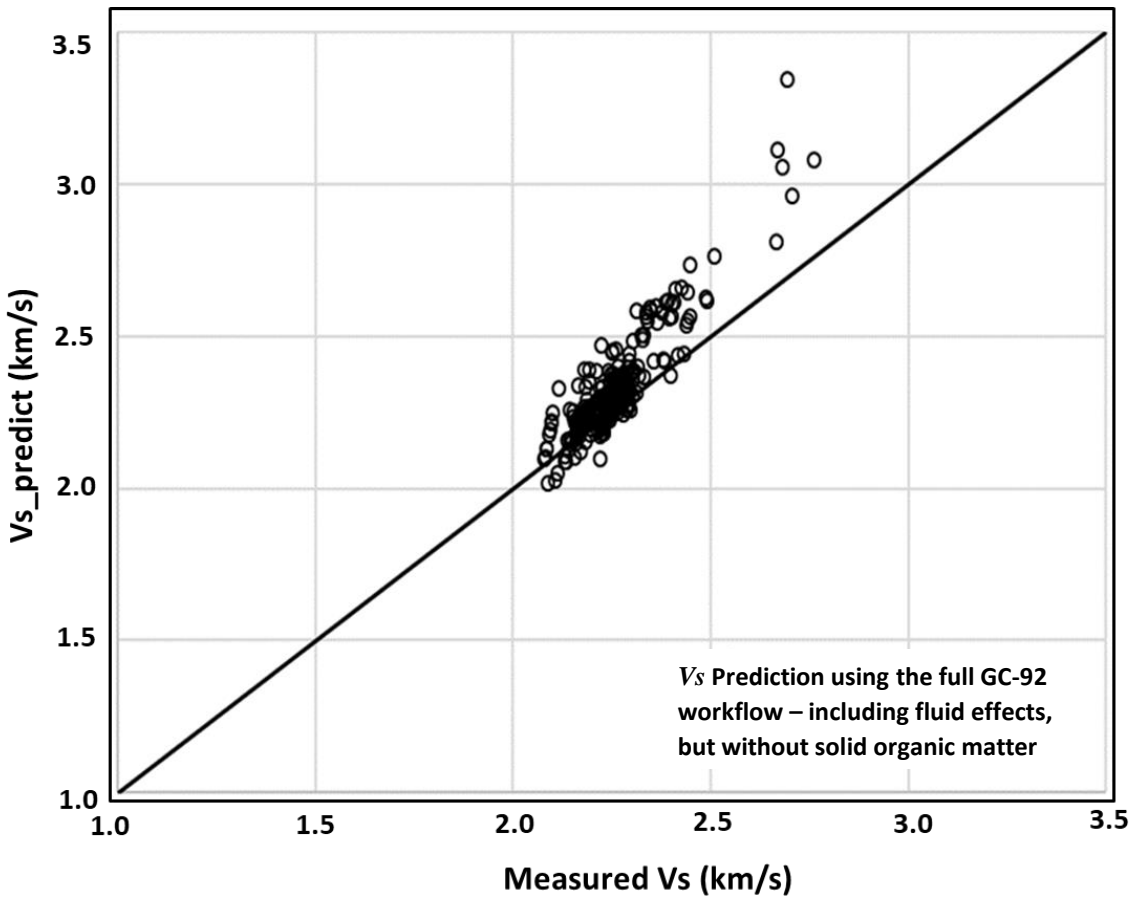


**Figure 3.8e:** Lower Cline shale. Cross plot of measured shear-wave velocity (x axis) and the shear-wave velocity prediction (y axis) obtained by implementing the full GC-92 workflow without solid organic matter. The black line is a 1-to-1 line. Percent mean signed error in  $V_s$  prediction is 0.44%, with percent standard error of 5.32%.

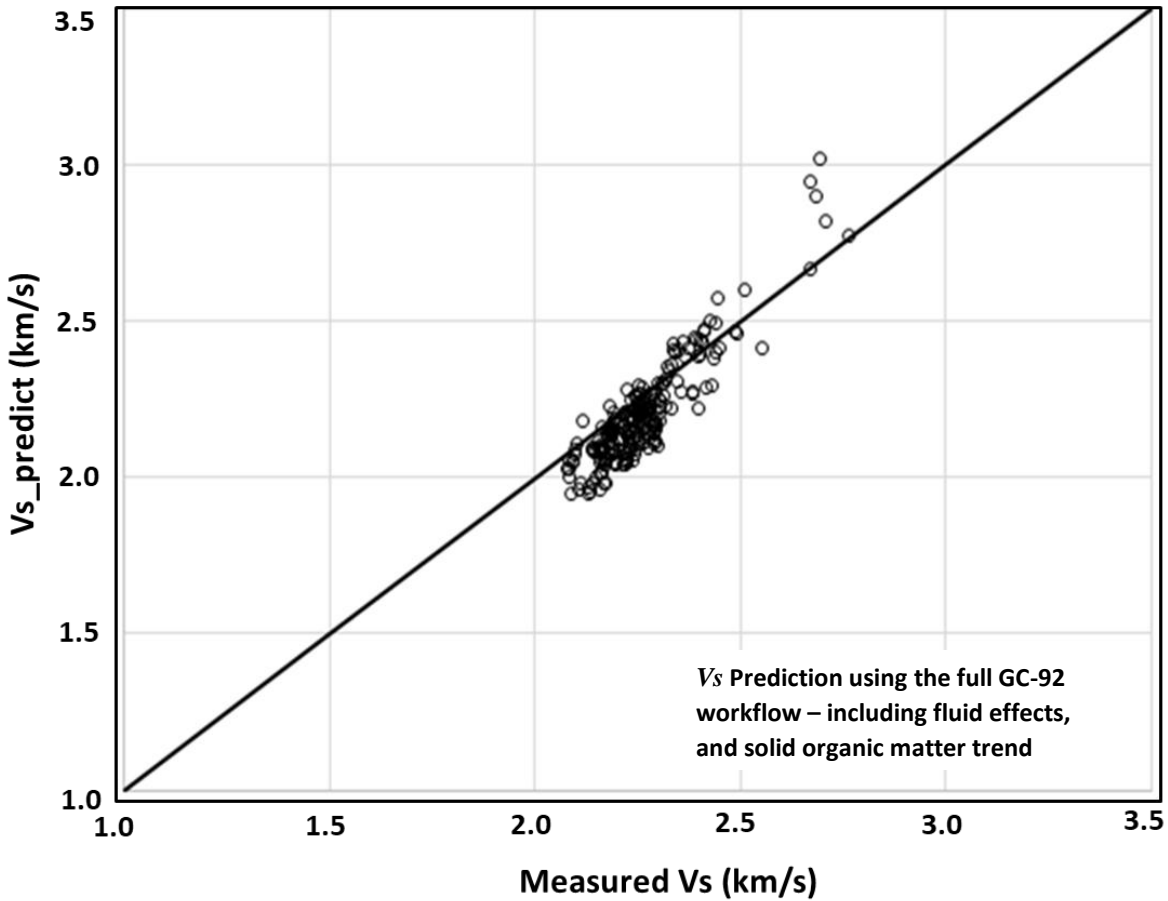


**Figure 3.8f:** Lower Cline shale. Cross plot of measured shear-wave velocity (x axis) and the shear-wave velocity prediction (y axis) obtained by implementing the full GC-92 workflow including the trend for solid organic matter. The black line is a 1-to-1 line. Percent mean signed error in  $V_s$  prediction is -2.59%, with percent standard error of 4.3%.

### 3.4.6 BAKKEN SHALE:

The Bakken shale is another shale play with significant volume of kerogen often exceeding 20 percent in the Williston basin. However, unlike the Avalon that is several hundred feet thick; the combined thickness of the upper and lower Bakken is less than 30 feet in the well evaluated here. Kerogen volume ranges from 19% to 33% over this interval, with an average of 25.6%. Average water saturation is 21%. Percent mean signed error was 0.17% with a percent

standard error of 1.84% after the modified GC-92 method was applied (figure 3.9a). On the other hand, when GC-92 equation 1 is applied – ignoring solid organic content and fluid effects – significant deviation from the 1-to-1 line is observed (figure 3.9b) as in the Avalon shale example. This is due to the relatively high organic content of the Bakken shale; percent mean signed error is -13.17%, with a percent standard error of 13.66%. When the solid organic matter trend is included in GC-92 equation 1, the percent mean signed error is -11.14% with a percent standard error of 11.41% (figure 3.9c). The result of the full GC-92 workflow implementation but ignoring kerogen is shown in figure 3.9d; percent mean signed error in  $V_s$  prediction is 17.71%, with a percent standard error of 17.865%. On the other hand, the  $V_s$  prediction percent mean signed error is 0.14% and a percent standard error of 3.05% when both the solid organic matter trend and fluid effects are included in the full GC-92 workflow (figure 3.9e). In the Bakken formation, both fluid and kerogen effects must be considered to achieve a good  $V_s$  prediction. In this case, the original GC-92 method including fluid substitution and solid organic matter and the modified GC-92 method have similar accuracy, though the modified GC-92 method has observably smaller standard error.

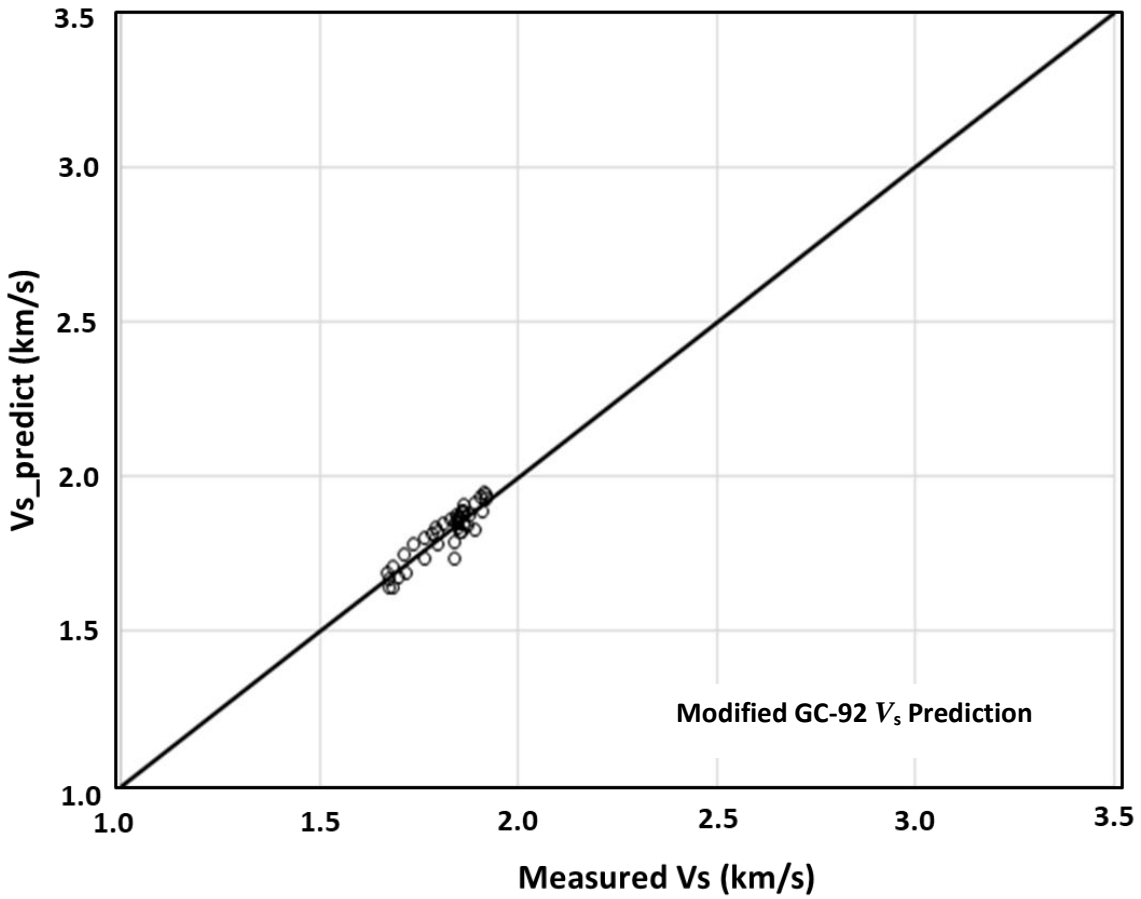


**Figure 3.9a:** Cross plot of measured shear-wave velocity (x axis) and the modified GC shear-wave velocity prediction (y axis) for the Bakken shale. The black line is a 1-to-1 line. Percent mean signed error in  $V_s$  prediction is 0.17%, with percent standard error of 1.84%.

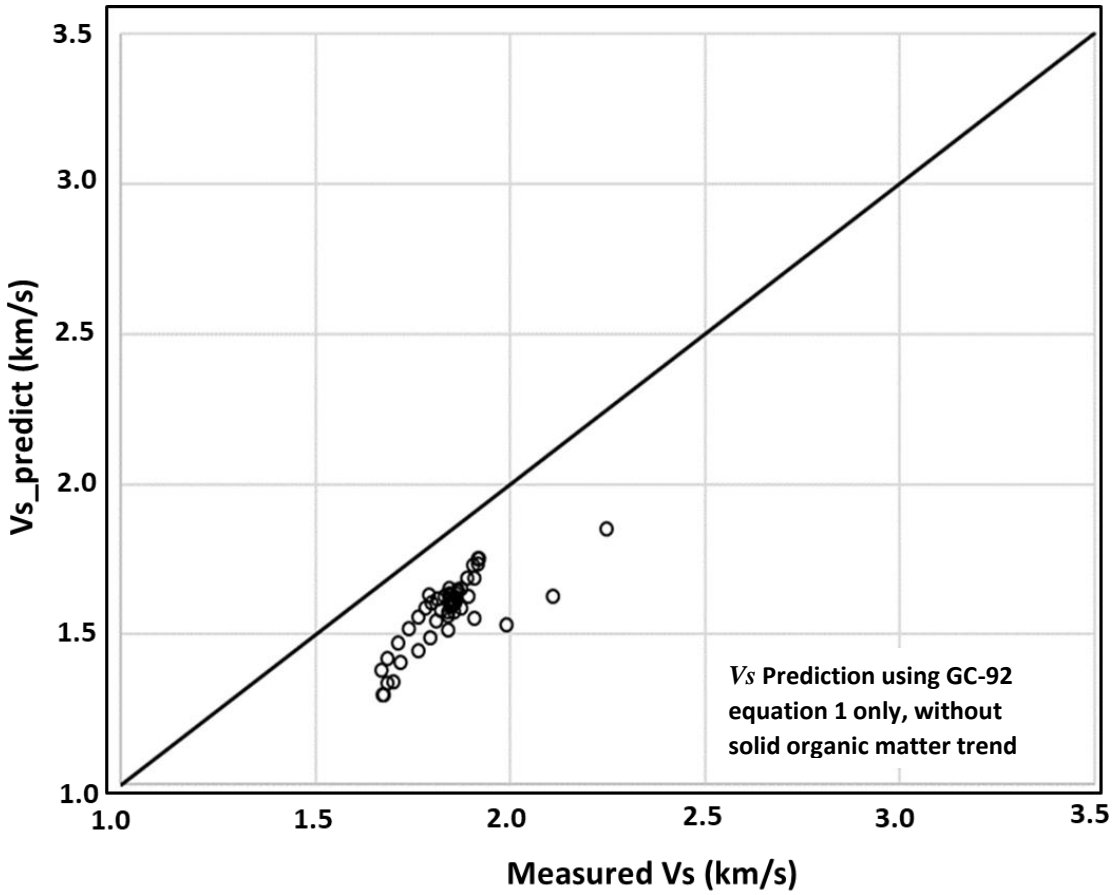


**Figure 3.9b:** Bakken shale. Cross plot of measured shear-wave velocity (x axis) and the shear-wave velocity prediction (y axis) obtained by simply implementing equation 1 of GC-92, i.e. ignoring solid organic matter and fluid effects. The black line is a 1-to-1 line. Percent mean signed error in  $V_s$  prediction is -13.17%, with percent standard error of 13.66%.

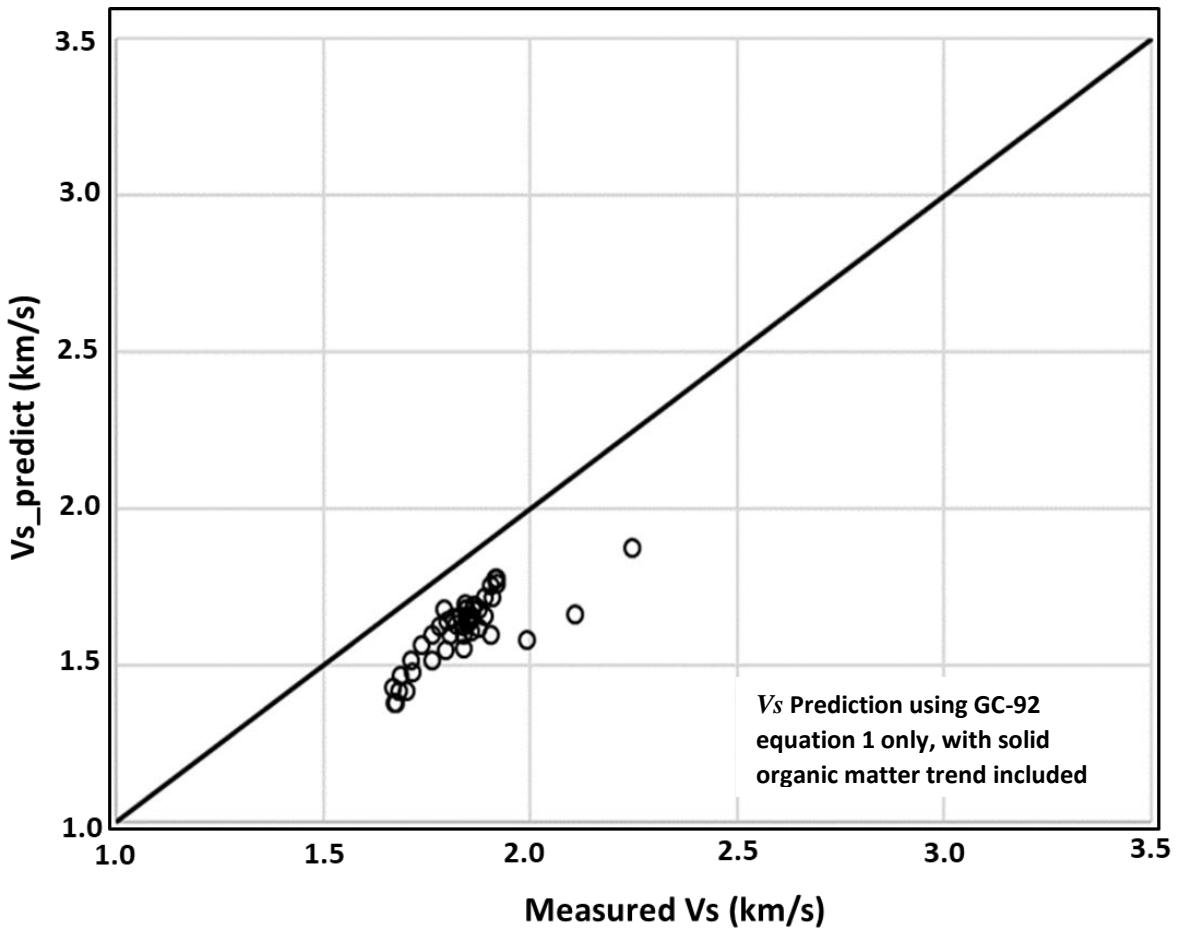


**Figure 3.9c:** Bakken shale. Cross plot of measured shear-wave velocity (x axis) and the shear-wave velocity prediction (y axis) obtained by implementing equation 1 of GC-92, including the trend for solid organic content. The black line is a 1-to-1 line. Percent mean signed error in  $V_s$  prediction is -11.13%, with percent standard error of 11.41%.

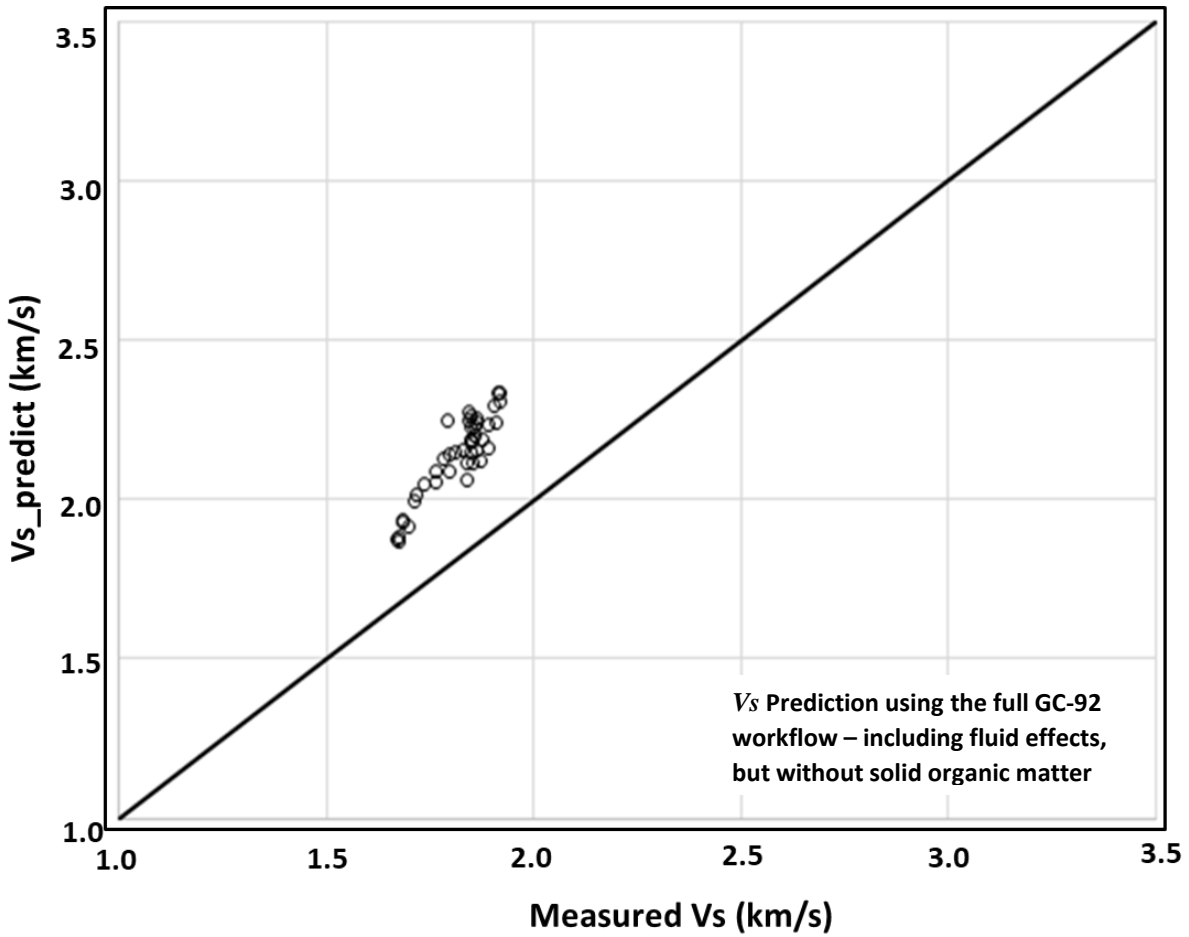


**Figure 3.9d:** Bakken shale. Cross plot of measured shear-wave velocity (x axis) and the shear-wave velocity prediction (y axis) obtained by implementing the full GC-92 workflow without solid organic matter. The black line is a 1-to-1 line. Percent mean signed error in  $V_s$  prediction is 17.71%, with percent standard error of 17.87%.

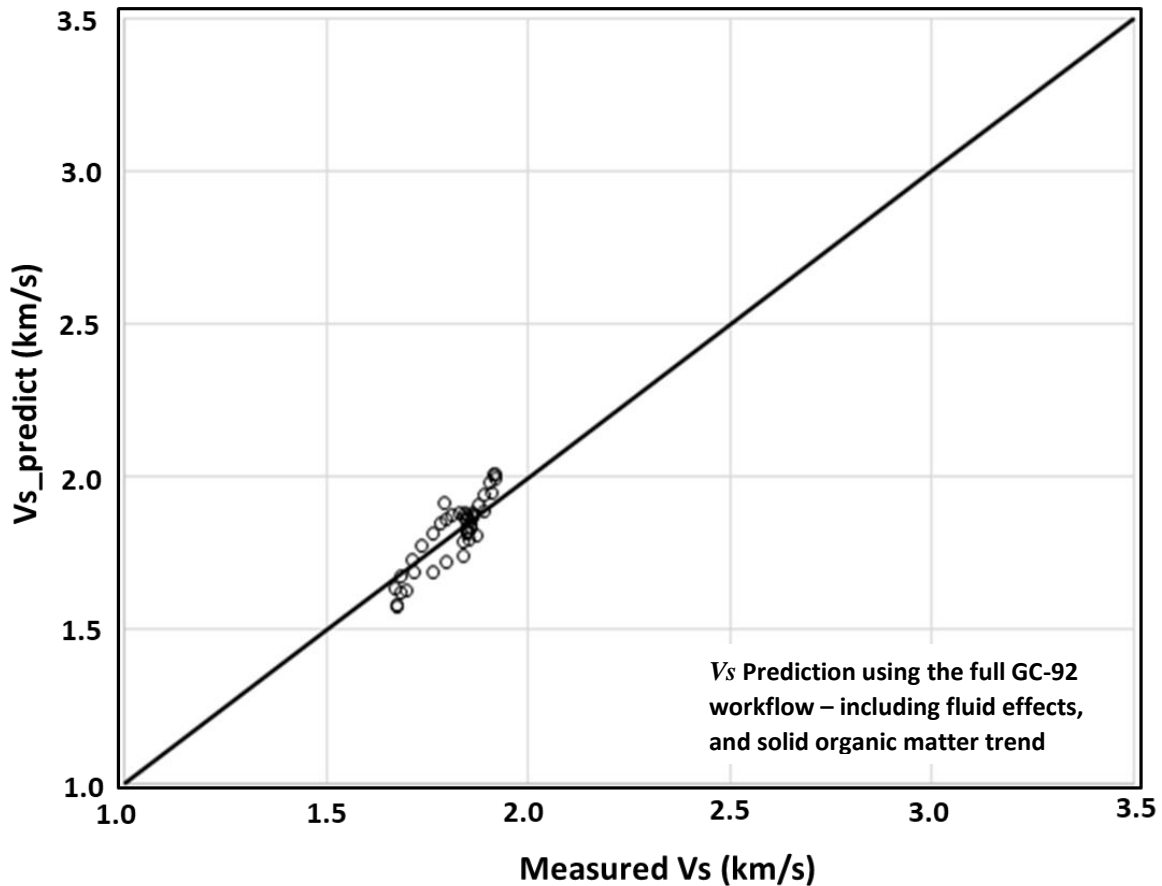


**Figure 3.9e:** Bakken shale. Cross plot of measured shear-wave velocity (x axis) and the shear-wave velocity prediction (y axis) obtained by implementing the full GC-92 workflow including the trend for solid organic matter. The black line is a 1-to-1 line. Percent mean signed error in  $V_s$  prediction is 0.14%, with percent standard error of 3.05%.

### 3.4.7 WOODFORD SHALE:

The Woodford is another late Devonian-age organic-shale play. It has been a prolific hydrocarbon shale play in and around the Anadarko basin. Our data set is however from the Midland basin, where it is an oil shale play. Kerogen volume in the well is between 7.9% and 14.6%, with an average of 10.6%. Average water saturation is 48.1%. The result after the modified workflow is applied has very small percent mean signed error of -0.57% and a percent

standard error of 1.46% (figure 3.10a, on the order of the reliability of the logging devices (for a comparison of repeat  $V_s$  logging runs see Greenberg and Castagna, 1992;). Simply applying GC-92 equation 1 without and with the trend for kerogen both yield percent mean signed error of -8.87% (figures 3.10b and 3.10c). When the original GC-92 workflow is implemented with fluid substitution and ignoring kerogen, percent mean signed error in  $V_s$  prediction is 1.84% and a percent standard error of 1.99% (figure 3.10d). When kerogen is included in the full GC-92 workflow with fluid substitution, the  $V_s$  percent mean signed error is 1.34% with a percent standard error of 1.57% (figure 3.10e). Clearly, fluid substitution is a major factor in achieving accurate predictions in this formation.

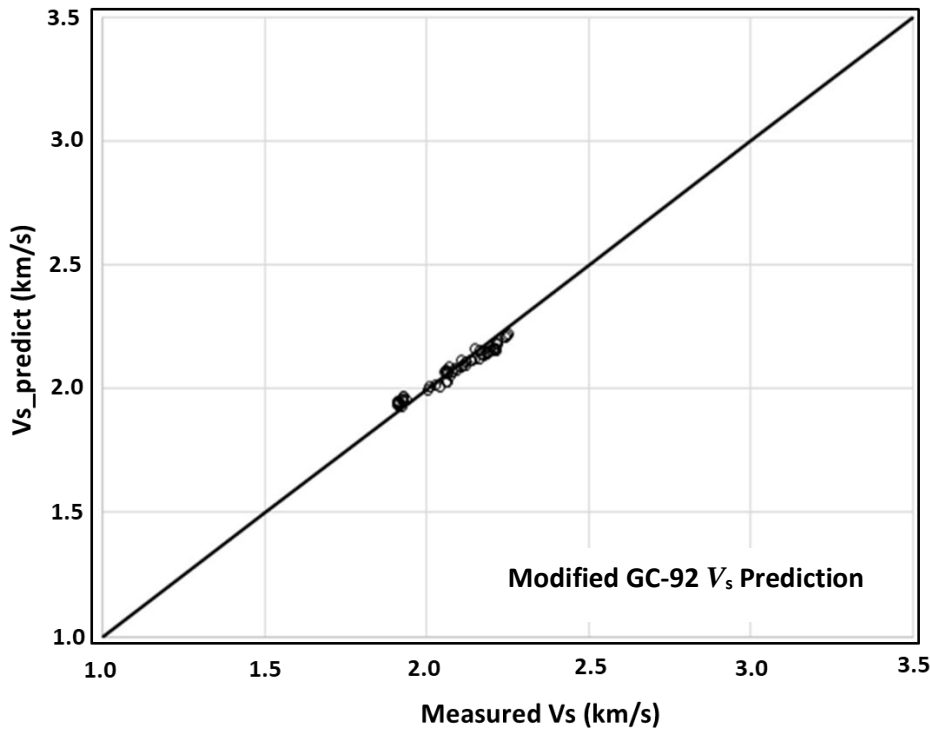


**Figure 3.10a:** Cross plot of measured shear-wave velocity (x axis) and the modified GC shear-wave velocity prediction (y axis) for the Woodford shale. The black line is a 1-to-1 line. Percent mean signed error in  $V_s$  prediction is -0.57%, with percent standard error of 1.46%.

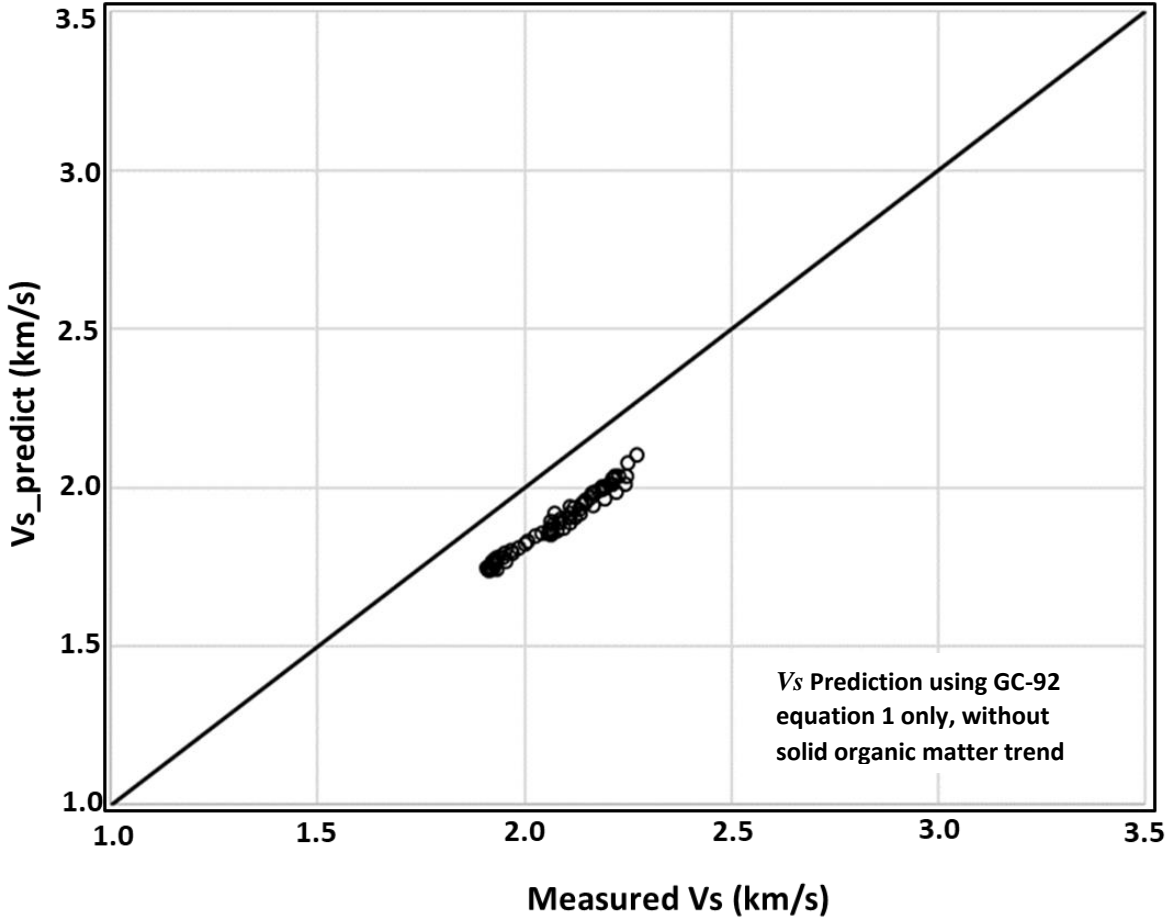


**Figure 3.10b:** Woodford shale. Cross plot of measured shear-wave velocity (x axis) and the shear-wave velocity prediction (y axis) obtained by simply implementing equation 1 of GC-92, i.e. ignoring solid organic matter and fluid effects. The black line is a 1-to-1 line. Percent mean signed error in  $V_s$  prediction is -8.87%, with percent standard error of 8.99%.

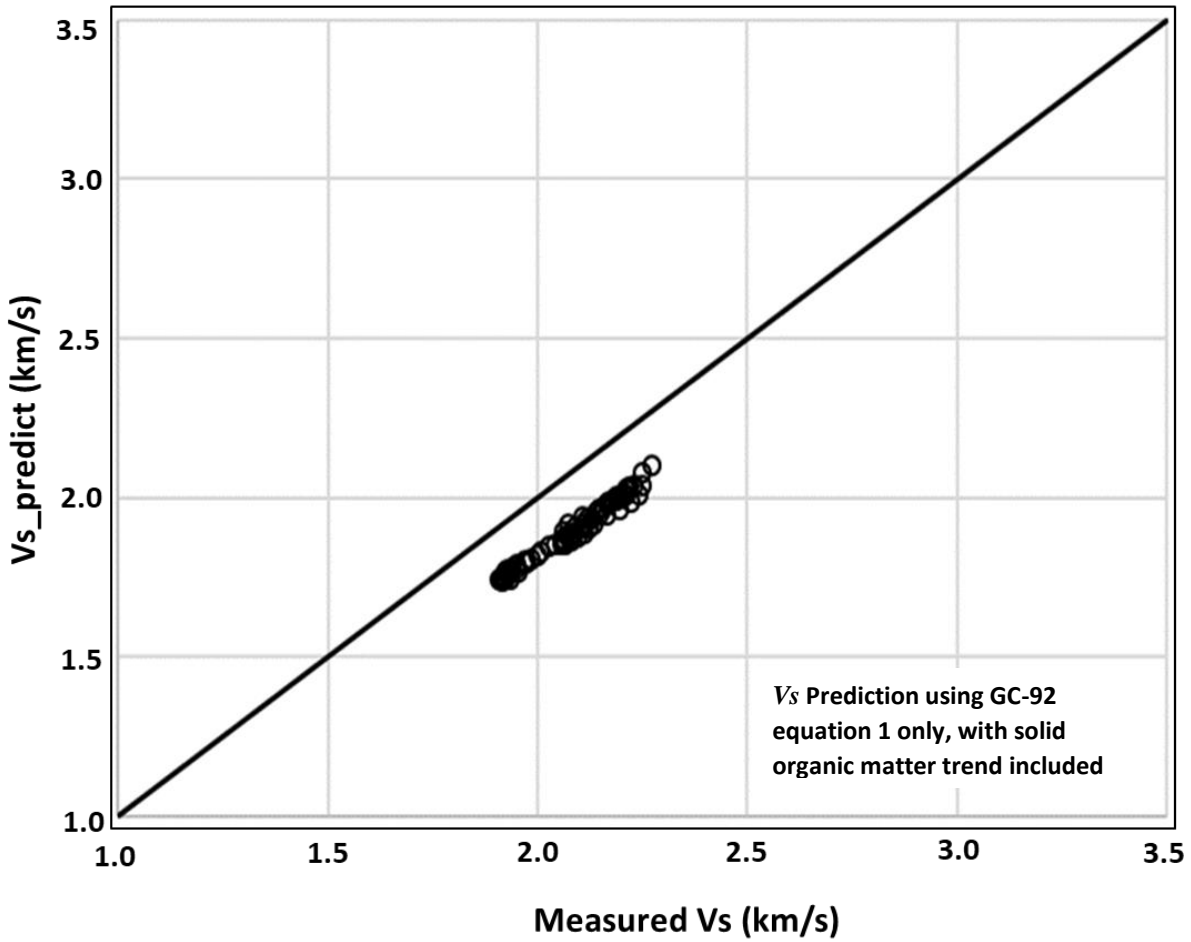


**Figure 3.10c:** Woodford shale. Cross plot of measured shear-wave velocity (x axis) and the shear-wave velocity prediction (y axis) obtained by implementing equation 1 of GC-92, including a regression trend for solid organic content. The black line is a 1-to-1 line. Percent mean signed error in  $V_s$  prediction is -8.87%, with percent standard error of 8.99%.

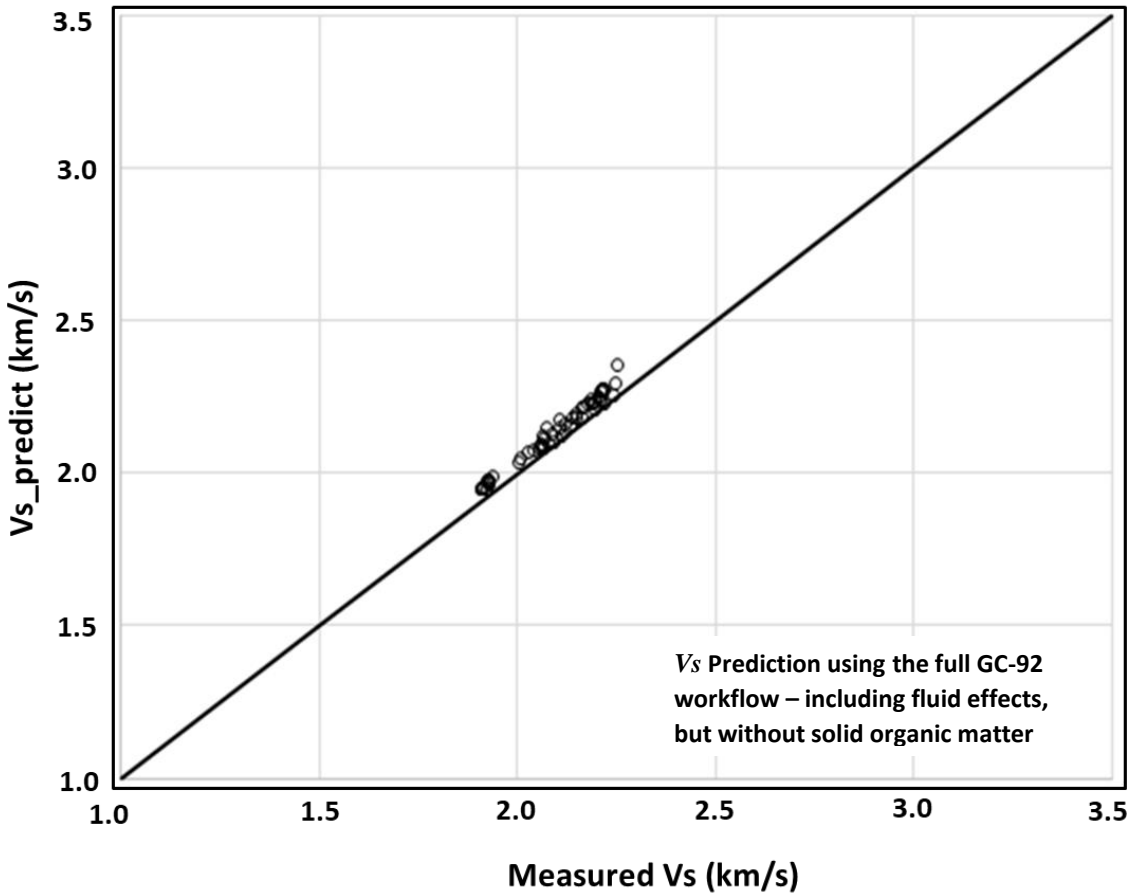


**Figure 3.10d:** Woodford shale. Cross plot of measured shear-wave velocity (x axis) and the shear-wave velocity prediction (y axis) obtained by implementing the full GC-92 workflow without solid organic matter. The black line is a 1-to-1 line. Percent mean signed error in  $V_s$  prediction is 1.84%, with percent standard error of 1.99%.

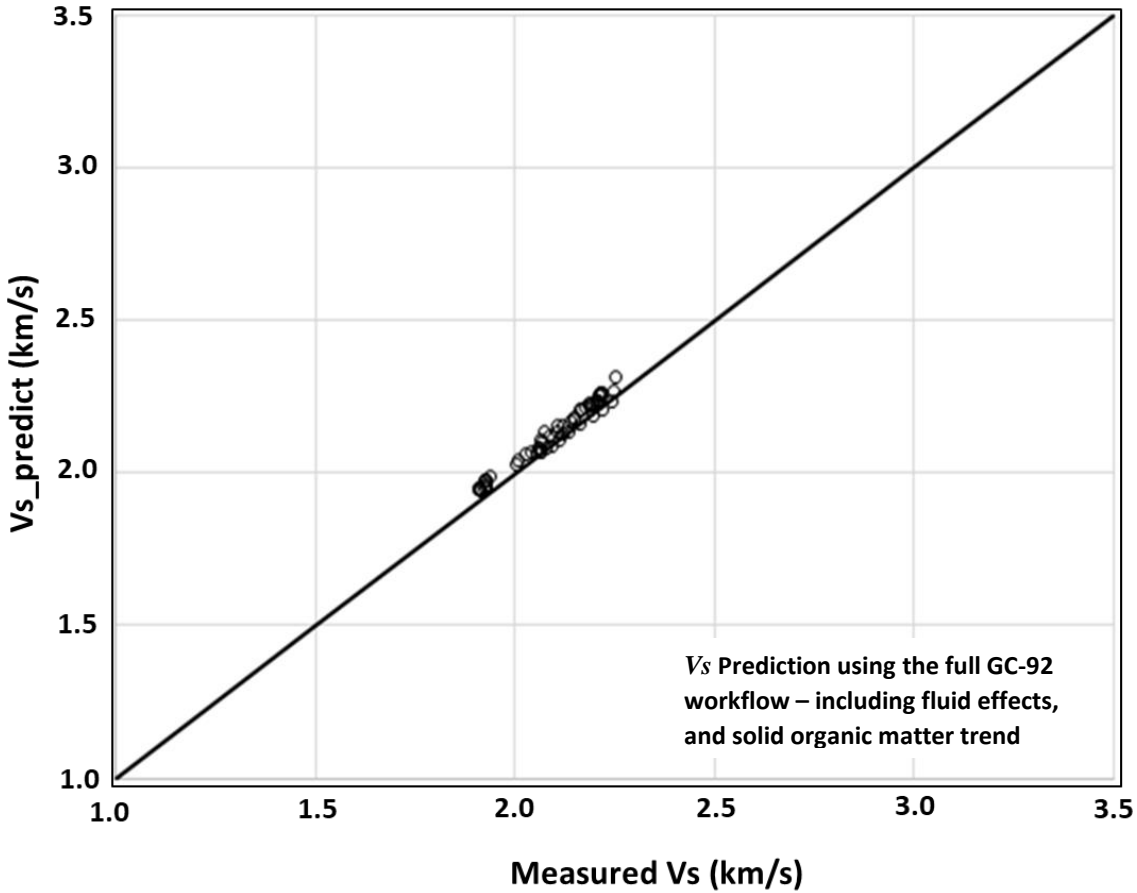


**Figure 3.10e:** Woodford shale. Cross plot of measured shear-wave velocity (x axis) and the shear-wave velocity prediction (y axis) obtained by implementing the full GC-92 workflow including fluid effects and the trend for solid organic matter. The black line is a 1-to-1 line. Percent mean signed error in  $V_s$  prediction is 1.34%, with percent standard error of 1.57%.

### 3.5 COMBINED RESULTS:

Figures 3.11 to 3.13 are the combined results for all 7 organic-shale formations for the following three scenarios: (1) the modified GC workflow, (2) GC-92 with fluid substitution and solid organic matter, and (3) GC-92 with fluid substitution but without solid organic matter. For the modified GC workflow, the combined percent mean signed error in  $V_s$  prediction is -0.21%, with a percent standard error of 2.64% (figure 3.11). The GC-92 workflow with fluid substitution

including the solid organic matter trend has a prediction error of -0.62% and a percent standard error of 3.24% (figure 3.12). The combined percent mean signed error is 1.57% and a percent standard error of 4.21% when GC-92 with fluid substitution but without solid organic matter is implemented (figure 3.13).

The Students t-Test (tables 3.5 and 3.6) falsifies the hypothesis that there is no significant difference in the mean errors between the modified GC workflow and other variations of GC-92 even when including both fluid and kerogen effects. We can conclude that the modified GC-92 method has statistically significant reduced mean and standard error as compared to these other methods.

We also present, in tables 3.7a, 3.7b, 3.7c, 3.7d, 3.7e and 3.7f the mean signed error, percent mean signed error, mean absolute error, percent mean absolute error, standard error and percent standard error respectively. Using the following equations:

$$\text{Mean signed error} = \frac{1}{N} \sum_{i=1}^N (V_{s\_prediction} - V_{s\_measured}), \quad (3.17)$$

$$\text{Mean absolute error} = \frac{1}{N} \sum_{i=1}^N |V_{s\_prediction} - V_{s\_measured}|, \quad (3.18)$$

$$\text{Standard error} = \frac{1}{\sqrt{N}} \sum_{i=1}^N (V_{s\_prediction} - V_{s\_measured})^2, \quad (3.19)$$

$$\text{Percent Mean signed error} = \frac{\text{Mean signed error}}{\text{average}_{V_{s\_measured}}} * 100, \quad (3.20)$$

$$\text{Percent Mean absolute error} = \frac{\text{Mean absolute error}}{\text{average}_{V_{s\_measured}}} * 100, \quad (3.21)$$

$$\text{Percent Standard error} = \frac{\text{Standard error}}{\text{average } V_s \text{ measured}} * 100, \quad (3.22)$$

where  $N$  is the number of observations,  $V_s \text{ prediction}$  is the predicted  $V_s$ , and  $V_s \text{ measured}$  is the measured  $V_s$ .

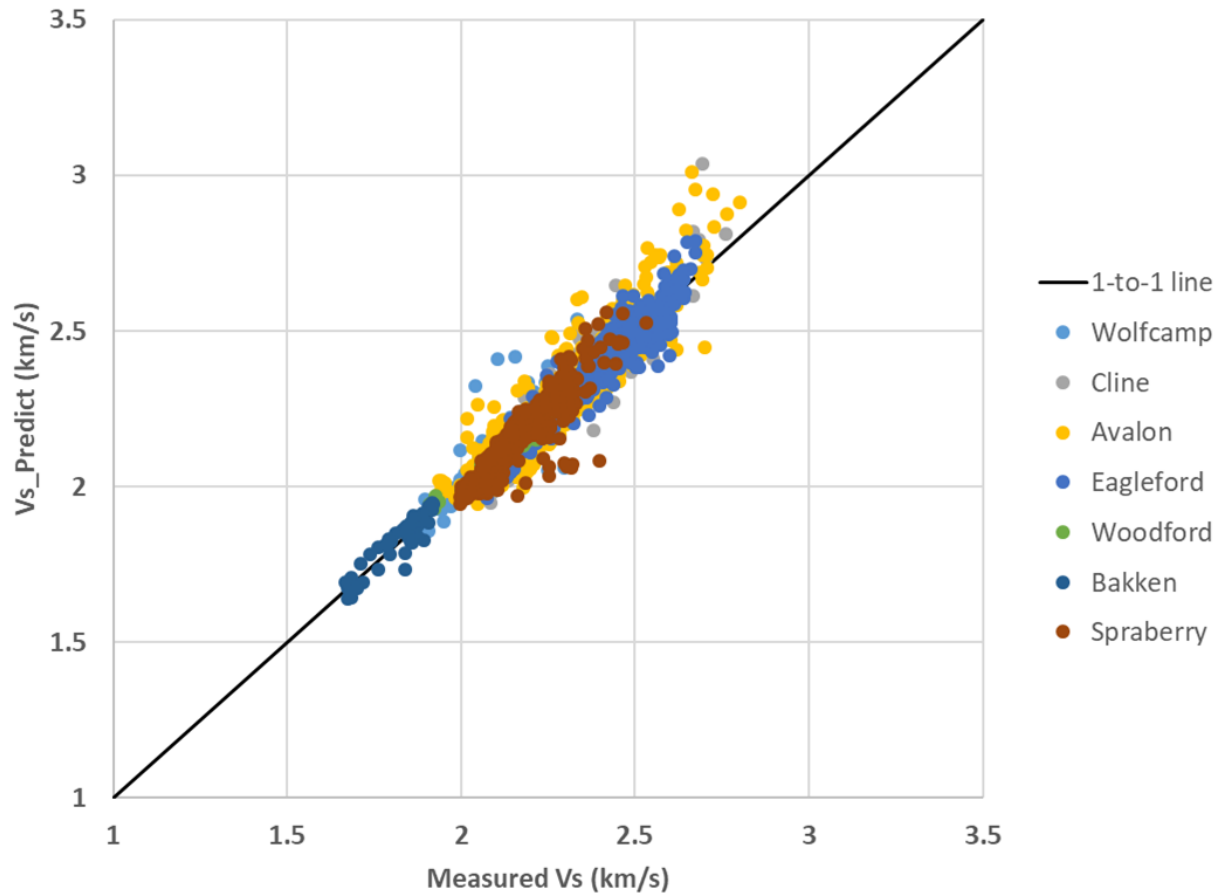


**Figure 3.11:** Cross plot of measured shear-wave velocity (x axis) and the modified GC shear-wave velocity prediction (y axis) for all 7 organic-shale formations. The black line is a 1-to-1 line. Combined percent mean signed error in  $V_s$  prediction is -0.21%, with a percent standard error of 2.64%.

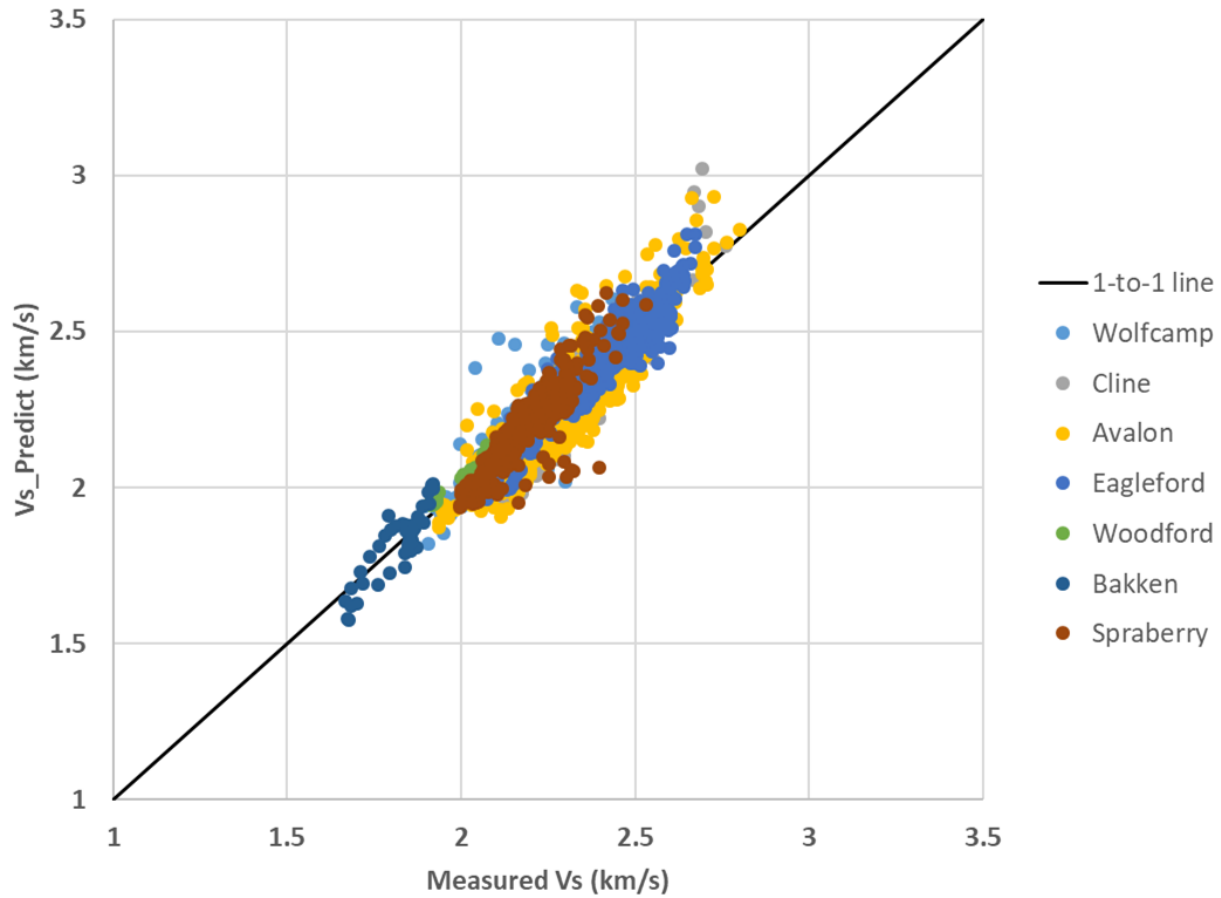


**Figure 3.12:** Cross plot of measured shear-wave velocity (x axis) and the shear-wave velocity prediction (y axis) obtained by implementing the full GC-92 workflow including the trend for solid organic matter for all 7 organic-shale formations. The black line is a 1-to-1 line. Combined percent mean signed error in  $V_s$  prediction is -0.62% and a percent standard error of 3.24%.

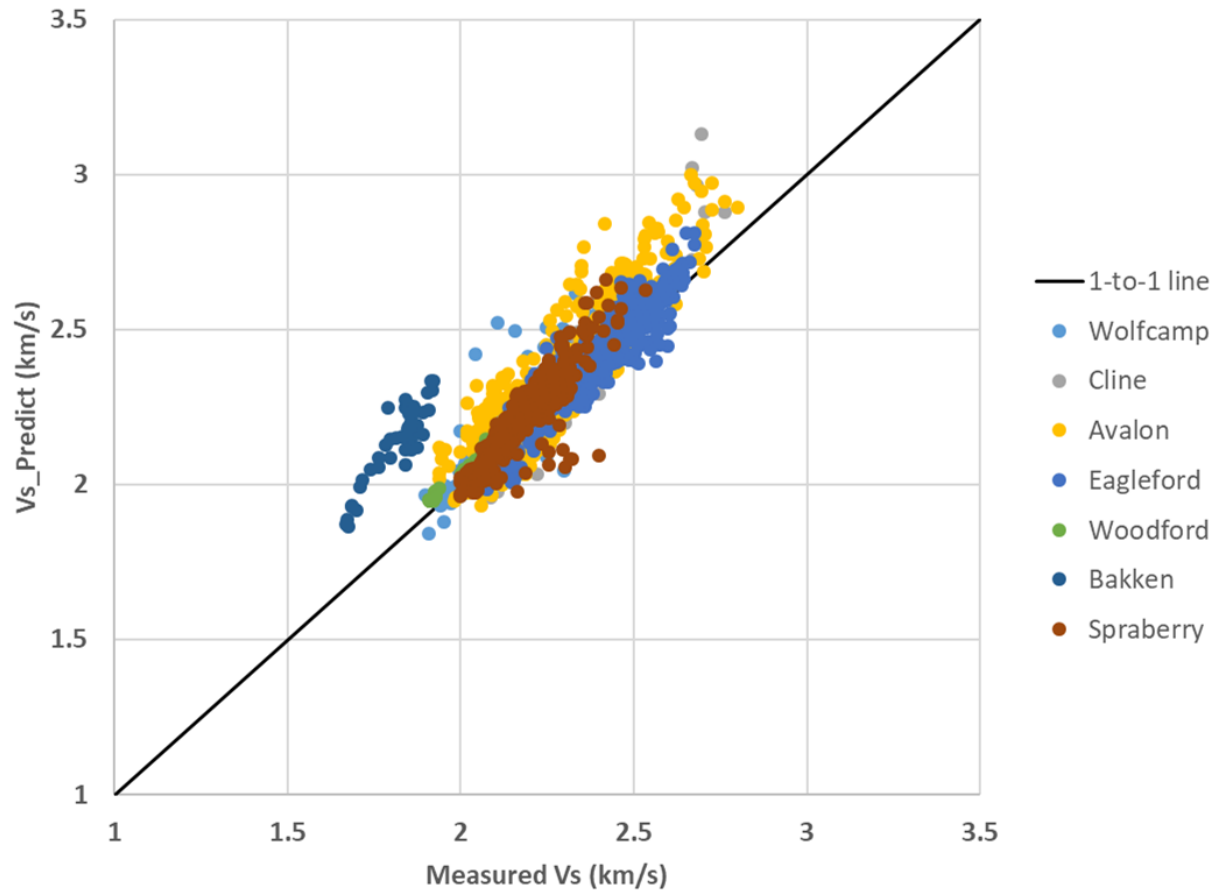


**Figure 3.13:** Cross plot of measured shear-wave velocity (x axis) and the shear-wave velocity prediction (y axis) obtained by implementing the full GC-92 workflow but without the trend for solid organic matter; for all 7 organic-shale formations. The black line is a 1-to-1 line. Combined percent mean signed error in  $V_s$  prediction is 1.57% and a percent standard error of 4.21%.

**Table 3.5a:** All 7 organic shales combined Students t-Test result comparison of the mean signed error in the modified GC-92  $V_s$  prediction (MSE\_GCM) and the mean signed error in the GC-92 prediction without solid organic matter (MSE\_GC92)

	<i>MSE_GC92</i>	<i>MSE_GCM</i>
Mean	0.0354	-0.0048
Variance	0.0077	0.0035
Observations	2160	2160
Hypothesized Mean Difference	0	
df	3788	
t Stat	17.6095	
P(T<=t) one-tail	4.45538E-67	
t Critical one-tail	1.6453	
P(T<=t) two-tail	8.91076E-67	
t Critical two-tail	1.9606	
<b>  t Stat   &gt; t critical; there is a significant difference between the means</b>		

**Table 3.5b:** All 7 organic shales combined Students t-Test result comparison of the mean signed error in the modified  $V_s$  prediction (MSE\_GCM) and the mean signed error of the GC-92 prediction with solid organic matter (MSE\_GC92K)

	<i>MSE_GC92K</i>	<i>MSE_GCM</i>
Mean	-0.0139	-0.0048
Variance	0.0051	0.0035
Observations	2160	2160
Hypothesized Mean Difference	0	
df	4172	
t Stat	-4.5506	
P(T<=t) one-tail	2.75129E-06	
t Critical one-tail	1.6452	
P(T<=t) two-tail	5.50258E-06	
t Critical two-tail	1.9605	
<b>  t Stat   &gt; t critical; there is a significant difference between the means</b>		

**Table 3.6a:** All 7 organic shales combined Students t-Test result comparison of the mean absolute error in the modified GC  $V_s$  prediction (MAbsE\_GCM) and the mean absolute error in the GC-92 prediction without solid organic matter (MAbsE\_GC92)

	<i>MAbsE_GC92</i>	<i>MAbsE_GCM</i>
Mean	0.0658	0.0430
Variance	0.0047	0.0017
Observations	2160	2160
Hypothesized Mean Difference	0	
df	3550	
t Stat	13.3048	
P(T<=t) one-tail	9.40884E-40	
t Critical one-tail	1.6453	
P(T<=t) two-tail	1.88177E-39	
t Critical two-tail	1.9606	
<b>  t Stat   &gt; t critical; there is a significant difference between the means</b>		

**Table 3.6b:** All 7 organic shales combined Students t-Test result comparison of the mean absolute error in the modified GC  $V_s$  prediction (MAbsE\_GCM) and the mean absolute error in the GC-92 prediction with solid organic matter (MAbsE\_GC92K)

	<i>MAbsE_GC92K</i>	<i>MAbsE_GCM</i>
Mean	0.0542	0.0430
Variance	0.0024	0.0017
Observations	2160	2160
Hypothesized Mean Difference	0	
df	4196	
t Stat	8.1720	
P(T<=t) one-tail	1.989E-16	
t Critical one-tail	1.6452	
P(T<=t) two-tail	3.97801E-16	
t Critical two-tail	1.9605	
<b>  t Stat   &gt; t critical; there is a significant difference between the means</b>		

**Table 3.7a:** Mean signed error in  $V_s$  prediction for the 7 organic shales for all 5 prediction methods, in km/s.

Shale Fm	MSE_GC92Eqn1	MSE_GC92KEqn1	MSE_GC92	MSE_GC92K	MSE_GCM
Wolfcamp	-0.075	-0.072	0.054	0.076	0.012
Lower Cline	-0.169	-0.163	0.010	-0.058	-0.011
Avalon	-0.216	-0.211	0.055	-0.045	-0.005
Eagleford	-0.155	-0.150	0.009	-0.005	-0.007
Woodford	-0.185	-0.185	0.038	0.028	-0.012
Bakken	-0.239	-0.202	0.322	0.003	0.003
Spraberry	-0.095	-0.089	0.030	0.000	-0.009
<b>Combined</b>	<b>-0.150</b>	<b>-0.144</b>	<b>0.035</b>	<b>-0.014</b>	<b>-0.005</b>

**Note:** Where MSE is mean signed error. GC92Eqn1 is  $V_s$  prediction using GC-92 equation 1 only. GC92KEqn1 is  $V_s$  prediction using GC-92 equation 1 only but with kerogen trend included. GC92 is the full GC-92 workflow without kerogen trend. GC92K is the full GC-92 workflow with kerogen trend included. And GCM is the modified GC workflow.

**Table 3.7b:** Percent mean signed error in  $V_s$  prediction for the 7 organic shales for all 5 prediction methods.

Shale Fm	%MSE_GC92Eqn1	%MSE_GC92KEqn1	%MSE_GC92	%MSE_GC92K	%MSE_GCM
Wolfcamp	-3.502	-3.334	2.529	3.532	0.579
Lower Cline	-7.464	-7.200	0.443	-2.589	-0.493
Avalon	-9.397	-9.182	2.408	-1.939	-0.239
Eagleford	-6.477	-6.283	0.363	-0.194	-0.314
Woodford	-8.870	-8.870	1.841	1.344	-0.567
Bakken	-13.169	-11.137	17.709	0.140	0.172
Spraberry	-4.413	-4.106	1.411	0.015	-0.407
<b>Combined</b>	<b>-6.638</b>	<b>-6.390</b>	<b>1.571</b>	<b>-0.619</b>	<b>-0.214</b>

**Note:** Where %MSE is percent mean signed error. GC92Eqn1 is  $V_s$  prediction using GC-92 equation 1 only. GC92KEqn1 is  $V_s$  prediction using GC-92 equation 1 only but with kerogen trend included. GC92 is the full GC-92 workflow without kerogen trend. GC92K is the full GC-92 workflow with kerogen trend included. And GCM is the modified GC workflow.

**Table 3.7c:** Mean absolute error in  $V_s$  prediction for the 7 organic shales for all 5 prediction methods, in km/s.

Shale Fm	MAbsE_GC92Eqn1	MAbsE_GC92KEqn1	MAbsE_GC92	MAbsE_GC92K	MAbsE_GCM
Wolfcamp	0.085	0.082	0.062	0.044	0.034
Lower Cline	0.176	0.170	0.069	0.080	0.054
Avalon	0.224	0.218	0.091	0.081	0.063
Eagleford	0.155	0.150	0.045	0.042	0.038
Woodford	0.189	0.189	0.038	0.029	0.027
Bakken	0.245	0.202	0.322	0.047	0.029
Spraberry	0.097	0.095	0.048	0.038	0.031
<b>Combined</b>	<b>0.154</b>	<b>0.149</b>	<b>0.066</b>	<b>0.054</b>	<b>0.043</b>

**Note:** Where MAbsE is mean absolute error. GC92Eqn1 is  $V_s$  prediction using GC-92 equation 1 only. GC92KEqn1 is  $V_s$  prediction using GC-92 equation 1 only but with kerogen trend included. GC92 is the full GC-92 workflow without kerogen trend. GC92K is the full GC-92 workflow with kerogen trend included. And GCM is the modified GC workflow.

**Table 3.7d:** Percent mean absolute error in  $V_s$  prediction for the 7 organic shales for all 5 prediction methods.

Shale Fm	%MAbsE_GC92Eqn1	%MAbsE_GC92KEqn1	%MAbsE_GC92	%MAbsE_GC92K	%MAbsE_GCM
Wolfcamp	3.957	3.782	2.887	2.035	1.597
Lower Cline	7.802	7.532	3.056	3.523	2.380
Avalon	9.758	9.480	3.962	3.522	2.741
Eagleford	6.493	6.299	1.883	1.759	1.573
Woodford	9.021	9.021	1.841	1.407	1.295
Bakken	13.475	11.137	17.709	2.600	1.569
Spraberry	4.502	4.405	2.227	1.755	1.448
<b>Combined</b>	<b>6.841</b>	<b>6.612</b>	<b>2.921</b>	<b>2.407</b>	<b>1.908</b>

**Note:** Where %MAbsE is percent mean absolute error. GC92Eqn1 is  $V_s$  prediction using GC-92 equation 1 only. GC92KEqn1 is  $V_s$  prediction using GC-92 equation 1 only but with kerogen trend included. GC92 is the full GC-92 workflow without kerogen trend. GC92K is the full GC-92 workflow with kerogen trend included. And GCM is the modified GC workflow.

**Table 3.7e:** Standard error in  $V_s$  prediction for the 7 organic shales for all 5 prediction methods, in km/s.

Shale Fm	StdError_GC92Eqn1	StdError_GC92KEqn1	StdError_GC92	StdError_GC92K	StdError_GCM
Wolfcamp	0.104	0.100	0.084	0.066	0.052
Lower Cline	0.203	0.197	0.121	0.097	0.069
Avalon	0.242	0.234	0.118	0.097	0.080
Eagleford	0.164	0.159	0.058	0.053	0.048
Woodford	0.188	0.188	0.042	0.033	0.030
Bakken	0.248	0.207	0.325	0.055	0.033
Spraberry	0.108	0.110	0.067	0.058	0.049
<b>Combined</b>	<b>0.177</b>	<b>0.171</b>	<b>0.095</b>	<b>0.073</b>	<b>0.060</b>

**Note:** Where StdError is Standard error. GC92Eqn1 is  $V_s$  prediction using GC-92 equation 1 only. GC92KEqn1 is  $V_s$  prediction using GC-92 equation 1 only but with kerogen trend included. GC92 is the full GC-92 workflow without kerogen trend. GC92K is the full GC-92 workflow with kerogen trend included. And GCM is the modified GC workflow.

**Table 3.7f:** Percent standard error in  $V_s$  prediction for the 7 organic shales for all 5 prediction methods.

Shale Fm	%StdError_GC92Eqn1	%StdError_GC92KEqn1	%StdError_GC92	%StdError_GC92K	%StdError_GCM
Wolfcamp	4.805	4.634	3.920	3.041	2.399
Lower Cline	9.012	8.726	5.360	4.303	3.078
Avalon	10.510	10.176	5.134	4.211	3.485
Eagleford	6.867	6.668	2.410	2.234	2.007
Woodford	8.993	8.993	1.989	1.571	1.459
Bakken	13.665	11.407	17.865	3.048	1.842
Spraberry	4.991	5.077	3.083	2.661	2.261
<b>Combined</b>	<b>7.865</b>	<b>7.601</b>	<b>4.207</b>	<b>3.244</b>	<b>2.643</b>

**Note:** Where %StdError is percent standard error. GC92Eqn1 is  $V_s$  prediction using GC-92 equation 1 only. GC92KEqn1 is  $V_s$  prediction using GC-92 equation 1 only but with kerogen trend included. GC92 is the full GC-92 workflow without kerogen trend. GC92K is the full GC-92 workflow with kerogen trend included. And GCM is the modified GC workflow.

### 3.6 DISCUSSION

By definition, our error computations assume perfect velocity measurements. As very low errors are approached, we must remember that the precision of the logging instruments is being approached and differences between the prediction and the measurement are not necessarily error. In fact, Greenberg and Castagna (1992) made the argument in one case that

their shear-wave velocity predictions were in fact superior to the measurements in thin layers as the discrepancy decreased with the semblance of the measurement which was poor in those thin layers. We also cannot attribute all of the error to the modified GC-92 workflow, as computed rock mineral and fluid fractions also contain error. Given these limitations, it would be unlikely that better predictions could be achieved with typical data quality. Also, our results were obtained without local optimization of some properties such as the  $V_p - V_s$  trends, solid organic matter bulk modulus and density, and the weighting factor between Reuss and Voigt bounds. When working in a specific locality, it is possible that even smaller prediction error could be achieved with local calibration; data quality permitting. For geophysical and engineering applications, the accuracy (as measured by mean signed error) is more important than precision if the predictions are unbiased and precision errors cancel to a large extent on vertical averaging. The very low mean signed errors that we have achieved suggest that the predictions are good enough for many applications.

The precision and accuracy achieved by the modified GC-92 is at least as good as the Vernik et al., (2018) results with mean absolute error within 3%. The fact that the method works for a variety of reservoirs and fluid types without local adjustment is a significant strength.

Omovie and Castagna (2019) have shown that the lower velocity ratio observed in organic shales is best explained by the presence of free hydrocarbons. This suggests that explicit consideration of fluid type should be useful in predicting velocities. The fact that explicit

consideration of the fluid substitution effect results in improved predictions further supports the Omovie and Castagna (2019) conclusion.

Omovie and Castagna (2019) also showed that the effect of kerogen on acoustic velocity measurements is to lower both the compressional-wave and shear-wave velocities. Thus, the effect of ignoring kerogen volume and fluid effects in shear-wave velocity prediction that relies on compressional-wave velocity and lithology constituents will always yield a shear-wave velocity prediction that is lower than the true or measured shear-wave velocity. This is because the measured compressional-wave velocity already incorporates kerogen or organic volume constituents; ignoring this softer component in shear-wave velocity prediction will thus make the predicted shear-wave velocity slower than the true shear-wave velocity for the rock. In organic-shale formations with small to negligible organic content, the above described effect may be negligible. But when kerogen volume is significant, ignoring solid organic volume will result in inaccurate shear-wave velocity prediction. This can be seen in the Avalon shale example shown in Figure 3.5a. The Greenberg and Castagna (1992)  $V_s$  prediction using equation 1 without consideration of solid organic volume or hydrocarbon effects is the green curve in the 'GC without TOC' track. Note that when kerogen volume is significant (kerogen volume is black shading in the lithology track), the  $V_s$  prediction is always lower than the measured shear-wave velocity. Percent mean signed error in  $V_s$  prediction using Greenberg-Castagna equation 1, ignoring both solid organic matter and fluid effects is -9.4%. This is the same effect observed in Figure 3.5c for the Avalon shale. Note that the predicted  $V_s$  in figure 3.5c is below the 1-to-1 line when solid organic matter volume fraction is ignored (a similar effect was observed for the

other organic-shale formations with appreciable solid organic matter content, see figure 3.9b for the Bakken or figure 3.10b for the Woodford shale). The effect, while noticeable, is not as significant in formations with low kerogen content (see figure 3.6c for example for the Spraberry shale).

However, the opposite effect is observed when GC-92 is applied including fluid effects but ignoring solid organic matter. In this case, GC-92 overestimates  $V_s$ . This is clearly seen in the Bakken shale example shown in Figure 3.9d. Percent mean signed error in the  $V_s$  prediction shown in Figure 3.9d is 17.7% with the predicted  $V_s$  significantly above the 1-to-1 line. The reason for this overestimation is explained in Omovie and Castagna (2019) - the strong correlation that exists between water saturation and kerogen volume. As a result, the slack variable in GC-92 is essentially also attempting to correct for the presence of kerogen or solid organic matter. But, in the  $V_s$  prediction step, this softer component (solid organic matter) is not included. For organic shales with high solid organic matter content, this overestimation of  $V_s$  could potentially be used to estimate kerogen volume, or validate other kerogen volume estimation methods, when measured  $V_s$  is available. For example, in figure 3.14 note the strong correlation between kerogen volume and the difference between the full GC-92 workflow with fluid substitution but without solid organic matter trend  $V_s$  prediction and measured  $V_s$ . When shear-wave logs are available, this could be a means of computing, or otherwise validating, computed TOC logs.

In addition, we find that for organic shales with low solid organic matter content, GC-92 including fluid substitution yields fairly accurate  $V_s$  predictions. With the exception of the

Avalon, Bakken and Clines shales; percent standard error in  $V_s$  prediction for the other 4 organic-shale formations is less than 4% as shown in table 3.5f.

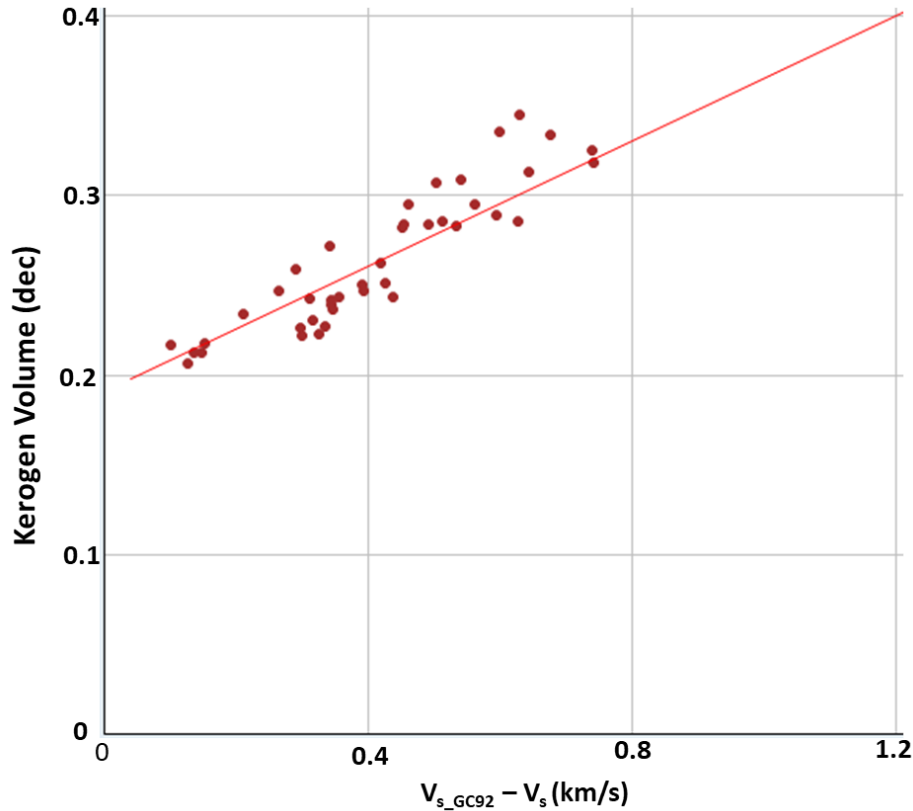


**Figure 3.14:** Cross plot of kerogen volume versus the difference between the full GC-92 shear-wave velocity prediction with fluid substitution but no solid organic matter trend ( $V_{s\_GC92}$ ) and measured shear-wave velocity ( $V_{s\_measured}$ ) for the Bakken shale. The trend is:  $X_{Kerogen} = 0.178 + 0.21*(V_{s\_GC92} - V_{s\_measured})$ , with  $R^2$  of 0.83, where  $X_{Kerogen}$  is the decimal volume fraction of solid organic matter.

**Table 3.8:** Regression statistics for the cross plot in Figure 14 using a linear equation:  $X_{Kerogen} = a*(V_{s\_GC92} - V_{s\_measured}) + b$ .  $R^2$  is the correlation coefficient squared and an indication of the variance in the data accounted for by the regression trend. The high  $F$ -statistic and low *significance of  $F$*  indicate that the regression is statistically significant.

<b><i>b</i></b>	<b><i>Standard error b</i></b>	<b><i>a</i></b>	<b><i>Standard error a</i></b>	<b><math>R^2</math></b>	<b><i>F</i></b>	<b><i>Significance F</i></b>
<b>0.178088</b>	<b>0.006736</b>	<b>0.209747</b>	<b>0.015186</b>	<b>0.830265</b>	<b>190.7704</b>	<b>1.32557E-16</b>

### 3.7 CONCLUSION

We have resolved the limitation of the Greenberg and Castagna (1992) shear-wave velocity prediction method, when applied to organic-rich shale rocks, by making a modification to the original Greenberg-Castagna algorithm: (1) including a compressional-to-shear-wave velocity trend for solid organic matter in the original Greenberg-Castagna workflow; and, (2) computing a non-kerogen compressional wave velocity from a weighted Reuss-Voigt bound mixture of kerogen with a hypothetical shale with the same mineralogical composition and porosity, but no organic matter, and its difference from the measured compressional wave velocity. The modified original Greenberg-Castagna method accurately (to within  $\pm 1\%$ ) predicts shear-wave velocity for organic-shale formations with appreciable TOC, significantly reducing the error when organic matter is ignored in the original Greenberg-Castagna method. For example, in the Bakken shale dataset percent mean signed error from measured shear-wave velocity was reduced from 17.7% to 0.17% (percent standard error was reduced from 17.86% to 1.84%).

Even in organic shales with relatively low kerogen content, we observe significant improvement in shear-wave velocity prediction accuracy when the modified workflow is applied. For example, in the lower Spraberry shale with average kerogen volume of 4.83%, percent mean signed error in  $V_s$  prediction after the application of the modified workflow was - 0.41%, compared to 1.41% with the application of the original GC-92 method with fluid substitution (percent standard error was reduced from 3.1% to 2.26%). For all 7 organic shales combined, percent mean signed error in  $V_s$  prediction using the modified GC workflow is -

0.21%; compared to 1.57% using the original Greenberg-Castagna workflow without kerogen but with fluid substitution (percent standard error was reduced from 4.2% to 2.6%). This improvement is statistically significant as evidenced by Students t-tests. Explicit consideration of both fluid substitution effects and solid organic matter in this formulation was necessary to achieve this degree of prediction accuracy and precision.

## Chapter 4

# ACOUSTIC DISPERSION IN LOW PERMEABILITY UNCONVENTIONAL RESERVOIR ROCKS AND SHALES AT *IN SITU* STRESS CONDITIONS

### 4.1 INTRODUCTION

Acoustic-wave dispersion is observed in fluid-saturated porous and permeable sedimentary rocks (e.g, Wang and Nur, 1990; Dvorkin et al., 1995; Spencer, 1981; Hoffman, 2005). Wang and Nur (1990) for example reported dispersion in rocks saturated with low viscosity fluids as high as 5%. Sams et al., (1997) observed a similar effect when measurements were made at seismic, sonic and ultrasonic frequencies. Similar dispersion magnitude has been reported for laboratory measurements made over a wide range of frequencies (Spencer, 1981). The question then arises as to the significance of dispersion in low-permeability unconventional reservoir rocks and shale formations. With the increased interest in development of unconventional reservoir rocks, it is necessary to address whether dispersion correction is necessary when comparing acoustic measurements made at different frequencies. For example, can ultrasonic laboratory measurement made on core samples be directly compared to sonic log measurements without first applying dispersion correction? For the Bakken shale formation, based on theoretical predictions using Biot (1956) and squirt-flow models (Dvorkin et al., 1995), Liu et al., (1994) concluded that seismic, sonic and ultrasonic frequencies are in the same frequency regime; if true, intrinsic dispersion correction is unnecessary. Sarker and Batzle (2010) and Hofmann (2005) based on experimental observations in the 2Hz to 0.8MHz

frequency range also did not observe significant dispersion in Mancos Shale and a West African shale, both having low porosity. On the other hand, Szewczyk et al., (2017) observed significant dispersion based on laboratory measurements on Mancos and Pierre shale core samples from outcrop. Hofmann (2005) also observed significant dispersion on a West Africa shale sample with high porosity.

We perform calculations based on Biot flow and squirt flow; then, compare them to measurements made both in the laboratory at ultrasonic frequencies (~1MHz) and in the field at sonic frequencies (10-30 KHz). Our focus is to determine if dispersion effects occur at *in situ* stress conditions. Our method is similar to the approach adopted by Wang and Nur (1990) and Winkler (1985). The initial assumption is that there is virtually no velocity dispersion in dry rocks consistent with Spencer (1981) and Peselnick and Outerbridge (1961). Using this approach, we are trying to answer the following three questions:

1. Does the low frequency Gassmann equation adequately predict the change that will result if a rock sample containing gas were fully saturated with brine?
2. Do we observe dispersion in these rocks when we compare ultrasonic measurements made in the laboratory to sonic log measurements made in the field?
3. Does the Biot-Gassmann or the squirt-flow model accurately predict the presence or absence of dispersion in these low-permeability formations at the frequency range used in the petroleum industry?

We address these questions for 4 different unconventional reservoir rock/shale formations.

## 4.2 THEORY

### 4.2.1 BIOT-GASSMANN MODEL:

The Biot-Gassmann model does not predict dispersion in dry rock samples. As discussed, this is evident from the work done by Spencer (1981). Spencer measured acoustic-wave velocities in the laboratory from 4-400Hz on sandstone, limestone and granite rock samples. He found that there is negligible dispersion in the dry samples independent of lithology, while fluid-saturated samples show significant dispersion. Peselnick and Outerbridge (1961) also observed negligible dispersion in dry rocks over a much wider frequency range. Winkler (1985) compared laboratory-measured dry and saturated velocities to investigate dispersion in Berea sandstone and observed significant dispersion. These investigations which show dispersion are all in more porous and permeable samples than investigated here.

Given acoustic measurements made on a dry sample, we determine the frame bulk and shear moduli. The mineral matrix modulus is determined using the Voigt-Reuss-Hill average of the constituents' lithologies matrix modulus. The Hill average is known to yield fairly accurate effective elastic moduli when the bounds are narrow, which occurs when the elastic properties of constituent minerals do not differ significantly (Wang et al., 2001; Jaeger et al., 2007). The Hill average is:

$$K_m = 0.5(\{\sum_{i=0}^L X_i K_i\} + \{\sum_{i=0}^L X_i / K_i\}^{-1}) \quad (4.1)$$

where  $K_m$  is the matrix bulk modulus,  $L$  is the number of pure mineral components making up the solid fraction,  $X_i$  is the fraction of solid volume occupied by mineral component  $i$ , and  $K_i$  is the bulk modulus of pure mineral component  $i$ .

The Gassmann fluid-saturated zero-frequency equation is:

$$K_c = K_{fr} + \frac{\left(1 - \frac{K_{fr}}{K_m}\right)^2}{\Omega - \frac{K_{fr}}{K_m^2}}, \quad (4.2)$$

$$\text{where } \Omega = \frac{\phi_t}{K_f} + \frac{(1-\phi_t)}{K_m}$$

and where  $K_{fr}$  is frame bulk modulus,  $\phi_t$  is total porosity, and  $K_f$  is fluid bulk modulus. From equation 4.2, the fluid-saturated low-frequency P-wave velocity can be determined given the rock bulk density and shear modulus.

For the Biot high-frequency limit prediction, we use the Geerstma and Smit (1961)

approximation, the high-frequency limit P-wave velocity ( $V_{P\infty}$ ) is given by:

$$V_{P\infty} = \left\{ \frac{1}{\rho_m(1-\phi_t) + \phi_t \rho_{fl}(1-\alpha^{-1})} \left[ \left( K_{fr} + \frac{4}{3} G_{fr} \right) + \frac{\phi_t \frac{\rho}{\rho_{fl}} \alpha^{-1} + \left(1 - \frac{K_{fr}}{K_m}\right) \left(1 - \frac{K_{fr}}{K_m} - 2\phi_t \alpha^{-1}\right)}{\left(1 - \frac{K_{fr}}{K_m} - \phi_t\right) \frac{1}{K_m} + \frac{\phi_t}{K_{fl}}} \right] \right\}^{1/2}, \quad (4.3)$$

where  $V_{P\infty}$  is the Biot high-frequency P-wave velocity,  $\rho_m$  is the grain density,  $\rho$  is the bulk density,  $\rho_{fl}$  is the fluid density,  $G_{fr}$  is the frame shear modulus and  $\alpha$  is the tortuosity parameter.

The Biot characteristic frequency is given by:

$$f_c = \frac{\mu \phi_t}{2\pi k \rho_f l} \quad , \quad (4.4)$$

where  $\mu$  is viscosity, and  $k$  is permeability. Since the permeability is in the denominator, all else being constant, the lower the permeability the higher the characteristic frequency. This is important for our very low-permeability samples.

Following the approach adopted by Winkler (1985) and Wang and Nur (1990), we define Biot dispersion as the percent difference between the Gassmann zero-frequency velocity prediction and the Biot high-frequency velocity prediction. Apparent dispersion is defined as the percent difference between measured velocity at ultrasonic frequency and the Gassmann prediction. Thus,

$$D_A = \left[ \frac{V_M - V_G}{V_G} \right] * 100 \quad , \quad (4.5)$$

and

$$D_B = \left[ \frac{V_B - V_G}{V_G} \right] * 100 \quad , \quad (4.6)$$

where  $D_A$  is percent apparent dispersion,  $V_M$  is measured velocity,  $V_G$  is Gassmann zero-frequency velocity prediction,  $V_B$  is Biot high-frequency velocity prediction and  $D_B$  is percent Biot dispersion.

#### 4.2.2 SQUIRT-FLOW MODEL:

The squirt-flow mechanism is based on experimental observations that, at high enough effective pressures, Biot's theory is sufficient to explain the small velocity dispersion observed, while at lower effective stresses the compliant pores are still open and are the source of the increased dispersion (Mavko and Jizba, 1991; Dvorkin et al., 1995). As the rock is deformed by the passage of an acoustic wave, some pores may close while others may open. This can produce localized variations in pore pressure which will cause fluids to "squirt" out of closing pores.

Building on earlier work done by Mavko and Jizba (1991); Shapiro (2003), Gurevich et al., (2010), and de Paula et al., (2012) showed that measured velocities in dry rocks and the compressibility computed from them at varying stresses is related to the closure of compliant and intermediate (moderately stiff) pores. They showed that squirt flow between these intermediate pores and stiff pores are responsible for dispersion observed at ultrasonic frequencies.

Our implementation of this model is based on the work of Dvorkin et al., (1995). Because of the squirt-flow model's complexity, we refer the reader to appendix E in Dvorkin et al., (1995). An explanation of the implementation is discussed in the method section. In the discussion section, we show that similar results will be expected if we had implemented the Gurevich et al., (2010) and de Paula et al., (2012) approach.

## 4.3 METHOD

### 4.3.1 SAMPLE DESCRIPTION:

Our measurements were performed on a Permian-age unconventional reservoir rock from the Delaware basin, a sub-basin of the Permian basin. Whole core from which the sample was cut was acquired from a depth of about 3110 m. Sample damage was minimized by careful handling.

The sample composition determined from X-ray diffraction (XRD) is shown in table 4.1. The 23.2% volume fraction of clay is composed primarily of illite (20%), the remaining 3.2% is made up of kaolinite and chlorite. Sample dimension was 1" in diameter and 2" in length.

The sample was vacuum dried at 80 degrees Celsius for several days until the sample weight stabilized. Figure 4.1 is a cross plot of sample weight versus time in hours during the course of drying the sample. The measured permeability of the sample is 0.2 microDarcy, the porosity is 5.65%. The *in situ* overburden stress is estimated from the density log to be 72.4 MPa. Estimated pore pressure was 34.47 MPa and the estimated horizontal stress is 55.16 MPa, leading to an estimated mean effective horizontal stress of 20.68 MPa.

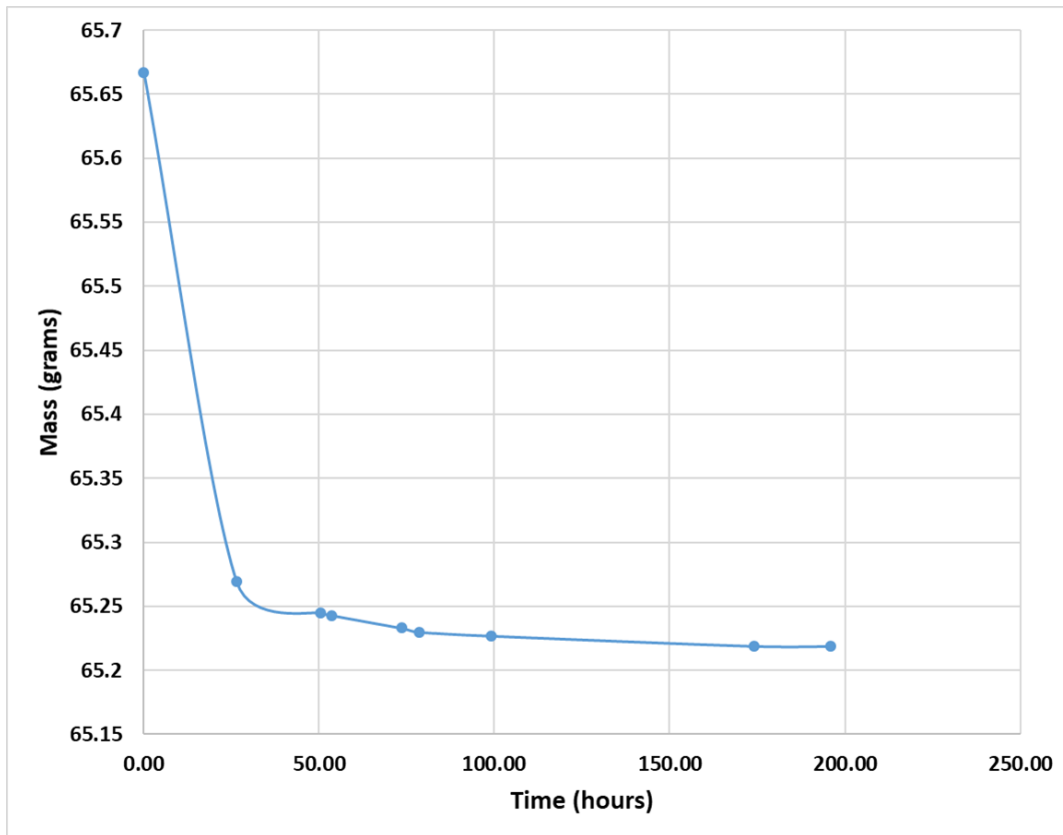


**Figure 4.1:** Sample weight versus time while drying the sample.

**Table 4.1:** Composition from XRD of the core sample

Mineralogy	Volume %
Quartz	51.0
K-Feldspar	4.0
Plagioclase	13.3
Calcite	2.5
Fe-Dolomite	4.5
Pyrite	1.5
Illite&Mica	20.0
Kaolinite	0.5
Chlorite	2.7

#### 4.3.2 EXPERIMENTAL PROCEDURE:

To prevent confining fluid from penetrating the dry sample, the sample was jacketed in an impermeable sleeve after being wrapped in a wire mesh. The sample was mounted between acoustic transducers and the assembly was placed in a tri-axial cell, as shown in figure 4.2a. Based on a prior tri-axial test on a twin sample, we had determined the rock sample elastic limit to be  $\sim 110$  MPa at confining stress of 20.68 MPa. A drained tri-axial test was carried out on the dry sample at deviatoric stresses below the elastic limit of the rock. The irrecoverable strain was 0.12%, indicating minimal sample damage. Ultrasonic P-wave and S-wave velocity measurements were made during the tri-axial experiment. Confining stress was kept constant at 20.68 MPa, while the deviatoric stresses (difference between axial and confining stress) were varied from zero to about 89.6 MPa, well below the maximum compressive strength of the twin sample, which was 193 MPa. The application of deviatoric stress is a better approximation to the sub-surface stress state than an isostatic stress test. We use acoustic data acquired during the loading cycle for our analysis. As shown in figures 4.3a and 4.3b, bedding-normal P-wave and S-wave velocities are computed from the recorded P-wave and S-waveforms. Sample weight prior to the experiment on the dry sample was 65.22 g, post-test sample weight was 65.23 g.

After the vacuum-dried measurement, the sample was again re-equilibrated under vacuum at 80° C and brine saturated. Figure 4.2b displays the experimental setup. The pressure vessel was evacuated using a cold trap for 30 minutes. The sample was then vacuum saturated using de-gassed brine. This ensures that there is no trapped air in the sample. The sample is

then pressurized to 6.9 MPa using a compressible chamber, which ensures none of the pressurized confining gas dissolves into the pore space. The sample is then allowed to equilibrate for several days, ensuring full saturation of the pore space. Sample weights before and after the saturation were consistent with a fully fluid-saturated pore space.

The tri-axial test is then repeated on the fully saturated sample while measuring P- and S-wave velocities. Sample weight before and after the test indicate no significant loss of fluids.

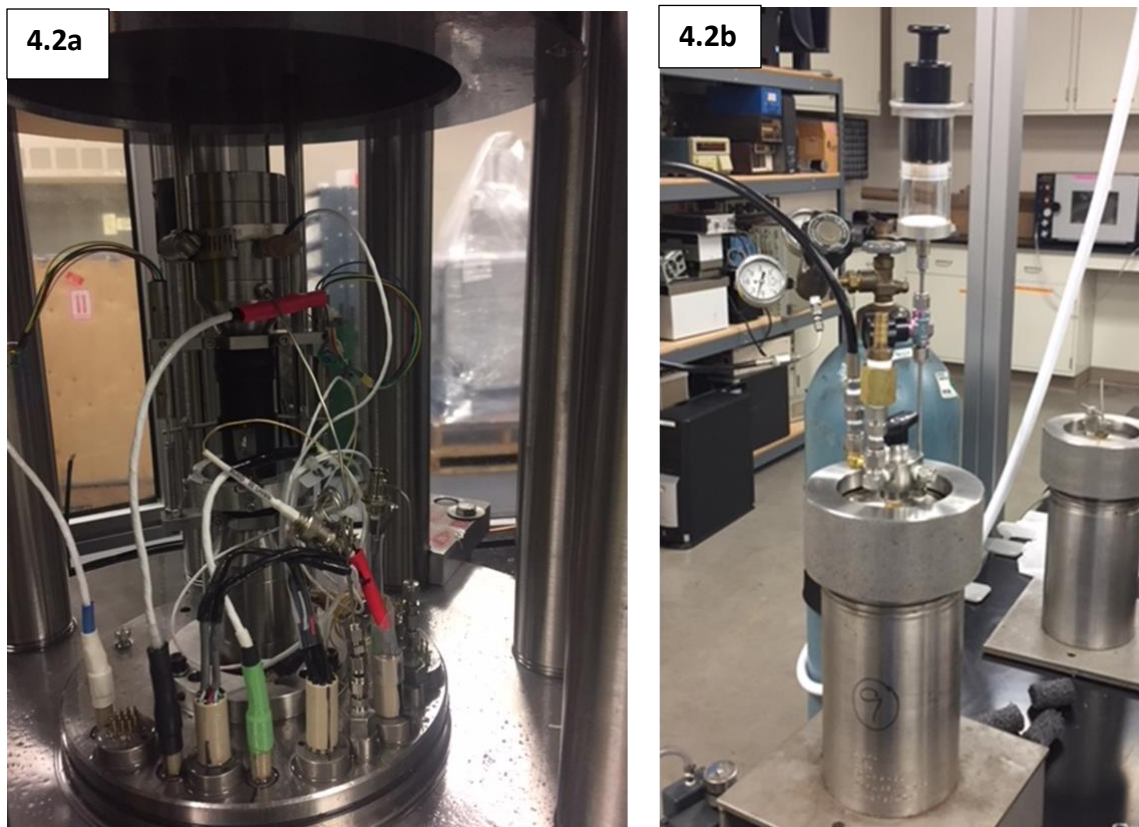
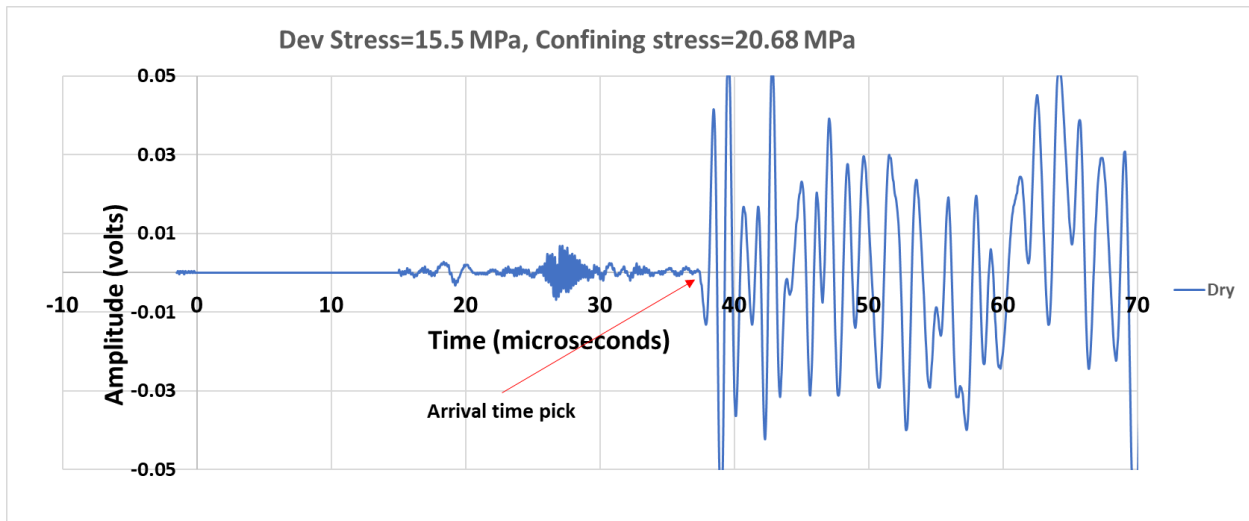
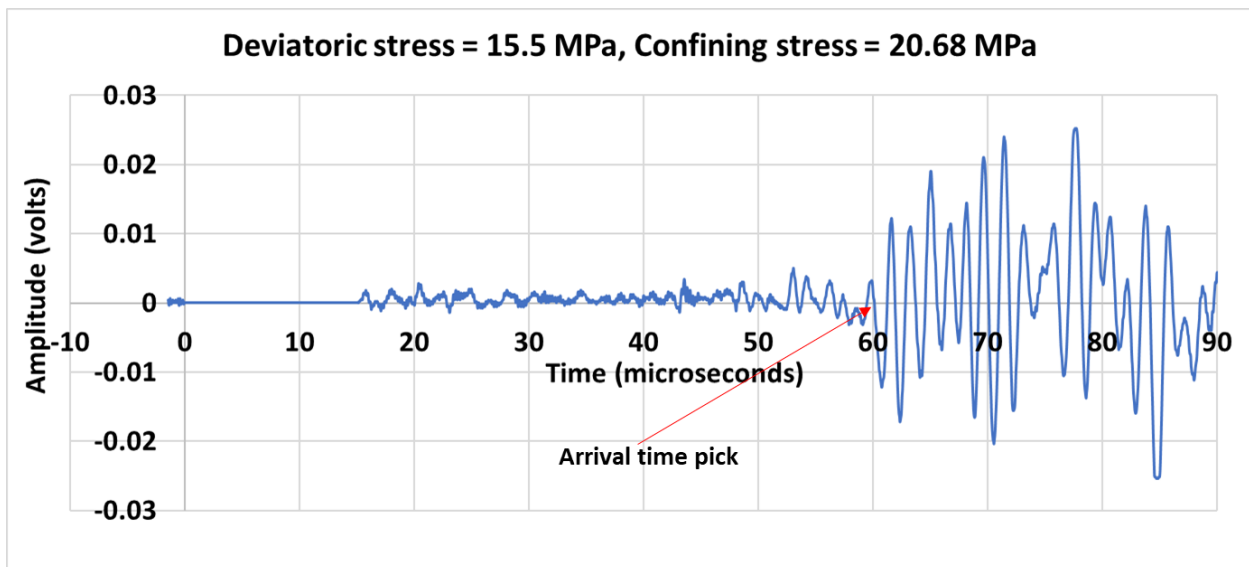


**Figure 4.2a:** Experimental setup for the dry and brine-saturated sample. Internal instrumentation includes load cell to measure deviatoric stress, 2 LVDTs (Linear variable differential transformer) for measurement of axial strain, a radial cantilever bridge and end caps housing the P and S-wave 1 MHz piezoelectric transducer. (Equipment provided by MetaRock® laboratories)

**Figure 4.2b:** Pressure vessel where sample was saturated; apparatus allows for first vacuum evacuating the sample before saturating with brine



**Figures 4.3a:** Recorded P-wave at confining stress of 20.68 MPa and deviatoric stress of 15.5 MPa of the dry sample. In view of the relatively higher stresses at which the measurements were made, there was no difficulty in picking the arrival times from the recorded waveforms.



**Figures 4.3b:** Recorded S-wave at confining stress of 20.68 MPa and deviatoric stress of 15.5 MPa of the dry sample.

To calibrate the acoustic transducer, we measured P-wave and S-wave velocities of a known metal. Figure 4.4 shows the P-wave arrival times measured across 1", 1.5", 2" and 2.5" aluminum billets. The inverse of the slope is the velocity of aluminum in inch/microsecond; while the intercept is the travel time across the acoustic transducer end caps.

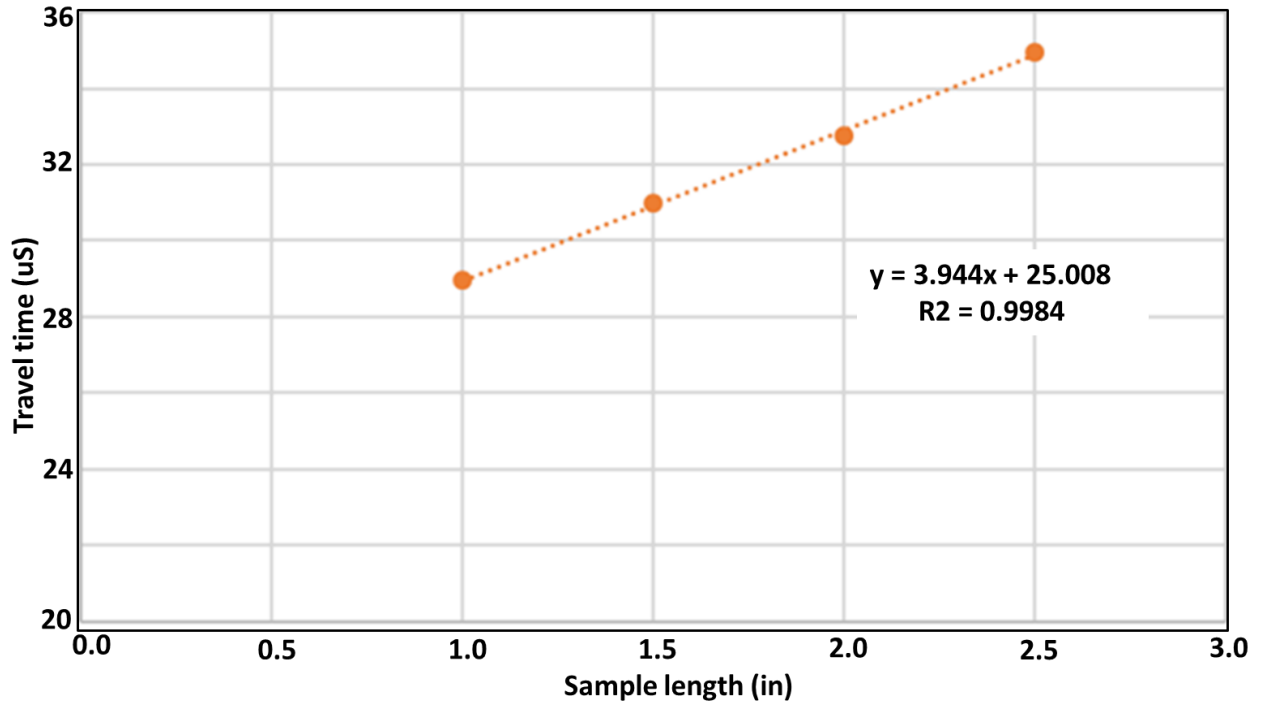


**Figure 4.4:** Plot of P-wave arrival times (in microsecond units) measured on 1", 1.5", 2" and 2.5" Aluminum billets. The inverse of the slope – 0.2535 in/us (6.439 km/s) – is the P-wave velocity of Aluminum; which is within 0.5% of published P-wave velocity for aluminum (6.42 km/s; Lide, D. R. ed., 2005)

## 4.4 RESULTS

### 4.4.1 BIOT-GASSMANN MODEL EVALUATION

Given the measured acoustic P-wave and S-wave velocities and bulk density of the dry rock, we determine the dry-frame bulk and shear modulus. Using equations 4.2 and 4.3 above we compute the Gassmann zero-frequency and Biot high-frequency P-wave velocities. Winkler (1983) used a tortuosity value of 2 for Berea sandstone and so does Wang and Nur (1990). The Berea sandstone is more porous and permeable than our core sample. Increasing the value of the tortuosity parameter has the effect of slightly lowering Biot velocity which brings it closer to the zero-frequency value, i.e. lowering the dispersion effect. We calculated the Biot high-frequency velocities for a range of values of tortuosity and found the result to not be very sensitive to this parameter. Table 4.2 shows the difference between using a value of 2 and 3 for tortuosity parameter.

Figure 4.5 is a cross plot showing the measured P-wave velocity for the brine saturated (blue) and dried sample (yellow), as well as the Gassmann (orange) and Biot (gray) predictions. With the exception of the sample close to zero deviatoric stress, the Gassmann P-wave velocity prediction is close to the measured P-wave velocity for the brine-saturated sample. As shown in table 4.2a, the apparent percent dispersion ( $D_A$ ) range from -1.67% to 2.4%. These calculated values are all on the order of the measurement error. The Biot dispersion ( $D_B$ ) is shown in table 4.2b. It ranges from 1.15% to 1.35% when the tortuosity parameter is 3 and 1.7 to 1.98 when the tortuosity parameter is 2.

The Biot characteristic frequency is determined using equation 4.4. The viscosity of brine, our saturating fluid, is 0.001 Pa.s (1cp), permeability is 0.2 microDarcy (or  $2 \cdot 10^{-19} \text{ m}^2$ ) and brine density is taken to be 1 g/cc. Using these values, the Biot characteristic frequency is calculated to be  $4.45 \cdot 10^{10} \text{ Hz}$ , far above the laboratory and logging tool frequencies. This is 4 orders of magnitude above the laboratory frequency and 6 orders of magnitude above the logging frequency. This is consistent with the experimental observations shown in figure 4.5. We observe that the zero-frequency Gassmann prediction is within 0.2% -2.4% of the measured P-wave velocity at ultrasonic frequency, this is close to experimental error in the measured velocities which is 1%.

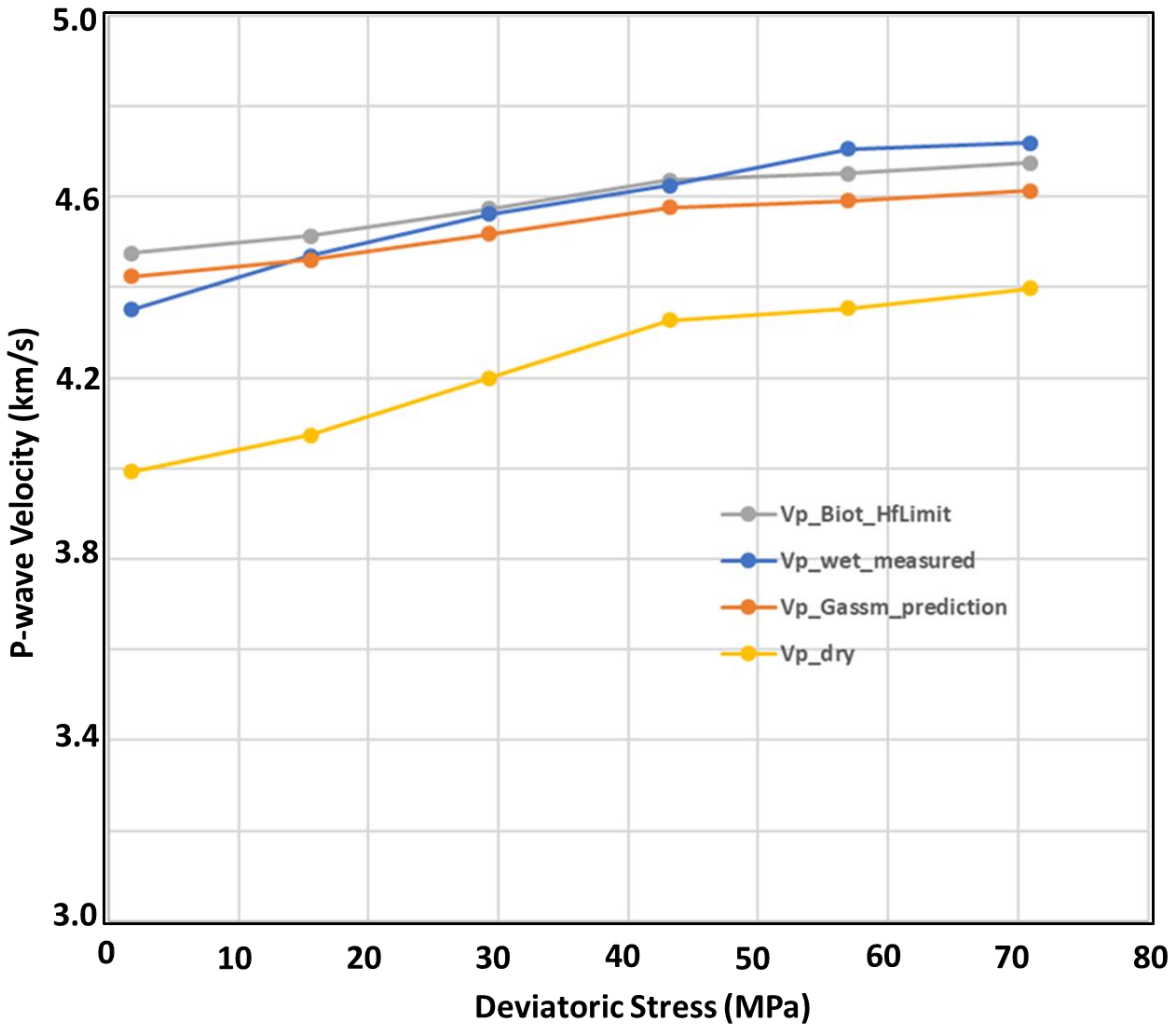


**Figure 4.5:** Plot of measured P-wave velocity on brine-saturated sample (blue), Biot P-wave velocity prediction (gray), Gassmann P-wave velocity prediction (orange) and measured P-wave velocity on dry sample (yellow) on y-axis; versus deviatoric stress on x-axis. Confining pressure was held constant at 20.68MPa.

**Table 4.2a:** Percent apparent dispersion

$D_A$ (%)	-1.6757	0.22	0.98	1.03	2.448	2.224
Dev_Stress (MPa)	1.72	15.51	29.32	43.15	56.95	70.95

**Table 4.2b:** Percent Biot dispersion with tortuosity parameter,  $\alpha$ , taken to be 2 or 3.

$D_B$ (%)	1.701	1.751	1.835	1.930	1.950	1.979		$\alpha = 2$
$D_B$ (%)	1.150	1.184	1.240	1.303	1.317	1.336		$\alpha = 3$
Dev Stress (MPa)	1.72	15.51	29.32	43.15	56.95	70.95		

#### 4.4.2 SQUIRT-FLOW MODEL EVALUATION

We apply the detailed squirt-flow computation procedure outlined in appendix E of Dvorkin et al., (1994) to acoustic measurements made at a deviatoric stress of 15.5MPa. The only free parameter,  $Z$ , is tuned to match one of 4 measurements. As recommended by Dvorkin et al., (1994) we have used P-wave velocity, because it has larger frequency dispersion than S-wave velocity. The value of the  $Z$  parameter obtained was  $5 \times 10^{-6}$ . This is equivalent to a characteristic squirt-flow length of 30.1 nm determined from equation 4.7. Pore throat radii computed from Mercury injection capillary pressure data from core acquired in a close offset well across the same formation range from 2 nm to 150 nm.

$$Z \approx \sqrt{\frac{R^2 \mu \alpha}{k K_S}} \quad , \quad (4.7)$$

with

$$\alpha = 1 - \frac{K_{msd}}{K_S} \quad .$$

where  $R$  is the characteristic squirt-flow length,  $K_s$  is the grain bulk modulus,  $k$  is permeability and  $\mu$  is viscosity,  $K_{msd}$  is the bulk modulus of dry “modified” rock frame, where modified means that the compliant pores are closed.

Once the  $Z$  parameter is determined at the measurement frequency, we compute the P-wave and S-wave velocities and attenuations as a function of frequency, varying frequencies from  $10^0$  to  $10^{15}$  Hz. Figure 4.6 is a plot of attenuation versus log frequency. There is no attenuation until  $\sim 10^9$  Hz – at which transition to the high frequency regime begins. The characteristic frequency is  $\sim 10^{11}$  Hz with a  $Q$  value of 37. Both the Biot-Gassmann model and the squirt-flow model predict that at *in situ* stress, the seismic, sonic and ultrasonic measurement frequencies are all in the low-frequency regime. In figure 4.7, we plot the squirt-flow P-wave and S-wave velocity prediction versus log frequency, both the black discrete data point (Gassmann low frequency prediction) and the red data point (measured P-wave velocity) are in the squirt-flow low frequency regime. Percent dispersion when the high frequency squirt-flow prediction is compared to measured P-wave velocity at ultrasonic frequency was 3%. S-wave velocity percent dispersion is 1.6%.

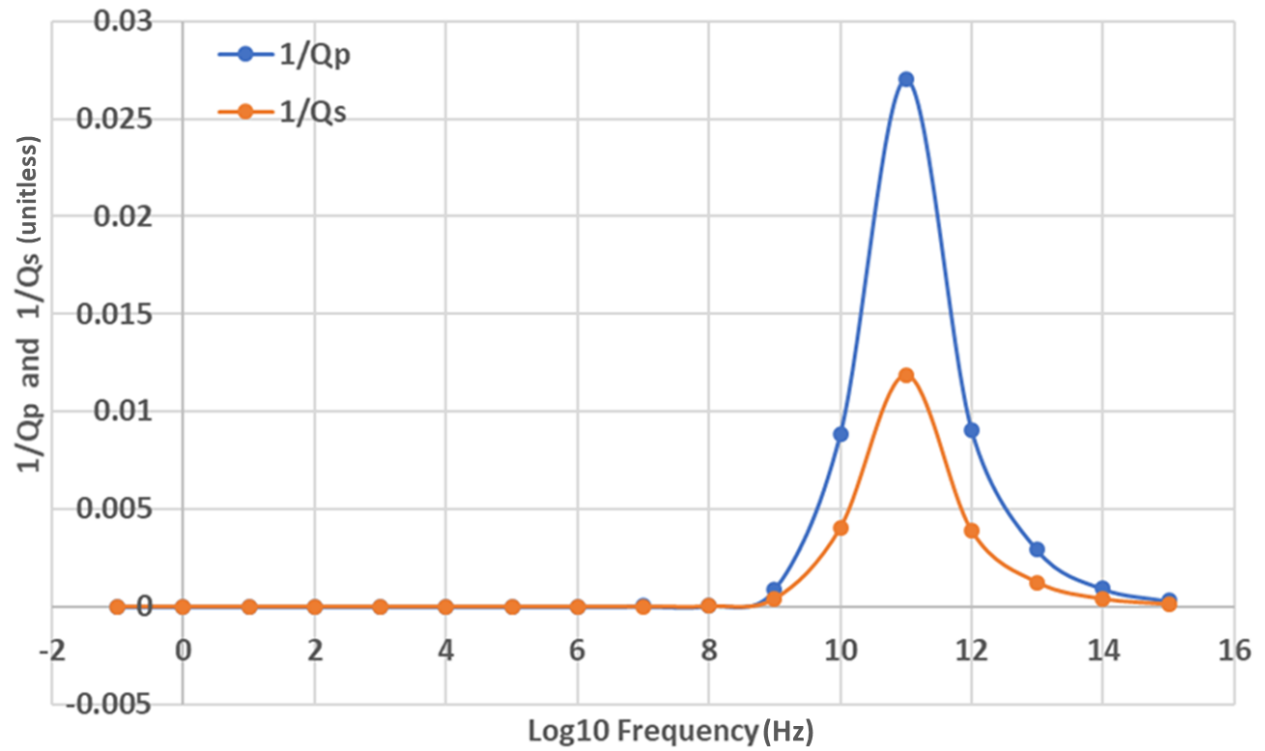


**Figure 4.6:** Cross plot of P-wave (blue) and S-wave (orange) attenuation based on Squirt-flow model on y-axis, versus log of frequency (Hz) for the Permian basin sample.  $Q_p$  = P-wave quality factor,  $Q_s$  = S-wave quality factor.

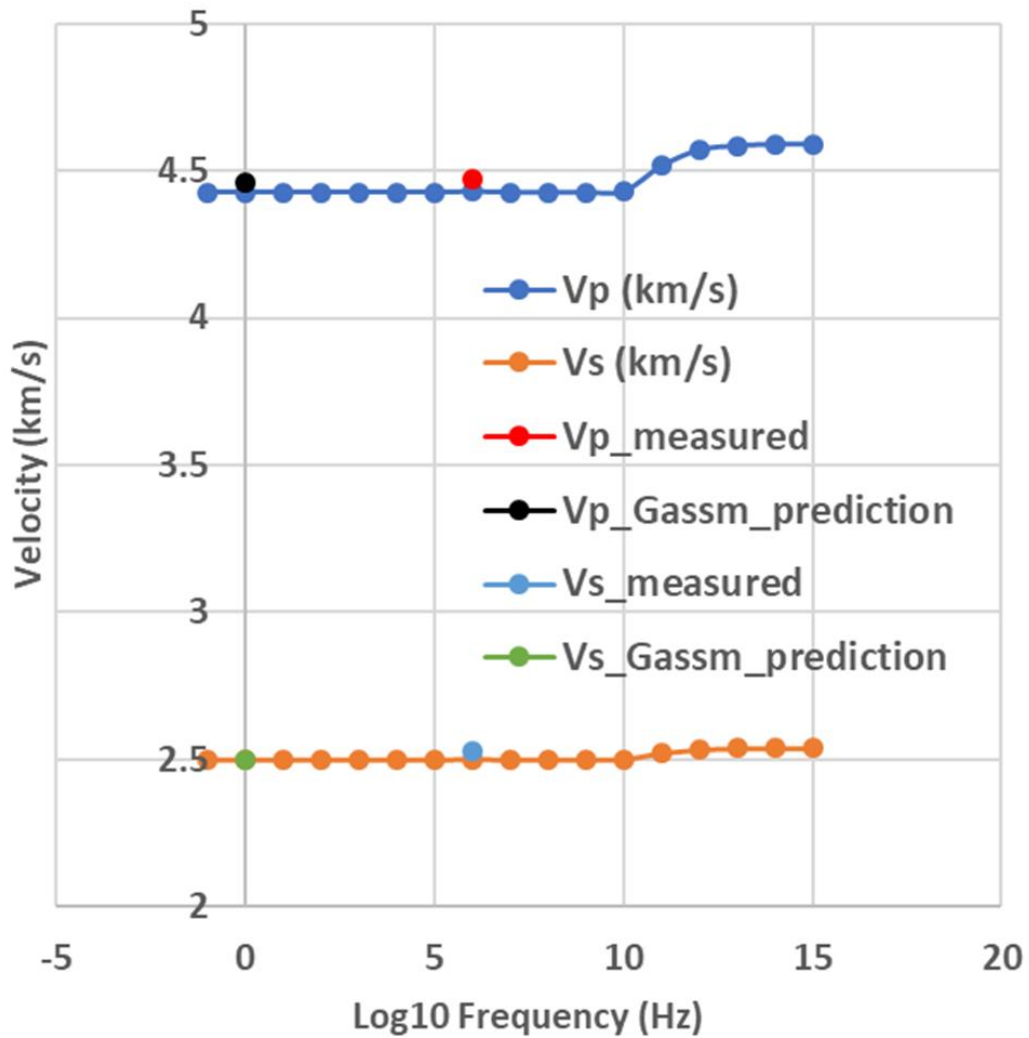


**Figure 4.7:** Plot of the squirt-flow P-wave (blue line) and S-wave (orange line) velocity predictions with log frequency. The low frequency limit P-wave velocity Gassmann prediction is the black data point. The red data point is the measured P-wave velocity at ultrasonic frequency on the fully brine-saturated sample. The blue discrete data point is the measured S-wave velocity on the fully brine-saturated sample, which agrees well with the squirt-flow predicted value. The low frequency limit S-wave velocity Gassmann prediction is the green data point.

#### 4.4.3 COTTON VALLEY SHALE EXAMPLE

The Cotton Valley shale dataset is from Tosaya (1982). Core was acquired from a depth of 9629 ft (2935 m) in east Texas and described as homogeneous silty shale. Sample mineralogy is 36% clay by volume dominated by illite, 49% quartz, 9.5% feldspars, 3% calcite, 2% siderite and 0.5% pyrite. The pore fluid used to saturate the sample was deionized water. Pore pressure was kept constant at 1 MPa during the course of this experiment. Figure 4.8 shows the measured and Biot-Gassmann predictions for P-wave velocity. The apparent dispersion ranges from -2.73% to -2.03%; this violates the low-frequency Gassmann prediction, and may indicate frame softening or measurement error. Tosaya report that the accuracy of their velocity measurement is 2%. This would imply that the observed difference between the measured data and Gassmann prediction is consistent with their measurement error. The stress dependent predicted Biot dispersion for this sample ranges from 1.18% to 1.34%. Biot characteristic frequency for the Cotton Valley shale sample is  $6.55 \times 10^{10}$  Hz.

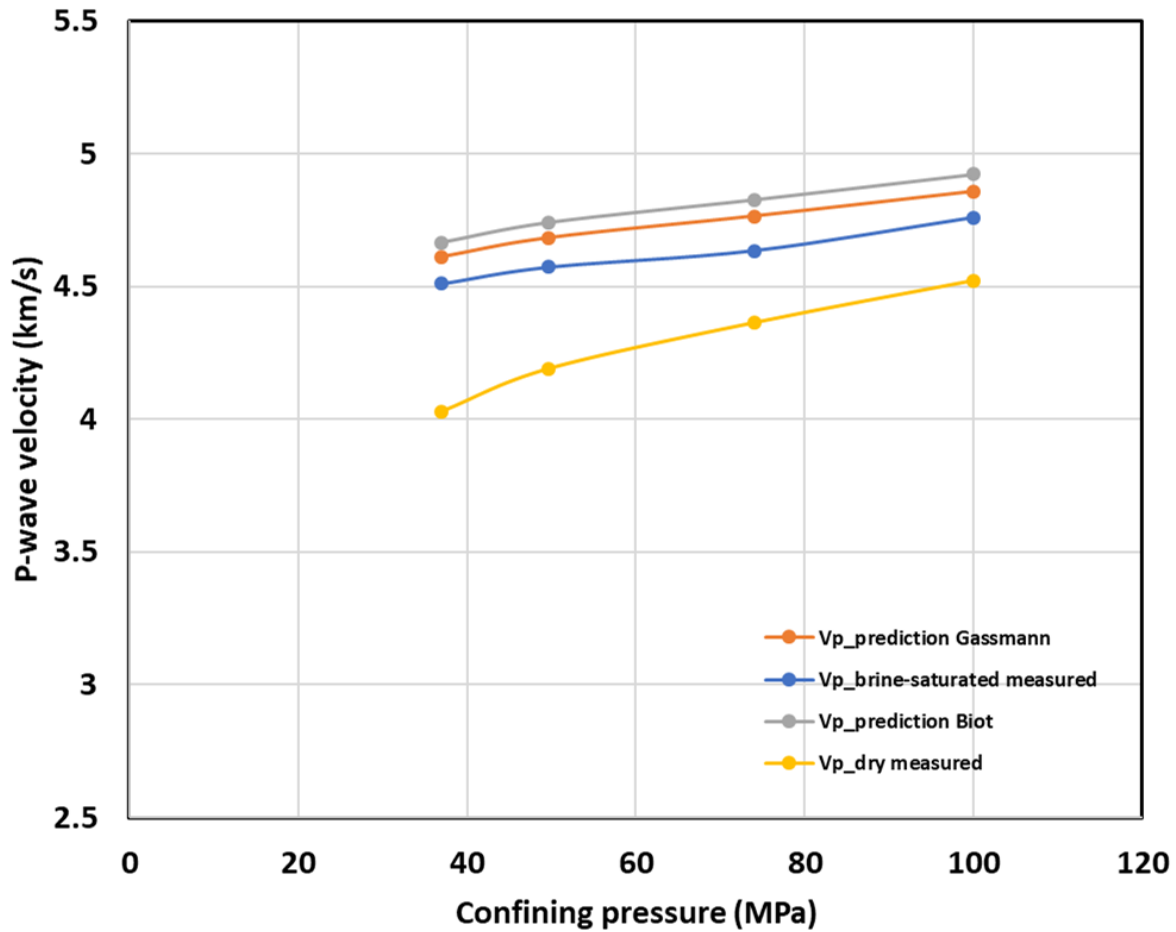


**Figure 4.8:** Tosaya (1982) P-wave velocity measurement of Cotton Valley shale. Similar to figure 5, we have plotted the measured P-wave velocities. (The water saturated P-wave velocity is in blue, the dry P-wave velocity is in yellow, the Biot P-wave velocity prediction is in gray, the Gassmann P-wave velocity prediction is in orange.) The predicted dispersion is within experimental error.

Applying the squirt-flow model, we used the acoustic measurement at 100 MPa to determine the dry bulk modulus at high confining pressure. This gave a dry modified solid bulk modulus of 22.4 GPa. The measured dry rock P-wave and S-wave velocities at 100 MPa are 4.521 km/s and 3.018 km/s respectively. We applied the squirt-flow model at the lowest measured stress of 37 MPa, where we expect the squirt-flow related effect to be the largest. The Z parameter that resulted in a match to P-wave velocity is  $2 \times 10^{-6}$ . This is equivalent to a

characteristic squirt-flow length of 7.3 nm (for comparison, water molecule diameter is 0.275 nm; methane molecule is about 0.3988 nm; n- butane is 0.415 nm). Figure 4.9 is a plot of attenuation versus log frequency for the Cotton Valley shale.

Like the Permian-basin example, there is no attenuation until  $\sim 10^9$  Hz – at which transition to the high frequency regime occurs. The characteristic frequency is  $10^{11}$  with a Q value of 21.14. The seismic, sonic and ultrasonic frequencies are well below the characteristic frequency, i.e. no dispersion is predicted in that frequency range.

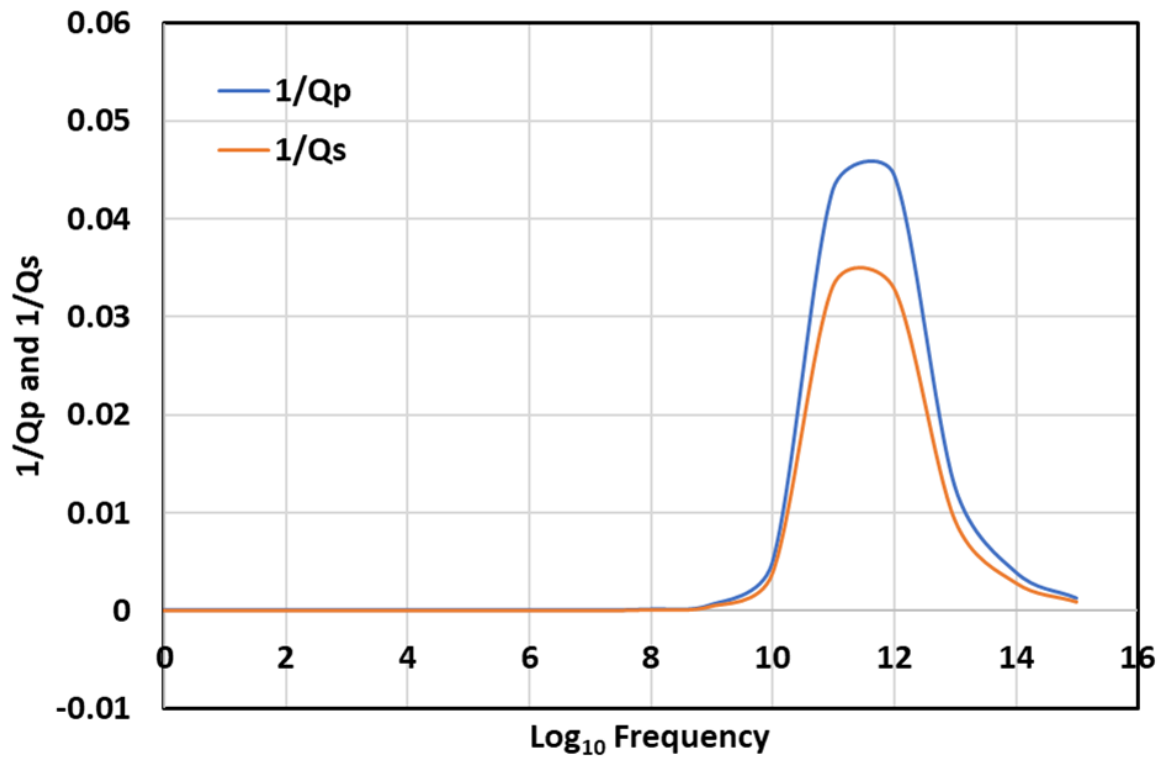


**Figure 4.9:** Cross plot of P-wave (blue) and S-wave (orange) attenuation based on Squirt-flow model on y-axis, versus log of frequency (Hz) for the Cotton Valley shale. Q<sub>p</sub> = P-wave quality factor, Q<sub>s</sub> = S-wave quality factor.

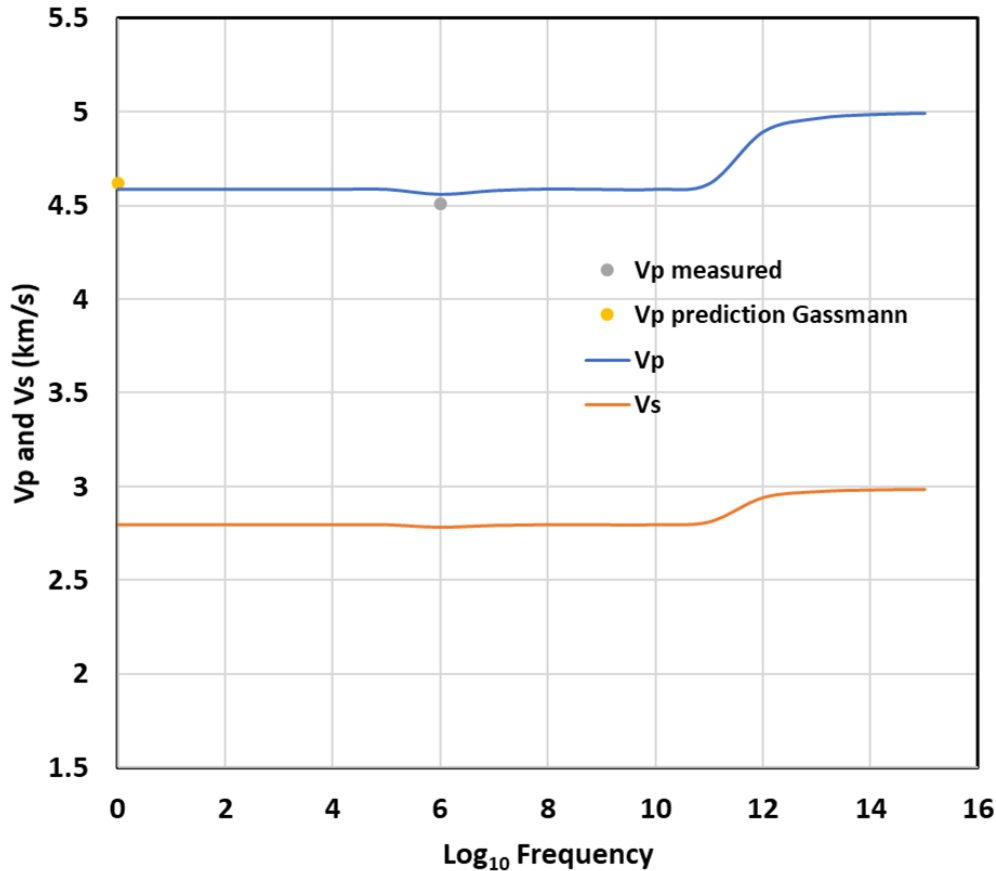


**Figure 4.10:** Cotton Valley shale. Cross plot of Squirt-flow P-wave (blue line) and S-wave (orange line) velocity predictions with log of frequency. Yellow data-point is the Gassmann P-wave velocity prediction, while the gray data-point is the measured P-wave velocity at ultrasonic frequency.

#### 4.5 COMPARISON OF SONIC LOG TO ULTRASONIC FREQUENCY MEASUREMENTS

We next compare sonic log measurements to laboratory measurements made at ultrasonic frequencies. We have done this in several lithofacies and applied the Student t distribution to compare if there is a statistically significant difference in the mean values.

While care was taken to preserve the core samples until laboratory measurements were made, fluid loss during core acquisition cannot be fully eliminated. For all 4 shale formations described in this section, *in situ* fluids are liquid hydrocarbon and brine – no free gas. However,

during the process of exhuming the rock from the subsurface – due to decreasing temperature and pressure, liquid hydrocarbon begins to shrink and dissolved gas bubbles forth. As such, even though there is usually no significant difference between *in situ* brine saturation and that measured in the laboratory for these very low permeability rocks, that is not the case for oil saturation. Especially in the case where reservoir fluid is volatile oil, it is not uncommon to measure significant gas saturation in the laboratory (e.g. for the Wolfcamp shale formation example from the Midland basin, the oil formation volume factor is 1.5, while brine formation volume factor is 1.01).

It is thus necessary to correct the laboratory ultrasonic measurement using the Gassmann equation to *in situ* saturation state for appropriate comparison to *in situ* sonic log measurements. Core fluid saturation was not measured on twin sample plugs for every one of the ultrasonic core sample measurements in this section. For each shale formation; however, we have reported (see table 4.3a) and used the average laboratory gas, oil and brine saturation over the interval compared to sonic log. Fluid densities and bulk modulus used in Gassmann for fluid substitution to *in situ* saturations is given in table 4.3b. In addition, we also present the combined result of the scenario where oil saturation is zero (i.e. all the liquid hydrocarbon is lost by the time ultrasonic measurements were made on the core samples. This rarely occurs if samples are properly preserved in the field) and gas saturation is zero (no fluid loss, this is also unlikely). Individual shale formation results are no different, but for want of space we only present the combined result for these 2 additional scenarios.

**Table 4.3a:** Average laboratory measured fluid saturations. Sg is gas saturation, So is oil saturation and Sw is brine saturation. *In situ* Sg=0 for all 4 formations considered in this section. Lab Sw = *In situ* Sw.

Formation	Average Sg (Dec)	Average So (Dec)	Average Sw (Dec)
BSPG_DB	0.40	0.10	0.50
WFMP_DB	0.48	0.17	0.35
WFMP_MB	0.40	0.15	0.45
LSBY_MB	0.40	0.15	0.45

**Table 4.3b:** Fluid Properties, required for fluid substitution to *in situ* fluid saturations.

Fluid	Density (g/cc)	Bulk Modulus (GPa)
Brine	1.050	3.200
Oil	0.700	1.100
Gas	0.250	0.200

#### 4.5.1 BONESPRING FORMATION EXAMPLE

Average clay volume across the interval of interest is 16%, with the rest being quartz, feldspars and minor amounts of carbonate. Figure 4.11 compares the sonic log measured P-wave and S-wave velocities with the ultrasonic measurement acquired at ~1 MHz. The core has been depth shifted to match log depths. This was done by matching core gamma ray depth – the black curve in the Correlation column - to well-log gamma ray depth. Laboratory ultrasonic acoustic measurements are made on a 5.08 cm long and 2.54 cm diameter sample, sonic log measurements have resolution that are in the 0.6096 m or higher range, therefore it is expected to see more variation in the core data than the log data.

The estimated minimum horizontal *in situ* confining stress ranges from 13.1 to 15.2 MPa, estimated maximum horizontal in-situ confining stress ranges from 19.3 to 21 MPa. The laboratory data were therefore acquired at an estimated average confining stress of 17.24 MPa and deviatoric stress of 21.4 MPa. With the exception of a few data-points – which are possibly due to differences in resolution between the sonic and ultrasonic measurements – there is a good match between both the sonic log and the higher frequency ultrasonic measurements.

We will statistically test for a significant difference in the mean values of these data using the Student t test. In order to do this, we assume a Gaussian distribution for both the laboratory and well-log data. Figure 4.12 is the histogram of the P-wave velocity for the 2<sup>nd</sup> Bonespring formation excluding the limestone interval, the dash green line is the Gaussian fit to the data. The average of the eleven laboratory-measured ultrasonic P-wave velocities is 4.45 km/s with a standard deviation of 0.21 km/s. After fluid substitution to *in situ* saturations using tables 4.3a and 4.3b, the average ultrasonic P-wave velocities for the 11 measurements is 4.58 km/s with a standard deviation of 0.186 km/s. The laboratory measured S-wave velocity mean and standard deviation are respectively 2.81 km/s and 0.18 km/s. After fluid substitution, the average and standard deviation are respectively: 2.80 km/s and 0.183 km/s. At the corresponding depths to the ultrasonic core measurements, the mean sonic log P-wave velocity for the 2<sup>nd</sup> Bonespring formation is 4.63 km/s with a standard deviation of 0.261 km/s. While the mean and standard deviation of sonic log S-wave velocity are respectively 2.76 km/s and 0.136 km/s. We address the question of whether there is any significant difference in the estimated means of both datasets using the well-known Student t-Test. The results for both P-

wave and S-wave velocities are shown in tables 4.4a and 4.4b, a detailed workflow of how these were obtained are shown in appendix C. At a confidence level of 99%, we cannot reject the null hypothesis that the means of the sonic log and ultrasonic measurements are the same, for both P-wave and S-wave velocities and their ratio (see tables 4.4a – 4.4c).

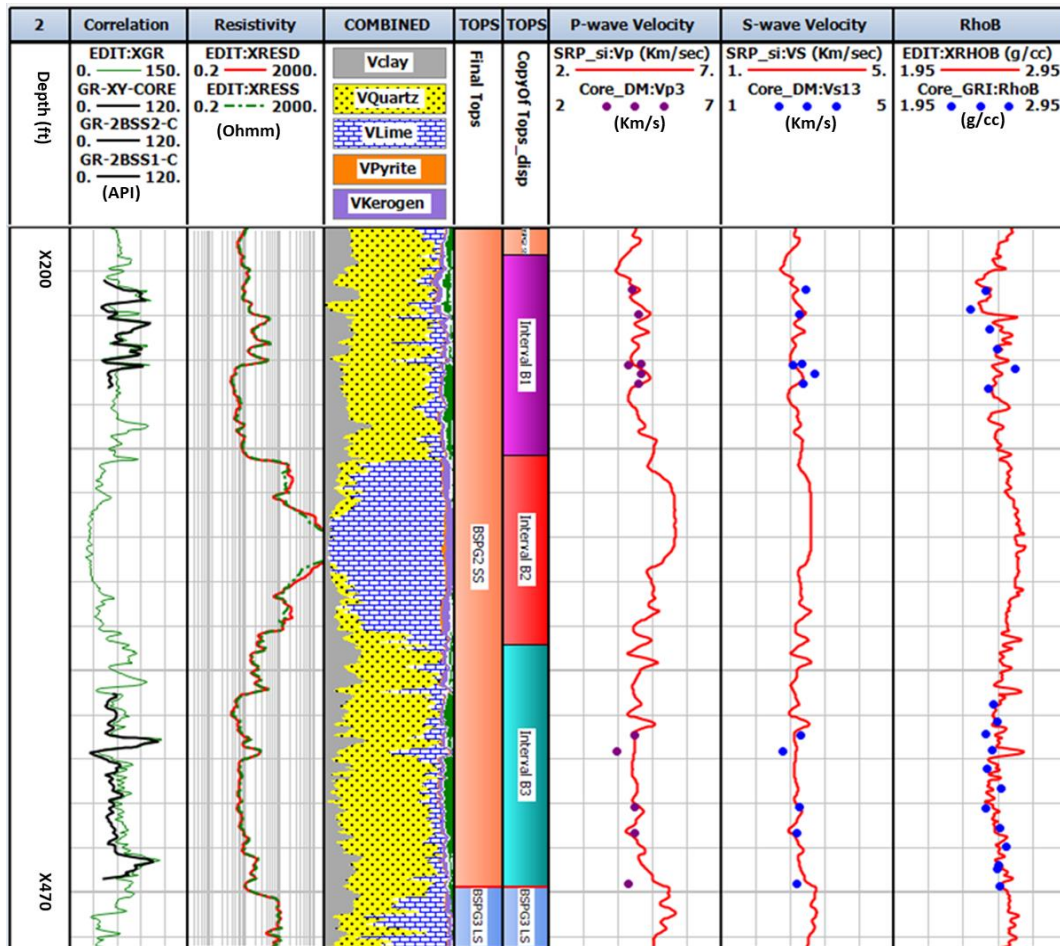


**Figure 4.11:** Log plot of the Bonespring formation. The Correlation track contains Gamma-ray (green curve) and core gamma ray (black curve). The Resistivity track contains resistivity log. The COMBINED track contains formation lithology fractional volumes determined by volumetric log analyses. The P-wave velocity track contains sonic P-wave velocity (red curve) and ultrasonic P-wave velocity (purple discrete data-points). The S-wave velocity track contains sonic S-wave velocity (red curve) and ultrasonic S-wave velocity (blue discrete data-points). The RhoB track contains log measured bulk density (red curve) and core measured bulk density (blue discrete data). Depths in the depth track are only to indicate depth scale, actual depths are not available for publication.

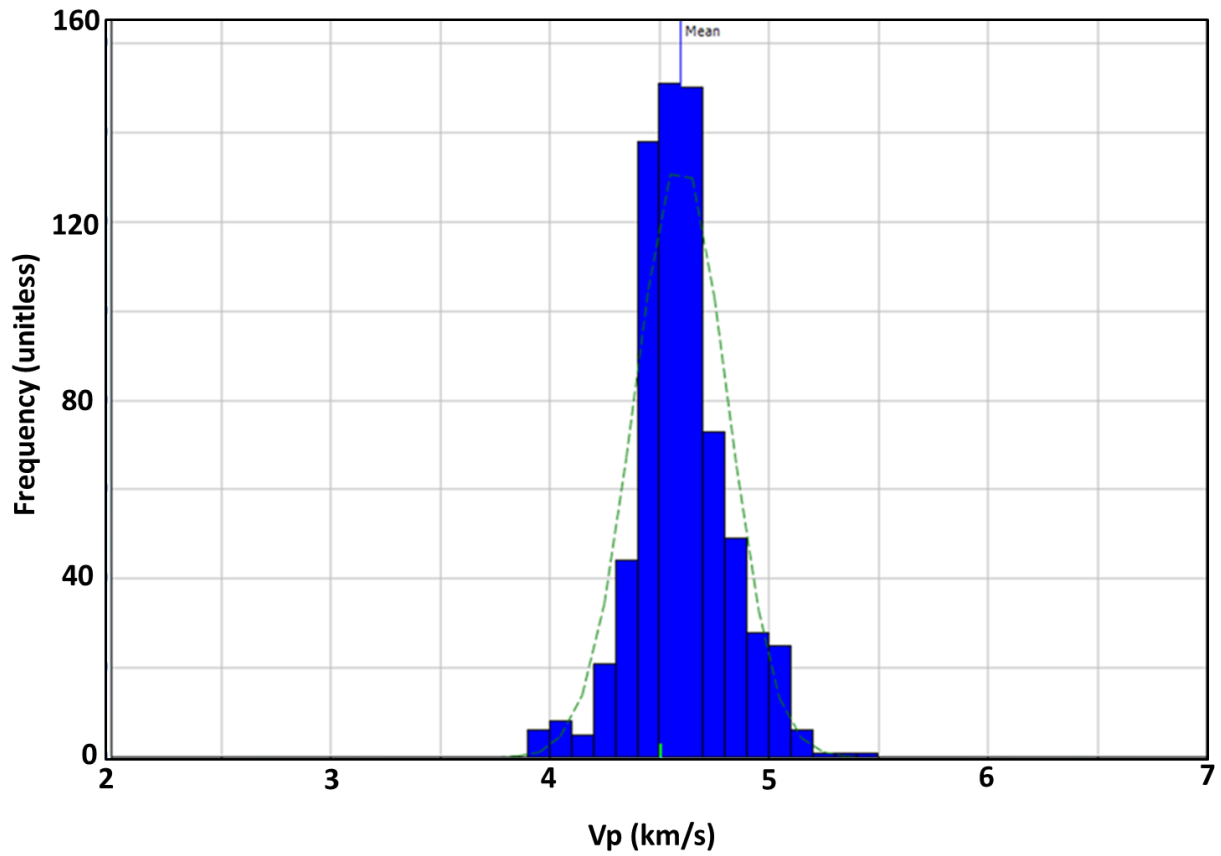


**Figure 4.12:** Histogram of the sonic log P-wave velocity in the 2<sup>nd</sup> Bonespring formation (BSPG2 SS) shown in figure 9, excluding the limestone interval. Green dash line is the Gaussian fit to the data

**Table 4.4a:** Student t-Test result for the co-located sonic log and ultrasonic core P-wave velocity measurements (after fluid substitution to *in situ* saturations) in the 2<sup>nd</sup> Bonespring formation. Result indicate there is no significant difference between the mean of the sonic log and ultrasonic core measurements.

	<i>Vp_log</i>	<i>Vp_core</i>
Mean	4.63	4.58
Variance	0.068	0.035
Observations	11	11
Pooled Variance	0.051	
Hypothesized Mean Difference	0	
df	20	
<b>t Stat</b>	<b>0.496</b>	
P(T<=t) one-tail	0.312	
<b>t Critical one-tail</b>	<b>2.528</b>	
P(T<=t) two-tail	0.625	
t Critical two-tail	2.845	
<b>  t stat   &lt; t critical; null hypothesis cannot be rejected</b>		

**Table 4.4b:** Student t-Test result for the co-located sonic log and ultrasonic core S-wave velocity measurements (after fluid substitution to *in situ* saturations) in the 2<sup>nd</sup> Bonespring formation. Result indicate there is no significant difference between the mean of the sonic log and ultrasonic core measurements.

	<i>Vs_log</i>	<i>Vs_core</i>
Mean	2.76	2.80
Variance	0.018	0.033
Observations	11	11
Pooled Variance	0.026	
Hypothesized Mean Difference	0	
df	20	
<b>t Stat</b>	<b>-0.560</b>	
P(T<=t) one-tail	0.291	
<b>t Critical one-tail</b>	<b>2.528</b>	
P(T<=t) two-tail	0.582	
t Critical two-tail	2.845	
<b>  t stat   &lt; t critical; null hypothesis cannot be rejected</b>		

**Table 4.4c:** Student t-Test result for the co-located sonic log and ultrasonic core  $V_p/V_s$  ratio measurements (after fluid substitution to *in situ* saturations) in the 2<sup>nd</sup> Bonespring formation. Result indicate there is no significant difference between the mean of the sonic log and ultrasonic core measurements.

	$V_p/V_s_{log}$	$V_p/V_s_{core}$
Mean	1.68	1.64
Variance	0.001	0.003
Observations	11	11
Pooled Variance	0.002	
Hypothesized Mean Difference	0	
df	20	
<b>t Stat</b>	<b>2.095</b>	
P(T<=t) one-tail	0.025	
<b>t Critical one-tail</b>	<b>2.528</b>	
P(T<=t) two-tail	0.049	
t Critical two-tail	2.845	
<b> t stat  &lt; t critical; null hypothesis cannot be rejected</b>		

#### 4.5.2 WOLFCAMP FORMATION – DELAWARE BASIN EXAMPLE

The Wolfcamp formation example is also from the Delaware basin. Matrix permeability determined through the GRI method range from 8 to 120 NanoDarcy. Average clay volume is 15%, average total porosity is 8.6%. Laboratory measurements were made at 17.24 MPa confining stress. The comparison of the sonic log with ultrasonic measurements is shown in figure 4.11. The obvious heterogeneity in the core is shown in figure 4.12. These core photos are each about 1.2 ft (0.366 m) in length. Note the significant change in rock facies over an interval that is less than 1 ft (0.3048 m). The vertical core plugs used for ultrasonic measurements are 2" (5.08 cm) in length, compared to the resolution of the sonic log measurement which is about 2 ft (0.6096 m). We therefore expect a significant variability in the

core data as compared to the logs. This is evident in the standard deviation of the core data. The mean laboratory measured ultrasonic P-wave velocity is 4.27 km/s with a standard deviation of 0.5 km/s. After fluid substitution the mean ultrasonic P-wave velocity is 4.42 km/s with a standard deviation of 0.417 km/s. The laboratory measured S-wave velocity mean and standard deviation (SD) are respectively 2.69 km/s and 0.24 km/s, after fluid substitution the mean and standard deviation are respectively: 2.69 km/s and 0.243 km/s.

For the corresponding depths, the mean sonic log P-wave velocity for the Wolfcamp formation is 4.27 km/s with a standard deviation of 0.23 km/s. The mean and standard deviation of sonic log S-wave velocity are respectively 2.58km/s and 0.14km/s. The Student t-Test results are shown in tables 4.5a, 4.5b and 4.5c, it indicates that we cannot reject the null hypothesis that the sonic log and ultrasonic core measurements for P-wave velocity, S-wave velocity and their ratio, have the same mean value.

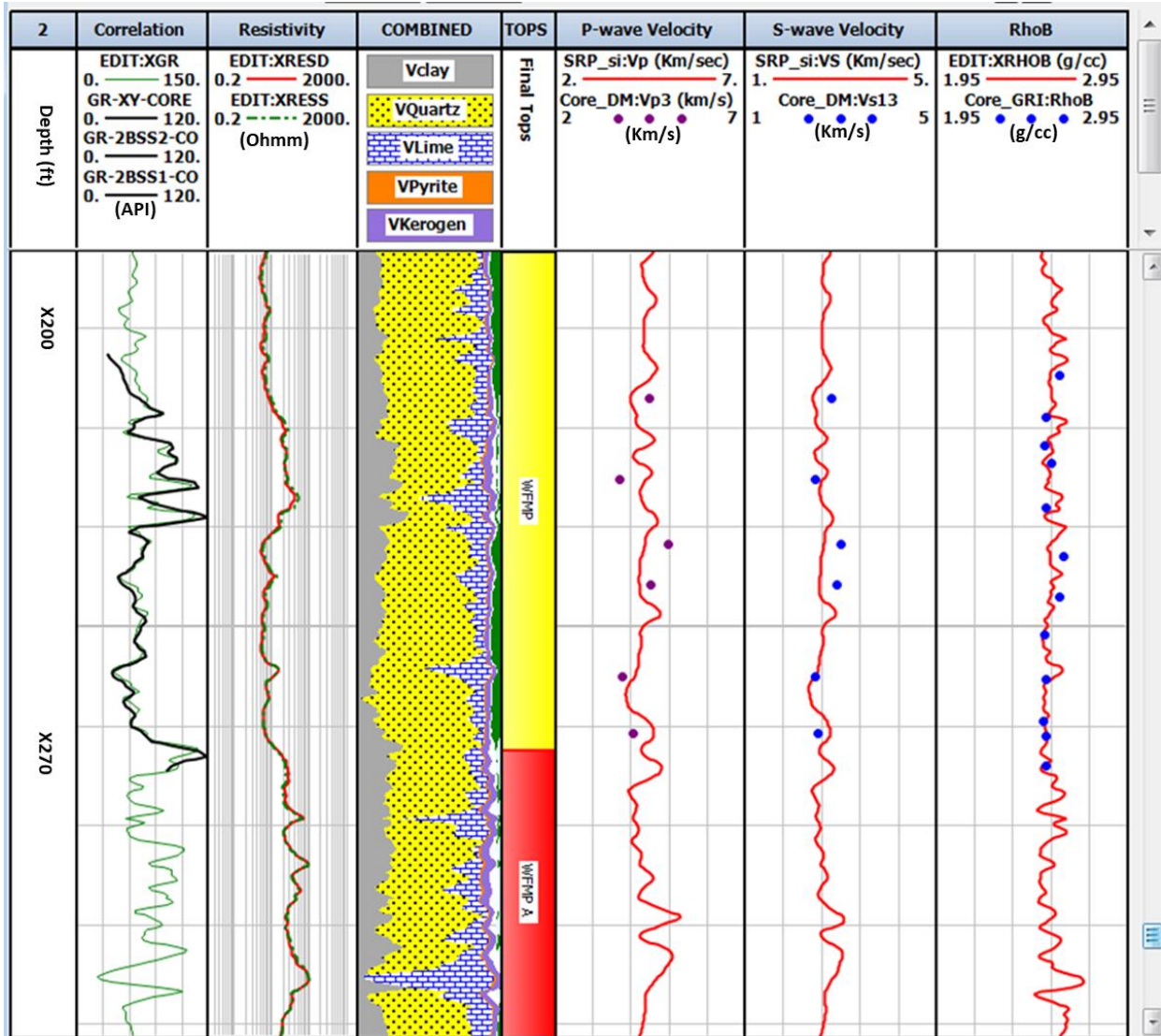


**Figure 4.13:** Log plot of the Wolfcamp formation. The correlation track contains log Gamma-ray (green curve) and core gamma ray (black curve). The RESISTIVITY track contains resistivity log. The COMBINED track contains formation lithology fractional volumes determined by volumetric log analyses. The P-wave velocity track contains sonic P-wave velocity (red curve) and ultrasonic P-wave velocity (purple discrete data-points). The S-wave velocity track contains sonic S-wave velocity (red curve) and ultrasonic S-wave velocity (blue discrete data-points). The RhoB track contains log measured bulk density (red curve) and core measured bulk density (blue discrete data). Depths in the depth track are only to indicate depth scale, actual depths are not available for publication.

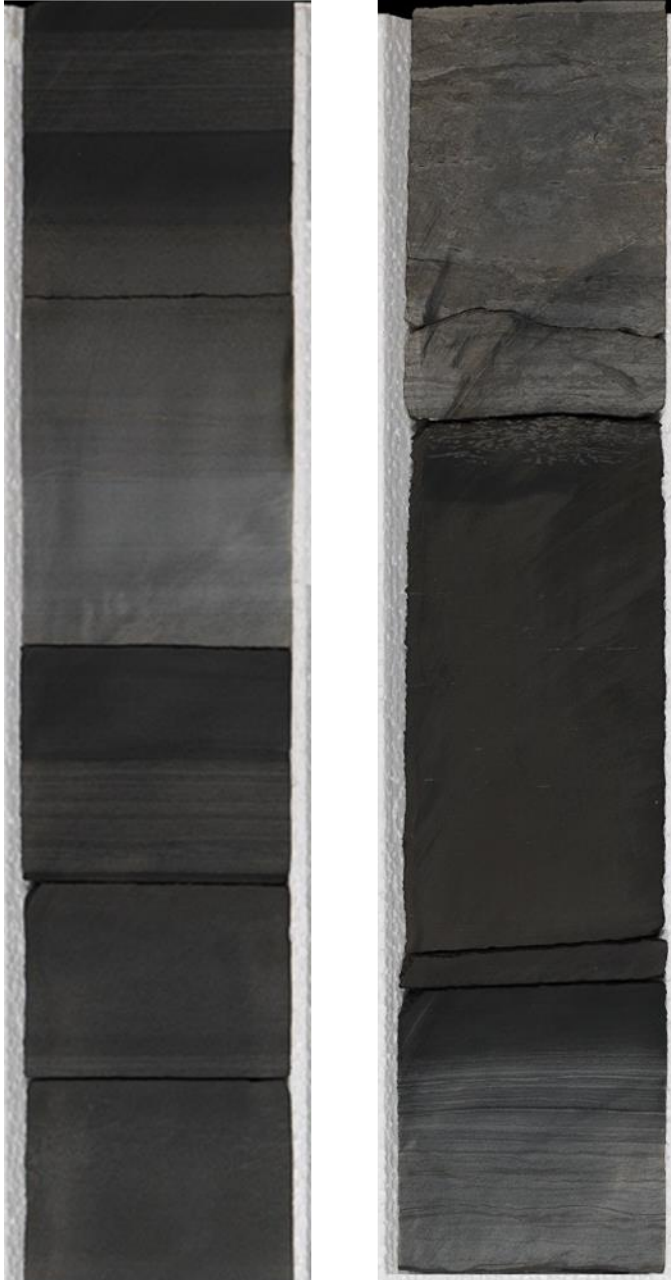


**Figure 4.14:** Core sample photo from the Wolfcamp cored interval. Sample length for each is 1.2ft

**Table 4.5a:** Student t-Test for the co-located sonic log and ultrasonic core P-wave velocity measurements (after fluid substitution to *in situ* saturations) in the Wolfcamp formation, Delaware basin. Result indicate there is no significant difference between the mean of the sonic log and ultrasonic core measurements.

	<i>Vp_log</i>	<i>Vp_core</i>
Mean	4.27	4.42
Variance	0.052	0.174
Observations	6	6
Pooled Variance	0.113	
Hypothesized Mean Difference	0	
df	10	
<b>t Stat</b>	<b>-0.754</b>	
P(T<=t) one-tail	0.234	
<b>t Critical one-tail</b>	<b>2.764</b>	
P(T<=t) two-tail	0.468	
t Critical two-tail	3.169	
<b> t stat  &lt; t critical; null hypothesis cannot be rejected</b>		

**Table 4.5b:** Student t-Test for the co-located sonic log and ultrasonic core S-wave velocity measurements (after fluid substitution to *in situ* saturations) in the Wolfcamp formation, Delaware basin. Result indicate there is no significant difference between the mean of the sonic log and ultrasonic core measurements.

	<i>Vs_log</i>	<i>Vs_core</i>
Mean	2.58	2.69
Variance	0.019	0.059
Observations	6	6
Pooled Variance	0.039	
Hypothesized Mean Difference	0	
df	10	
<b>t Stat</b>	<b>-0.968</b>	
P(T<=t) one-tail	0.178	
<b>t Critical one-tail</b>	<b>2.764</b>	
P(T<=t) two-tail	0.356	
t Critical two-tail	3.169	
<b> t stat  &lt; t critical; null hypothesis cannot be rejected</b>		

**Table 4.5c:** Student t-Test for the co-located sonic log and ultrasonic core  $V_p/V_s$  ratio (after fluid substitution to *in situ* saturations) in the Wolfcamp formation, Delaware basin. Result indicate there is no significant difference between the mean of the sonic log and ultrasonic core velocity ratios.

	$V_p/V_s_{log}$	$V_p/V_s_{core}$
Mean	1.66	1.64
Variance	0.000	0.001
Observations	6	6
Pooled Variance	0.001	
Hypothesized Mean Difference	0	
df	10	
<b>t Stat</b>	<b>0.921</b>	
P(T<=t) one-tail	0.189	
<b>t Critical one-tail</b>	<b>2.764</b>	
P(T<=t) two-tail	0.379	
t Critical two-tail	3.169	
<b> t stat  &lt; t critical; null hypothesis cannot be rejected</b>		

#### 4.5.3 WOLFCAMP FORMATION – MIDLAND BASIN EXAMPLE

This Wolfcamp shale formation is from Midland basin – a sub-basin of the Permian basin. For the log plot interval shown in figure 4.14, average clay volume is 24%, average total porosity is 7.9%. Matrix permeabilities range from 2 nanoDarcy to 2 microDarcy. Confining stress at which ultrasonic measurements were made was 13.79 MPa. There is a fairly good match between the *in situ* sonic log and laboratory measured ultrasonic velocities. But as in the Delaware basin Wolfcamp formation, there is significant lamination within the Wolfcamp shale.

The mean and standard deviation of the log measured P-wave velocity are 3.87 km/s and 0.32 km/s respectively, while the S-wave velocity mean and standard deviation are 2.29 km/s and 0.18 km/s respectively. For the P-wave velocity laboratory measurements the mean

and standard deviation are respectively 3.90 km/s and 0.18 km/s. The mean laboratory S-wave velocity is 2.45 km/s with a standard deviation of 0.1km/s. After fluid substitution, the mean and standard deviation of the laboratory P-wave velocities are respectively: 2.45 km/s and 0.177 km/s. S-wave velocity mean and standard deviation are 2.45 km/s and 0.1 km/s respectively. The Student t-Test results are shown in tables 4.6a, 4.6b and 4.6c for both P-wave, S-wave velocities and velocity ratio. They indicate that with better than 99% confidence, we cannot reject the null hypothesis that the mean of the sonic log measured velocities is equal to the ultrasonic measurements after fluid substitution; despite the observed significant lamination.

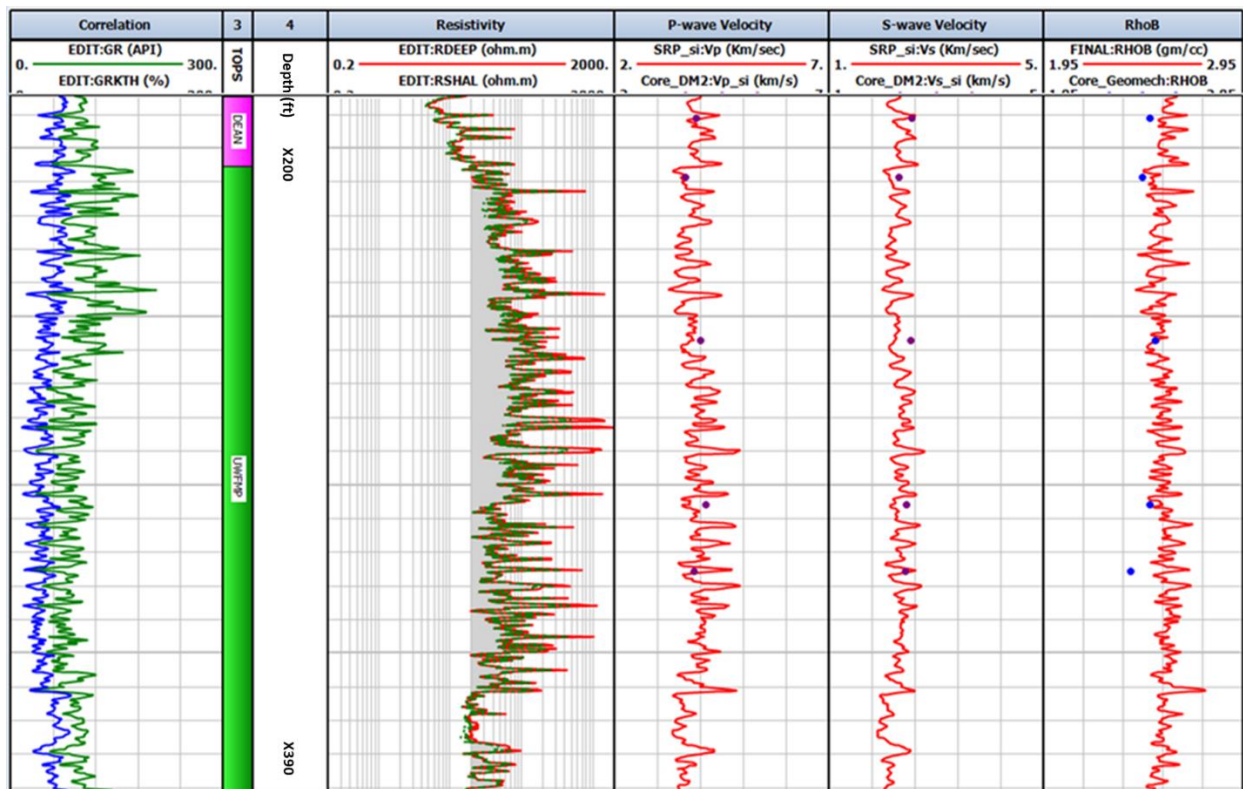


**Figure 4.15:** Log plot of the Wolfcamp shale formation – Midland basin. The GAMMA RAY track contains Gamma-ray (green curve) and spectral gamma-ray (blue curve). The RESISTIVITY track contains resistivity log. The P-wave velocity track contains sonic P-wave velocity (red curve) and ultrasonic P-wave velocity (purple discrete data-points). The S-wave velocity track contains sonic S-wave velocity (red curve) and ultrasonic S-wave velocity (purple discrete data-points). The RhoB track contains log measured bulk density (red curve) and core measured bulk density (blue discrete data). Depths in the depth track are only to indicate depth scale, actual depths are not available for publication.

**Table 4.6a:** Student t-Test for the co-located sonic log and ultrasonic core P-wave velocity measurements (after fluid substitution to *in situ* saturations) in the Wolfcamp formation, Midland basin. The result indicates there is no significant difference between the mean of the sonic log and ultrasonic core measurements.

	<i>Vp_log</i>	<i>Vp_core</i>
Mean	3.87	4.17
Variance	0.105	0.031
Observations	5	5
Pooled Variance	0.068	
Hypothesized Mean Difference	0	
df	8	
<b>t Stat</b>	<b>-1.835</b>	
P(T<=t) one-tail	0.052	
<b>t Critical one-tail</b>	<b>2.896</b>	
P(T<=t) two-tail	0.104	
t Critical two-tail	3.355	
<b>  t stat   &lt; t critical; null hypothesis cannot be rejected</b>		

**Table 4.6b:** Student t-Test for the co-located sonic log and ultrasonic core S-wave velocity measurements (after fluid substitution to *in situ* saturations) in the Wolfcamp formation, Midland basin. The result indicates there is no significant difference between the mean of the sonic log and ultrasonic core measurements.

	<i>Vs_log</i>	<i>Vs_core</i>
Mean	2.29	2.45
Variance	0.033	0.010
Observations	5	5
Pooled Variance	0.022	
Hypothesized Mean Difference	0	
df	8	
<b>t Stat</b>	<b>-1.652</b>	
P(T<=t) one-tail	0.069	
<b>t Critical one-tail</b>	<b>2.896</b>	
P(T<=t) two-tail	0.137	
t Critical two-tail	3.355	
<b>  t stat   &lt; t critical; null hypothesis cannot be rejected</b>		

**Table 4.6c:** Student t-Test for the co-located sonic log and ultrasonic core  $V_p/V_s$  ratio (after fluid substitution to *in situ* saturations) in the Wolfcamp formation, Midland basin. The result indicates there is no significant difference between the mean of the sonic log and ultrasonic core velocity ratios.

	$V_p/V_s_{log}$	$V_p/V_s_{core}$
Mean	1.69	1.71
Variance	0.001	0.002
Observations	5	5
Pooled Variance	0.002	
Hypothesized Mean Difference	0	
df	8	
<b>t Stat</b>	<b>-0.743</b>	
P(T<=t) one-tail	0.239	
<b>t Critical one-tail</b>	<b>2.896</b>	
P(T<=t) two-tail	0.479	
t Critical two-tail	3.355	
<b> t stat  &lt; t critical; null hypothesis cannot be rejected</b>		

#### 4.5.4 LOWER SPRABERRY SHALE EXAMPLE:

The lower Spraberry shale is a liquids rich Permian-age unconventional reservoir formation in the Midland basin. Average clay volume is 26.6% and average total porosity is 6.5% in the lower Spraberry shale interval shown in figure 4.16. In figure 4.16 ultrasonic acoustic measurements made on preserved core samples are compared to *in situ* sonic log measurement. The core data are the discrete data points in the plot, the ultrasonic measurements shown in the plot are those made at a confining stress that is close to *in situ* confining stress at the depths sampled. Measurements were made at 15 MPa, estimated *in situ* confining stress ranges from 12.4 MPa to 15.86 MPa over the sampled interval.

At the log depths where we have ultrasonic core measurements, the mean and standard deviation of the sonic log measurements are 4.36 km/s and 0.12 km/s respectively for P-wave velocity, while S-wave velocity mean and standard deviation are respectively 2.73 km/s and 0.16 km/s. The mean and standard deviation of the laboratory measured P-wave velocity are 4.44 km/s and 0.25 km/s respectively, after fluid substitution the mean and standard deviation are 4.57 km/s and 0.212 km/s respectively. S-wave velocity mean is 2.69 km/s with a standard deviation of 0.24 km/s; after fluid substitution the mean and standard deviation are 2.73 km/s and 0.074 km/s respectively. The Student t-Test results are shown in tables 4.7a, 4.7b and 4.7c for  $V_p$ ,  $V_s$  and their ratio. The results indicate that we cannot reject the null hypothesis that the sonic log and ultrasonic core measurements have the same mean value.

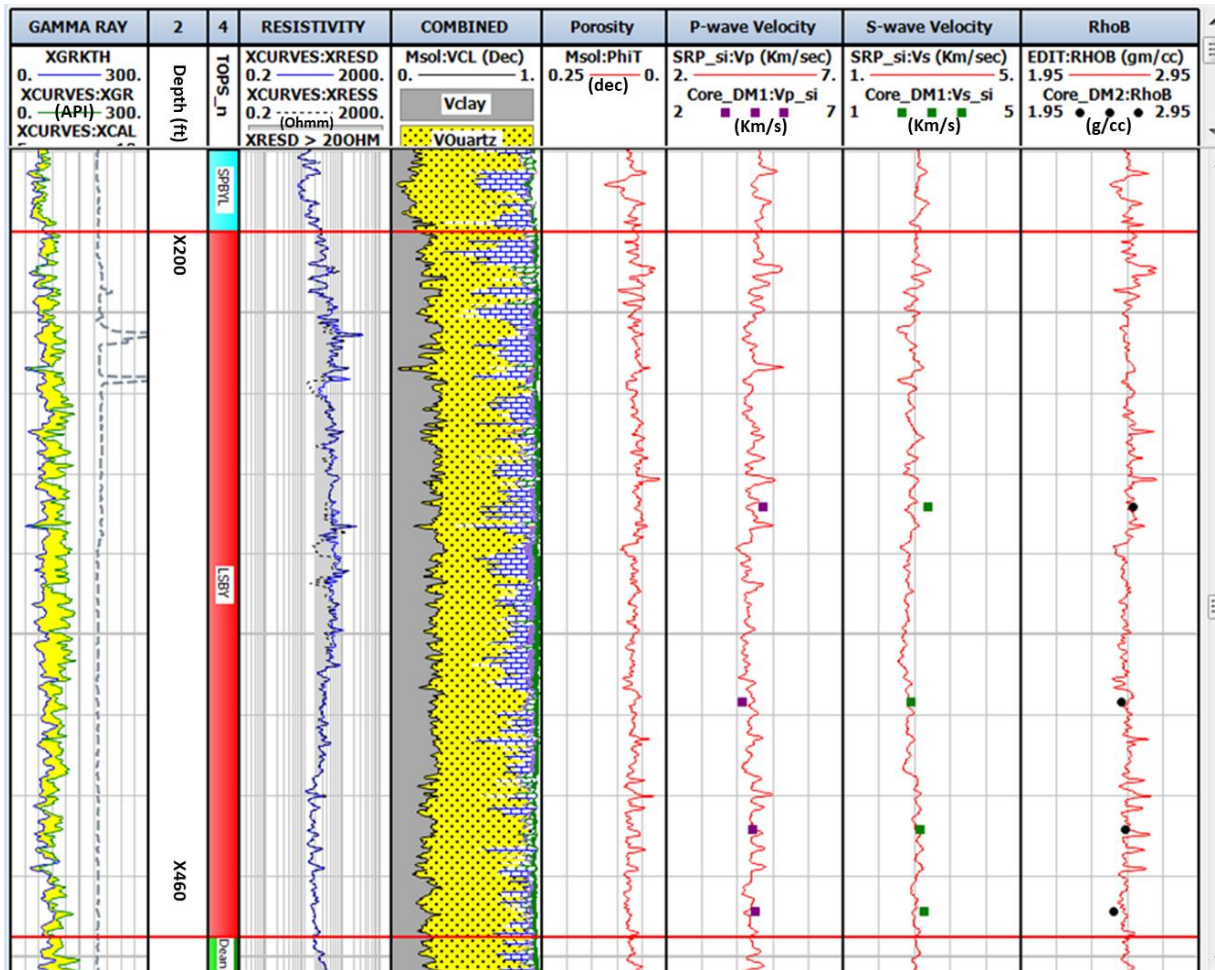


**Figure 4.16:** Log plot of the lower Spraberry shale formation. The GAMMA RAY track contains Gamma-ray (green curve) and spectral gamma-ray (blue curve). The RESISTIVITY track contains resistivity log. The COMBINED track contains formation lithology fractional volumes determined by volumetric log analyses. The porosity track contains total porosity. The P-wave velocity track contains sonic P-wave velocity (red curve) and ultrasonic P-wave velocity (purple square discrete data-points). The S-wave velocity track contains sonic S-wave velocity (red curve) and ultrasonic S-wave velocity (green discrete data-points). The RhoB track contains log measured bulk density (red curve) and core measured bulk density (black discrete data). Depths in the depth track are only to indicate depth scale, actual depths are not available for publication.

**Table 4.7a:** Student t-Test for the co-located sonic log and ultrasonic core P-wave velocity measurements (after fluid substitution to *in situ* saturations) in the lower Spraberry shale formation, Midland basin. The result indicates there is no significant difference between the mean of the sonic log and ultrasonic core measurements.

	<i>Vp_log</i>	<i>Vp_core</i>
Mean	4.36	4.57
Variance	0.014	0.045
Observations	4	4
Pooled Variance	0.030	
Hypothesized Mean Difference	0	
df	6	
<b>t Stat</b>	<b>-1.695</b>	
P(T<=t) one-tail	0.071	
<b>t Critical one-tail</b>	<b>3.143</b>	
P(T<=t) two-tail	0.141	
t Critical two-tail	3.707	
<b> t stat  &lt; t critical; null hypothesis cannot be rejected</b>		

**Table 4.7b:** Student t-Test for the co-located sonic log and ultrasonic core S-wave velocity measurements (after fluid substitution to *in situ* saturations) in the lower Spraberry shale formation, Midland basin. The result indicates there is no significant difference between the mean of the sonic log and ultrasonic core measurements.

	<i>Vs_log</i>	<i>Vs_core</i>
Mean	2.52	2.73
Variance	0.005	0.026
Observations	4	4
Pooled Variance	0.016	
Hypothesized Mean Difference	0	
df	6	
<b>t Stat</b>	<b>-2.322</b>	
P(T<=t) one-tail	0.030	
<b>t Critical one-tail</b>	<b>3.143</b>	
P(T<=t) two-tail	0.059	
t Critical two-tail	3.707	
<b> t stat  &lt; t critical; null hypothesis cannot be rejected</b>		

**Table 4.7c:** Student t-Test for the co-located sonic log and ultrasonic core  $V_p/V_s$  ratio (after fluid substitution to *in situ* saturations) in the lower Spraberry shale formation, Midland basin. The result indicates there is no significant difference between the mean of the sonic log and ultrasonic core velocity ratios.

	$V_p/V_s_{log}$	$V_p/V_s_{core}$
Mean	1.73	1.68
Variance	0.003	0.001
Observations	4	4
Pooled Variance	0.002	
Hypothesized Mean Difference	0	
df	6	
<b>t Stat</b>	<b>1.405</b>	
P(T<=t) one-tail	0.105	
<b>t Critical one-tail</b>	<b>3.143</b>	
P(T<=t) two-tail	0.209	
t Critical two-tail	3.707	
<b> t stat  &lt; t critical; null hypothesis cannot be rejected</b>		

#### 4.5.5 COMBINED RESULTS

For all 4 formations combined, the mean and standard deviation of the sonic log measurements are 4.361 km/s and 0.372 km/s respectively for P-wave velocity, while S-wave velocity mean and standard deviation are respectively 2.594 km/s and 0.221 km/s. The mean and standard deviation of the laboratory measured P-wave velocity for all 4 formations combined are 4.3 km/s and 0.353 km/s respectively; after fluid substitution, the mean and standard deviation are 4.36 and 0.291 respectively. S-wave velocity mean is 2.703 km/s with a standard deviation of 0.219 km/s; after fluid substitution, the mean and standard deviation are 2.73 km/s and 0.218 km/s respectively. The Student t-Test results are shown in tables 4.8a , 4.8b and 4.8c for P-wave, S-wave velocities and velocity ratio respectively; as in the case with

the individual formations, the result indicate that there is no difference between the mean sonic log and ultrasonic measured P-wave and S-wave velocity measurements.

In addition, in tables 4.9a – 4.9c we present the combined result assuming all hydrocarbon liquid is zero during the ultrasonic measurements in the laboratory (i.e., laboratory  $S_o = 0$ ; and laboratory  $S_g = 1 - S_w$ ). Since the core samples were preserved, this scenario is unlikely. However, it is instructive to make the calculations and see even with this unlikely scenario, if dispersion is observed. Tables 4.9a and 4.9b show that there is no significant difference between the mean of the *in situ* sonic log and ultrasonic measurement after fluid substitution assuming all liquid hydrocarbon is lost, for P-wave and S-wave velocities respectively. We similarly observed no significant difference in the mean velocity ratio of the sonic log and ultrasonic measurements after fluid substitution.

The scenario presented in tables 4.10a-4.10c assumes that *in situ* saturation state is equivalent to laboratory saturation state i.e., we are directly comparing the *in situ* sonic log with the laboratory ultrasonic measurements without fluid substitution. This scenario is also unlikely, as there will be some fluid loss due to decreasing temperature and pressure especially for volatile oil when exhuming the rock from the subsurface. But by including this scenario, we have essentially sampled all the possible saturation states that could potentially impact the ultrasonic measurements, even though this scenario is not probable. As shown in tables 4.10a and 4.10b, we cannot reject the null hypothesis that the mean of the sonic log and ultrasonic measurements for both P-wave and S-wave velocities have the same value. However, as shown in table 4.10c, we did not reach the same conclusion for velocity ratio i.e., there is a significant

difference between the mean velocity ratio of the sonic log and ultrasonic measurement when they are compared directly.

**Table 4.8a:** Student t-Test for the sonic log and ultrasonic core P-wave velocity measurements (after fluid substitution to *in situ* saturations) for all 4 formations combined. The results indicate there is no significant difference between the mean of the sonic log and ultrasonic core measurements.

	<i>Vp_log</i>	<i>Vp2</i>
Mean	4.36	4.46
Variance	0.138	0.085
Observations	26	26
Pooled Variance	0.111	
Hypothesized Mean Difference	0	
df	50	
<b>t Stat</b>	<b>-1.116</b>	
P(T<=t) one-tail	0.135	
<b>t Critical one-tail</b>	<b>2.403</b>	
P(T<=t) two-tail	0.270	
t Critical two-tail	2.678	
<b>  t stat   &lt; t critical; null hypothesis cannot be rejected</b>		

**Table 4.8b:** Student t-Test for the sonic log and ultrasonic core S-wave velocity measurements (after fluid substitution to *in situ* saturations) for all 4 formations combined. The results indicate there is no significant difference between the mean of the sonic log and ultrasonic core measurements.

	<i>V<sub>s</sub>_log</i>	<i>V<sub>s</sub>2</i>
Mean	2.59	2.70
Variance	0.049	0.048
Observations	26	26
Pooled Variance	0.048	
Hypothesized Mean Difference	0	
df	50	
<b>t Stat</b>	<b>-1.687</b>	
P(T<=t) one-tail	0.049	
<b>t Critical one-tail</b>	<b>2.403</b>	
P(T<=t) two-tail	0.098	
t Critical two-tail	2.678	
<b> t stat  &lt; t critical; null hypothesis cannot be rejected</b>		

**Table 4.8c:** Student t-Test for the sonic log and ultrasonic core  $V_p/V_s$  ratio (after fluid substitution to *in situ* saturations) for all 4 shale formations combined. The results indicate that there is no significant difference between the mean of the sonic log and ultrasonic core velocity ratios.

	<i>V<sub>p</sub>/V<sub>s</sub>_log</i>	<i>V<sub>p</sub>/V<sub>s</sub>_core</i>
Mean	1.68	1.66
Variance	0.001	0.003
Observations	26	26
Pooled Variance	0.002	
Hypothesized Mean Difference	0	
df	50	
<b>t Stat</b>	<b>1.932</b>	
P(T<=t) one-tail	0.030	
<b>t Critical one-tail</b>	<b>2.403</b>	
P(T<=t) two-tail	0.059	
t Critical two-tail	2.678	
<b> t stat  &lt; t critical; null hypothesis cannot be rejected</b>		

**Table 4.9a:** Student t-Test for the sonic log and ultrasonic core P-wave velocity measurements (after fluid substitution to *in situ* saturations; with the unlikely assumption that Laboratory  $S_o = 0$ ) for all 4 formations combined. The results indicate there is no significant difference between the mean of the sonic log and ultrasonic core measurements.

	<i>Vp_log</i>	<i>Vp2</i>
Mean	4.36	4.47
Variance	0.138	0.082
Observations	26	26
Pooled Variance	0.110	
Hypothesized Mean Difference	0	
df	50	
<b>t Stat</b>	<b>-1.202</b>	
P(T<=t) one-tail	0.118	
<b>t Critical one-tail</b>	<b>2.403</b>	
P(T<=t) two-tail	0.235	
t Critical two-tail	2.678	
<b>  t stat   &lt; t critical; null hypothesis cannot be rejected</b>		

**Table 4.9b:** Student t-Test for the sonic log and ultrasonic core S-wave velocity measurements (after fluid substitution to *in situ* saturations; with the unlikely assumption that Laboratory  $S_o = 0$ ) for all 4 formations combined. The results indicate there is no significant difference between the mean of the sonic log and ultrasonic core measurements.

	<i>Vs_log</i>	<i>Vs2</i>
Mean	2.59	2.69
Variance	0.049	0.048
Observations	26	26
Pooled Variance	0.048	
Hypothesized Mean Difference	0	
df	50	
<b>t Stat</b>	<b>-1.656</b>	
P(T<=t) one-tail	0.052	
<b>t Critical one-tail</b>	<b>2.403</b>	
P(T<=t) two-tail	0.104	
t Critical two-tail	2.678	
<b>  t stat   &lt; t critical; null hypothesis cannot be rejected</b>		

**Table 4.9c:** Student t-Test for the sonic log and ultrasonic core  $V_p/V_s$  ratio measurements (after fluid substitution to *in situ* saturations; with the unlikely assumption that Laboratory  $S_o = 0$ ) for all 4 formations combined. The results indicate there is no significant difference between the mean of the sonic log and ultrasonic core velocity ratios.

	$V_p/V_s_{log}$	$V_p2/V_s2$
Mean	1.68	1.66
Variance	0.001	0.003
Observations	26	26
Pooled Variance	0.002	
Hypothesized Mean Difference	0	
df	50	
<b>t Stat</b>	<b>1.582</b>	
P(T<=t) one-tail	0.060	
<b>t Critical one-tail</b>	<b>2.403</b>	
P(T<=t) two-tail	0.120	
t Critical two-tail	2.678	
<b>  t stat   &lt; t critical; null hypothesis cannot be rejected</b>		

**Table 4.10a:** Student t-Test for the sonic log and ultrasonic core P-wave velocity measurements (after fluid substitution to *in situ* saturations; with the very unlikely assumption that Laboratory  $S_g = 0$ ) for all 4 formations combined. The results indicate there is no significant difference between the mean of the sonic log and ultrasonic core measurements.

	$V_p_{log}$	$V_p_{core}$
Mean	4.36	4.44
Variance	0.138	0.086
Observations	26	26
Pooled Variance	0.112	
Hypothesized Mean Difference	0	
df	50	
<b>t Stat</b>	<b>-0.854</b>	
P(T<=t) one-tail	0.199	
<b>t Critical one-tail</b>	<b>2.403</b>	
P(T<=t) two-tail	0.397	
t Critical two-tail	2.678	
<b>  t stat   &lt; t critical; null hypothesis cannot be rejected</b>		

**Table 4.10b:** Student t-Test for the sonic log and ultrasonic core S-wave velocity measurements (after fluid substitution to *in situ* saturations; with the very unlikely assumption that Laboratory  $S_g = 0$ ) for all 4 formations combined. The results indicate there is no significant difference between the mean of the sonic log and ultrasonic core measurements.

	<i>Vs_log</i>	<i>Vs_core</i>
Mean	2.59	2.69
Variance	0.049	0.048
Observations	26	26
Pooled Variance	0.048	
Hypothesized Mean Difference	0	
df	50	
<b>t Stat</b>	<b>-1.640</b>	
P(T<=t) one-tail	0.054	
<b>t Critical one-tail</b>	<b>2.403</b>	
P(T<=t) two-tail	0.107	
t Critical two-tail	2.678	
<b> t stat  &lt; t critical; null hypothesis cannot be rejected</b>		

**Table 4.10c:** Student t-Test for the sonic log and ultrasonic core  $V_p/V_s$  ratio measurements (after fluid substitution to *in situ* saturations; with the very unlikely assumption that Laboratory  $S_g = 0$ ) for all 4 formations combined. The results indicate there we cannot conclude that there is no significant difference between the mean of the sonic log and ultrasonic core velocity ratios.

	<i>Vp/Vs_log</i>	<i>Vp/Vs_core</i>
Mean	1.68	1.65
Variance	0.001	0.002
Observations	26	26
Pooled Variance	0.002	
Hypothesized Mean Difference	0	
df	50	
<b>t Stat</b>	<b>2.539</b>	
P(T<=t) one-tail	0.007	
<b>t Critical one-tail</b>	<b>2.403</b>	
P(T<=t) two-tail	0.014	
t Critical two-tail	2.678	
<b> t stat  &gt;t critical</b>		

## 4.6 DISCUSSION

Why is it that the squirt-flow model predicts a transition to higher frequency to be in the  $10^9$  Hz range, when for more permeable rocks squirt-flow effects are observed at much lower frequencies? (de Paula et al., 2012; Gurevich, 2012; Mavko and Jizba, 1995). Even in low-permeability rocks, characteristic frequency has been observed to occur at a much lower frequency. Hoffmann (2005), for example, observed that the transition to higher frequency occurs at about 1000 Hz for a high-porosity West Africa shale (Low-frequency measurements by Hoffmann (2005) were based on a forced oscillator setup). To answer that question, we note that the squirt-flow model predicts that increased dispersion is due to open compliant pores at lower effective stresses. In other words, at relatively higher stresses, when the compliant pores are closed, one is unlikely to observe squirt flow between compliant and stiff pores, since the compliant pores will already be closed. Shapiro (2003) concluded that the stress dependencies of velocities and elastic moduli are due to the compliant and stiff pores in the rock. The compliant porosity relation with stress is exponential, at relatively higher stresses when all the compliant pores are closed - the relation between stiff porosity and stress is linear. Note the linear change of porosity with deviatoric stress for our Permian basin sample in figure 4.17, indicating that at the stresses the measurements were made only the stiff pores are open. That this is the case is also evident in the P-wave velocity versus stress plot in figure 4.18.

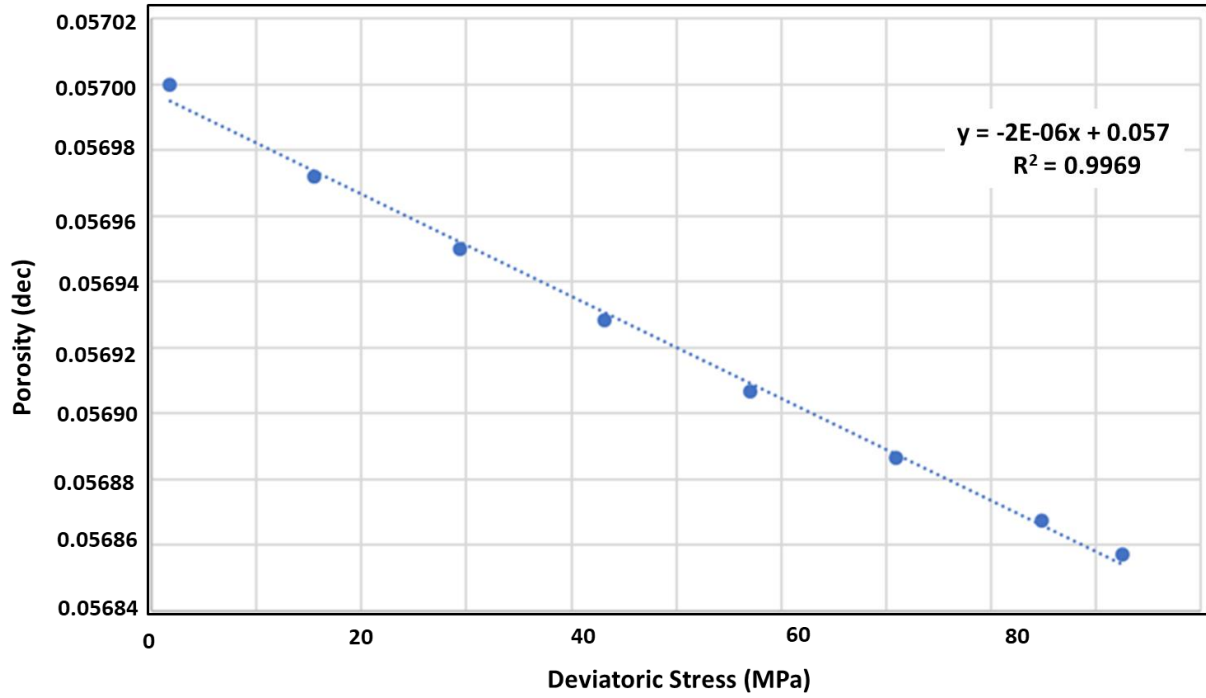


**Figure 4.17:** Change in porosity with deviatoric stress for the dry sample measurement at confining stress of 20.68 MPa.

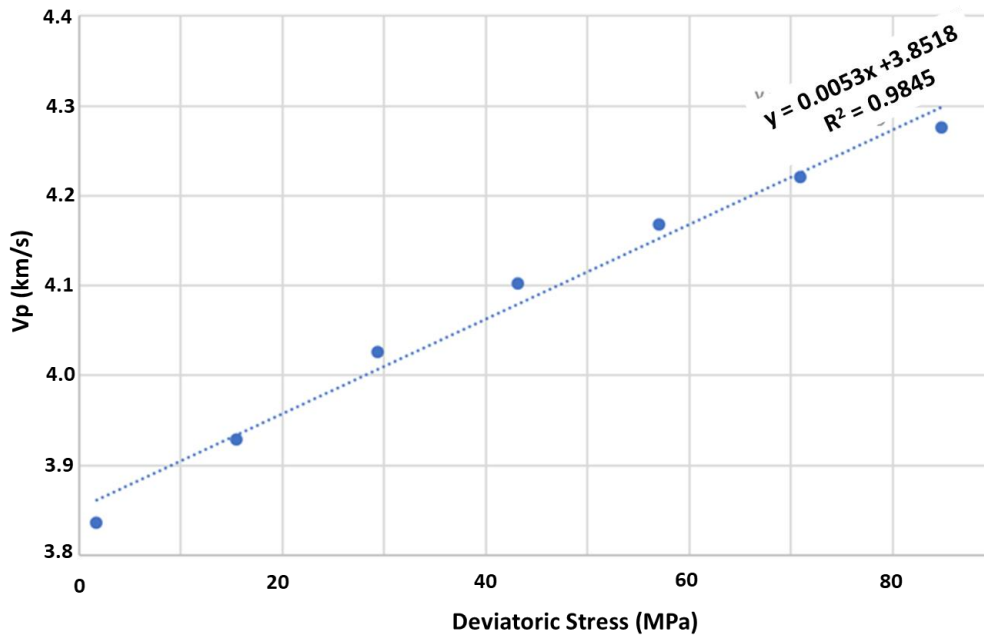


**Figure 4.18:** Change in P-wave velocity with deviatoric stress for the dry sample measurement at confining stress of 20.68 MPa.

However, de Paula et al., (2012) showed that it is possible to further split the stiff pores into moderately stiff pores (intermediate pores) with aspect ratio in the 0.001 to 0.2 range and equant pores with aspect ratio closer to 1. Thus, even when compliant pores are closed, squirt flow between intermediate and equant pores at stresses where the compliant pores are all closed can still occur. We find that we are able to model all the stiff pores with a single effective aspect ratio (de Paula et al., 2012) of 0.06 using the self-consistent approximation for ellipsoidal inclusions (Berryman, 1980). Using equation 31 from de Paula et al., (2012), squirt flow due to the intermediate porosity will yield a characteristic frequency of  $6.46 \times 10^9$  Hz, well above the frequency of ultrasonic experiments in the laboratory. Thus, for our well-consolidated shale samples, the Gurevich (2010) squirt-flow model also predicts that sonic and ultrasonic frequencies are in the same frequency regime.

Our results confirm the experimental observations made by Hofmann (2005) for a low-porosity West Africa shale and by Sarker and Batzle (2010) for the Mancos shale where they observed no significant dispersion on measurements made from seismic to ultrasonic frequencies. These results complement ours, which include a comparison of ultrasonic laboratory and sonic well-log data.

While Liu et al., (1996) also find that seismic, sonic and ultrasonic-frequency measurements in shales are also in the same frequency regime, their determination that squirt-flow transition frequency occurs at about 5 Hz is flawed. This is due to the unusually high characteristic squirt-flow length they assumed ( $10^{-4}$ m) and used to determine the transition

frequency. Loucks et al., (2009) for example, determined from capillary pressure analyses that the dominant pore throat diameter for the low-porosity Barnett shale is in the 5-15 nm range, this is also consistent with dimensions they measured from SEM (scanning electron microscope) images. Similar nanometer range pore throat diameter have been determined by several other authors for low-porosity shales (Saidian et al., 2014; Xu and Sonnenberg, 2017; Milliken et al., 2013 etc.). If instead, we use characteristic squirt-flow length we determined for the Cotton Valley shale (7.3 nm) in the example presented in Liu et al., (1994); the transition frequency will be  $\sim 10^9$  Hz. Which again will place seismic, sonic and ultrasonic frequencies in the same regime and is consistent with what we have determined here.

The positive dispersion effects observed by Szewczyk et al., (2017) are possibly due to their outcrop shale samples having inherent weathering effects. This would require high confining pressures to close compliant pores and cracks, before they would represent a shale at *in situ* stress conditions (Mavko and Jizba, 1990). The same reason likely applies to the dispersion effects observed by Hofmann (2005) in their high-porosity West Africa shale sample; i.e., that it is possibly due to the fact that at the stresses their measurements were made, compliant pores were still open. Best and Sams (1997) for example, noted significant dispersion on near surface sandstones when P-wave velocity was measured at low confining pressures and attribute this to the presence of micro-cracks and fractures. Pimienta et al., (2016) were making a similar point when they observed that the primary contributor to the magnitude of attenuation are open micro-cracks. We emphasize that the focus of this study is on well

consolidated shales. In addition, our measurements were made at *in situ* stress conditions, in part to aid comparison with *in situ* sonic log measurements.

#### 4.6.1 FLUID TYPE:

Our rock samples were saturated with low-salinity brine and the Cotton Valley shale was saturated with de-ionized water. What if the saturating-fluid filling the rock's pore space were liquid hydrocarbons? Consider live oil for example with viscosity of 0.0005 Pa.s, and density of 500 kg/m<sup>3</sup> at *in situ* conditions. Using equation 4.4, characteristic frequency for this fluid will be  $3.78 \times 10^{10}$  Hz based on the Biot-Gassmann model. This will still be about 4 orders of magnitude higher than the ultrasonic frequency measurements. If the saturating fluid is dead oil with viscosity of 0.1 Pa.s and a density of 900 kg/m<sup>3</sup> at surface conditions, the Biot model characteristic frequency will be  $5.04 \times 10^{12}$  Hz, which is even higher frequency when compared to brine-saturated pore space.

#### 4.7 CONCLUSION

For all the low-porosity and permeability lithologies discussed in this study, we find no indication of statistically significant intrinsic dispersion due to fluid effects. We expect this to be a general result for low-permeability consolidated samples. At *in situ* stress conditions, the Gassmann zero-frequency P-wave velocity prediction for the Permian-basin sample was within 0.3% of the measured velocity on the brine-saturated sample at ultrasonic frequency. We observe similar results for this type of data in the Cotton Valley shale. Based on the Biot-Gassmann model, we find that the characteristic frequency occurs at about  $10^{10}$  Hz. Applying a squirt-flow model also predicts a transition to the high frequency regime occurring at about  $10^9$

Hz for both formations. Comparison of *in situ* sonic log measurements for four different shale/tight rock formations to ultrasonic measurements made on core samples at *in situ* stress conditions confirm these findings. There is no significant dispersion due to fluid effects at *in situ* stress conditions within the frequency range typically used in the petroleum industry. There were differences due to scale effects in the variability of the two datasets. The lack of dispersion means that it is possible to compare acoustic measurements at ultrasonic frequencies to measurements made at sonic frequencies without the need for intrinsic dispersion correction. While we have no seismic-frequency measurements to compare to, our modeling using squirt-flow and Biot-Gassmann theory indicate that at normal *in situ* stress conditions, compliant pores are closed and as such seismic, sonic and ultrasonic frequency measurements are all in the same frequency regime for well-consolidated tight rocks.

## BIBLIOGRAPHY

Alfred, D., and L. Vernik, 2012, A new petrophysical model for organic shales: 53rd Annual Logging Symposium, SPWLA conference paper 2012-217.

Altowairqi, Y., R. Rezaee, B. Evans, and M. Urosevic, 2015, Shale elastic property relationships as a function of total organic carbon content using synthetic samples: *Journal of petroleum science* 133, 392-400

Backus, G.E., 1962, Long-wave elastic anisotropy produced by horizontal layering: *Journal of Geophysical Research* 67, 4427-4440

Batzle, M., and Han, D., 2000, Velocity, Density and Modulus of Hydrocarbon Fluids Empirical Modeling: SEG Technical Program Expanded Abstracts

Batzle, M., and Z. Wang, 1992, Seismic properties of pore fluids: *GEOPHYSICS* 57, 1396-1408

Berryman, J.G., 1980, Long-wavelength propagation in composite elastic media II. Ellipsoidal inclusions: *The Journal of the Acoustical Society of America*, 68, 1820;

Berryman, J.G., and G.W. Milton, (1991). Exact results for generalized Gassmann's equations in composite porous media with two constituents. *GEOPHYSICS*, 56(12), 1950-1960;

Best, A.I., and M.S. Sams, 1997, Compressional wave velocity and attenuation at ultrasonic and sonic frequencies in near-surface sedimentary rocks. *Geophysical Prospecting*, 45, 327-344;

Biot, M.A. 1956, Theory of propagation of elastic waves in a fluid saturated porous solid. II higher frequency range. *Journal of the Acoustical Society of America* 28, 179-191;

Brown, R.J.S, 1980, Connection between formation factor for electrical resistivity and fluid-solid coupling factor in Biot's equations for acoustic waves in fluid-filled porous media. *GEOPHYSICS*, 45(8), 1269-1275

Cui, Y.J., M. Yahia-Aissa, and P. Delage, 2002, A model for the volume change behaviour of heavily compacted swelling clays. *Engineering Geology* 64 (2–3), 233–250

de Paula, O. S., Pervukhina, M., Makarynska, D., and Gurevich, B., 2012, Modeling squirt dispersion and attenuation in fluid-saturated rocks using pressure dependency of dry ultrasonic velocities: *GEOPHYSICS*, 77:3, WA157-WA168

Di Maio, C., L. Santoli, and P. Schiavone, 2004, Volume change behavior of clays: the influence of mineral composition, pore fluid composition and stress state. *Mechanics of Materials* 36, 435–451

Domenico, S., N., 1976, Effect of brine-gas mixture on velocity in an unconsolidated sand reservoir., *Geophysics*, 41(5), 882-89

Dvorkin, Gary Mavko, and Amos Nur, 1995, Squirt flow in fully saturated rocks., *Geophysics*, 60(1), 97-107

Gas Research Institute (GRI), 1996, Development of laboratory and petrophysical techniques for evaluating shale reservoirs: GRI-95/0496.

Gassmann, F., 1951, *Über die elastizität poroser medien: Mitteilungen Inst. Geophysik (Zurich)*, 17, 1–23. Translated and reprinted as: *On elasticity of porous media*, in, M. A. Pelissier, ed., *Classics of elastic wave theory*: SEG, 2007.

Geertsma, J., and D. C. Smit, 1961, Some aspects of elastic wave propagation in fluid-saturated porous solids: *GEOPHYSICS*, 26, 169–181

Gong, F., B. Di, J. Wei, P. Ding, X. Pan, and S. Zu, 2018, Ultrasonic-velocity and mechanical anisotropy of synthetic-shale with different types of clay minerals: *GEOPHYSICS* 83, MR57-MR66

Gor, G.Y., and B. Gurevich, 2018, Gassmann theory applies to nanoporous media: *Geophysical Research Letters*, 45, 146-155

Greenberg, M.L., and J. P. Castagna, 1992, Shear-wave velocity estimation in porous rocks: theoretical formulation, preliminary verification and applications: *Geophysical Prospecting* 40, 195-209

Gurevich, B., D. Makarynska, O. B. de Paula, and M. Pervukhina, 2010, A simple model for squirt-flow dispersion and attenuation in fluid-saturated granular rocks: *GEOPHYSICS*, 75, no. 6, 109–120

Hashin, Z., and S. Shtrikman, 1963, A variational approach to the theory of the elastic behavior of multiphase materials: *Journal of the Mechanics and Physics of Solids*, Volume 11, Issue 2, p. 127-140

Hill, R., 1952, The elastic behavior of a crystalline aggregate: *Proceedings of the Physical Society, Section A*, Volume 65, Issue 5, 349–354

Hofmann R., 2005, Frequency dependent elastic and anelastic properties of clastic rocks: PhD Thesis, Colorado School of Mines.

Holt, R. M., E. F. Sonstebø, P. Horsrud, and R. Skaflestad, 1996, Fluid Effects on Acoustic Wave Propagation in Shales. *International Society for Rock Mechanics*;

Jaeger, J. C., N.G.W. Cook and R.W. Zimmerman, 2007, Fundamentals of rock mechanics 4<sup>th</sup> edition: Blackwell Publishing.

Johnson, D.L., T.J. Plona, C. Scala, F. Pasierb and H. Kojima, 1982. Tortuosity and acoustic slow waves. Physical review letters, 49(25), 1840-1844

Johnston J.E., and N.I. Christensen, 1995, Seismic anisotropy of shales: Journal of Geophysical Research, 100, No. B4, 5991-6003

Johnston, D. H., 1999, Physical properties of shale at temperature and pressure: SEG Technical Program Expanded Abstracts 4(1)

Katahara, K. W., 1996, Clay mineral elastic properties. SEG Technical Program Expanded Abstracts 1996: pp. 1691-1694

Lide, D.R., ed., CRC Handbook of Chemistry and Physics, Internet Version 2005, <<http://www.hbcnetbase.com>>, CRC Press, Boca Raton, FL.

Liu, X., L. Vernik, and A. Nur, 1994, Effects of saturating fluids on seismic velocities in shale. SEG Technical Program Expanded Abstracts 1994: pp. 1121-1124

Loucks, R.G., R.M. Reed, S.C. Ruppel, and D.M. Jarvie, 2009, Morphology, Genesis, and Distribution of Nanometer-Scale Pores in Siliceous Mudstones of the Mississippian Barnett Shale. Journal of Sedimentary Research 79 (12): 848-861

Lucier, A.M., R. Hofmann, and L. T. Bryndzia, 2011, "Evaluation of variable gas saturation on acoustic log data from the Haynesville Shale gas play, NW Louisiana, USA." The Leading Edge, 30(3), 300-311

Luffel, D. L., F. K. Guidry, and J. B. Curtis, 1992, Evaluation of Devonian shale with new core and log analysis methods: *Journal of Petroleum Technology*, 44, 1192–1197, 10.2118/21297-PA

Marcote, A., Mavko, G., and Prasad, M., 2010, Dynamic elastic properties of coal: *GEOPHYSICS*, **75**, no. 6, E227-E234

Marion, D., T. Mukerji, and G. Mavko, 1994, Scale effects on velocity dispersion: from ray theory to effective medium theories in stratified media: *GEOPHYSICS*, 59, no. 10, 1613-1619

Mavko, G. and D. Jizba, 1991, Estimating grain scale fluid effects on velocity dispersion in rocks: *GEOPHYSICS*, 56, no. 12, 1940-1949

McDonal, F.J., F.A., Angona, R.L. Mills, R.L. Sengbush, R.G Van Nostrand, and J.E White, 1958, Attenuation of shear and compressional waves in Pierre shale: *GEOPHYSICS* Vol 23, No. 3

Milliken, K.L, M. Rudnicki, D. N. Awwiller, and T. Zhang, 2013, Organic matter–hosted pore system, Marcellus Formation (Devonian), Pennsylvania. *AAPG Bulletin*, v. 97, no. 2 (February 2013), pp. 177–200

Myers, M.T., and L.A. Hathon, 2009, Staged Differential effective medium (SDEM) models for acoustic velocity. *SEG Technical Program Expanded Abstracts 2009*: pp. 2130-2134

Nguyen, X.P., Y.J. Cui, A.M. Tang, Y.F. Deng, X.L. Li, and L. Wouters, 2013, Effects of pore water chemical composition on the hydro-mechanical behavior of natural stiff clays. *Engineering Geology* 166 (2013) 52–64

Omovie, S.J. and J.P. Castagna, 2019, P-to-S-wave velocity ratio in Organic shales: *GEOPHYSICS* Vol. 84, No. 6

Passey, Q.R., S. Creaney, J.B. Kulla, F.J. Moretti, and J.D. Stroud, 1990, A practical model for organic richness from porosity and resistivity logs: AAPG Bulletin, 74, 1777-1794

Peselnick, L. and W.F. Outerbridge, 1961, Internal friction in shear and shear modulus of Solenhofen limestone over a frequency range of  $10^7$  cycles per second: JOURNAL OF GEOPHYSICAL RESEARCH, VOL. 66, no. 2, 581-588

Quirein, J., J. Witkowsky, J. Truax, J. Galford, D. Spain, and T. Odumosu, 2010, Integrating core data and wireline geochemical data for formation evaluation and characterization of shale gas reservoirs: SPE 134559, SPE Annual Technical Conference and Exhibition

Robinson, R.G., and M.M. Allam, 1998. Effect of mineralogy on coefficient of consolidation. Clays and Clay Minerals 46 (5), 596–600

Saidian, M., U. Kuila, S. Rivera, L. J. Godinez, and M. Prasad, 2014, Porosity and Pore Size Distribution in Mudrocks: A Comparative Study for Haynesville, Niobrara, Monterey and Eastern European Silurian Formations. Unconventional Resources Technology Conference (URTeC)

Sams, M. S., J. P. Neep, M. H. Worthington, and M. S. King, 1997, The measurement of velocity dispersion and frequency-dependent intrinsic attenuation in sedimentary rocks: GEOPHYSICS VOL 62, NO. 5

Sarker, R. and M. Batzle, 2010, Anisotropic elastic moduli of the Mancos B Shale- An experimental study: SEG Technical Program Expanded Abstracts 1994: pp. 1121-1124

Sayers, C., K. Fisher, and J. Walsh, 2015, Rock physics of the Eagle Ford Shale. SEG Technical Program Expanded Abstracts 2015: pp. 3036-3041

Schmoker, J.W., 1979, Determination of Organic Content of Appalachian Devonian Shales from Formation-Density Log: AAPG Bulletin, 63(9), 1504-1509

Schmoker, J.W. and Hester, T.C., 1983, Organic Carbon in Bakken Formation, United States Portion of Williston Basin, AAPG Bulletin, **67**, no. 12, 2165-2174

Shapiro, S. A., 2003, Elastic piezosensitivity of porous and fractured rocks: GEOPHYSICS, 68, 482–486

Spencer J. W., 1981, Stress relaxations at low Frequencies in fluid-Saturated rocks: attenuation and modulus dispersion: JOURNAL OF GEOPHYSICAL RESEARCH, VOL. 86, NO. B3, PAGES 1803-1812

Szewczyk, D., R.M. Holt, and A. Bauer, 2017, The impact of saturation on seismic dispersion in shales - Laboratory measurements: GEOPHYSICS, VOL. 83, NO. 1

Tosaya C. A., 1982, Acoustical properties of clay bearing rocks: PhD Thesis, Stanford University.

Tran, M.T., 2014, Formation Evaluation of an Unconventional Shale Reservoir: Application to the North Slope Alaska, M.S., Thesis, Stanford University

Vernik, L., 2016, Seismic Petrophysics in Quantitative Interpretation: Society of Exploration Geophysicists

Vernik, L., and C. Landis, 1996, Elastic anisotropy of source rocks: Implications for hydrocarbon generation and primary migration, AAPG Bulletin, 80, 531–544

Vernik, L., and Kachanov, M., 2010, Modeling elastic properties of siliclastic rocks: GEOPHYSICS, **75**, no. 6, E171-E182

Vernik, L., and X. Liu, 1996, Velocity anisotropy in shales: A petrophysical study: *GEOPHYSICS*, 62, 521-532

Vernik, L., and J. Milovac, 2011, Rock physics of organic shales: *The Leading Edge*, 30, no. 3, 318–323

Vosburgh, E.T., O.A. Djordjevic, and J.A. Rushing, 2013, Liquids-rich resource play characterization using well-log analysis calibrated with rock properties from drill cuttings: URTEC 1620306, Unconventional Resources Technology Conference

Wang, Z., H. Wang, and M.E. Cates, 2001, Effective elastic properties of solid clays: *GEOPHYSICS*, 66, no. 2, P428-440

Wang, Z. and A. Nur, 1990, Dispersion Analysis of acoustic velocities in rocks: *Journal of Acoustical Society of America*, 87, 2384-2395

Xie, J., J. Cao, D.R. Schmitt, B. Di, L. Xiao, X. Wang, K. Wang, and Y. Chen, 2019, Effects of kerogen content on elastic properties-based on artificial organic-rich shale (AORS): *JOURNAL OF GEOPHYSICAL RESEARCH*

Xu, J., and S. A. Sonnenberg, 2017, An SEM Study of Porosity in the Organic-rich Lower Bakken Member and Pronghorn Member, Bakken Formation, Williston Basin. Unconventional Resources Technology Conference (URTEC)

Xu, S., and White, R.E., 1996, A new velocity model for clay-sand mixtures: *Geophysical Prospecting* **43**, 91-118

Yan, F., and Han, D., 2013, Measurement of elastic properties of kerogen: SEG Technical Program Expanded Abstracts

Zhang, J., T. Al-Bazali, M. Chenevert, M. Sharma, D. Clark, S. Benaissa, and S. Ong, 2006, Compressive Strength and Acoustic Properties Changes in Shale with Exposure to Water-Based Fluids. American Rock Mechanics Association

## APPENDIX A

### ***Ultrasonic Measurements on Dry and Partially Saturated Inorganic shales***

We would like guidance from laboratory measurements and theoretical modeling in determining the relative contribution from solid kerogen and free fluid hydrocarbons. Along with the usual difficulties in interpreting laboratory data (such as dispersion, sampling, achieving full saturation in low permeability rocks and experimental error), many of the relevant laboratory measurements performed by us and reported in the literature are made on “dry” samples. Can a dry sample be taken as representative for the velocities of water-wet hydrocarbon-saturated shales? Figure A-1 shows bedding-normal ultrasonic-velocity measurements comparing velocity trends for dry and partially water-saturated shale samples from a cored offshore Gulf of Mexico well to the GC-92 global trend for fully brine-saturated shales. Although TOC measurements were not performed on these shales, the samples were described as being of normal low organic content; certainly not approaching the kerogen volumes in onshore shale reservoirs. Mineralogical composition from X-ray diffraction is primarily clays and quartz. Clay plus quartz fractional volumes varied between .9 and 1.0, the calcite content was less than .1 and other constituents totaled less than .01 fractional volume. The *in situ* saturations were not preserved upon coring. The samples were first dried, and velocity measurements were made over a range of confining pressures (7 - 55 MPa). Afterward, the partial saturations were obtained by immersing the same samples in saline water for several hours, but not allowing sufficient time for the samples to become fully water saturated (see Johnston, 1999). The differential pressure range for the partially saturated

velocity measurements was also 7 - 55 MPa. Given the differing pressure histories for the measurements, a detailed comparison of velocities on individual samples is not very informative. However, comparing the regression trends (summarized in Table A-1) is instructive. For practical purposes, there is no significant difference between the dry and partially saturated regression lines at these pressures, and both exhibit significantly lower  $V_p/V_s$  at a given  $V_p$  than the GC-92 brine-saturated shale line (Figure A-1). Fluid substitution performed on the regression lines essentially reproduced the GC-92 trend, although given the uncertainties in the reported shale physical properties, the errors in the calculation are too large to draw definitive conclusions other than the direction of the saturation effect, which is consistent with the data. However, we are confident in concluding directly from the measurements that, given sufficient porosity, air (and presumably free compressible hydrocarbons) in the pore space will significantly reduce the  $V_p/V_s$  ratio in shales, without high solid organic content.

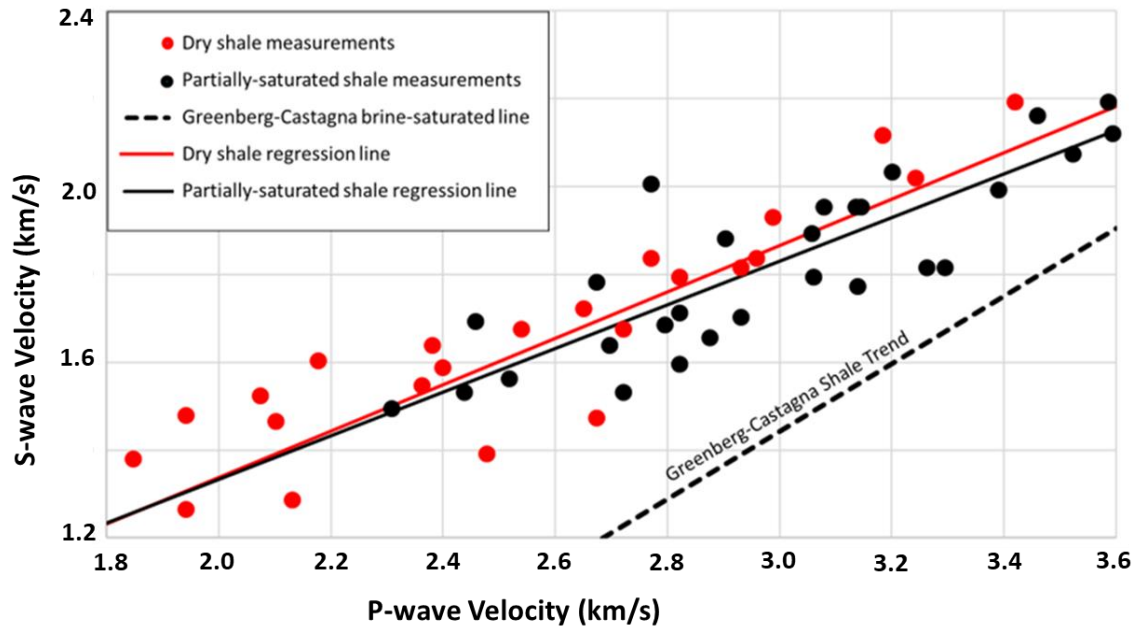


**Figure A-1:** P-wave versus S-wave ultrasonic-velocity measurements on offshore Gulf of Mexico dry (red circles) and partially saturated (black circles) shale core samples. Regression fits to the dry (red line) and partially saturated (black line) are compared to the GC-92 fully brine-saturated shale trend (dashed black line) given by  $V_s = .77 V_p - .867$ .

**Table A-1:** Regression statistics for the shale data in Figure B-2 using a linear equation:  $V_s = a V_p + b$ . The combined regression is for all the dry and partially saturated shale datapoints.  $R^2$  is the correlation coefficient squared and an indication of the variance in the data accounted for by the regression trend. The high F-statistic and low sig F indicate that the regressions are all statistically highly significant. The standard error of the estimate is .11 km/s for all the regressions. a is unitless and b has units of km/s.

Measurement type	b	Standard error b	a	Standard error a	$R^2$	F	Sig F
Dry shale	0.282	0.132	0.527	0.0513	0.833	109.7	5.00E-10
Partially saturated shale	0.341	0.168	0.496	0.0556	0.747	79.7	2.00E-09
Combined	0.385	0.092	0.488	0.0325	0.816	225.7	2.00E-20
GC-92 shale	-0.867		0.77				

## APPENDIX B

### ***Anisotropic Gassmann Fluid Substitution***

While we have assumed isotropy in our fluid substitution implementation, most of the rock samples and shale formations we have studied are weakly anisotropic (Thomsen, 1986). The use of the isotropic Gassmann equation is partly motivated by the fact that we often do not measure all the parameters required to fully characterize the stiffness tensor of an anisotropic rock sample. In this section we seek to determine the errors incurred in assuming isotropy for a weakly anisotropic rock or formation.

For anisotropic porous rock, Gassmann's equation in terms of linear elastic stiffness components is given by (Gassmann, 1951):

$$C_{ijkl}^{sat} = C_{ijkl}^{dry} + \frac{(K_m \delta_{ij} - \frac{C_{ij\alpha\alpha}^{dry}}{3})(K_m \delta_{kl} - \frac{C_{\beta\beta kl}^{dry}}{3})}{\phi \left( \frac{K_m}{K_{fl}} \right) (K_m - K_{fl}) + (K_m - \frac{C_{ppqq}^{dry}}{9})} \quad (B1)$$

Where  $\delta_{ij} = 1, \text{ for } i = j; \delta_{ij} = 0, \text{ for } i \neq j$

In rocks having vertical transverse isotropy, Mavko and Bandyopadhyay (2009) came up with an approximate anisotropic fluid substitution equation for vertical P-wave velocity. They also showed by means of numerical simulation the validity of the approximate equation for Thomsen anisotropic parameter  $\delta$  as high as 0.3. Mavko and Banyoypadhyay (2009) approximate equation is given below:

$$C_{33}^{sat} \approx C_{33}^{dry} + \frac{\left( \frac{K_{fl}}{K_m} \right) \left[ K_m - K_{iso}^{dry} - \left( \frac{2}{3} \right) C_{33}^{dry} \delta \right]^2}{\phi \left( K_m - K_{fl} \right) + \left( \frac{K_{fl}}{K_m} \right) \left( K_m - K_{iso}^{dry} \right)} \quad (B2)$$

Where  $K_{iso}^{dry}$ ,  $K_{fl}$ ,  $K_m$  are the elastic bulk moduli of the dry rock, the saturating pore fluid, and the solid mineral respectively.  $C_{33}^{sat}$  and  $C_{33}^{dry}$  are the vertical P-wave modulus of the saturated and dry rock respectively.

For the Cotton Valley shale, Tosaya (1982) obtained the stiffness tensor required to fully characterize this rock. We apply the above equation to the sample measurement at confining stress of 49.63 MPa for which we have both dry and saturated vertical velocities. The stiffnesses for the saturated measurements are shown in table B-1. We then compare the result to what was obtained assuming isotropy shown in table 2.2 in the fluid effect sub-section.

**Table B-1:** Cotton Valley shale elastic moduli from Tosaya (1982). Stiffnesses are in GPa.

<b>Pc (MPa)</b>	<b>C11</b>	<b>C33</b>	<b>C66</b>	<b>C13</b>	<b>C44</b>	<b>C12</b>
49.63	66.480	54.280	26.388	24.601	19.089	13.900

The Thomsen anisotropy parameter  $\delta$ , required in equation B2 is given by (Thomsen, 1986):

$$\delta = \frac{(C_{13} + C_{44})^2 - (C_{33} - C_{44})^2}{2C_{33}(C_{33} - C_{44})} \quad (B3)$$

The vertical P-wave velocity determined from applying equation B2 is 4.51 Km/s. This yields a 1.4% error when compared to the measured vertical P-wave velocity. This is a significant improvement when compared to the 2.5% error obtained by applying the isotropic Gassmann fluid substitution equation.

## APPENDIX C

In this section, we describe how the Student t-Test results reported for each formation was calculated

### Student t-Test: Comparing 2 independent samples – Colocated log and core datapoints

- Null Hypothesis:

$H_0: \mu_1 - \mu_2 = 0$ , where  $\mu_1$  is the mean of all sonic log velocity in the formation, and  $\mu_2$  is the mean of all core measured ultrasonic-velocity measurements in the formation

- Step 1: Compute t-value using the following formula

$$t = \frac{\bar{X}_1 - \bar{X}_2}{s_{\bar{\Delta}}}$$

where

$$s_{\bar{\Delta}} = \sqrt{\frac{s_1^2}{n_1} + \frac{s_2^2}{n_2}}$$

$$d. f. = \frac{\left(\frac{s_1^2}{n_1} + \frac{s_2^2}{n_2}\right)^2}{\frac{(s_1^2/n_1)^2}{n_1-1} + \frac{(s_2^2/n_2)^2}{n_2-1}}$$

$\bar{X}_1$  is mean of sample 1

$\bar{X}_2$  is mean of sample 2

$n_1$  is number of sample 1 observations

$n_2$  is number of sample 2 observations

$s_1$  is standard deviation of sample 1

$s_2$  is standard deviation of sample 2

df is degree of freedom

CI confidence interval is 99%

$\alpha$  is  $1 - CI/100$

Step 2: Compute critical t value (one and two-tail) at df and  $\alpha=0.01$

- If calculated t-value is greater than the critical t-value, the means are significantly different (compare absolute values)
- Else, If calculated t-value is less than the critical t-value, we cannot reject the null hypothesis
- Note that while we are only interested in the one-tail test, we have included both the one-tail and two-tail results

## APPENDIX D

**Table D-1:** Sonic log and ultrasonic core measured P-wave and S-wave velocities for the 4 formations. BSPG\_DB is Bonespring formation Delaware basin. WFMP\_DB is Wolfcamp formation Delaware basin. WFMP\_MB is Wolfcamp formation Midland basin. And LSBY\_MB is Lower Spraberry formation Midland basin.

Formation	Vp_log	Vs_log	PhiT	Vp_core	Vs_core	RhoB_core
BSPG_DB	km/s	km/s	Dec	km/s	km/s	g/cc
	4.6149	2.7631	0.0883	4.393	2.942	2.48
	4.9093	2.9219	0.1284	4.595	2.807	2.38
	4.4299	2.6105	0.0679	4.678	2.87	2.50
	4.4592	2.6301	0.0667	4.306	2.673	2.55
	4.8568	2.8602	0.039	4.68	3.152	2.65
	4.6876	2.767	0.093	4.61	2.908	2.49
	4.4083	2.6752	0.075	4.495	2.851	2.48
	4.4838	2.7323	0.0678	3.965	2.41	2.52
	4.6315	2.7982	0.0911	4.483	2.793	2.49
	4.3	2.6152	0.0678	4.486	2.748	2.57
	5.1759	3.0407	0.063	4.312	2.759	2.56
<b>WFMP_DB</b>						
	3.977	2.4107	0.0728	4.479	2.81	2.52
	4.3917	2.6189	0.0669	3.708	2.467	2.55
	4.3668	2.6447	0.0276	4.986	2.995	2.63
	4.2166	2.5494	0.0589	4.528	2.917	2.60
	4.0853	2.4548	0.069	3.777	2.454	2.53
	4.6032	2.7886	0.065	4.046	2.521	2.54
<b>WFMP_MB</b>						
	4.039	2.435	0.065	3.891	2.534	2.480
	3.560	2.127	0.084	3.642	2.291	2.440
	3.852	2.221	0.053	3.999	2.527	2.510
	3.575	2.148	0.045	4.132	2.480	2.480
	4.324	2.533	0.046	3.858	2.421	2.390
<b>LSBY_MB</b>						
	4.249	2.452	0.057	4.725	2.898	2.580
	4.476	2.476	0.065	4.118	2.520	2.520
	4.447	2.614	0.051	4.417	2.714	2.540
	4.269	2.551	0.081	4.501	2.807	2.480